

Ministry of Education and Science of the Russian Federation
Saint Petersburg National Research University of Information
Technologies, Mechanics, and Optics

NANOSYSTEMS:
PHYSICS, CHEMISTRY, MATHEMATICS

2018, volume 9(3)

Наносистемы: физика, химия, математика

2018, том 9, № 3



NANOSYSTEMS:

PHYSICS, CHEMISTRY, MATHEMATICS

ADVISORY BOARD MEMBERS

Chairman: V.N. Vasiliev (*St. Petersburg, Russia*),
V.M. Buznik (*Moscow, Russia*); V.M. Ievlev (*Voronezh, Russia*), P.S. Kop'ev (*St. Petersburg, Russia*), N.F. Morozov (*St. Petersburg, Russia*), V.N. Parmon (*Novosibirsk, Russia*),
A.I. Rusanov (*St. Petersburg, Russia*),

EDITORIAL BOARD

Editor-in-Chief: I.Yu. Popov (*St. Petersburg, Russia*)

Section Co-Editors:

Physics – V.M. Uzdin (*St. Petersburg, Russia*),
Chemistry, material science – V.V. Gusarov (*St. Petersburg, Russia*),
Mathematics – I.Yu. Popov (*St. Petersburg, Russia*).

Editorial Board Members:

V.M. Adamyan (*Odessa, Ukraine*); O.V. Al'myasheva (*St. Petersburg, Russia*);
A.P. Alodjants (*Vladimir, Russia*); S. Bechta (*Stockholm, Sweden*); J. Behrndt (*Graz, Austria*);
M.B. Belonenko (*Volgograd, Russia*); V.G. Bepalov (*St. Petersburg, Russia*); J. Brasche (*Clausthal, Germany*);
A. Chatterjee (*Hyderabad, India*); S.A. Chivilikhin (*St. Petersburg, Russia*); A.V. Chizhov (*Dubna, Russia*);
A.N. Enyashin (*Ekaterinburg, Russia*); P.P. Fedorov (*Moscow, Russia*); E.A. Gudilin (*Moscow, Russia*);
V.K. Ivanov (*Moscow, Russia*); H. Jónsson (*Reykjavik, Iceland*); A.A. Kiselev (*Durham, USA*); Yu.S. Kivshar (*Canberra, Australia*);
S.A. Kozlov (*St. Petersburg, Russia*); P.A. Kurasov (*Stockholm, Sweden*); A.V. Lukashin (*Moscow, Russia*);
V.A. Margulis (*Saransk, Russia*); I.V. Melikhov (*Moscow, Russia*); G.P. Miroshnichenko (*St. Petersburg, Russia*);
I.Ya. Mittova (*Voronezh, Russia*); H. Neidhardt (*Berlin, Germany*); V.V. Pankov (*Minsk, Belarus*); K. Pankrashkin (*Orsay, France*);
A.V. Ragulya (*Kiev, Ukraine*); V. Rajendran (*Tamil Nadu, India*); A.A. Rempel (*Ekaterinburg, Russia*);
V.Ya. Rudyak (*Novosibirsk, Russia*); D. Shoikhet (*Karmiel, Israel*); P. Stovicek (*Prague, Czech Republic*);
V.M. Talanov (*Novocherkassk, Russia*); A.Ya. Vul' (*St. Petersburg, Russia*); A.V. Yakimansky (*St. Petersburg, Russia*); V.A. Zagrebnev (*Marseille, France*).

Editors:

I.V. Blinova; A.I. Popov; A.I. Trifanov; E.S. Trifanova (*St. Petersburg, Russia*),
R. Simoneaux (*Philadelphia, Pennsylvania, USA*).

Address: University ITMO, Kronverkskiy pr., 49, St. Petersburg 197101, Russia.

Phone: +7(812)312-61-31, **Journal site:** <http://nanojournal.ifmo.ru/>,

E-mail: popov1955@gmail.com.

AIM AND SCOPE

The scope of the journal includes all areas of nano-sciences. Papers devoted to basic problems of physics, chemistry, material science and mathematics inspired by nanosystems investigations are welcomed. Both theoretical and experimental works concerning the properties and behavior of nanosystems, problems of its creation and application, mathematical methods of nanosystem studies are considered.

The journal publishes scientific reviews (up to 30 journal pages), research papers (up to 15 pages) and letters (up to 5 pages). All manuscripts are peer-reviewed. Authors are informed about the referee opinion and the Editorial decision.

CONTENT

MATHEMATICS

- B.I. Islomov, A.A. Abdullaev
On a problem for an elliptic type equation of the second kind with a conormal and integral condition 307
- E.Yu. Rakhimov
Method of application three-dimensional billiard systems in passive heating systems 319
- Z.R. Rakhmonov, A.I. Tillaev
On the behavior of the solution of a nonlinear polytropic filtration problem with a source and multiple nonlinearities 323

PHYSICS

- E.V. Boroznina, O.A. Kakorina, M.B. Belonenko
Double-layered boron. The adsorption of gas-phase atom 330
- V.S. Molchanov, I.A. Klepikov, I.V. Razumovskaya, O.E. Philippova
Magnetically tunable viscoelastic response of soft magnetic nanocomposites with wormlike surfactant micellar matrix 335
- A.G. Petrashen, N.V. Sytenko
Theoretical study of the slow light in the assembly of helium atoms 342
- V. Rudyak, A. Belkin
Molecular dynamics simulation of fluid viscosity in nanochannels 349
- A.S. Varentsova, M.N. Potkina, S. von Malottki, S. Heinze, P.F. Bessarab
Interplay between size and stability of magnetic skyrmions 356
- A.S. Vorokh
Scherrer formula: estimation of error in determining small nanoparticle size 364

CHEMISTRY AND MATERIAL SCIENCE

- A.N. Bokarev, I.L. Plastun
Possibility of drug delivery due to hydrogen bonds formation in nanodiamonds and doxorubicin: molecular modeling 370
- A.N. Bugrov, R.Yu. Smyslov, A.Yu. Zavialova,
D.A. Kirilenko, D.V. Pankin
Phase composition and photoluminescence correlations in nanocrystalline $ZrO_2:Eu^{3+}$ phosphors synthesized under hydrothermal conditions 378

S.I. Gusev, P.S. Demchenko, E.A. Litvinov, O.P. Cherkasova, I.V. Meglinski, M.K. Khodzitsky Study of glucose concentration influence on blood optical properties in THz frequency range	389
I.V. Kolesnik, V.A. Lebedev, A.V. Garshev Optical properties and photocatalytic activity of nanocrystalline TiO₂ doped by 3d-metal ions	401
A.A. Krasilin, I.S. Bodalyov, A.A. Malkov, E.K. Khrapova, T.P. Maslennikova, A.A. Malygin On an adsorption/photocatalytic performance of nanotubular Mg₃Si₂O₅(OH)₄/TiO₂ composite	410
I.A. Milyaeva, N.S. Perov, V.V. Bessalova, M.V. Berezhnaya, V.O. Mittova, Anh Tien Nguyen, I.Ya. Mittova Synthesis and properties of nanoscale films of the Y₂O₃-Fe₂O₃ system on silicon	417
Anh Tien Nguyen, Chau Hong Diem, Nguyen Thi Truc Linh, V.O. Mittova, Do Tra Huong, I.Ya. Mittova Structural and magnetic properties of YFe_{1-x}Co_xO₃ (0.1 ≤ x ≤ 0.5) perovskite nanomaterials synthesized by co-precipitation method	424
A.L. Popov, I.V. Savintseva, E.A. Mysina, A.B. Shcherbakov, N.R. Popova, O. S. Ivanova, D.D. Kolmanovich, V.K. Ivanov Cytotoxicity analysis of gadolinium doped cerium oxide nanoparticles on human mesenchymal stem cells	430
Information for authors	439

On a problem for an elliptic type equation of the second kind with a conormal and integral condition

B. I. Islomov¹, A. A. Abdullaev²

¹National University of Uzbekistan named after Mirzo Ulugbek,
Differential equations and Mathematical physics, 100174, Tashkent, Uzbekistan

²Tashkent Institute of Irrigation and Agricultural Mechanization Engineers,
Higher mathematics, Str. Kari Niyaziy, 39, 100000, Tashkent, Uzbekistan

islomovbozor@yandex.ru, akmal09.07.85@mail.ru

DOI 10.17586/2220-8054-2018-9-3-307-318

In this paper, we prove the uniqueness of a solution of the boundary value problem for an elliptic type equation of the second kind with the conormal and integral condition.

Keywords: elliptic type equation of the second kind, boundary value problems, boundary problems with Poincaré condition, integral equation.

Received: 11 January 2018

Revised: 3 March 2018

1. Introduction

The Poincaré problem with the conormal derivative are studied by Tricomi, Lavrentyev–Bitsadze and Gellerstedt [1–5].

Boundary value problems with the conormal derivative for the elliptic type equation with one and two lines of degeneration of the first kind is considered when on the lines of degeneration a function or its derivative is given by M. A. Usanatashvili [6], M. S. Salokhitdinov and B. Islomov [7, 8], H. Islomov [9].

In this paper, we prove the unique solvability of a boundary value problem with the conormal and integral condition for the elliptic type equation of the second kind.

Stationary processes of a various physical nature (oscillations, heat conductivity, diffusion, electrostatics, etc.) are described by equations of the elliptic type [10]. In particular, in some nanophysical models such as hydrodynamics and gas dynamics elliptic equations are considered.

2. Boundary value problem with a conormal and integral condition

We consider the boundary value problem with a conormal and integral conditions for the following elliptic type equation of the second kind:

$$y^m u_{xx} + u_{yy} = 0, \quad (1)$$

where $-1 < m < 0$ is a real number. Let D be a simply connected domain in the plane (x, y) bounded by a curve σ at the first quadrant ($x > 0, y > 0$) with its end points $A(0, 0)$, $B(1, 0)$ and with the line segment AB of the real axis Ox .

Let us introduce the following notations:

$$J = \{(x, y) : 0 < x < 1, y = 0\}, \quad \partial D = \bar{\sigma} \cup \overline{AB}, \quad 2\beta = \frac{m}{m+2},$$

note that as it is defined, we have:

$$-\frac{1}{2} < \beta < 0. \quad (2)$$

We denote by $C(D)$ the space of continuous functions defined on a set D on the (x, y) plane or on the real line and $C^k(D)$ denotes the space of k continuously differentiable functions on D .

In the domain D , we consider the following Problem Conormal (Problem CN) for the equation (1):

Problem CN. Find a function $u(x, y)$ with the following properties:

- (1) $u(x, y) \in C(\bar{D}) \cup C^1(D \cup \sigma \cup J)$ and u_x, u_y can tend to infinity of the order less than -2β at points $A(0, 0)$ and $B(1, 0)$;
- (2) $u(x, y) \in C^2(D)$ is a solution of the equation (1) in D ;

(3) $u(x, y)$ – satisfies the following boundary conditions:
for all $0 < s < l$

$$\left\{ \delta(s)A_s[u] + \rho(s)u \right\} \Big|_{\sigma} = \varphi(s) \tag{3}$$

for all $0 < x < 1$

$$a_0(x)u_y(x, 0) + \sum_{j=1}^n a_j(x)D_{0x}^{\alpha_j}u(x, 0) + a_{n+1}(x)u(x, 0) = b(x), \tag{4}$$

where $\delta(s)$, $\rho(s)$, $\varphi(s)$, $a_j(x)$, and $b(x)$ are given functions with the following conditions:

$$b(0) = 0, \quad a_0(1) \neq 0, \tag{5}$$

$$a_0(x) \neq 0, \quad \forall x \in \bar{J}, \tag{6}$$

$$\delta^2(s) + \rho^2(s) \neq 0, \quad \forall s \in [0, l], \tag{7}$$

$$\sum_{j=0}^{n+1} a_j^2(x) \neq 0, \quad \forall x \in \bar{J}, \tag{8}$$

$$\delta(s), \rho(s), \varphi(s) \in C[0, l], \tag{9}$$

$$a_j(x), b(x) \in C(\bar{J}) \cap C^2(J), \quad (j = \overline{0, n+1}), \tag{10}$$

and

$$A_s[u] = y^m \frac{dy}{ds} \frac{\partial u}{\partial x} - \frac{dx}{ds} \frac{\partial u}{\partial y},$$

$\frac{dx}{ds} = -\cos(n, y)$, $\frac{dy}{ds} = \cos(n, x)$, where n is the external normal to the curve σ , l is the length of the curve σ , s is the length of an arc of the curve σ , starting from the point $B(1, 0)$, and $D_{0x}^{\alpha_j}[*]$ is the Riemann–Liouville integral operator of a fractional order α [11]:

$$D_{0x}^{\alpha_j}f(x) = \frac{1}{\Gamma(-\alpha_j)} \int_0^x \frac{f(t)dt}{(x-t)^{\alpha_j+1}}, \quad -1 < \alpha_j < 0. \tag{11}$$

Let $\alpha = \max_{1 \leq j \leq n} \{|\alpha_j|\}$, and

$$\alpha \leq -2\beta. \tag{12}$$

We assume that the curve σ satisfies the following conditions:

- (1) functions $x(s)$, $y(s)$, which are the parametric representations of the curve σ , have continuous derivatives $x'(s)$, $y'(s)$, and don't tend to zero at the same time, moreover, they have the second derivatives that satisfy Hölder condition of an exponent κ ($0 < \kappa < 1$) in the interval $0 \leq s \leq l$;
- (2) near the endpoints of the curve σ , they satisfy inequalities:

$$\left| \frac{dx}{ds} \right| \leq const \cdot y^{m+1}(s), \tag{13}$$

and $x(l) = y(0) = 0$, $x(0) = 1$, $y(l) = 0$.

3. Uniqueness of the solution of Problem CN

Assume we have:

$$-1 < \alpha_j < 0, \quad \delta(s) \neq 0, \quad \forall s \in [0, l], \tag{14}$$

then the uniqueness of a solution of Problem CN can be proved by the method of integral energy. We have the following.

Theorem 1. *If conditions (2), (5), (6), (7), (8) are satisfied and:*

$$\delta(s)\rho(s) \geq 0, \quad 0 \leq s \leq l, \tag{15}$$

$$\frac{a_{n+1}(x)}{a_0(x)} \leq 0, \tag{16}$$

$$\left(\frac{a_j(x)}{a_0(x)} \right)'_x \geq 0, \quad \frac{a_j(1)}{a_0(1)} \leq 0, \quad (j = \overline{1, n}), \tag{17}$$

then Problem CN in the domain D can't have more than one solution.

Proof of Theorem 1. Let (x, y) be a point inside the domain D . Consider a domain $D_\delta^\varepsilon \in D$, bounded by a curve σ_ε , parallel to σ , and a segment of the straight line $y = \delta$ ($\delta > \varepsilon > 0$). We choose δ, ε small enough such that the point (x, y) belongs to the domain D_δ^ε and $u(x, y) \in C^2(\bar{D}_\delta^\varepsilon)$.

We use the following identity:

$$u[y^m u_{xx} + u_{yy}] = \frac{\partial}{\partial x}[y^m u u_x] + \frac{\partial}{\partial y}[u u_y] - y^m u_x^2 - u_y^2. \tag{18}$$

Integrating (18) on domain D_δ^ε results in:

$$0 = \iint_{D_\delta^\varepsilon} u[y^m u_{xx} + u_{yy}] dx dy = \iint_{D_\delta^\varepsilon} \left\{ \frac{\partial}{\partial x}[y^m u u_x] + \frac{\partial}{\partial y}[u u_y] \right\} dx dy - \iint_{D_\delta^\varepsilon} [y^m u_x^2 + u_y^2] dx dy,$$

and applying Gauss–Ostrogradsky formula (the Green’s theorem) (see [11]):

$$\iint_{D_\delta^\varepsilon} \left\{ \frac{\partial P}{\partial x} - \frac{\partial Q}{\partial y} \right\} dx dy = \int_{\partial D_\delta^\varepsilon} Q dx + P dy$$

we obtain:

$$0 = \iint_{D_\delta^\varepsilon} u[y^m u_{xx} + u_{yy}] dx dy = - \iint_{D_\delta^\varepsilon} [y^m u_x^2 + u_y^2] dx dy + \int_{\partial D_\delta^\varepsilon} u[y^m u_x dy - u_y dx].$$

From here on, by considering AB : $y = 0 \Rightarrow dy = 0$, and $dy = \cos(n, x) ds$, $dx = -\cos(n, y) ds$ we have:

$$0 = - \iint_{D_\delta^\varepsilon} [y^m u_x^2 + u_y^2] dx dy - \int_{x_1}^{x_2} u(x, \delta) u_y(x, \delta) dx + \int_{\sigma_\varepsilon} u A_s[u] ds, \tag{19}$$

where x_1, x_2 – are the abscissas of the points of the intersection of the straight line $y = \delta$ with the curve σ_ε . Taking into account the conditions (1) of Problem CN and $\varphi(s) \equiv b(x) \equiv 0$ from (19) with (3) at $\delta(s) \neq 0$ and $\varepsilon \rightarrow 0, \delta \rightarrow 0$ we get the following:

$$\iint_D [y^m u_x^2 + u_y^2] dx dy + \int_0^1 \tau(x) \nu(x) dx + \int_\sigma \frac{\delta(s) \rho(s)}{\delta^2(s)} u^2 ds = 0, \tag{20}$$

where:

$$u(x, 0) = \tau(x), \quad (x, 0) \in \bar{J}, \quad u_y(x, 0) = \nu(x), \quad (x, 0) \in J. \tag{21}$$

Due to the condition (15), the third integral of equality (20) implies that:

$$R_3 = \int_\sigma \frac{\delta(s) \rho(s)}{\delta^2(s)} u^2 ds \geq 0. \tag{22}$$

Now, we show that the second term of the left-hand side of (20) is nonnegative.

By (8) and (21), taking into account (4), we get:

$$\nu(x) = - \left[\sum_{j=1}^n \frac{a_j(x)}{a_0(x)} D_{0x}^{\alpha_j} \tau(x) + \frac{a_{n+1}(x)}{a_0(x)} \tau(x) \right].$$

Using (12), we rewrite the second term of (20) in the form:

$$R_2 = \int_0^1 \tau(x) \nu(x) dx = - \int_0^1 \sum_{j=1}^n \frac{a_j(x) \tau(x)}{\Gamma(-\alpha_j) a_0(x)} dx \int_0^x \frac{\tau(t) dt}{(x-t)^{1+\alpha_j}} - \int_0^1 \frac{a_{n+1}(x)}{a_0(x)} \tau^2(x) dx = R_{21} + R_{22}. \tag{23}$$

Using the following formula (see [1]):

$$|x-t|^{-\gamma} = \frac{1}{\Gamma(\gamma) \cos \frac{\pi\gamma}{2}} \int_0^\infty z^{\gamma-1} \cos[z(x-t)] dz, \quad 0 < \gamma < 1$$

and from the equality (23), we obtain:

$$\begin{aligned}
 R_{21} &= - \int_0^1 \sum_{j=1}^n \frac{a_j(x)\tau(x)dx}{a_0(x)\Gamma(-\alpha_j)\Gamma(1+\alpha_j)\cos\pi(1+\alpha_j)/2} \int_0^x \tau(t)dt \int_0^\infty z^{\alpha_j} \cos z(x-t)dz \\
 &= -2 \sum_{j=1}^n \cos \frac{\pi\alpha_j}{2} \int_0^\infty z^{\alpha_j} dz \int_0^1 \frac{a_j(x)\tau(x)}{a_0(x)} dx \int_0^x [\cos zx \cos zt + \sin zx \sin zt] \tau(t)dt \\
 &= - \sum_{j=1}^n \cos \frac{\pi\alpha_j}{2} \int_0^\infty z^{\alpha_j} dz \int_0^1 \frac{a_j(x)}{a_0(x)} \cdot \frac{\partial}{\partial x} \left[\left(\int_0^x \tau(t) \cos ztdt \right)^2 + \left(\int_0^x \tau(t) \sin ztdt \right)^2 \right].
 \end{aligned}$$

Integrating the last integrals by parts on x , we have:

$$\begin{aligned}
 R_{21} &= - \sum_{j=1}^n \cos \frac{\pi\alpha_j}{2} \int_0^\infty z^{\alpha_j} dz \left\{ \frac{a_j(x)}{a_0(x)} \left[\left(\int_0^x \tau(t) \cos ztdt \right)^2 + \left(\int_0^x \tau(t) \sin ztdt \right)^2 \right] \right\} \Big|_{x=0}^{x=1} \\
 &\quad - \int_0^1 \left(\frac{a_j(x)}{a_0(x)} \right)'_x \left[\left(\int_0^x \tau(t) \cos ztdt \right)^2 + \left(\int_0^x \tau(t) \sin ztdt \right)^2 \right] dx \Big\} \\
 &= - \sum_{j=1}^n \cos \frac{\pi\alpha_j}{2} \int_0^\infty z^{\alpha_j} \frac{a_j(1)}{a_0(1)} \left[\left(\int_0^x \tau(t) \cos ztdt \right)^2 + \left(\int_0^x \tau(t) \sin ztdt \right)^2 \right] dz \\
 &\quad + \sum_{j=1}^n \cos \frac{\pi\alpha_j}{2} \int_0^\infty z^{\alpha_j} dz \int_0^1 \left(\frac{a_j(x)}{a_0(x)} \right)'_x \left[\left(\int_0^x \tau(t) \cos ztdt \right)^2 + \left(\int_0^x \tau(t) \sin ztdt \right)^2 \right] dx.
 \end{aligned}$$

Hence, by (17) we have

$$R_{21} \geq 0. \tag{24}$$

Furthermore, by (16) and (23), we have:

$$R_{22} \geq 0. \tag{25}$$

Finally, using (24) and (25), by (23), we obtain:

$$R_2 \geq 0. \tag{26}$$

Using the relations (22) and (26), by (20) it follows that $u_x = u_y = 0$ in D , that is, $u = const$ for all $(x, y) \in D$. The fact that each term in (20) tends to zero concludes $u = 0$ on $\bar{\sigma}$. Thus, $u \equiv 0$ in \bar{D} for $\delta(s) \neq 0$.

Remark. The uniqueness of a solution of Problem CN for $\rho(s) \neq 0, \forall s \in [0, l]$ is proved using the maximum principle [7].

Theorem 1 is proved.

4. Existence of a solution of Problem CN for $\delta(s) \neq 0$

We consider the following auxiliary problem.

Problem DK. Find a solution $u(x, y) \in C(\bar{D}) \cap C^1(D \cup \sigma \cup J) \cap C^2(D)$ of the equation (1) in the domain D that satisfies conditions (3) and the following:

$$u|_{y=0} = \tau(x), \quad 0 \leq x \leq 1, \tag{27}$$

where $\tau(x)$ is a continuous function that satisfies Hölder condition with the exponent $\gamma_0 \geq 1 - 2\beta$ in the interval $(0, 1)$ and it have the following representation:

$$\tau(x) = \int_x^1 (t-x)^{-2\beta} T(t)dt, \tag{28}$$

where a function $T(t)$ is continuous in $(0, 1)$ and it is integrated in $[0, 1]$.

The uniqueness of a solution of Problem DK follows from identity (20).

The solution of Problem DK that satisfies conditions (3) and (27) for the equation (1) in the domain D exists and unique, moreover it has the following representation (see [11, eq. (10.78)]):

$$u(x, y) = \int_0^1 \tau(\xi) \frac{\partial}{\partial \eta} G_2(\xi, 0; x, y) d\xi + \int_0^l \frac{\varphi(s)}{\delta(s)} G_2(\xi, \eta; x, y) ds, \tag{29}$$

where $G_2(\xi, \eta; x, y)$ is the Green's function of Problem DK for equation (1), and it has the following form (see, [11]):

$$G_2(\xi, \eta; x, y) = G_{02}(\xi, \eta; x, y) + H_2(\xi, \eta; x, y), \tag{30}$$

where $G_{02}(\xi, \eta; x, y)$ is the Green's function of Problem DK for equation (1) on the normal domain D_0 bounded with the segment \overline{AB} and the normal curve $\sigma_0 : \left(x - \frac{1}{2}\right)^2 + \frac{4}{(m+2)^2} y^{m+2} = \frac{1}{4}$

$$\begin{aligned} H_2(\xi, \eta; x, y) &= G_2(\xi, \eta; x, y) - G_{02}(\xi, \eta; x, y) \\ &= \int_0^l \lambda_2(s; \xi, \eta) \left\{ A_s[G_{02}(\xi(s), \eta(s); x, y)] + \frac{\rho(s)}{\delta(s)} G_{02}(\xi(s), \eta(s); x, y) \right\} ds, \end{aligned} \tag{31}$$

where $\lambda_2(s; \xi, \eta)$ is a solution of the integral equation:

$$\begin{aligned} \lambda_2(s; \xi, \eta) + 2 \int_0^l \lambda_2(t; \xi, \eta) \left\{ A_s[q_2(\xi(t), \eta(t); x(s), y(s))] + \frac{\rho(s)}{\delta(s)} q_2(\xi(t), \eta(t); x(s), y(s)) \right\} dt \\ = -2q_2(\xi(s), \eta(s); \xi, \eta), \end{aligned} \tag{32}$$

where $q_2(x, y, x_0, y_0)$ is the fundamental solution of the equation (1) and it has the following form:

$$q_2(x, y, x_0, y_0) = k_2 \left(\frac{4}{m+2} \right)^{4\beta-2} (r_1^2)^{-\beta} (1-\sigma)^{1-2\beta} F(1-\beta, 1-\beta, 2-2\beta; 1-\sigma), \tag{33}$$

where:

$$\begin{aligned} \left. \begin{aligned} r_1^2 \} &= (x-x_0)^2 + \frac{4}{(m+2)^2} \left(y^{\frac{m+2}{2}} \mp y_0^{\frac{m+2}{2}} \right)^2, \\ \sigma &= \frac{r^2}{r_1^2}, \quad \beta = \frac{m}{2(m+2)} < 0, \quad k_2 = \frac{1}{4\pi} \left(\frac{4}{m+2} \right)^{2-2\beta} \frac{\Gamma^2(1-\beta)}{\Gamma(2-2\beta)}, \end{aligned} \right\} \end{aligned}$$

where $F(a, b, c; z)$ is the Gauss hypergeometric function [7].

Differentiating the equation (29) by y , then by tending y to zero and by (30) and (33), we obtain a functional relation between $\tau(x)$ and $\nu(x)$, transferred from the domain D to J :

$$\nu(x) = k_2 \int_0^1 |t-x|^{2\beta-2} \tau(t) dt - k_2 \int_0^1 \frac{\tau(t) dt}{(t+x-2tx)^{2-2\beta}} + \int_0^1 \tau(t) \frac{\partial^2 H_2(t, 0; x, 0)}{\partial \eta \partial y} dt + \int_0^l \chi(s) \frac{\partial q_2(t, \eta; x, 0)}{\partial y} ds, \tag{34}$$

where $\chi(s)$ is a solution of the integral equation:

$$\chi(s) + 2 \int_0^l \chi(t) \left\{ A_s[q_2(\xi(t), \eta(t); x(s), y(s))] + \frac{\rho(s)}{\delta(s)} q_2(\xi(t), \eta(t); x(s), y(s)) \right\} dt = \frac{2\varphi(s)}{\delta(s)}. \tag{35}$$

Lemma 1. Let a function $\tau(x)$ belongs to the class $C^{(1, \gamma_1)}(0, 1)$, $\gamma_1 \geq -2\beta$, then the following identities hold on $(0, 1)$:

$$\int_0^x (x-t)^{2\beta-2} \tau(t) dt = \frac{1}{2\beta(2\beta-1)} \frac{d^2}{dx^2} \int_0^x (x-t)^{2\beta} \tau(t) dt, \tag{36}$$

$$\int_x^1 (t-x)^{2\beta-2} \tau(t) dt = \frac{1}{2\beta(2\beta-1)} \frac{d^2}{dx^2} \int_x^1 (t-x)^{2\beta} \tau(t) dt, \tag{37}$$

where $0 < -2\beta < 1$.

Proof. We rewrite identities (36) and (37) as follows:

$$T_1(x) = \lim_{\varepsilon \rightarrow 0} T_{1\varepsilon}(x) = \lim_{\varepsilon \rightarrow 0} \left\{ \frac{d^2}{dx^2} \int_0^{x-\varepsilon} (x-t)^{2\beta} \tau(t) dt \right\}$$

and

$$T_2(x) = \lim_{\varepsilon \rightarrow 0} T_{2\varepsilon}(x) = \lim_{\varepsilon \rightarrow 0} \left\{ \frac{d^2}{dx^2} \int_{x+\varepsilon}^1 (t-x)^{2\beta} \tau(t) dt \right\}.$$

It follows that:

$$\begin{aligned} T_{1\varepsilon}(x) &= \frac{d}{dx} \left[\varepsilon^{2\beta} \tau(x-\varepsilon) + 2\beta \int_0^{x-\varepsilon} (x-t)^{2\beta-1} \tau(t) dt \right] \\ &= \varepsilon^{2\beta} \tau'(x-\varepsilon) + 2\beta \varepsilon^{2\beta-1} \tau(x-\varepsilon) + 2\beta(2\beta-1) \int_0^{x-\varepsilon} (x-t)^{2\beta-2} \tau(t) dt, \end{aligned} \quad (38)$$

$$\begin{aligned} T_{2\varepsilon} &= \frac{d}{dx} \left[-\varepsilon^{2\beta} \tau(x+\varepsilon) - 2\beta \int_{x+\varepsilon}^1 (t-x)^{2\beta-1} \tau(t) dt \right] \\ &= -\varepsilon^{2\beta} \tau'(x+\varepsilon) + 2\beta \varepsilon^{2\beta-1} \tau(x+\varepsilon) + 2\beta(2\beta-1) \int_{x+\varepsilon}^1 (t-x)^{2\beta-2} \tau(t) dt. \end{aligned} \quad (39)$$

The conditions of the Lemma 1 and relations (38) and (39) at $\varepsilon \rightarrow 0$ imply the identities (36) and (37). This completes the proof.

Lemma 2. Let $\tau(x) \in C^{(1, \gamma_1)}(0, 1)$, $\gamma_1 \geq -2\beta$ and it is representable in the form of (28), then the following identities hold on $(0, 1)$:

$$\begin{aligned} \int_0^x (x-t)^{2\beta-2} \tau(t) dt &= \frac{1}{2\beta(2\beta-1)} \frac{d^2}{dx^2} \int_0^x (x-t)^{2\beta} \tau(t) dt \\ &= \frac{\Gamma(1+2\beta)\Gamma(1-2\beta)}{2\beta(2\beta-1)} D_{0x}^{1-2\beta} D_{x1}^{2\beta-1} T(x) \\ &= \frac{\pi \cot \pi 2\beta}{1-2\beta} T(x) - \frac{1}{1-2\beta} \int_0^1 \left(\frac{t}{x}\right)^{1-2\beta} \frac{T(t)}{t-x} dt, \end{aligned} \quad (40)$$

$$\begin{aligned} \int_x^1 (t-x)^{2\beta-2} \tau(t) dt &= \frac{1}{2\beta(2\beta-1)} \frac{d^2}{dx^2} \int_x^1 (t-x)^{2\beta} \tau(t) dt \\ &= \frac{\Gamma(1+2\beta)\Gamma(1-2\beta)}{2\beta(2\beta-1)} D_{x1}^{1-2\beta} D_{x1}^{2\beta-1} T(x) \\ &= \frac{\pi}{(2\beta-1) \sin 2\beta\pi} T(x), \end{aligned} \quad (41)$$

$$\begin{aligned} \int_0^1 (t+x-2tx)^{2\beta-2} \tau(t) dt &= \int_0^1 (t+x-2tx)^{2\beta-2} dt \int_t^1 (z-t)^{-2\beta} T(z) dz \\ &= \frac{1}{1-2\beta} \int_0^1 \left(\frac{t}{x}\right)^{1-2\beta} \frac{T(t) dt}{x+t-2xt}, \end{aligned} \quad (42)$$

where $(0 < -2\beta < 1)$.

Proof. Using definitions of the integro-differential operator with a fractional order (see [11, §4, (4.1), (4.6)]):

$$D_{px}^\sigma f(x) = \begin{cases} \frac{1}{\Gamma(-\sigma)} \int_p^x (x-t)^{-\sigma-1} f(t) dt, & x \in (p, q), \sigma < 0, \\ f(x), & \sigma = 0, \\ \frac{d^n}{dx^n} [D_{px}^{\sigma-n} f(x)], & n-1 < \sigma \leq n, n \in \mathbb{N}, \end{cases}$$

and representation (28) and the identity $\Gamma(z)\Gamma(1-z) = \pi/\sin \pi z$ from the right-hand side of (40) implies that:

$$\begin{aligned} A_1 &= \int_0^x (x-t)^{2\beta-2} \tau(t) dt = \frac{1}{2\beta(2\beta-1)} \frac{d^2}{dx^2} \int_0^x (x-t)^{2\beta} \tau(t) dt \\ &= \frac{1}{2\beta(2\beta-1)} \frac{d^2}{dx^2} \int_0^x (x-t)^{2\beta} dt \int_t^1 (z-t)^{-2\beta} T(z) dz \\ &= \frac{\Gamma(1+2\beta)\Gamma(1-2\beta)}{2\beta(2\beta-1)} \frac{d^2}{dx^2} D_{0x}^{-(1+2\beta)} D_{x1}^{2\beta-1} T(x) = \frac{\pi}{(2\beta-1)\sin 2\beta\pi} D_{0x}^{1-2\beta} D_{x1}^{2\beta-1} T(x). \end{aligned} \quad (43)$$

Using the formula (see [11, p. 24, lemma 4.5]):

$$D_{ax}^\alpha D_{xb}^{-\alpha} \Phi(x) = \cos \pi\alpha \Phi(x) + \frac{\sin \pi\alpha}{\pi} \int_a^b \left(\frac{t-a}{x-a}\right)^\alpha \frac{\Phi(t)}{t-x} dt, \quad 0 < \alpha < 1$$

and the equality (43) we have:

$$A_1 = \frac{\pi \cot 2\beta\pi}{1-2\beta} T(x) - \frac{1}{1-2\beta} \int_0^1 \left(\frac{t}{x}\right)^{1-2\beta} \frac{T(t)}{t-x} dt.$$

The last equality implies the identity (40).

Now we prove the identity (41). Due to the representation (28) we have:

$$\begin{aligned} A_2 &= \int_x^1 (t-x)^{2\beta-2} \tau(t) dt = \frac{1}{2\beta(2\beta-1)} \frac{d^2}{dx^2} \int_x^1 (t-x)^{2\beta} \tau(t) dt \\ &= \frac{1}{2\beta(2\beta-1)} \frac{d^2}{dx^2} \int_x^1 (t-x)^{2\beta} \tau(t) dt \int_t^1 (z-t)^{-2\beta} T(z) dz. \end{aligned}$$

Using definitions of the integro-differential operator with a fractional order (see, [11, §4, see (4.13), (4.14)]):

$$D_{xq}^\sigma f(x) = \begin{cases} \frac{1}{\Gamma(-\sigma)} \int_x^b (t-x)^{-\sigma-1} f(t) dt, & x \in (p, q), \sigma < 0, \\ f(x), & \sigma = 0, \\ (-1)^n \frac{d^n}{dx^n} [D_{xb}^{-(n-\sigma)} f(x)], & n-1 < \sigma \leq n, n \in \mathbb{N}, \end{cases} \quad (44)$$

and the formula $D_{xb}^\alpha D_{xb}^{-\alpha} f(x) = f(x)$, we have:

$$A_2 = \frac{\pi}{(2\beta-1)\sin 2\beta\pi} D_{x1}^{1-2\beta} D_{x1}^{-(1-2\beta)} T(x) = \frac{\pi}{(2\beta-1)\sin 2\beta\pi} T(x).$$

The last equality implies the identity (41).

We consider the expression:

$$A_3 = \int_0^1 (t+x-2tx)^{2\beta-2} \tau(t) dt. \quad (45)$$

Substituting (28) into (42), and changing the order of the integrations, we have:

$$A_3 = \int_0^1 (t+x-2tx)^{2\beta-2} dt \int_t^1 (z-t)^{-2\beta} T(z) dz = \int_0^1 T(z) dz \int_0^z (z-t)^{-2\beta} (t+x-2tx)^{2\beta-2} dt.$$

Putting $t = z(1-s)$ in internal integral and using the formula (see [11, p.8, (2.10)])

$$\int_0^1 t^{a-1} (1-t)^{c-a-1} (1-zt)^{-b} dt = \frac{\Gamma(a)\Gamma(c-a)}{\Gamma(c)} F(a, b, c; z),$$

$$0 < \operatorname{Re} a < \operatorname{Re} c, \quad |\arg(1-z)| < \pi. \tag{46}$$

We obtain:

$$\begin{aligned} A_3 &= \int_0^1 T(z) z^{-2\beta+1} (z+x-2xz)^{2\beta-2} dz \int_0^1 s^{-2\beta} \left[1 - \frac{(1-2x)zs}{(z+x-2xz)} \right]^{2\beta-2} ds \\ &= \frac{\Gamma(1-2\beta)\Gamma(1)}{\Gamma(2-2\beta)} \int_0^1 \left(\frac{z}{x+z-2xz} \right)^{1-2\beta} \frac{T(z)}{x+z-2xz} F\left(1-2\beta, 2-2\beta, 2-2\beta; \frac{(1-2x)z}{x+z-2xz}\right) dz. \end{aligned}$$

Using the formulas $F(a, b, b; z) = (1-z)^{-a}$ and $\Gamma(1+a) = a\Gamma(a)$, from the last expression we have:

$$A_3 = \frac{1}{1-2\beta} \int_0^1 \left(\frac{t}{x} \right)^{1-2\beta} \frac{T(t) dt}{x+t-2xt}.$$

The last equality implies the identity (42). Lemma 2 is proved.

Thus, putting (40), (41), (42) and (28) into (34), we get a functional relation between $T(x)$ and $\nu(x)$, transferred from the domain D to J :

$$\begin{aligned} \nu(x) &= -\frac{k_2\pi \tan \beta\pi}{1-2\beta} T(x) \\ &+ \frac{k_2}{1-2\beta} \int_0^1 \left(\frac{t}{x} \right)^{1-2\beta} T(t) \left[\frac{1}{x-t} - \frac{1}{x+t-2xt} \right] dt \int_0^t T(t) dt \int_0^t \frac{\partial^2 H_2(z, 0; x, 0)}{\partial \eta \partial y} (t-z)^{-2\beta} dz \tag{47} \\ &+ \int_0^l \frac{\partial q_2(t, \eta; x, 0)}{\partial y} \chi(s) ds, \quad (x, 0) \in J. \end{aligned}$$

By the conditions (21) and the relations (8), (11), (28), from (4) on the interval J , we get a functional relation between $\tau(x)$ and $\nu(x)$:

$$\begin{aligned} \nu(x) &= -\sum_{j=1}^n \frac{a_j(x)}{a_0(x)} \cdot \frac{1}{\Gamma(-\alpha_j)} \int_0^x (x-t)^{-\alpha_j-1} dt \int_t^1 (z-t)^{-2\beta} T(z) dz \\ &- \frac{a_{n+1}(x)}{a_0(x)} \int_x^1 (t-x)^{-2\beta} T(t) dt + \frac{b(x)}{a_0(x)}, \quad (x, 0) \in J. \end{aligned} \tag{48}$$

Theorem 2. *If the conditions (2), (5)–(10) and (12)–(14) are satisfied, then there exists the solution of Problem CN in the domain D .*

Proof. Excluding $\nu(x)$ from relation (47) and (48) we have:

$$\begin{aligned} T(x) & - \frac{\cot \beta \pi}{\pi} \int_0^1 \left(\frac{t}{x}\right)^{1-2\beta} \left[\frac{1}{x-t} - \frac{1}{x+t-2xt} \right] T(t) dt \\ & - \frac{(1-2\beta) \cot \beta \pi}{k_2 \pi} \int_0^1 T(t) dt \int_0^t (t-z)^{-2\beta} \frac{\partial^2 H_2(z, 0; x, 0)}{\partial \eta \partial y} dz \\ & - \frac{(1-2\beta) \cot \beta \pi}{k_2 \pi} \sum_{j=1}^n \frac{a_j(x)}{a_0(x)} \cdot \frac{1}{\Gamma(-\alpha_j)} \int_0^x T(t) dt \int_0^t (x-z)^{-\alpha_j-1} (t-z)^{-2\beta} dz \\ & - \frac{(1-2\beta) \cot \beta \pi}{k_2 \pi} \sum_{j=1}^n \frac{a_j(x)}{a_0(x)} \cdot \frac{1}{\Gamma(-\alpha_j)} \int_x^1 T(t) dt \int_0^x (x-z)^{-\alpha_j-1} (t-z)^{-2\beta} dz \\ & - \frac{(1-2\beta) \cot \beta \pi}{k_2 \pi} \cdot \frac{a_{n+1}(x)}{a_0(x)} \int_x^1 (t-x)^{-2\beta} T(t) dt \\ & = \frac{(2\beta-1) \cot \beta \pi}{k_2 \pi} \cdot \frac{b(x)}{a_0(x)} + \frac{(1-2\beta) \cot \beta \pi}{k_2 \pi} \int_0^l \chi(s) \frac{\partial q_2(\xi(s), \eta(s); x, 0)}{\partial y} ds, \end{aligned}$$

or

$$\tilde{T}(x) - \gamma_3 \int_0^1 \left[\frac{1}{x-t} - \frac{1}{x+t-2xt} \right] \tilde{T}(t) dt - \int_0^1 K(x, t) \tilde{T}(t) dt = F(x), \tag{49}$$

where, $\gamma_3 = \frac{1}{\pi} \cot \beta \pi$, $\tilde{T}(x) = x^{1-2\beta} T(x)$,

$$K(x, t) = \begin{cases} K_1(x, t), & 0 \leq t \leq 1, \\ K_2(x, t), & 0 \leq t \leq x, \\ K_3(x, t) + K_4(x, t), & x \leq t \leq 1, \end{cases} \tag{50}$$

$$K_1(x, t) = \frac{(1-2\beta) \cdot \gamma_3}{k_2} \left(\frac{x}{t}\right)^{1-2\beta} \int_0^t (t-z)^{-2\beta} \cdot \frac{\partial^2 H_2(z, 0; x, 0)}{\partial \eta \partial y} dz, \tag{51}$$

$$K_2(x, t) = \frac{(1-2\beta) \cdot \gamma_3}{k_2} \left(\frac{x}{t}\right)^{1-2\beta} \sum_{j=1}^n \frac{a_j(x)}{a_0(x)} \frac{1}{\Gamma(-\alpha_j)} \int_0^t (x-z)^{-\alpha_j-1} (t-z)^{-2\beta} dz, \tag{52}$$

$$K_3(x, t) = \frac{(1-2\beta) \cdot \gamma_3}{k_2} \left(\frac{x}{t}\right)^{1-2\beta} \sum_{j=1}^n \frac{a_j(x)}{a_0(x)} \frac{1}{\Gamma(-\alpha_j)} \int_0^x (x-z)^{-\alpha_j-1} (t-z)^{-2\beta} dz, \tag{53}$$

$$K_4(x, t) = \frac{(1-2\beta) \gamma_3}{k_2} \left(\frac{x}{t}\right)^{1-2\beta} \frac{a_{n+1}(x)}{a_0(x)} (t-x)^{-2\beta}, \tag{54}$$

$$F(x) = \frac{(2\beta-1) \gamma_3 x^{1-2\beta}}{k_2} \left[\frac{b(x)}{a_0(x)} - \int_0^l \chi(s) \frac{\partial q_2(\xi(s), \eta(s); x, 0)}{\partial y} ds \right]. \tag{55}$$

We investigate the kernel and the right-hand side of the singular integral equation (49).

Lemma 3. Let $0 < x < 1$, $0 < z < 1$, then the following inequality holds:

$$\left| \frac{\partial^2 H_2(z, 0; x, 0)}{\partial \eta \partial y} \right| < C_1 (x+z-2xz)^{2\beta-1}. \tag{56}$$

where C_1 is a constant depending only on the domain D .

The proof of Lemma 3 is similar to that of Lemma 18.1 (see [11, p. 133–136]).

Using (56) by (51) we have

$$|K_1(x, t)| \leq C_1 \frac{(1-2\beta)\gamma_3}{k_2} \left(\frac{x}{t}\right)^{1-2\beta} \left| \int_0^t (t-z)^{-2\beta} (x+z-2xz)^{2\beta-1} dz \right|. \tag{57}$$

Changing variables $z = t(1 - \sigma)$ and using formulas (46) from (57) we have:

$$|K_1(x, t)| \leq C_1 \frac{(1-2\beta)\gamma_3}{k_2} \left(\frac{x}{x+t-2xt}\right)^{1-2\beta} \int_0^1 \sigma^{-2\beta} \left[1 - \frac{(1-2x)t}{x+t-2xt}\sigma\right]^{2\beta-1} d\sigma. \tag{58}$$

Using (46) from (57), we get:

$$|K_1(x, t)| \leq C_1 \frac{(1-2\beta)\gamma_3}{k_2} \left(\frac{x}{x+t-2xt}\right)^{1-2\beta} F\left(1-2\beta, 1-2\beta, 2-2\beta; \frac{t(1-2x)}{x+t-2xt}\right). \tag{59}$$

Since $c - a - b = 2 - 2\beta - 2 + 4\beta = 2\beta < 0$, using a formula [7]:

$$F(a, b, c, z) = (1-z)^{c-a-b} F(c-a, c-b, c; z), \quad |\arg(1-z)| < \pi \tag{60}$$

and an estimate

$$F(a, b, c, z) \leq \begin{cases} \text{const} & \text{at } c-a-b > 0, & 0 \leq z \leq 1, \\ \text{const}(1-z)^{c-a-b} & \text{at } c-a-b < 0, & 0 < z < 1, \\ \text{const}[1+l(1-z)] & \text{at } c-a-b = 0, & 0 < z < 1 \end{cases} \tag{61}$$

from (59) we have the following:

$$|K_1(x, t)| \leq C_1 C_2 \frac{(1-2\beta)\gamma_3}{k_2} \left(\frac{x}{x+t-2xt}\right)^{1-2\beta} \left(\frac{x}{x+t-2xt}\right)^{2\beta} \leq \frac{C_3 x}{x+t-2xt}. \tag{62}$$

We consider the kernel (52). We make a replacement $z = t\mu$ in (52) and taking into account (46) we get:

$$\begin{aligned} K_2(x, t) &= \frac{(1-2\beta) \cdot \gamma_3}{k_2} \left(\frac{x}{t}\right)^{1-2\beta} \sum_{j=1}^n \frac{a_j(x)}{a_0(x)} \frac{x^{-\alpha_j-1} t^{1-2\beta}}{\Gamma(-\alpha_j)} \int_0^1 (1-s)^{-2\beta} \left(1 - \frac{t}{x}s\right)^{-\alpha_j-1} ds \\ &= \frac{(1-2\beta) \cdot \gamma_3}{k_2} \frac{\Gamma(1-2\beta)}{\Gamma(2-2\beta)} \left(\frac{x}{t}\right)^{1-2\beta} \sum_{j=1}^n \frac{a_j(x)}{a_0(x)} \frac{x^{-\alpha_j-1} t^{1-2\beta}}{\Gamma(-\alpha_j)} F\left(1, 1+\alpha_j, 2-2\beta; \frac{t}{x}\right) \\ &= \frac{\gamma_3}{k_2} \sum_{j=1}^n \frac{a_j(x)}{a_0(x)} \frac{x^{-\alpha_j-2\beta}}{\Gamma(-\alpha_j)} F\left(1, 1+\alpha_j, 2-2\beta; \frac{t}{x}\right). \end{aligned} \tag{63}$$

Considering (6), (10), (12), (61) and taking into account $c - a - b = 2 - 2\beta - 1 - 1 - \alpha_j = -2\beta - \alpha_j \geq -2\beta - \alpha \geq 0$, $0 \leq t \leq x \leq 1$ from (63) we have an estimation:

$$|K_2(x, t)| \leq \frac{\gamma_3}{k_2} \sum_{j=1}^n \frac{C_4 C_6}{C_5} \frac{x^{-\alpha_j-2\beta}}{\Gamma(-\alpha_j)} \leq \frac{\gamma_3 C_4 C_6}{k_2 C_5} x^{-2\beta} \sum_{j=1}^n \frac{1}{x^{\alpha_j} \Gamma(-\alpha_j)} \leq C_7 x^{-\alpha-2\beta},$$

or

$$|K_2(x, t)| \leq C_7 x^{-(\alpha+2\beta)} \leq C_8. \tag{64}$$

Similarly, we estimate $K_3(x, t)$. Due to (6), (10), (12), (61) and taking into account $c - a - b = 1 - \alpha_j - 1 - 2\beta = -2\beta - \alpha_j$, $0 \leq x \leq t \leq 1$ from (53) we have

$$|K_3(x, t)| \leq \frac{\gamma_3}{k_2} \left(\frac{x}{t}\right)^{1-2\beta} \sum_{j=1}^n \frac{C_4 C_9}{C_5} \frac{x^{-\alpha_j} t^{-2\beta}}{\Gamma(-\alpha_j)} \leq \frac{\gamma_3 C_4 C_9}{k_2 C_5} \cdot \frac{x}{t} \cdot x^{-2\beta} \sum_{j=1}^n \frac{1}{x^{\alpha_j} \Gamma(-\alpha_j)} \leq C_{10} x^{-(\alpha+2\beta)} \leq C_{11},$$

or

$$|K_3(x, t)| \leq C_{11}. \tag{65}$$

Due to (6), (10) with $x \leq t \leq 1$, from (54) it follows that:

$$|K_4(x, t)| \leq \frac{(1-2\beta) \gamma_3}{k_2} \left(\frac{x}{t}\right)^{1-2\beta} \frac{C_{12}}{C_5 (t-x)^{2\beta}} \leq C_{13} (t-x)^{-2\beta},$$

or

$$|K_4(x, t)| \leq C_{13} (t-x)^{-2\beta} \leq C_{14}. \tag{66}$$

Now we estimate the right-hand side of the equality (49). Differentiating (33) with respect to y and at $y = 0$, we obtain:

$$\frac{\partial q_2(\xi, \eta; t, 0)}{\partial y} = k_2 \eta \left[(\xi - t)^2 + \frac{4}{(m+2)^2} \eta^{m+2} \right]^{\beta-1}. \tag{67}$$

Substituting (67) to (55) we have:

$$F(x) = \frac{(2\beta - 1) \gamma_3 x^{1-2\beta}}{k_2} \left[\frac{b(x)}{a_0(x)} - k_2 \int_0^l \frac{\eta(s)\chi(s)}{\left[(\xi(s) - t)^2 + \frac{4}{(m+2)^2} \eta^{m+2}(s) \right]^{1-\beta}} ds \right]. \tag{68}$$

It is clear that the function $F(x)$ has derivatives of any order in the interval $(0,1)$. Let us study the behavior of the function $F(x)$ and its derivative at $x \rightarrow 0$ and $x \rightarrow 1$.

In this regard, we consider the following expression:

$$F_1(x) = k_2 \int_0^l \frac{\eta(s)\chi(s)}{\left[(\xi(s) - t)^2 + \frac{4}{(m+2)^2} \eta^{m+2}(s) \right]^{1-\beta}} ds. \tag{69}$$

By (9) for the sufficiently small $x > 0$, we have

$$\begin{aligned} |F_1(x)| &\leq k_2 \int_{l-\varepsilon}^l |\chi(s)| \frac{\eta}{\left[(\xi - x)^2 + \frac{4}{(m+2)^2} \eta^{m+2} \right]^{1-\beta}} ds + O(1) \\ &< C_{15} \int_{l-\varepsilon}^l \frac{\eta}{\left[(\xi - x)^2 + \frac{4}{(m+2)^2} \eta^{m+2} \right]^{1-\beta}} ds + O(1). \end{aligned}$$

Hence, using (13) for sufficiently small $\varepsilon > 0$, we get

$$|F_1(x)| < C_{16} \int_{l-\varepsilon}^l \frac{\eta^{\frac{m}{2}} \left| \frac{d\eta}{ds} \right|}{\left[x^2 + \frac{4}{(m+2)^2} \eta^{m+2} \right]^{\frac{1}{2}+\beta}} ds + O(1) < C_{17} \int_0^\delta \frac{d\tilde{\eta}}{[x^2 + \tilde{\eta}^2]^{\frac{1}{2}+\beta}} + O(1). \tag{70}$$

Substituting $\mu^2 = \omega$ in (70) and by relations (46), (61) and formulas [11, (2.17), (2.14), (2.22), p. 10-13], we have:

$$\begin{aligned} |F_1(x)| &< \\ &\frac{\delta^2}{x^{2\beta+1}} \left| \frac{\Gamma(1, 5)\Gamma(\beta)}{\Gamma(0, 5 + \beta)} \right| \left(\frac{\delta^2}{x^2} \right)^{-\frac{1}{2}} + \frac{\delta}{x^{2\beta+1}} \left| \frac{\Gamma(1, 5)\Gamma(-\beta)}{\Gamma(0, 5)\Gamma(1 - \beta)} \right| (x^2 + \delta^2)^{-\beta} x^{2\beta+1} F\left(\beta, \frac{1}{2}, 1 + \beta; \frac{x^2}{x^2 + \delta^2}\right) \\ &< \frac{\delta}{x^{2\beta}} \left| \frac{\Gamma(1, 5)\Gamma(\beta)}{\Gamma(0, 5 + \beta)} \right| + \left| \frac{\delta \Gamma(1, 5)\Gamma(-\beta)}{\Gamma(0, 5)\Gamma(1 - \beta)} \right| (x^2 + \delta^2)^{-\beta} < C_{18} x^{-2\beta}, \end{aligned}$$

or

$$|F_1(x)| < C_{18} x^{-2\beta}. \tag{71}$$

If $1 - x$ is sufficiently small, then as before, we get:

$$|F_1(x)| = C_{19} (1 - x)^{-2\beta}. \tag{72}$$

By the same arguments, we obtain:

$$|F'_1(x)| < C_{20} x^{-2\beta-1}, \quad |F'_1(x)| = C_{21} (1 - x)^{-2\beta-1}. \tag{73}$$

From the relations (6), (10), (71), (72), (73) from (68), we conclude that:

$$F(x) \in C(\bar{J}) \cap C^1(J). \tag{74}$$

The function $F'(x)$ tends to infinity of the order less $2\beta + 1$ at $x \rightarrow 1$, and when $x \rightarrow 0$ it is bounded. Introducing new variables:

$$\zeta = \frac{t^2}{1 - 2t + 2t^2}, \quad z = \frac{x^2}{1 - 2x + 2x^2}, \tag{75}$$

in the equation (49), we have:

$$\omega(z) + \gamma_3 \int_0^1 \frac{\omega(\zeta)d\zeta}{\zeta - z} - \int_0^1 \bar{K}(z, \zeta)\omega(\zeta)d\zeta = \tilde{F}(z), \quad (76)$$

where:

$$\begin{aligned} \omega(z) &= (1 - 2x + 2x^2)\tilde{T}(x), \quad \tilde{F}(z) = (1 - 2x + 2x^2)F(x), \\ \bar{K}(z, \zeta) &= \frac{1 - 2t + 2t^2}{2t(1-t)(1-2x+2x^2)}K(x, t) + \gamma_3 \frac{(1-2x+2x^2)(1-2t+2t^2)}{(1-t)(t+x-2xt)}, \\ x &= \frac{\sqrt{z}}{\sqrt{z} + \sqrt{1-z}}, \quad t = \frac{\sqrt{\zeta}}{\sqrt{\zeta} + \sqrt{1-\zeta}}. \end{aligned}$$

Since $1 + \gamma_3^2 \neq 0$, the equation (49) is the normal type. Its index is equal to zero in a class of h_2 functions $\omega(z) \in H(0, 1)$, bounded at the ends of the segment \bar{J} (see [12]).

We apply the method of regularization of Carleman–Vekua [12] to the equation (76). This method is developed by S. G. Mikhlin [13] and M. M. Smirnov [11, p. 258]. This results in the Fredholm's integral equation of the second kind, solvability of which follows from the uniqueness of a solution of Problem CN. By the notations $\tilde{T}(x) = x^{1-2\beta}T(x)$, $\omega(z) = (1 - 2x + 2x^2)\tilde{T}(x)$, we obtain a function $T(x)$ that is continuous on $(0, 1)$ and is integrable in $[0, 1]$.

Substituting the solution $T(x)$ of Fredholm's equation of the second kind in (28), we get $\tau(x)$. Furthermore, knowing the function $\tau(x)$, the solution of Problem CN for equation (1) in the domain D is defined as a solution of Problem DK for equation (1) with conditions (3) and (27).

Thus, the existence of a solution of Problem CN for $\delta(s) \neq 0$ is proved.

Theorem 2 is proved.

References

- [1] Vostrova L.K. Mixed boundary value problem for the general Lavrentyev–Bitsadze equation. *Scientific notes Kuibyshev State pedagogical college*, 1959, **29**, P. 45–66.
- [2] Melentyev B.V. On a boundary problem for the mixed type equations. *Soviet Math. Doklady*, 1964, **154** (6), P. 1262–1265.
- [3] Salakhitdinov M.S., Kadyrov Z. A problem with a normal derivative for an equation of mixed type with nonsmooth lines of degeneracy. *Differ. Uravn.*, 1986, **22** (1), P. 103–114
- [4] Salakhitdinov M.S., Mingziyaev B. A boundary value problem with the conormal derivative for the mixed type equation with two lines of degeneration. In *Differential equations and their applications*, Tashkent, 1979, P. 3–14 (in Russian).
- [5] Islomov B.I. Gellerstedt's boundary value problem for the mixed type equation of first kind. In *Boundary value problems for the nonclassical equations of mathematical physics*, Tashkent, 1986, P. 121–134.
- [6] Usanatashvili M.A. A problem with an inclined fractional derivative for an equation of mixed type. *Soobsheniye AN GSSR*, 1978, **90** (34), P. 10–16.
- [7] Salokhitdinov M.S., Islomov B.I. *The equations of the mixed type with two lines of degeneration*. Tashkent, "MUMTOZ SO'Z", 2009, 264 p.
- [8] Salokhitdinov M.S., Islomov B.I. Nonlocal boundary value problem of a conormal derivative for the mixed type equation with two internal lines and various orders of degeneration. *News of higher education institutions. Mathematics*, 2011, **1**, P. 49–58.
- [9] Islomov H. A problem with a conormal derivative for the elliptic type equation with one line of degeneration. *Uzbek mathematical journal*, 2012, **1**, P. 47–60.
- [10] Tikhonov A.N., Samarskii A.A. *Equations of Mathematical Physics*. Nauka, Moscow, 1977, 742 p.
- [11] Smirnov M.M. *The mixed type equations*. Moscow, 1985, 304 p.
- [12] Muskhelishvili N.I. *Singular integral equations*. Nauka, 1968, 512 p.
- [13] Mikhlin S.G. On the integral equations of F. Tricomi. *Soviet Math. Doklady*, 1948, **59** (6), P. 1053–1056.

Method of application three-dimensional billiard systems in passive heating systems

E. Yu. Rakhimov

Physical-Technical Institute, SPA “Physics-Sun”, Uzbek Academy of Sciences, Tashkent, Uzbekistan

rey_86@mail.ru

PACS 05.20, 05.70

DOI 10.17586/2220-8054-2018-9-3-319-322

In this article, the method of determining ray absorption ability by premises with insolation passive heating system by numerical experiments was studied. A heated premise (HP), having a translucent enclosure (TE), walls covered with a special smooth enclosure, was chosen as the object of study. The dynamics of the solar rays were studied as a billiard system and the reflection equations are given. Verification of result reliability was performed.

Keywords: ray absorption ability, insolation passive heating systems, 3D billiard systems.

Received: 14 March 2018

Revised: 29 March 2018

1. Introduction

Many systems of differential equations cannot be solved by numerous analytical calculations, if they can be solved, then with assumptions, constraints and waste of time. If they are solved with the help of numerical methods, then concrete new results are obtained. In this way, a physical process is studied that is difficult to study, with the help of mathematical modeling. The same way, one can study the dynamics of light, laser beams [1], radio and sound waves in a specific environment [2–4], and also thermal effects at heating systems [5, 6].

It is easy to study the processes which occur in the modeling of light-related phenomena (to the law of geometric optics) as a billiard system (small particle movement) [4, 7–11]. In this case, the solar rays propagate along straight lines and can be investigated in the system of two or three-dimensional coordinates, in the processes which occur colliding with a barrier, its energy is conserved or not (i.e. its intensity decreases without changing its velocity).

In this paper, a method of mathematical modeling is considered to determine ray absorption ability capacity by premises with insolation passive heating system.

2. The numerical experimental part

In order to solve this problem, a three-dimensional billiard system was used, and the model of the HP with a TE (window with widths b_{te} and heights h_{te}) was chosen as the object of the study (Fig. 1).

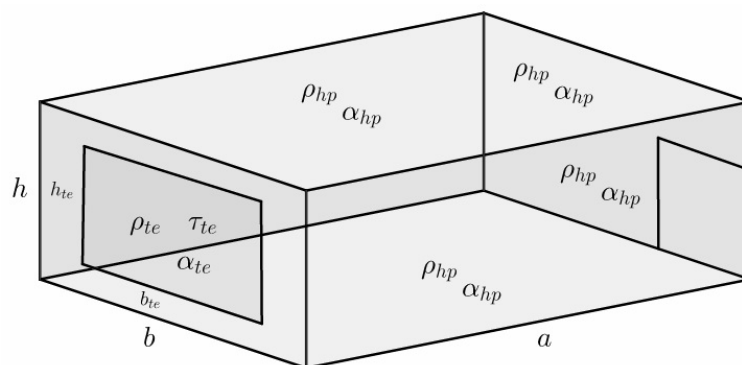


FIG. 1. Schematic diagram of the model of the HP

The following notations and conditions were introduced to simplify the modeling:

- The reflection, absorption and transmission coefficients of solar radiation (SR) of the TE HP are equal ρ_{te} , α_{te} and τ_{te} , respectively;
- The walls of HP, the ceiling, the floor and the door are covered with smooth material, and solar rays falling on them obey the laws of linear geometric optics;
- The reflection and absorption coefficients of SR of a smooth material are equal to ρ_{hp} and α_{hp} , respectively;
- For direct solar radiation the reflection, absorption and transmission coefficients depend on the incidence angle of the radiation.

The part of the absorbing energy of the flux of the SR (Q_{hp}^{abs}) inside the HP that comes through the surface of the TE HP is determined by the following equation:

$$Q_{hp}^{abs} = \tau_{te} \cdot \alpha_{hp} \cdot Q_{te}^{fall}, \quad (1)$$

where Q_{te}^{fall} – part of the falling energy of the flux of the direct SR falling on the surface of the TE HP.

If calculated by the traditional method of multiplication, $\tau_{te} \cdot \alpha_{hp}$ from expression (1) shows that what part of the energy of the flux of the SR falling on the surface of the TE is absorbed inside the HP and is equal to:

$$\tau_{te} \alpha_{hp} = \frac{Q_{hp}^{abs}}{Q_{te}^{fall}}. \quad (2)$$

According to the law of geometrical optics, part of the falling energy of the flux of direct SR falling on the surface of the TE HP is reflected from the surface by a factor equal to the multiplication of the $\rho_{te} \cdot Q_{te}^{fall}$ and a part is equal to the multiplication $\alpha_{te} \cdot Q_{te}^{fall}$ is absorbed inside the TE HP itself. Thus, the values of the part of the falling incident energy flux of the direct SR (Q_{hp}^{fall}) to the HP, which coming through the surface of the TE HP, is defined as following equation:

$$Q_{hp}^{fall} = \tau_{te} \cdot Q_{te}^{fall}. \quad (3)$$

During the motion of the solar rays in the HP, many times falling (collide) and reflecting on the surface of the HP and also the reverse side surfaces of the TE HP. Each time solar rays falling on the wall of the HP, part of the energy of the flux of the SR is absorbed equal to $Q_{hp_i}^{abs} = \alpha_{hp} \cdot Q_{hp_i}^{fall}$ (where i is the number of falls and reflects) and part of the energy of the flux of the SR is reflected equal to $Q_{hp_i}^{refl} = \rho_{hp} \cdot Q_{hp_i}^{fall}$, which is equal to the new value of the part of the energy of the flux of the SR for the next falling on the surface, that is, $Q_{hp_{i+1}}^{fall} = Q_{hp_i}^{refl}$. Also, every time when solar rays collide with the reverse side surfaces of the TE HP, part of the energy of the flux of the SR equal to $Q_{hp_i}^{refl} = \rho_{te} \cdot Q_{hp_i}^{fall}$ is reflected on the inside of the HP and it becomes a new value for the next collision, that is, $Q_{hp_{i+1}}^{fall} = Q_{hp_i}^{refl}$.

The trajectories of solar rays as the dynamics of particle motion in the billiard system are determined.

In this case, the boundary conditions for the initial point of particle motion can be written in the plane YOZ (that is, the initial point of the particle to the area of the billiard system a located in the surface of the TE):

$$y_0(z) = \begin{cases} (b + b_{te})/2, & \text{if } (h - h_{te})/2 \leq z \leq (h + h_{te})/2; \\ (b - b_{te})/2, & \end{cases} \quad (4)$$

$$z_0(y) = \begin{cases} (h + h_{te})/2, & \text{if } (b - b_{te})/2 \leq y \leq (b + b_{te})/2. \\ (h - h_{te})/2, & \end{cases}$$

The boundary conditions of the motion of a particle in HP is in the region of XYZ and is expressed as:

$$x(y, z) = \begin{cases} a, & \text{if } 0 \leq y \leq b \text{ and } 0 \leq z \leq h; \\ 0, & \end{cases}$$

$$y(x, z) = \begin{cases} b, & \text{if } 0 \leq x \leq a \text{ and } 0 \leq z \leq h; \\ 0, & \end{cases} \quad (5)$$

$$z(x, y) = \begin{cases} h, & \text{if } 0 \leq x \leq a \text{ and } 0 \leq y \leq b. \\ 0, & \end{cases}$$

Let the particle begin its motion with a certain velocity ϑ_0 from the surface of the TE HP, that is, from the point $(x_0, y_0, z_0) \in XYZ$. Then the projections of the velocity $\vartheta_x, \vartheta_y, \vartheta_z$ are defined as follows:

$$\vartheta_x = \vartheta_0 \cdot \cos \beta \cdot \sin \phi; \quad \vartheta_y = \vartheta_0 \cdot \sin \beta \cdot \sin \phi; \quad \vartheta_z = \vartheta_0 \cdot \sin \phi, \quad (6)$$

where β and ϕ are the angles that form between the velocity vector ϑ_0 and the unit vectors $e_x(i)$ and $e_z(i)$. Then the particle coordinates after the time t can be determined by the following mappings:

$$\begin{aligned} \theta_1 &= \begin{cases} (b - y_i)/\vartheta_y, & \text{if } \vartheta_y \geq 0; \\ y_i/\vartheta_y, & \text{if } \vartheta_y < 0; \end{cases} & \theta_2 &= \begin{cases} (a - x_i)/\vartheta_x, & \text{if } \vartheta_x \geq 0; \\ x_i/\vartheta_x, & \text{if } \vartheta_x < 0; \end{cases} \\ \theta_3 &= \begin{cases} (h - z_i)/\vartheta_z, & \text{if } \vartheta_z \geq 0; \\ z_i/\vartheta_z, & \text{if } \vartheta_z < 0; \end{cases} & t &= \min(\theta_1, \theta_2, \theta_3); \\ & & & x_{i+1} = x_i + \vartheta_x \cdot t; \quad y_{i+1} = y_i + \vartheta_y \cdot t; \quad z_{i+1} = z_i + \vartheta_z \cdot t. \end{aligned} \quad (7)$$

If one constructs a graphical representation of the mappings (7), obtained Fig. 2 shows the trajectories of particle motion on the planes XOY and YOZ , and also at the space XYZ .

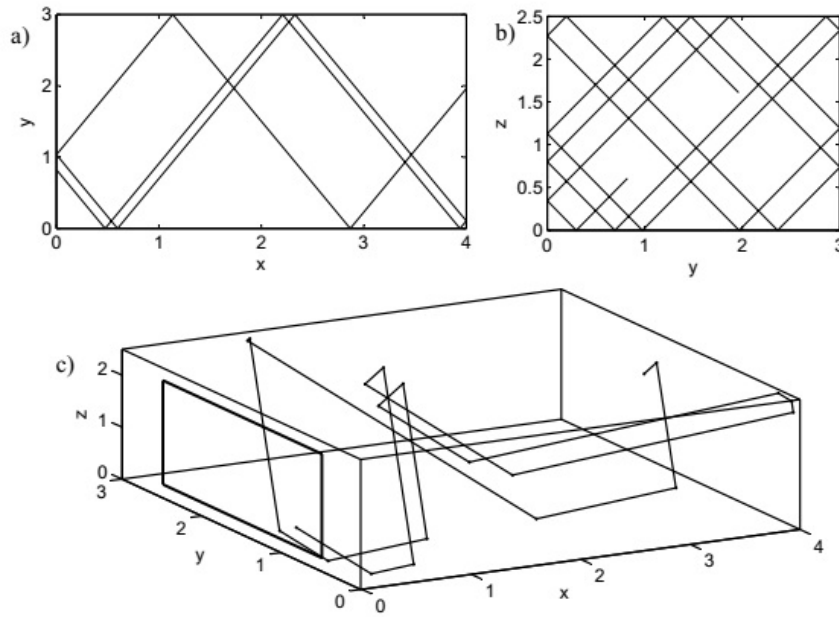


FIG. 2. Trajectory of particles in the chosen model HP: (a) at the plane XOY ; (b) at the plane YOZ ; (c) at the space XYZ

Considering the optical properties of the collision of a particle with surfaces, we obtain the following result:

- when colliding with the wall surface of the HP:

$$Q_{hp_{i+1}}^{abs} = Q_{hp_i}^{abs} + \alpha_{hp} \cdot Q_{hp_i}^{fall}; \quad Q_{hp_{i+1}}^{refl} = \rho_{hp} \cdot Q_{hp_i}^{fall}; \quad Q_{hp_{i+1}}^{fall} = Q_{hp_{i+1}}^{refl}; \quad (8)$$

- when colliding with the surface of the TE HP:

$$Q_{hp_{i+1}}^{refl} = \rho_{te} \cdot Q_{hp_i}^{fall}; \quad Q_{hp_{i+1}}^{fall} = Q_{hp_{i+1}}^{refl}. \quad (9)$$

Considering the above, we carry out the following concrete numerical experiment and for the approximation of the actual process, propagation of diffuse SR is considered. In connection with the fact that multiple internal reflection of radiation between the walls of the room is diffuse, in calculations it is used by the concept of “equivalent incidence angle of diffuse SR” which, according to [12], is taken to be 60° . Let the ratio of the size of the side of the HP equal to $a : b : h = 3 : 4 : 2.5$, as well as the coefficient of absorption and reflection of the smooth material is equal to $\rho_{hp} = 0.55$ and $\alpha_{hp} = 0.45$. Dimensions of the TE HP with the ratio $b_{te} : h_{hp} = 2 : 2$, and its optical parameters are equal to $\rho_{te} = 0.29$, $\alpha_{te} = 0.11$ and $\tau_{te} = 0.6$ [12]. During the numerical experiment, the optical process of 10^4 times of collision and reflection of $5 \cdot 10^3$ particles is considered.

The results show that the ray absorption ability capacity by premises with insolation passive heating system is equal to $Q_{hp}^{abs}/Q_{te}^{fall} = 0.608$. This value is more than 2.22 times the classical value ($\tau_{te} \cdot \alpha_{hp} = 0.27$), determined from the expressions (1). The results obtained as a result of numerical experiments are consistent with the results obtained using the analytical method [13].

3. Conclusion

The results show that such experiments can be used to aid the design of solar devices, at the design and alignment of solar ovens, as well as focusing systems by using parabolocylindric mirrors and designing a light-receiving system of solar tower type.

References

- [1] Creagh S.C. Directional emission from weakly eccentric resonators. *Phys Rev Lett.*, 2007, **98**(15), P. 153901.
- [2] Dembowski C., Gräf H-D., Heine A, Hesse T., Rehfeld H., Richter A. First experimental test of a trace formula for billiard systems showing mixed dynamics. *Phys Rev Lett.*, 2001, **86**(15), P. 3284-7.
- [3] Abdullaev S.S. and Zaslavskii G.M. Classical nonlinear dynamics and chaos of rays in problems of wave propagation in inhomogeneous media. *Sov. Phys. Usp.*, 1991, **34**(8), P. 645.
- [4] Loskutov A.Yu., Ryabov A.B., Akinshin L.G. Mechanism of Fermi acceleration in dispersing billiards with time-dependent boundaries. *Journal of Experimental and Theoretical Physics*, 1999, **89**(2), P. 966–974.
- [5] Eckmann J.P., Mejía-Monasterio C. Thermal Rectification in Billiardlike Systems. *Phys Rev Lett.*, 2006, **97**(9), P. 094301.
- [6] Lee K.Y., Chi D.Y., Kim S.H., Seo K.W., and Yoon J. Passive residual heat removal system of an open-pool type research reactor using gravity core cooling tank, in Proceedings of the European Research Reactor Conference (RRFM '14), Ljubljana, Slovenia, March-April, 2014, P. 593–599.
- [7] Weiss D., Roukes M.L. and et al. Electron pinball and commensurate orbits in a periodic array of scatterers. *Phys. Rev. Lett.*, 1991, **66**, P. 2790.
- [8] Markarian R., Kamphorst S.O., de Carvalho S.P. Chaotic Properties of the Elliptical Stadium. *Commun. Math. Phys.* 1996, **174**, P. 661–679.
- [9] Berry M.V. Regularity and chaos in classical mechanics, illustrated by three deformations of a circular billiard. *Eur. J. Phys.* 1981, **2**, P. 91–102.
- [10] Edson D.L., Carl P.D. Recurrence of particles in static and time varying oval billiards. *Physics Letters A*, 2012, **376** (20), P. 1669–1674.
- [11] Akhmadjanov T., Rakhimov E. and Otajanov D. Particle dynamics in corrugated rectangular billiard. *Nanosystems: Phys., Chem., Math.*, 2015, **6**(2), P. 262–267.
- [12] Duffie J.A., Beckman W.A. *Solar Engineer of Thermal Processes*. Fourth Solution. Hoboven New Jersey: John Wiley Sons. Inc., 2013, 910 p.
- [13] Avezov R.R., Avezova N.R. and et al. Ray absorption ability capacity by premises with insolation passive heating system. *Alternative Energy and Ecology*, 2017, **07-09**, P. 034–042.

On the behavior of the solution of a nonlinear polytropic filtration problem with a source and multiple nonlinearities

Z. R. Rakhmonov, A. I. Tillaev

National University of Uzbekistan, Applied Mathematics and Computer Analysis,
Universitet, 4, Tashkent, 100174, Uzbekistan

zraxmonov@inbox.ru, tillayev1@mail.ru

PACS 02.30.Jr, 02.30.Mv, 02.60.-x, 11.10.Jj, 11.10.Lm

DOI 10.17586/2220-8054-2018-9-3-323-329

In this paper, we study the global solvability and unsolvability conditions of a nonlinear filtration problem with nonlinear boundary flux. We establish the critical global existence exponent and critical Fujita exponent of nonlinear filtration problem in inhomogeneous medium. An asymptotic representation of the solution with a compact support is obtained, which made it possible to carry out a numerical experiment.

Keywords: filtration, global solutions, blow-up, critical curve, asymptotic behavior, numerical analysis.

Received: 23 April 2018

1. Introduction

Consider the following parabolic equation

$$\rho(x) \frac{\partial u}{\partial t} = \frac{\partial}{\partial x} \left(\left| \frac{\partial u}{\partial x} \right|^{p-2} \frac{\partial u}{\partial x} \right) + \rho(x) u^\beta, \quad (x, t) \in \mathbb{R}_+ \times (0, +\infty), \quad (1)$$

with nonlinear boundary flux

$$-\left| \frac{\partial u}{\partial x} \right|^{p-2} \frac{\partial u}{\partial x} (0, t) = u^q (0, t), \quad t > 0, \quad (2)$$

and initial value condition

$$u(x, 0) = u_0(x) \geq 0, \quad x \in \mathbb{R}_+, \quad (3)$$

where $p > 2$, $\beta, q > 0$, $\rho(x) = x^{-n}$, $n \in \mathbb{R}$, $u_0(x)$ – is a bounded, continuous, nonnegative and nontrivial initial data.

Equations (1) occur in various fields of natural science [1, 3–5]. For example, equation (1) arises in the mathematical modeling of thermal conductivity of nanofluids, in the study of problems of fluid flow through porous media, in problems of the dynamics of biological populations, polytropic filtration, and the formation of structures in synergetics and in nanotechnologies, and in a number of other areas [1, 4].

Equation (1) is called a parabolic equation with inhomogeneous density [1] and the case $p > 2$ corresponds to the slow diffusion equation [2]. The problem (1) – (3) has been intensively studied by many authors (see [2, 6–17] and references therein) in different values of numerical parameters.

The authors in [2] considered the Cauchy problem for the equation (1) at $n = 0$, proving that if $0 < \beta < 1$, then all solutions of (1) are global in time, while for $\beta > 1$ there are solutions with finite time blow-up. Also in this paper the following statements were proved:

– If $1 < \beta < 2p - 1$, then every solutions of Cauchy problem (1), (3) blow up in finite time;

– If $\beta > 2p - 1$, then the Cauchy problem (1), (3) admits nontrivial global solutions with small initial data.

The value $\beta = 2p - 1$ is Fujita type critical exponent.

Some properties of the solutions of (1)–(3) at $\rho(x) = 1$ were studied in [9] by Zhongping Li, Chunlai Mu and Li Xie. They obtained the critical global existence exponent and the critical Fujita exponent by constructing sub and supersolutions.

In [6, 7], the authors studied the unboundedness of the solution for the following reaction-diffusion model with nonlocal nonlinearities

$$\begin{aligned} u_t &= \Delta u^m + u^\beta, \quad (x, t) \in \Omega \times (0, T), \\ \frac{\partial u}{\partial \eta} &= u^q, \quad (x, t) \in \partial\Omega \times (0, T), \\ u(x, 0) &= u_0(x), \quad x \in \Omega, \end{aligned}$$

where $\Omega \in \mathbb{R}^N$ is a bounded domain. Authors obtained that all positive solutions exist globally if and only if $\beta, q \leq 1$ when $m > 1$ and if and only if $\beta \leq 1, q \leq 2m/(m + 1)$ when $m \leq 1$.

The authors of the work [15] have studied problem (1)–(3) at $n = 0$. They obtained the principal terms for the asymptotic of self-similar solutions.

As it is well known, degenerate equations need not possess classical solutions. Therefore, its solution is understood in the generalized sense.

Definition 1. The function $u(x, t)$ is said to be the weak solution to problem (1)–(3) in $\Omega = \{\mathbb{R}_+ \times (0, T)\}$, if $0 \leq u(x, t) \in C(\Omega), \left| \frac{\partial u}{\partial x} \right|^{p-2} \frac{\partial u}{\partial x} \in C(\Omega)$ and if it satisfies (1)–(3) in the sense of distribution in Ω , where $T > 0$ is the maximal existence time.

2. Main results

In this section, we show the critical global existence curve and critical Fujita curve, and characterize when all solutions to the problem (1)–(3) are global in time or they blow up.

Theorem 1. If $0 < \beta \leq 1$ and $0 < q \leq \frac{(2 - n)(p - 1)}{p - n}$ then each solution of problem (1)–(3) is global in time.

Proof. We look for a globally defined in time supersolution of the following self-similar form

$$\bar{u}(x, t) = e^{Bt} (D + e^{-L\xi}), \quad \xi = xe^{-Jt},$$

where $D > \|u_0\|_\infty, L^{(p-1)/q} - e^{-L} = D, B = \frac{L^p(p-1) + (D + e^{-L})^\beta}{D}, J = \frac{B(p-2)}{p-n}$.

After computation, we have:

$$\begin{aligned} \rho(x) \frac{\partial \bar{u}}{\partial t} &= \left(B e^{Bt} (D + e^{-L\xi}) + L J e^{(B-J)t} (1 + x) \right) e^{-nJt} \xi^{-n} \geq B D e^{(B-nJ)t}, \\ \bar{u}^\beta &= e^{\beta Bt} (D + e^{-L\xi})^\beta e^{-nJt} \xi^{-n} \leq e^{(\beta B - nJ)t} (D + e^{-L})^\beta, \\ \frac{\partial}{\partial x} \left(\left| \frac{\partial \bar{u}}{\partial x} \right|^{p-2} \frac{\partial \bar{u}}{\partial x} \right) &= L^p (p - 1) e^{(B(p-1) - Jp)t} e^{-L(p-1)\xi}, \\ - \left| \frac{\partial \bar{u}}{\partial x} \right|^{p-2} \frac{\partial \bar{u}}{\partial x} (0, t) &= L^{p-1} e^{(B-J)(p-1)t} e^{-B(p-1)}. \end{aligned}$$

Now, we shall show that the function $\bar{u}(x, t)$ is a supersolution of problem (1)–(3). According to the comparison principle it must satisfy the following inequality:

$$\rho(x) \frac{\partial \bar{u}}{\partial t} \geq \frac{\partial}{\partial x} \left(\left| \frac{\partial \bar{u}}{\partial x} \right|^{p-2} \frac{\partial \bar{u}}{\partial x} \right) + \rho(x) \bar{u}^\beta, \quad (x, t) \in \mathbb{R}_+ \times (0, +\infty), \tag{4}$$

$$- \left| \frac{\partial \bar{u}}{\partial x} \right|^{p-2} \frac{\partial \bar{u}}{\partial x} (0, t) \geq \bar{u}^q(0, t), \quad t > 0. \tag{5}$$

It is not difficult to verify that if $0 < \beta \leq 1$ and $0 < q \leq \frac{(2 - n)(p - 1)}{p - n}$, by definition B, L, D, J the inequalities (4) and (5) are valid. Hence, $\bar{u}(x, 0) \geq u_0(x)$ and $\bar{u}(0, 0) \geq u_0(0)$. Thus, by comparison principle, Theorem 1 is proved.

Remark 1. Theorem 1 shows that the critical global existence exponent of the problem (1)–(3) is $\left\{ \beta = 1, 0 < q \leq \frac{(2 - n)(p - 1)}{p - n} \right\} \cup \left\{ q = \frac{(2 - n)(p - 1)}{p - n}, \beta \leq 1 \right\}$.

Theorem 2. If $\beta < 1$ and $q > \frac{(2 - n)(p - 1)}{p - n}$ then every solution of problem (1)–(3) blows up in time.

Proof. We shall seek a blow up subsolution of the self-similar form:

$$u_-(x, t) = t^\sigma \varphi(\eta), \quad \eta = xt^{-\gamma} \tag{6}$$

where $\sigma = \frac{1}{1 - \beta}, \gamma = \frac{p - 1 - \beta}{(1 - \beta)(p - n)}$ and $\varphi(\eta)$ is the solution of the following problem

$$\frac{d}{d\eta} \left(\left| \frac{d\varphi}{d\eta} \right|^{p-2} \frac{d\varphi}{d\eta} \right) + \gamma \eta^{1-n} \frac{d\varphi}{d\eta} - \sigma \eta^{-n} \varphi + \eta^{-n} \varphi^\beta = 0, \tag{7}$$

$$\left| \frac{d\varphi}{d\eta} \right|^{p-2} \frac{d\varphi}{d\eta} (0) = \varphi^q (0). \tag{8}$$

In order $u_-(x, t)$ to be a subsolution of problem (1)-(3) function $\varphi(\eta)$ should satisfy following:

$$\frac{d}{d\eta} \left(\left| \frac{d\varphi}{d\eta} \right|^{p-2} \frac{d\varphi}{d\eta} \right) + \gamma \eta^{1-n} \frac{d\varphi}{d\eta} - \sigma \eta^{-n} \varphi + \eta^{-n} \varphi^\beta \geq 0, \tag{9}$$

$$\left| \frac{d\varphi}{d\eta} \right|^{p-2} \frac{d\varphi}{d\eta} (0) \leq \varphi^q (0). \tag{10}$$

We set:

$$\varphi(\eta) = E \left(a - \eta^{\frac{p-n}{p-1}} \right)_+^{\frac{p-1}{p-2}}, \tag{11}$$

where E, a are constants to be determined. It is easy to see that

$$\begin{aligned} \varphi'(\eta) &= -\frac{p-n}{p-2} E \eta^{\frac{1-n}{p-1}} \left(a - \eta^{\frac{p-n}{p-1}} \right)_+^{\frac{p-1}{p-2}}, \\ \frac{d}{d\eta} \left(\left| \frac{d\varphi}{d\eta} \right|^{p-2} \frac{d\varphi}{d\eta} \right) &= -E^{p-1} \left(\frac{p-n}{p-2} \right)^{p-1} \eta^{-n} \left(a - \eta^{\frac{p-n}{p-1}} \right)_+^{\frac{p-1}{p-2}}, \\ \left| \frac{d\varphi}{d\eta} \right|^{p-2} \frac{d\varphi}{d\eta} (0) &= 0. \end{aligned}$$

By taking

$$E^{p-2} \left(\frac{p-n}{p-2} \right)^{p-1} \geq \gamma, \quad a^{\frac{(p-1)(\beta-1)}{p-2}} \geq E^{p-2-\beta} \left(\frac{p-n}{p-2} \right)^{p-1} + E^{1-\beta} \sigma$$

it is easy to check that if $\beta < 1$, then (9) and (10) are valid. Thus $u_-(x, t)$ is a subsolution of the problem (1)-(3) with every nontrivial initial data.

Theorem 3. *If $\beta > 2p - 1$ and $q < \frac{(2-n)(p-1)}{p-n}$ then every solution of problem (1)-(3) blows up in time.*

Proof. In this case we prove that the flux condition makes the solution large enough to be in the set of initial data for which the reaction term alone is enough to cause blow up. We consider the self-similar subsolution of the problem (1)-(3) without a source:

$$u_b(x, t) = t^\alpha g(\xi), \quad \xi = xt^{-\gamma} \tag{12}$$

where $\alpha = \frac{p-1}{(p-1)(2-n)-q(p-n)}$, $\gamma = \frac{p-1-q}{(p-1)(2-n)-q(p-n)}$. Let us show that function $u_b(x, t)$ defined by (12) is a subsolution. Then, according to the comparison principle, function $g(\xi)$ should satisfy the following inequalities:

$$\frac{d}{d\xi} \left(\left| \frac{dg}{d\xi} \right|^{p-2} \frac{dg}{d\xi} \right) + \gamma \xi^{1-n} \frac{dg}{d\xi} - \alpha g(\xi) \geq 0, \tag{13}$$

$$-\left| \frac{dg}{d\xi} \right|^{p-2} \frac{dg}{d\xi} (0) \leq g^q(0). \tag{14}$$

Let us set

$$\bar{g}(\xi) = B \left(b - \xi \right)_+^{\frac{p-1}{p-2}},$$

where b and B are positive constants to be determined. After some computations, we have

$$\bar{g}'(\xi) = -B \frac{p-1}{p-2} \left(b - \xi \right)_+^{\frac{1}{p-2}},$$

$$\left| \frac{d\bar{g}}{d\xi} \right|^{p-2} \frac{d\bar{g}}{d\xi} = -B^{p-1} \left(\frac{p-1}{p-2} \right)^{p-1} \left(b - \xi \right)_+^{\frac{p-1}{p-2}},$$

$$\frac{d}{d\xi} \left(\left| \frac{d\bar{g}}{d\xi} \right|^{p-2} \frac{d\bar{g}}{d\xi} \right) = B^{p-1} \left(\frac{p-1}{p-2} \right)^p \left(b - \xi \right)_+^{\frac{1}{p-2}}.$$

Noting that

$$\begin{aligned} \gamma \xi^{1-n} \frac{d\bar{g}}{d\xi} - \alpha \bar{g}(\xi) &\geq -\gamma B \frac{p-1}{p-2} (b-\xi)_+^{\frac{1}{p-2}} b - \alpha B (b-\xi)_+^{\frac{1}{p-2}} b = \\ &= -Bb (b-\xi)_+^{\frac{1}{p-2}} \left(\gamma \frac{p-1}{p-2} + \alpha \right). \end{aligned}$$

By taking:

$$B^{p-2} \left(\frac{p-1}{p-2} \right)^p \geq b \left(\gamma \frac{p-1}{p-2} + \alpha \right), \quad B^{p-1-q} \left(\frac{p-1}{p-2} \right)^{p-1} \leq b^{\frac{(q-1)(p-1)}{p-2}}$$

and $q < \frac{(2-n)(p-1)}{p-n}$, it is easy to check that (13) and (14) are valid. It follows from the comparison principle that the problem (1)–(3) exists a solution blowing up in a finite time.

Theorem 4. *If $\beta > 1$ and $q < (2-n)(p-1)$, then every solution of problem (1)–(3) blows up in time.*

Remark 2. *Theorem 3 and Theorem 4 shows that the critical Fujita curve of the problem (1)–(3) is $\{\beta = 2p-1, q \geq 2(p-1)\} \cup \{\beta \geq 2p-1, q = 2(p-1)\}$.*

Theorem 5. *If $\beta > \frac{(p-n)q-p+1}{p-1}$ and $q > (2-n)(p-1)$ then each solution of problem (1)–(3) is global in time.*

Theorems 4 and 5 can be proved in the same manner as it was done in [13, 16].

Let us show the asymptotics of self-similar solutions.

The case $1/(p-1) < \beta \leq 1, q > \frac{(2-n)(p-1)}{p-n}$. Consider the following self-similar solution of problem (1)–(3):

$$u_1(x, t) = t^\alpha \varphi(\xi), \quad \xi = xt^{-\gamma}, \tag{15}$$

where $\alpha = \frac{1}{1-\beta}, \gamma = \frac{p-1-\beta}{(p-n)(1-\beta)}$ and $\varphi(\xi)$ is solution of the following problem

$$\frac{d}{d\xi} \left(\left| \frac{d\varphi}{d\xi} \right|^{p-2} \frac{d\varphi}{d\xi} \right) + \gamma \xi^{1-n} \frac{d\varphi}{d\xi} - \alpha \xi^{-n} \varphi + \xi^{-n} \varphi^\beta = 0 \tag{16}$$

$$-\left| \frac{d\varphi}{d\xi} \right|^{p-2} \frac{d\varphi}{d\xi} \Big|_{\xi=0} = \varphi^q(0) \tag{17}$$

Consider the function

$$\bar{\varphi}(\xi) = \left(a - \frac{p-2}{p-n} \gamma^{\frac{1}{p-1}} \xi^{\frac{p-n}{p-1}} \right)_+^{\frac{p-1}{p-2}}, \tag{18}$$

where $a > 0, (y)_+ = \max(0, y)$. We show that the function (18) is the asymptotics of the solutions of problem (16), (17).

Theorem 6. *The compactly supported solution of problem (16), (17) has the asymptotic*

$$\varphi(\xi) = \bar{\varphi}(\xi) (1 + o(1)),$$

when $\xi \rightarrow \left(\frac{a(p-n)}{(p-2)\gamma^{1/(p-1)}} \right)^{(p-1)/(p-n)}$.

Proof. We seek a solution of equation (16) in the following form

$$\varphi = \bar{\varphi}(\xi) w(\tau), \tag{19}$$

with $\tau = -\ln \left(a - b\xi^{\frac{p-n}{p-1}} \right), b = \frac{p-2}{(p-n)} \gamma^{1/(p-1)}$, where $\tau \rightarrow +\infty$ at $\xi \rightarrow (a/b)^{(p-1)/(p-n)}$.

Substituting (19) into equation (16) with regard to (18), it takes the form:

$$\frac{d}{d\tau} (L_1 w)^{p-1} + \left(k_1 \phi_1(\tau) - \frac{p-1}{p-2} \right) (L_1 w)^{p-1} + k_2 L_1 w - k_3 w \phi_2(\tau) - k_4 w^\beta \phi_3(\tau) = 0, \tag{20}$$

where $L_1 w = \frac{w}{p-2} - \frac{w'}{p-1}, \phi_1(\tau) = e^{-\tau}, \phi_2(\tau) = e^{-\tau}/(a - e^{-\tau}), \phi_3(\tau) = e^{-\frac{\beta(p-1)-1}{p-2}\tau} / (a - e^{-\tau}),$

$$k_1 = \frac{p-1}{b(p-n)}, k_2 = \frac{\gamma(p-1)}{(b(p-n))^{p-1}}, k_3 = \frac{\alpha(p-1)}{b^{p-1}(p-n)^p}, k_4 = \frac{p-1}{(b(p-n))^p}.$$

We note that the study of the solutions of the last equation is equivalent to the study of those solutions of equation (1), each of which satisfies the inequalities in some interval $[\tau_0, +\infty)$:

$$w(\tau) > 0, \quad \frac{w(\tau)}{p-2} - \frac{w'(\tau)}{p-1} \neq 0.$$

We verify that the solution $w(\tau)$ of the equation (20) has a finite limit w_0 or not at $\tau \rightarrow +\infty$. Let $\nu(\tau) = (L_1 w)^{p-1}$. Then, for the derivative of the function $\nu(\tau)$, we have:

$$\nu' = - \left(k_1 \phi_1(\tau) - \frac{p-1}{p-2} \right) \nu - k_2 L_1 w + k_3 w \phi_2(\tau) + k_4 w^\beta \phi_3(\tau).$$

We introduce the auxiliary function to analyze the solutions of the last equation:

$$\theta(\tau, \mu) = - \left(k_1 \phi_1(\tau) - \frac{p-1}{p-2} \right) \mu - k_2 L_1 w + k_3 w \phi_2(\tau) + k_4 w^\beta \phi_3(\tau) \tag{21}$$

where $\mu \in \mathbb{R}$. Hence, it is easy to see that for each value of μ the function $\theta(\tau, \mu)$ keep the sign on some interval $[\tau_1, +\infty) \subset [\tau_0, +\infty)$ and for all $\tau \in [\tau_1, +\infty)$ holds one of the inequalities $\nu'(\tau) > 0, \nu'(\tau) < 0$. Then, analyzing (21) with the help of Bohl's theorem [13], we conclude that there for the function $\nu(\tau)$ exists a limit at $\tau \in [\tau_1, +\infty)$. It is easy to see that

$$\lim_{\tau \rightarrow +\infty} \phi_1(\tau) \rightarrow 0, \quad \lim_{\tau \rightarrow +\infty} \phi_2(\eta) \rightarrow 0, \quad \lim_{\tau \rightarrow +\infty} \phi_3(\eta) \rightarrow 0$$

at $\xi \rightarrow (a/b)_-^{(p-1)/(p-n)}$. Then taking into account the last limit and $w' = 0$ from (20), we obtain following algebraic equation for w

$$(p-1) \left(\frac{w}{p-2} \right)^{p-1} - k_2 w = 0.$$

From this equation, we get that $w = 1$, thus we have $\varphi(\xi) = \bar{\varphi}(\xi) (1 + o(1))$.

The case $\beta > 2p - 1, q < \frac{(2-n)(p-1)}{(p-n)}$.

Theorem 7. *The compactly supported solution of problem (1)-(3) has the asymptotic:*

$$u(x, t) = C t^\alpha \bar{g}(\xi) (1 + o(1)),$$

where $C = \left(\frac{p-2}{p-1} b \gamma \right)^{1/(p-2)} \frac{p-2}{B(p-1)}$, \bar{g} is above defined function.

The critical case $(p-n)q = (2-n)(p-1)$. In this case, we consider following exponential form solution of problem (1)-(3):

$$u_4(x, t) = e^{\alpha(t-\tau)} \phi(\eta), \quad \eta = x e^{-\gamma(t-\tau)},$$

where $\alpha = \frac{p-n}{2p-1}, \gamma = \frac{p-2}{2p-1}$ and $\phi(\eta)$ is the solution of the problem

$$\frac{d}{d\eta} \left(\left| \frac{d\phi}{d\eta} \right|^{p-2} \frac{d\phi}{d\eta} \right) + \gamma \eta^{1-n} \frac{d\phi}{d\eta} - \alpha \eta^{-n} \phi = 0, \tag{22}$$

$$- \left| \frac{d\phi}{d\eta} \right|^{p-2} \frac{d\phi}{d\eta} \Big|_{\eta=0} = \phi^q(0). \tag{23}$$

We take:

$$\bar{\phi}(\eta) = D \left(D^{p-2} \left(\frac{p-1}{p-2} \right)^p - \eta \right)_+^{\frac{p-1}{p-2}},$$

where $D > 0$.

Theorem 8. *The compactly supported solution of problem (22)-(23) has the asymptotic*

$$\phi(\eta) = C \bar{\phi}(\eta) (1 + o(1)),$$

at $\eta \rightarrow D^{p-2} \left(\frac{p-1}{p-2} \right)^p$, where $C = \left(\frac{p-1}{p-2} \gamma \right)^{1/(p-2)}$.

Theorem 7 and Theorem 8 are proved similarly to the proofs of Theorems 6.

Numerical experiments. It is known that choosing a suitable initial approximation preserving nonlinear properties is very important in numerical analysis. For this purpose, a computer experiment was conducted on the basis of the above qualitative properties of solutions for the case of global solvability. Since equation (1) approximated the

second order of accuracy respect to x and first order of accuracy respect to t . The iterative process for numerical modeling was constructed, in the inner steps of iteration the node values are calculated by the Thomas algorithm. It is well known that, the iteration methods required a good initial approximation, which quickly converge to the exact solution and retain the qualitative properties of the studied nonlinear processes. This is the difficulty of the numerical analysis of the nonlinear problem. It depends on the values of the numerical parameters of the equation and can be overcome by successful choice initial approximations. We present some results of numerical experiments.

Figures 1–3 show that filtration process depends on the density of the medium. Numerical experiments show rapid convergence of iterations to the exact solution. It is due to the choice of a suitable initial approximation. The number of iterations is not more than 5 for various values of numerical parameters.

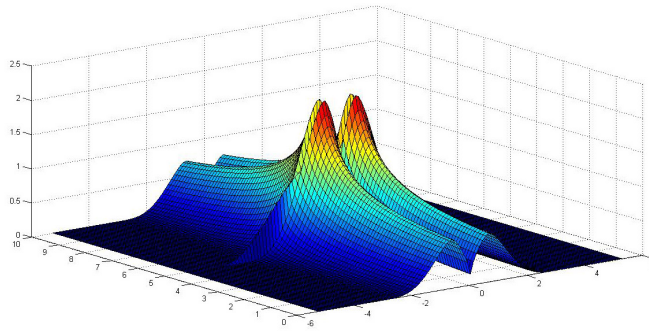


FIG. 1. Numerical solution of (1)–(3): $\beta = 2.1$, $p = 2.65$, $n = 1.2$, $q = 2.5$

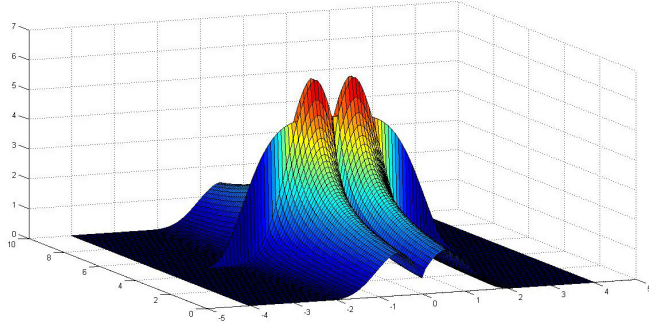


FIG. 2. Numerical solution of (1)–(3): $\beta = 2.1$, $p = 2.35$, $n = 3.5$, $q = 3$

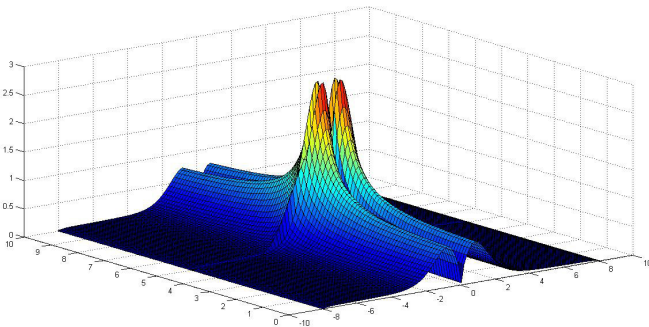


FIG. 3. Numerical solution of (1)–(3): $\beta = 1.6$, $p = 2.25$, $n = 0.8$, $q = 2.5$

References

- [1] Kalashnikov A.S. Some problems of the qualitative theory of nonlinear degenerate second-order parabolic equations. *Russian. Math. Surveys*, 1987, **42** (2), P. 169–222.
- [2] Galaktionov V.A. On global nonexistence and localization of solutions to the Cauchy problem for some class of nonlinear parabolic equations. *Zh. Vychisl. Mat. Mat. Fiz.*, 1983, **23**, P. 1341–1354. English transl.: *Comput. Math. Math. Phys.* 1983, **23**, P. 36–44.
- [3] M.Aripov. *Standard Equation's Methods for Solutions to Nonlinear problems*, Tashkent, FAN, 1988, 138 p.
- [4] Galaktionov V.A., Vazquez J.L. The problem of blow-up in nonlinear parabolic equations. *Discrete and continuous dynamical systems*, 2002, **8** (2), P. 399–433.
- [5] Galaktionov V.A., Levine H.A. On critical Fujita exponents for heat equations with nonlinear flux boundary condition on the boundary. *Israel J. Math.*, 1996, **94**, P. 125–146.
- [6] Pablo A.D., Quiros F., Rossi J.D. Asymptotic simplification for a reaction-diffusion problem with a nonlinear boundary condition. *IMA J. Appl. Math.*, 2002, **67**, P. 69–98.
- [7] Song X., Zheng S. Blow-up and blow-up rate for a reaction-diffusion model with multiple nonlinearities. *Nonlinear Anal.*, 2003, **54**, P. 279–289.
- [8] Li Z., Mu Ch. Critical exponents for a fast diffusive polytropic filtration equation with nonlinear boundary flux. *J. Math. Anal. Appl.*, 2008, **346**, P. 55–64.
- [9] Zhongping Li, Chunlai Mu, Li Xie. Critical curves for a degenerate parabolic equation with multiple nonlinearities. *J. Math. Anal. Appl.*, 2009, **359**, P. 39–47.
- [10] Wanjuan Du, Zhongping Li. Critical exponents for heat conduction equation with a nonlinear Boundary condition. *Int. Jour. of Math. Anal.*, 2013, **7** (11), P. 517–524.
- [11] Mersaid Aripov, Shakhlo A. Sadullaeva. To properties of solutions to reaction-diffusion equation with double nonlinearity with distributed parameters. *Jour. Sib. Fed. Univ. Math. Phys.*, 2013, **6** (2), P. 157–167.
- [12] Aripov M., Rakhmonov Z. On the asymptotic of solutions of a nonlinear heat conduction problem with gradient nonlinearity. *Uzbek Mathematical Journal*, 2013, **3**, P. 19–27.
- [13] Rakhmonov Z. On the properties of solutions of multidimensional nonlinear filtration problem with variable density and nonlocal boundary condition in the case of fast diffusion. *Journal of Siberian Federal University. Mathematics & Physics*, 2016, **9** (2), P. 236–245.
- [14] Aripov M., Rakhmonov Z. Estimates and Asymptotic of Self-similar Solutions to a Nonlinear Filtration Problem with Variable Density and Nonlocal Boundary Conditions. *Universal Journal of Computational Mathematics*, 2016, **4**, P. 1–5.
- [15] Aripov M.M., Rakhmonov Z.R. On the asymptotics of solutions of the heat conduction problem with a source and a nonlinear boundary condition. *Computational technologies*, 2015, **20** (2), P. 216–223.
- [16] Aripov M.M., Matyakubov A.S. To the qualitative properties of solution of system equations not in divergence form of polytropic filtration in variable density. *Nanosystems: Physics, Chemistry, Mathematics*, 2017, **8** (3), P. 317–322.
- [17] Aripov M.M., Matyakubov A.S. Self-similar solutions of a cross-diffusion parabolic system with variable density: explicit estimates and asymptotic behavior. *Nanosystems: Physics, Chemistry, Mathematics*, 2017, **8** (1), P. 5–12.

Double-layered boron. The adsorption of gas-phase atom

E. V. Boroznina, O. A. Kakorina, M. B. Belonenko

Volgograd State University, University Ave. 100, Volgograd 400062, Russia

boroznina.evgeniya@volsu.ru, davletova.olesya@volsu.ru

DOI 10.17586/2220-8054-2018-9-3-330-334

In this paper, we have considered hexagonal double-layered boron and its adsorption properties in particular. The main adsorption characteristics have been elucidated by using the semi-empirical quantum-chemical scheme MNDO. We have investigated both external adsorption and internal infiltration of atoms (H, O, F, Cl) between boron monolayers.

Keywords: Boron sheet, double-layered materials, semi-empirical research, atomic adsorption.

Received: 28 September 2017

Revised: 16 October 2017

Final revision: 4 April 2018

1. Introduction

Recently, two-dimensional structures have become the subject of much research interests. Graphene, boron nitride, molybdenum disulfide, silicene and pyrolyzed polyacrylonitriles are the most known two-dimensional structures which have been found in a large number of application variants [1, 2].

However, these are insufficient to cover all needs of modern technology. So, today the world of two-dimensional materials has just gotten a little more crowded. The 2D universe was extended by the “borophene” [3]. This is a new allotropic form of boron which has triangular boron lattices with hexagonal arrangement of vacancies. Borophene is predicted as an excellent electrode material with a high electrochemical performance for both Li-ion and Na-ion batteries, as a component of superconducting nanodevices but several applications of borophene still await for further research and realization [4, 5]. Boron is a unique element. It is capable of forming a wide range of its structure modifications in the condensed state [6–9]. So, in this paper we have considered the new boron structure and its adsorption properties. It is the double-layered boron sheet. We believe that the double-layered nanomaterials may greatly enrich the nanodevice applications [10, 11].

2. Double-layered boron. Research of structural modification

There are several sheet configurations divided into several distinct categories, namely hexagonal graphene-like sheet, idealized and buckled sheets, reconstructed sheets, sheets based on the icosahedral configuration, low-symmetry sheets, and hybrid sheets. It is to be noted that our preliminary work considered only idealized and reconstructed sheet configurations [12].

The first step of our research was to model and to find the most stable configurations of hexagonal double-layered boron (DLB). We used the semi-empirical MNDO scheme and the model of molecular cluster (MC) [13]. The matrix elements of the Hamiltonian are given by equation 1 and 2:

$$F_{\mu\nu}^{AA} = \delta_{\mu\nu} U_{\mu\mu} + \sum_{\mu', \nu'}^{(A)} P_{\mu' \nu'} \cdot \left[\langle \mu\nu | \mu' \nu' \rangle - \frac{1}{2} \langle \mu\mu' | \nu\nu' \rangle \right] + \sum_{B(\neq A)}^{(EUC)} \left[\sum_{\lambda, \sigma}^{(B)} P_{\lambda\sigma} \cdot \langle \mu\nu | \lambda\sigma \rangle - Z_B \cdot \langle \mu\nu | s_B s_B \rangle \right], \quad (1)$$

$$F_{\mu\lambda}^{AB} = \beta_{\mu\lambda} - \frac{1}{2} \sum_{\nu}^{(A)} \sum_{\sigma}^{(B)} P_{\nu\sigma} \cdot \langle \mu\nu | \lambda\sigma \rangle, \quad (2)$$

$U_{\mu\mu}$ are the single-center energies, which are the sum of the kinetic energy of an electron of atomic orbital χ_{μ} of atom A and the interaction potential energy between electron and nucleus of atom A ; $\langle \mu\mu | \nu\nu \rangle = g_{\mu\nu}$, $\langle \mu\nu | \mu\nu \rangle = h_{\mu\nu}$ are the single-center two-electron Coulomb integrals and exchange integrals, respectively; $\beta_{\mu\lambda} = \frac{1}{2} (\beta_{\mu}^A + \beta_{\lambda}^B) \cdot S_{\mu\lambda}$ are the two-center one-electron core-resonance integrals; $V_{\mu\nu, B} = -Z_B \cdot \langle \mu\nu | s_B s_B \rangle$ is the potential of interaction between an distributed electron over atom A $\chi_{\mu} \chi_{\nu}$ and the core of atom B ; $\langle \mu\nu | \lambda\sigma \rangle$ are the two-center two-electron repulsion integrals.

The hexagonal boron sheet has a planar structure with a honeycomb lattice similar to that of graphene. The lengths of B–B bonds are 1.67 Å [14]. The choice of MC as a model of the considered structures has been

determined primarily by the fact that within of this model is possible to quite accurately investigate a local phenomenon in the structure as an adsorption, catalysis, and the formation of point defects of the structure (local centers). The extended unit cell of a hexagonal boron sheet is shown on Fig. 1. The size of the considered clusters has been optimized to exclude the boundary effect taking into account the machine time of our calculations. We have studied a rectangular molecular cluster with x and y dimensions of $7a$ and $2\sqrt{3}a$, respectively, where a is the in-plane lattice parameter of borophene. The dangling bonds at the cluster boundary have been saturated by pseudoatoms of hydrogen. The initial interplanar distance between two layers of boron was chosen as that in graphite, 3.4 Å; afterward, we optimized the interlayer distance to create double-layered boron. The variants of sheets' positions considered relative to each other are shown on Fig. 2. We have studied several configurations of double-layered boron. The first family of configuration has been formed by displacing one of the boron sheets in a sliding motion along the x axis with displacement rates $0a$, $\frac{1}{2}a$ or $\frac{1}{4}a$ (Fig. 2). The second family of configurations has been formed by displacing one of the boron sheets in a sliding motion along the y axis. The coefficient of displacement was $0a$, $\frac{1}{2}a$, $\frac{1}{4}a$ or $1a$. The lower boron sheet is shown by a dotted line. The interplanar distance of double-layered boron has been found to be 3.68 Å after quantum-chemical calculations and geometrical optimization. The values of double-layered boron cohesive energy are given in the Table 1. One can see that the structure with the coefficient of displacement 1 (along the y axis) is energetically more likely. But the difference of cohesive energy of another type of configurations is negligible and falls within the error of the method, hence, all of the considered variants of double-layered boron are possible and could be stable.

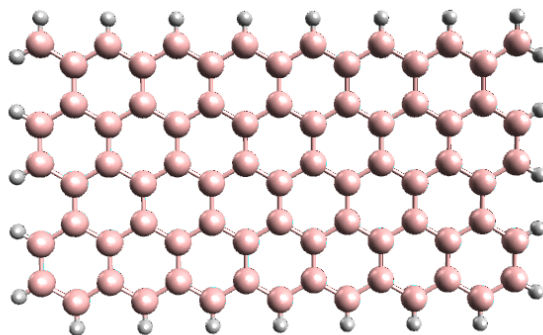


FIG. 1. The extended unit cell of molecular cluster of hexagonal boron sheet

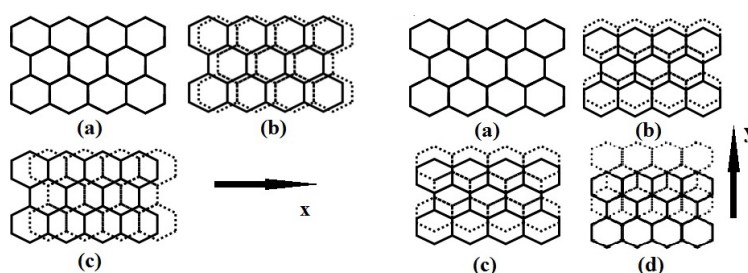


FIG. 2. Configuration of double-layered boron with x axis displacement: a) without displacement; b) with the displacement rate $\frac{1}{2}a$; c) with the displacement rate $\frac{1}{4}a$. Configuration of double-layered boron with y axis displacement: a) without displacement; b) with the displacement rate $\frac{\sqrt{3}}{3}a$; c) with the displacement rate $\frac{\sqrt{3}}{6}a$; d) with the displacement rate $\frac{2\sqrt{3}}{3}a$

3. External adsorption of gas-phase atoms on the surface of double-layered boron

The investigation of the binding opportunity between double-layered boron and atoms H, O, F, Cl has been performed by a stepwise approach of the adsorbed atom to the surface of DLB. The potential energy of considered ad-complexes has been found on each step of our calculations. Molecular clusters of DLB with adsorbed atoms are shown on Fig. 3. The profiles of surface potential energy of the atoms interaction with the surface of DLB are shown on Fig. 4. The energy curves of these processes show a minimum which points to a chemical bond formation

TABLE 1. Values of cohesive energy of double-layered boron (E_c). x – displacement, y – displacement

E_c , eV	Rate of displacement in a and $\sqrt{3}/3 \times a$ for x and y directions							
	0		1/2		1/4		1	
	x	y	x	y	x	y	x	y
	3.60	3.60	3.57	3.61	3.62	3.63	—	3.65

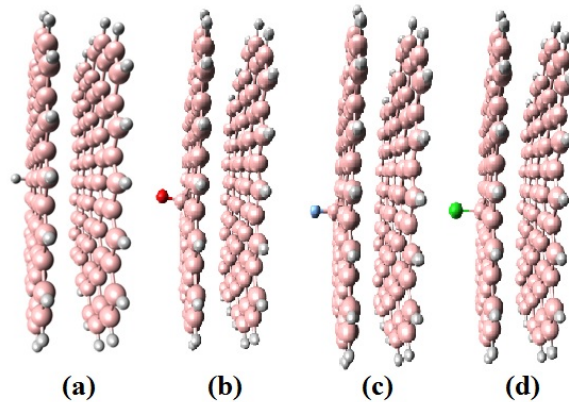


FIG. 3. Structures of double-layered boron with gas-phase atoms on the surface: a) hydrogen; b) oxygen; c) fluorine; d) chlorine

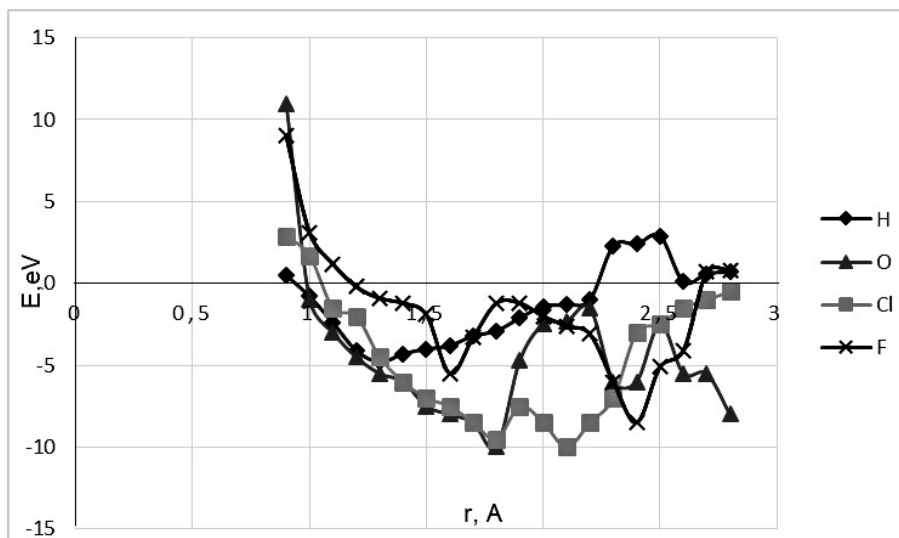


FIG. 4. Profiles of surface potential energy of the atoms interaction with the surface of double-layered boron: a) hydrogen; b) oxygen; c) fluorine; d) chlorine

between atoms and a B atom on the surface of DLB. The adsorption energy and the distance of adsorption are given in Table 2. In the case of hydrogen atom adsorption we can see the electron density transfer from the H atom to the surface of the boron layer. In other words, we can conclude the fact of proton formation.

4. Infiltration of gas-phase atoms into the interplanar space of double-layered boron

The atoms infiltration into the interplanar space of DLB has been carried through the local vacancy of the boron sheet. The fragment of the defective boron sheet structure after total parameters optimization is shown on Fig. 5.

TABLE 2. The basic characteristics of external DLB adsorption. E_{ad} – the adsorption energy, R_{ad} – the distance of adsorption

	Adsorbed atom			
	H	O	F	Cl
E_{ad} , eV	-4.8	-11.1	-5.8	-9.7
R_{ad} , Å	1.3	1.8	1.6	1.8

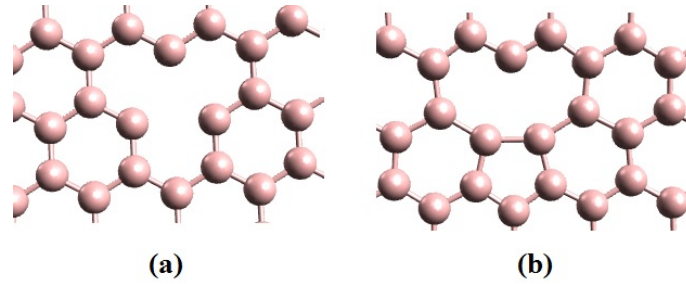


FIG. 5. Fragment of boron sheet structure with vacancy defect: a) initial structure; b) after geometry optimization

The process of infiltration was simulated by a stepwise approach (with a step of 0.1 Å) of hydrogen, oxygen, fluorine or chlorine atom along a dummy perpendicular to the surface of DLB and through the vacancy center (Fig. 6). So, the atoms have been moved from 4.5 Å to 0.0 Å through the DLB. The initial distance of atoms from the DLB is about 2.8 Å. The energy curves give proof that the penetration of all atoms has to overcome the energy barrier. The atoms introduced have the maximum potential energy when they are lodged completely at the boron sheets vacancy (Fig. 7). Then, at inward distance of about 1 Å from the defective boron layer, we can see a stable minimum of energy for all considered atoms. Hence, if the adatoms would have the possibility of overcoming the energy barrier in the classic manner, i.e. when the value of potential energy of the approaching atom is greater than the energy of potential barrier, or by tunnel effect, they will be in a stable position between two boron sheets. The heights of barriers which can be identified like the energy of infiltration activation are shown in Table 3. Hydrogen, the lightest atom, demonstrates the lowest energy activation of 3.94 eV.

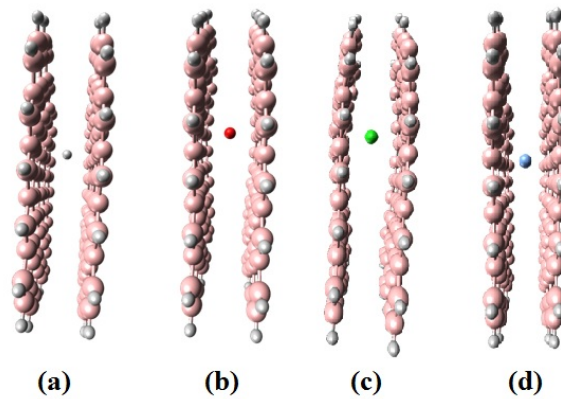


FIG. 6. Structures of double-layered boron with gas-phase atoms penetrated into the interplanar space of the double-layered boron: a) hydrogen; b) oxygen; c) fluorine; d) chlorine

5. Conclusion

We have found that hexagonal boron sheets can be used as a base for composite materials. It is possible to create double-layered boron and we guess that it is possible to create multi-layered materials of boron as well.

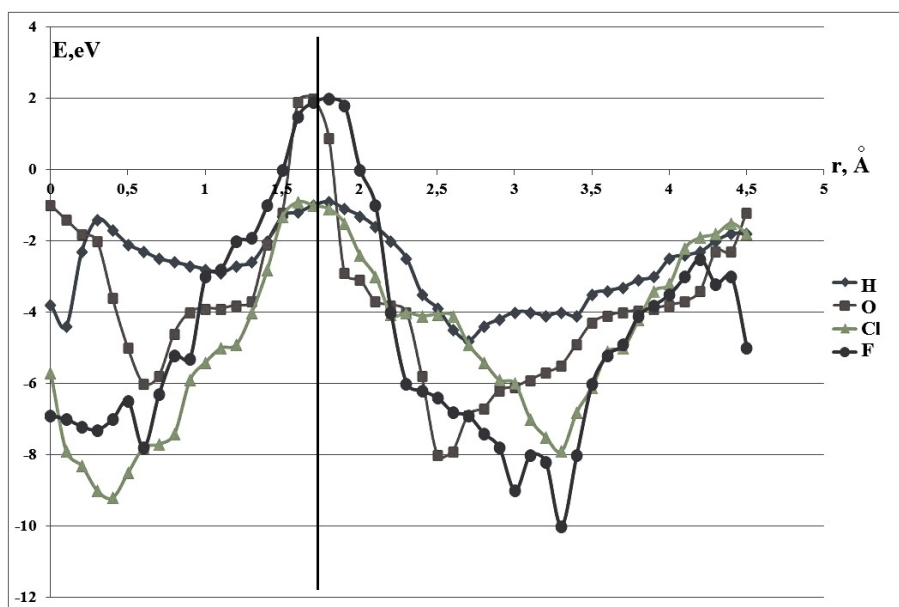


FIG. 7. Profiles of surface potential energy of the atoms infiltration into the interplanar space of the double-layered boron: a) hydrogen; b) oxygen; c) fluorine; d) chlorine. The boundary of a boron sheet with vacancy (first boron layer) has been marked by vertical line

TABLE 3. Values of activation energy E_{act} of double-layered boron for considered atoms

Infiltration atom	H	O	F	Cl
E_{act} , eV	3.94	9.92	6.92	12.44

We also have found that double-layered boron has good adsorption characteristics of gas-phase atoms. One of the applications of this new nanostructure could be the hydrogen storage inside interplanar space.

References

- [1] Wang K.-P., Teng H. Structural feature and double-layer capacitive performance of porous carbon powder derived from polyacrylonitrile-based carbon fiber. *J. Electrochem. Soc.*, 2007, **154** (11), P. 993–998.
- [2] Wang Y., Fugetsu B., Wang Z., Gong W. Nitrogen-doped porous carbon monoliths from polyacrylonitrile (PAN) and carbon nanotubes as electrodes for supercapacitors. *Sci. Rep.*, 2017, **7**, P. 40259.
- [3] Oganov A.R., Guisinger N.P. Nanomaterials, synthesis of borophenes: Anisotropic, two-dimensional boron polymorphs. *Science*, **350** (6267), P. 1513–1516.
- [4] Zhang X., Hu J., et al. Borophene as an extremely high capacity electrode material for Li-ion and Na-ion batteries. *Nanoscale*, 2016, **8** (33), P. 15340.
- [5] Xiao R.C., et al. Enhanced superconductivity by strain and carrier-doping in borophene: A first principles prediction. *Applied Physics Letters*, 2016, **109**, P. 122604.
- [6] Chernozatonskii L.A., Sorokin P.B., Yakobson B.I. New boron barrelenes and tubulenes. *JETP Lett.*, 2008, **87** (9), P. 489–493.
- [7] Penev E.S., Bhowmick S., Sadzadeh A., Yakobson B.I. Polymorphism of two-dimensional boron. *Nano Lett.*, 2012, **12** (5), P. 2441–2445.
- [8] Enyashin A.N., Bamburov V.G., Ivanovskii A.L. Composition, stability, and elastic moduli of higher allotropes of boron (β -B and tII-B) according to SCC-DFTB calculations. *Doklady Physical Chemistry*, 2011, **438** (2), P. 118–121.
- [9] Shirai K., Uemura N., Dekura H. Structure and stability of pseudo-cubic tetragonal boron. *Jpn J. Appl. Phys.*, 2017, **56**, 5S3.
- [10] Khairullin A.R., Nikolaeva M.N., Bugrov A.N. Resistance of composite films based on polystyrene and graphene oxide. *Nanosystems: Phys. Chem. Math.*, 2016, **7** (6), P. 1055–1058.
- [11] Ostroushko A.A., Russkikh O.V. Oxide material synthesis by combustion of organic-inorganic compositions. *Nanosystems: Phys. Chem. Math.*, 2017, **8** (4), P. 476–502.
- [12] Kah Chun Lau, Ravindra Pandey. Stability and electronic properties of atomistically-engineered 2D boron sheets. *J. Phys. Chem. C*, 2007, **111** (7), P. 2906–2912.
- [13] Dewar M.J.S., Thiel W. Ground states of molecules. 38. The MNDO method. Approximations and Parameters. *J. Am. Chem. Soc.*, 1977, **99** (15), P. 4899–4907.
- [14] Boroznina E.V., Zhiganova T.A., Boroznina S.V. Research of vacancy defect formation on the surface of two-dimensional boron sheets. *J. Phys.: Conf. Ser.*, 2015, **586**, P. 012010.

Magnetically tunable viscoelastic response of soft magnetic nanocomposites with wormlike surfactant micellar matrix

V. S. Molchanov^{1,*}, I. A. Klepikov², I. V. Razumovskaya², O. E. Philippova¹

¹Physics Department, Moscow State University, 119991 Moscow, Russia

²Moscow State University of Education, 119991 Moscow, Russia

*molchan@polly.phys.msu.ru

DOI 10.17586/2220-8054-2018-9-3-335-341

Magnetorheological effects in viscoelastic soft magnetic nanocomposites (SMNs) composed of submicron magnetite particles embedded in a network of wormlike micelles (WLMs) of surfactant were studied in a homogeneous magnetic field. In field, the SMNs showed rapid rise of storage and loss moduli by a few orders of magnitude as a result of the ordering of magnetized particles into chain-like or columnar structures. Moreover, solid-like behavior and yield stress of the SMNs were observed. Study of rheological response on periodic switching of field revealed that the initial viscoelasticity of SMNs did not recover completely after removing field, which was attributed to extremely long relaxation time of the WLM network. It was found that the variation of storage and moduli loss was associated with the stepwise change in magnetic field; this can be fitted by two-exponential functions, a characteristic time for the slower process being almost the same as the relaxation time of SMN without field, indicating that this process is essentially determined by the viscoelastic properties of the matrix.

Keywords: magnetorheological fluid, viscoelasticity, wormlike micelles of surfactant, magnetic particles.

Received: 28 November 2017

Revised: 11 March 2018

1. Introduction

Magnetorheological fluids (MRFs) [1–4] and magnetic elastomers [5,6] or gels [7,8] have attracted increasing attention, because their rheological properties can be changed continuously, rapidly and reversibly, by applying a magnetic field. In the absence of an external magnetic field, the magnetizable particles are randomly dispersed in the medium. When a certain field strength is imposed, the dispersed particles build up the chain-like structures or columns in the field's direction due to an induced magnetic dipole–dipole interaction [2,3,9,10]. Owing to the arrangement of particles, the properties (viscoelasticity, yield stress, heat conduction) of the bulk material can be tuned in milliseconds by orders of magnitude. Such smart materials have found many engineering applications providing semi-active control in various devices such as dampers, shock absorbers, torque transducers, clutches, brakes and ultrafine polishing technology [2,5]. They are employed, in particular, in the automobile industry.

High magnetorheological effects can be achieved when particles are close to each other and have large magnetization values [3]. Therefore, it is necessary to provide high volume fraction and particle sizes. For this reason, the submicron particles are considered more promising for soft magnetic nanocomposite preparation. Carbonyl iron and iron oxide particles are widely used in MRFs due to their high magnetic response and availability [11,12], but their density is very high – nearly 8 g/cm³ and 5 g/cm³, respectively. This makes it difficult to disperse the submicron- or micron-sized particles in a liquid carrier. To resolve this problem, highly viscous carriers [11] or polymer network matrices [13,14] can be used. However, these carriers deteriorate the mechanical properties of the system in magnetic field because of the restriction of the motion of the particles within the network [14] and the delay rate of the response [13]. To compensate these negative effects, the concentration of particles should be increased considerably (up to 30 vol %) [14].

Recently, a new type of carrier for magnetic particles was proposed [15]. This carrier is based on soft matrix of WLMs of surfactants. The advantage of such SMNs is the linear viscoelasticity of the WLM network [16–19]. Linear viscoelastic properties of SMNs allow investigation of the dynamic moduli of the system. Also, the WLMs are “living” objects, they can reversibly break under stress [18,20,21] that makes them promising as a matrix where particles can move freely enough even at low particle concentrations. This shows that WLMs are perfect for the stabilization of particle suspensions, because they are able to link to the particles by their end-caps. However, the rheological behavior of the SMNs was studied mainly in the absence of magnetic field.

Therefore, the present paper is devoted to the investigation of the rheological properties of SMNs composed of submicron magnetite particles embedded in the network of WLMs in magnetic field. The WLMs were built by cationic surfactant erucyl bis-(hydroxyethyl)methylammonium chloride (EHAC) in the presence of low-molecular-weight salt KCl. EHAC containing a long mono-unsaturated C22 tail is known to impart high viscosity to aqueous

solutions even at rather low surfactant concentrations. To provide stronger interaction with particles [22], the experiments were performed at pH 11, when magnetite particles were negatively charged [15].

2. Experimental section

2.1. Materials

The cationic surfactant EHAC $C_8H_{17}CH=CHC_{12}H_{24}N(CH_2CH_2OH)_2CH_3Cl$ was provided by Akzo Nobel as a solution in 2-propanol. EHAC powder was obtained by freeze drying this solution. 1H NMR spectroscopy data proved the absence of 2-propanol in EHAC thus purified. Potassium chloride (purity > 99%) from Acros Organics was used without further purification. Distilled water was obtained with a Milli-Q system (Millipore).

Magnetite particles iron (II,III) oxide Fe_3O_4 were supplied by Sigma-Aldrich. By scanning electron microscopy, it was shown that the average diameter of the particles is about 250 nm [15]. These particles possess ferrimagnetic properties [23], their saturation magnetization is 100 emu/g, the residual magnetization is 19 emu/g, and the coercive force – 95 Oe [15]. Dispersions of these magnetic particles in WLM viscoelastic solutions were prepared following a previously developed procedure [15]. The homogeneity of the suspensions was examined by visual observation after 2 months storage at 25 °C.

2.2. Rheological Measurements

The dynamic and static controlled stress rheological measurements of the SMNs in the absence and in the presence of a homogeneous magnetic field were carried out with a commercial rheometer Physica MCR 301 (Anton Paar, Austria). The temperature was fixed at 20 °C. The samples were placed between rotated cone or plate and static plate. Static rheological measurements were performed at shear stress from 0.009 Pa to 100 Pa. Zero-shear viscosity was obtained from plateau of flow curve while yield stress was obtained from stress-strain curve. Dynamic frequency-dependent measurements were performed at frequencies from 0.01 to 10 rad/s and a fixed strain amplitude within the linear viscoelastic region. Latter was measured at frequency of 1 rad/s and a strain amplitude from 0.05 to 10 %. The measuring system's geometries were a cone-plate set with diameter 50 mm and angle 1 ° for tests without the field because lower shear stress and a parallel-plate set with 20 mm diameter as part of a specific magnetic equipment. The gap thickness in the latter cell was 300 μm in all measurements [24]. The magnetic field with the strength of up to 1 T was applied in the direction perpendicular to the shear stress 27 – 23.

3. Results and discussion

Fig. 1 allows one to compare the values of the storage G' and loss G'' moduli for some SMNs before and after the application of magnetic field. It is seen that in the absence of magnetic field, the SMN sample containing 0.2 vol % magnetite has a storage modulus G' of 0.2 Pa and a loss modulus G'' of 0.02 Pa. When 1 T magnetic field is applied, G' and G'' moduli increase by 2 orders of magnitude (Fig. 1). This can be explained by the formation of chain-like structures of particles along the magnetic field lines oriented perpendicular to the direction of flow [2, 3, 25]. Among the chain-like structures, one can distinguish long ones, which spread from one plate of the measuring cell to the other, and shorter ones possessing at least one free end. The long structures attached to both measuring plates are suggested to contribute to the storage modulus G' thus enhancing the elasticity of the system, whereas short structures give input into the loss modulus G'' thus increasing the viscous contribution.

In the absence of magnetic field, the SMN with 3 vol % magnetite has almost the same value of storage modulus G' as the sample with 0.2 vol % magnetite (data not shown here), which is expected, because at these concentrations, the dependencies of G' and G'' on the content of the particles level off [15]. However, in 1 T magnetic field the values of G' and G'' for the SMN sample with 3 vol % of particles are by two orders of magnitude higher than for the sample with 0.2 vol % of particles. It indicates to increasing input of both long and short chain-like structures into viscoelastic properties of SMNs, when the amount of particles making up these structures increases.

Let us consider the evolution of storage G' and loss G'' moduli with increasing mechanical strain depicted in Fig. 1. One can see that in the absence of magnetic field, the SMN sample containing 0.2 vol % magnetite demonstrates a linear viscoelasticity at all studied strain values up to 10 %. This feature of the SMNs is provided by viscoelastic matrix composed of entangled WLMs [19]. When 1 T magnetic field is applied, the sample continues to exhibit a wide linear viscoelastic region, similar to that observed without the field. However, SMN with higher volume fraction of particles (0.3 vol %) has a shorter range of linear viscoelasticity (up to the strain of nearly 1 %). At higher strains, storage modulus G' starts to decrease, indicating the appearance of nonlinearity. It can be attributed to the reorganization (for instance, partial destruction) of the chain-like structures of particles formed in the magnetic field, when the mechanical deformations become rather high [26, 27]. However, the deviations from

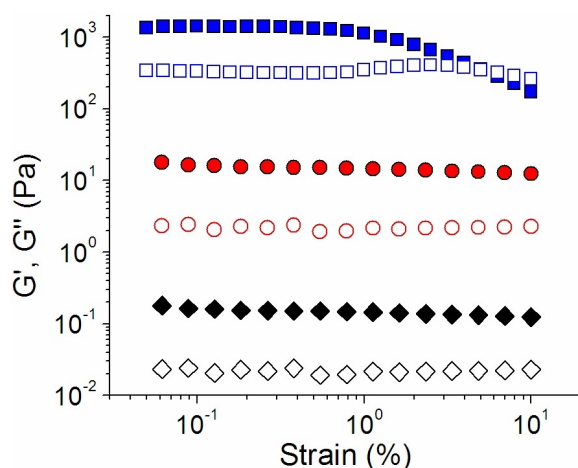


FIG. 1. Dependence of storage G' (filled symbols) and loss G'' (open symbols) moduli on mechanical strain (at 1 rad/s frequency) for SMN containing 0.2 vol % magnetite and 0.6 wt % EHAC without field (black diamonds) and at magnetic field strength of 1 T (red circles) and for SMN containing 3 vol % magnetite and 0.6 wt % EHAC at magnetic field strength of 1 T (blue squares). Solvent: 1.5 wt % KCl in water

linear viscoelasticity occur at rather large strains, which are much higher than in MRFs based on Newtonian liquids (0.003 – 0.1 % [8, 12, 23]). Therefore, the SMNs under study show a rather wide range of linear viscoelasticity even at magnetic field strength as high as 1 T. This feature is quite important since the dynamic rheological data obtained within linear viscoelastic region characterize the structure undisturbed by mechanical strain [11], and these data are most suitable for further investigation of the structure transformations induced by magnetic field. Therefore, in the present system, a broad range of linear viscoelastic response within a wide range of deformations (Fig. 1) permits to perform the oscillatory measurements under optimum conditions.

Figure 2 shows the frequency dependences of storage $G'(\omega)$ and loss $G''(\omega)$ moduli obtained at fixed strain in linear viscoelasticity region. It is seen that without field, the loss modulus has a minimum and the $G''(\omega)$ curve as a tendency to intercept with $G'(\omega)$ curve so that at lower frequencies loss modulus is expected to exceed the storage modulus. Upon application of magnetic field, the G' and G'' values increase by several orders of magnitude and become independent of frequency (Fig. 2).

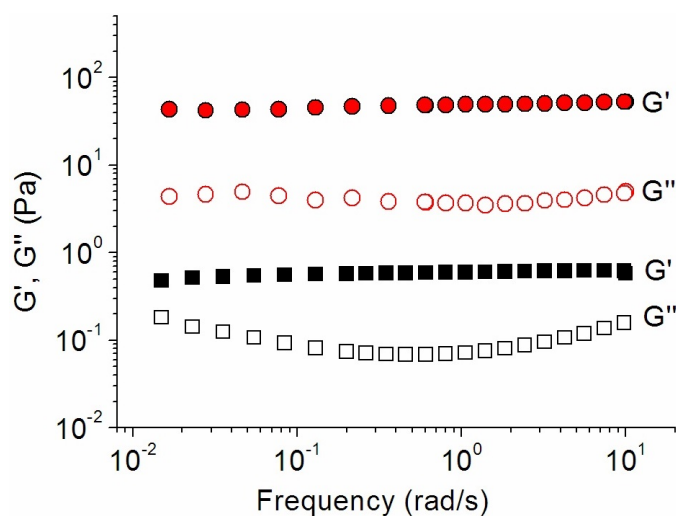


FIG. 2. Frequency dependences of storage (filled symbols) and loss (open symbols) moduli without field (black squares) and in 0.2 T magnetic field (red circles) at constant strain of 1 % for SMN containing 0.6 vol % magnetite and 0.6 wt % EHAC. Solvent: 1.5 wt % KCl in water

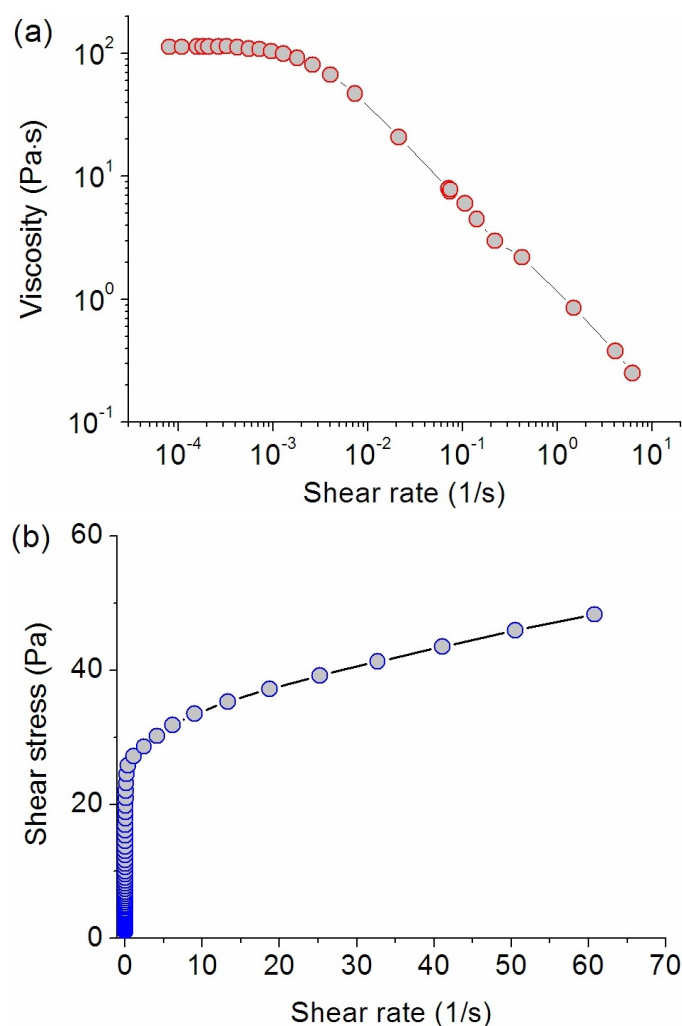


FIG. 3. Viscosity (a) and shear stress (b) plotted as a function of shear rate for SMN sample containing 0.6 vol % magnetite and 0.6 wt % EHAC without field (a) and in 0.2 T magnetic field (b). Solvent: 1.5 wt % KCl in water

The results of steady-state rheological measurements are presented in Fig. 3. It is seen that in the absence of magnetic field (Fig. 3a) the SMN shows a flow curve with a shear thinning behavior and a plateau at low shear rates giving the value of zero-shear viscosity. The shear-thinning behavior can be attributed to the alignment of WLMs along the direction of flow [16]. By contrast, in the presence of magnetic field (0.2 T), the sample does not flow below some critical stress (Fig. 3b). It indicates that upon application of the magnetic field the system acquires a yield stress [28–30]. For the SMN sample with 3 vol % magnetite and 0.6 wt % EHAC the yield stress is equal to 24 Pa. Thus, under the action of magnetic field the SMN undergoes a transformation from viscoelastic to a solid-like state.

Figure 4 shows the response of storage G' and loss G'' moduli in oscillatory testing of SMN sample under periodical switching of the 0.2 T magnetic field every 300 s. In this experiment, the G' and G'' values were determined at a fixed frequency of shear strain equal to 1 rad/s. From Fig. 4 it is seen that the moduli increased synchronically with the magnetic field, but did not fully recover the original values after switching the field off. During several cycles of periodical application of magnetic field the storage G' and loss G'' moduli under the field are the same, whereas without field the residual values of G' and G'' increase with time and finally level off (Fig. 4). The effect can be explained by the impact of the viscoelastic network of WLMs. Indeed, the micelles attached to particles have to be stretched when particles move in order to self-organize in the chain-like or column structures because latter process is quite rapid. Then, WLMs move in direction of the structures of particles and reorganize around new chain-like or column structures. After removing field particles have tendency to disperse randomly [13] but the reorganized WLM network formed around chains/columns retain them in partly ordered

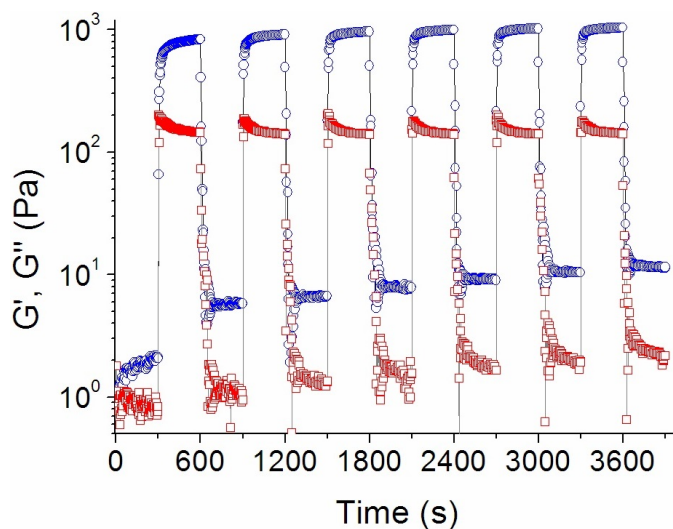


FIG. 4. Evolution of storage G' (blue circles) and loss G'' (red squares) moduli with time in response to periodical switching of 0.2 T magnetic field for SMN sample containing 0.3 vol % magnetite and 0.6 wt % EHAC. Solvent: 1.5 wt % KCl in water. G' and G'' values were determined at 1 rad/s frequency of shear strain

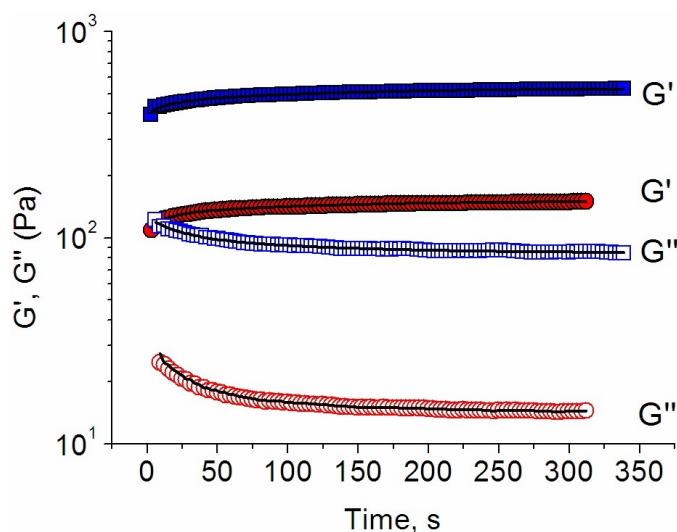


FIG. 5. Evolution of the storage G' (filled) and loss G'' (open) moduli with time in magnetic field of 0.04 T (blue squares) and of 0.07 T (red circles) for SMN sample containing 0.3 vol % magnetite and 0.6 wt % EHAC. Solvent: 1.5 wt % KCl in water. G' and G'' values were determined at 1 rad/s frequency of shear strain. Curves fitting $G'(t)$ and $G''(t)$ dependences by two-exponential function are depicted by solid lines

conditions. After certain cycles of repeated magnetic field action, the WLMs organize a network around the structures of particles, which is responsible for the residual values of moduli being one order of magnitude higher than the original moduli without field. Thus, with periodical switching of magnetic field the viscoelasticity of the WLM network produces enhanced G' and G'' moduli, which do not acquire their original values. It can be suggested that the system needs longer time to fully recover the initial state because of extremely long relaxation time of the WLM network, especially with embedded particles [15].

Figure 5 displays the change in storage and loss moduli associated with the stepwise change in magnetic field of 0.04 T and 0.07 T. It is seen that the storage G' and loss G'' moduli response fits well to the two-exponential increase and decrease, correspondingly. The fitting for both moduli results in two values of characteristic time: a shorter one $t_1 = 15 \pm 5$ s and a longer one $t_2 = 110 \pm 10$ s. In literature, the fast time was associated with

the formation of particles having chain-like structures and the slower time was attributed to the migration of these chains into thicker clusters [13]. Also, it was shown that the characteristic time t_2 for the slow process is essentially determined by the viscoelastic properties of the matrix [13], which is in agreement with our data, since the t_2 value is almost the same as the relaxation time for SMN without field [15].

4. Conclusions

This paper describes the variation of rheological properties of new SMNs upon application of a homogeneous magnetic field. It was shown that the studied SMNs possess very large linear viscoelasticity regions, which allows one to perform dynamic oscillatory shear tests over a wide range of applied mechanical deformations. Such tests are important for modeling the behavior of magnetorheological system under oscillatory shear stress conditions, for instance, in damper applications for vibration control. Despite this fact, such oscillatory tests are rarely used for studying MRFs because the linear viscoelastic region for most of them is limited to extremely low deformations. Periodical switching of magnetic field demonstrated that at each cycle the G' and G'' values in the magnetic field are higher by several orders of magnitude than in its absence. The data obtained show that the new SMNs are very promising for various magnetorheological applications under dynamic conditions.

Acknowledgements

This work was supported by Russian Foundation for Basic Research and Moscow city Government (project No 15-33-70046 “mol_a_mos”).

References

- [1] Odenbach S. Recent Progress in Magnetic Fluid Research. *J. Phys.: Condens. Matter*, 2004, **16**, P. R1135–R1150.
- [2] Park B.J., Fang F.F., Choi H.J. Magnetorheology: Materials and Application. *Soft Matter*, 2010, **6**, P. 5246–5253.
- [3] De Vicente J., Klingenberg D.J., Hidalgo-Alvarez R. Magnetorheological Fluids: a Review. *Soft Matter*, 2011, **7**, P. 3701–3710.
- [4] Barabanova A., Molchanov V., Philippova O., Khokhlov A., Magnetorheological Fluids Based on Associating Polymers. *Macromol. Symp.*, 2014, **337**, P. 80–86.
- [5] Filipcsei G., Csetneki I., Szilgyi A., Zrinyi M. *Magnetic Field-Responsive Smart Polymer Composites*. In Advances in Polymer Science, Oligomers, Polymer Composites, Molecular Imprinting, Springer-Verlag, Berlin, 2007, P. 137–189.
- [6] Molchanov V.S., Stepanov G.V., Vasiliev V.G., Kramarenko E.Yu., Khokhlov A.R., Xu Z.-D., Guo Y.-Q. Viscoelastic Properties of Magnetorheological Elastomers for Damping Applications. *Macromol. Mater. Eng.*, 2014, **299**, P. 1116–1125.
- [7] Zhou Y., Sharma N., Deshmukh P., Lakhman R.K., Jain M., Kasi R.M. Hierarchically Structured Free-Standing Hydrogels with Liquid Crystalline Domains and Magnetic Nanoparticles as Dual Physical Cross-Linkers. *J. Am. Chem. Soc.*, 2012, **134**, P. 1630–1641.
- [8] An H.-N., Sun B., Picken S.J., Mendes E. Long Time Response of Soft Magnetorheological Gels. *J. Phys. Chem. B*, 2012, **116**, P. 4702–4711.
- [9] McLeish T.C.B., Jordan T., Shaw M.T. Viscoelastic Response of Electrorheological Fluids. I. Frequency dependence. *J. Rheol.*, 1991, **35**, P. 427–448.
- [10] Ginder J.M., Davis L.C., Elie L.D. Rheology of Magnetorheological Fluids: Models and Measurements. *Int. J. Mod. Phys. B*, 1996, **10**, P. 3293–3303.
- [11] Claracq J., Sarrazin J., Montfort J.-P. Viscoelastic Properties of Magnetorheological Fluids. *Rheol. Acta*, 2004, **43**, P. 38–49.
- [12] De Vicente J., Segovia-Gutiérrez J.P., Andablo-Reyes E., Vereda F., Hidalgo-Alvarez, R. Dynamic Rheology of Sphere- and Rod-Based Magnetorheological Fluids. *J. Chem. Phys.*, 2009, **131**, P. 194902.
- [13] An H.-N., Sun B., Picken S.J., Mendes E. Long Time Response of Soft Magnetorheological Gels. *J. Phys. Chem. B*, 2012, **116**, P. 4702–4711.
- [14] Mitsumata T., Honda A., Kanazawa H., Kawai M. Magnetically Tunable Elasticity for Magnetic Hydrogels Consisting of Carrageenan and Carbonyl Iron Particles. *J. Phys. Chem. B*, 2012, **116**, P. 12341–12348.
- [15] Pletneva V.A., Molchanov V.S., Philippova O.E. Viscoelasticity of Smart Fluids Based on Wormlike Surfactant Micelles and Oppositely Charged Magnetic Particles. *Langmuir*, 2015, **31**, P. 110–119.
- [16] Magid L.J. The Surfactant-Polyelectrolyte Analogy. *J. Phys. Chem. B*, 1998, **102**, P. 4064–4074.
- [17] Oda R., Narayanan J., Hassan P.A., Manohar C., Salkar R.A., Kern F., Candau S.J. Effect of the Lipophilicity of the Counterion on the Viscoelasticity of Micellar Solutions of Cationic Surfactants. *Langmuir*, 1998, **14**, P. 4364–4572.
- [18] Molchanov V.S., Philippova O.E. Dominant Role of Wormlike Micelles in Temperature-Responsive Viscoelastic Properties of their Mixtures with Polymeric Chains. *J. Colloid Interface Sci.*, 2013, **394**, P. 353–359.
- [19] Kwiatkowski A.L., Molchanov V.S., Orekhov A.S., Vasiliev A.L., Philippova O.E. Impact of Salt Co- and Counterions on Rheological Properties and Structure of Wormlike Micellar Solutions. *J. Phys. Chem. B*, 2016, **120**, P. 12547–12556.
- [20] Shibaev A.V., Tamm M.V., Molchanov V.S., Rogachev A.V., Kuklin A.I., Dormidontova E.E., Philippova O.E. How a Viscoelastic Solution of Wormlike Micelles Transforms into a Microemulsion upon Absorption of Hydrocarbon: New Insight. *Langmuir*, 2014, **30**, P. 3705–3714.
- [21] Philippova O.E., Chitcheglova L.A., Karybants N.S., Khokhlov A.R. Two Mechanisms of Gel/Surfactant Binding. *Polymer Gels Networks*, 1998, **6**, P. 409–421.
- [22] Kwiatkowski A.L., Sharma H., Molchanov V.S., Orekhov A.S., Vasiliev A.L., Dormidontova E.E., Philippova O.E. Wormlike Surfactant Micelles with Embedded Polymer Chains. *Macromolecules*, 2017, **50**, P. 7299–7308.

- [23] Chin B.D., Park J.H., Kwon M.H., Park O.O. Rheological Properties and Dispersion Stability of Magnetorheological (MR) Suspensions. *Rheol. Acta*, 2001, **40**, P. 211–219.
- [24] Martin J.M., Odinek J. Evolution of Structure in Quiescent Electrorheological Fluid. *Phys. Ref. Lett.*, 1992, **69**, P. 1524–1528.
- [25] Otsubo Y. Electrorheological Properties of Barium Titanate Suspensions under Oscillatory Shear. *Colloids Surf.*, 1991, **58**, P. 73–86.
- [26] Parthasarathy M., Ahn K.H., Belongia B., Klingenberg D.J. The Role of Suspension Structure in the Dynamic Response of Electrorheological Suspensions. *Int. J. Mod. Phys. B*, 1994, **8**, P. 2789–2809.
- [27] López-López M.T., Rodríguez-Arco L., Zubarev A., Iskakova L., Durán D.G. Effect of Gap Thickness on the Viscoelasticity of Magnetorheological Fluids. *J. Appl. Phys.*, 2010, **108**, P. 083503.
- [28] Viota J.L., Delgado A.V., Arias J.L., Durán J.D.G. Study of the Magnetorheological Response of Aqueous Magnetite Suspensions Stabilized by Acrylic Acid Polymers. *J. Colloid Interface Sci.*, 2008, **324**, P. 199–204.
- [29] Li W.H., Chen G., Yao S.H. Viscoelastic Properties of MR Fluids. *Smart Mater. Struct.*, 1999, **8**, P. 460–468.
- [30] López-López M.T., Gómez-Ramírez A., Rodríguez-Arco L., Durán D.G., Iskakova L., Zubarev A. Colloids on the Frontier of Ferrofluids. Rheological Properties. *Langmuir*, 2012, **28**, P. 6232–6245.

Theoretical study of the slow light in the assembly of helium atoms

A. G. Petrashen, N. V. Sytenko

ITMO University, Kronverkskiy, 49, Saint Petersburg, 197101, Russia

apetrashen@mail.ru, nsitenko@yandex.ru

PACS 32.8.QK, 32.10.Dk, 32.80.-t

DOI 10.17586/2220-8054-2018-9-3-342-348

The problem of solving light was installed about thirty years ago and was widely considered in different approximations. In this paper, this process is investigated using both perturbation theory and numerical integration of the system of Liouville–Maxwell differential equations.

Keywords: coherent excitation, density matrix, Liouville equation.

Received: 14 March 2018

Revised: 29 March 2018

Final revision: 25 April 2018

1. Introduction

Effects caused by the quantum-mechanical coherence and interference of states have been extensively studied over the past few decades. Electromagnetically induced transparency give rise to a new direction of research, which deals with the fact that an anomalously strong dispersion of a weak beam in the field of a strong beam leads to a change in group velocity of weak beam photons. In the extreme case, this can lead to the stopping of low intensity photons, which in turn can lead to the creation of optical memory. The change in group velocity of a low intensity beam was discussed in the work of Harris et al. [1]. Later, this phenomenon was investigated in the papers of [2–4]. Among other works, in our opinion, special note should be made of the papers of Lukin [5, 6], where the author used the solution of the Heisenberg–Langevin equations for the density matrix in perturbation theory to analyze the dependence of the velocity on the parameters of the problem under consideration. In this paper, we will use both perturbation theory and numerical integration of differential equations to obtain expression for group velocity of radiation of a real atomic system. Similar methods of investigations were previously applied to the problem of influence of strong magnetic field on characteristics of emission of ensemble of helium atoms and the problem of possibility of lasering without inversion [7, 8]. The results of such an approximate calculation will be checked against similar results obtained by numerical integration of the Liouville–Maxwell partial differential equations.

2. The interaction of the atomic system with the field

In this work, we will consider a system of three atomic states of the helium atom: 2^3P_2 - (level c), 2^3P_1 - (level a) and 2^3S_1 - (level b), and we will assume that levels “ a ” and “ c ” are coherently excited from level “ b ” as according to the V -type excitation scheme. This trio of levels was chosen because the line that corresponds to a transition 2^3P-2^3S lies near the visible wavelength range, the upper 3P states relax relatively weakly, while the lower 2^3S_1 state practically does not decay [9] and can be impact-excited from the ground state. The imposition of a time-dependent alternating electric field on the atomic system leads to charge displacement or, in other words, to the creation of currents, and, consequently, to the appearance an alternating electric and magnetic field. A joint influence of these quantities is described by a set of Maxwell equations, from which, using well-known transformations, it is not difficult to obtain equations that describes the mutual variation in the electric field vector \mathbf{E} and polarization of the medium \mathbf{P} :

$$\nabla^2 \mathbf{E} = \frac{\mu}{c^2} \frac{\partial^2 \mathbf{E}}{\partial t^2} + \frac{4\pi\mu}{c^2} \frac{\partial^2 \mathbf{P}}{\partial t^2}. \quad (1)$$

From here forward, we will assume that the field and the polarization depend only on one spatial variable and time, and that the amplitudes of these magnitudes are slowly varying functions of their variables. Then, if we seek the amplitudes of these fields in the form of $E(x, t) = \mathcal{E}(x, t)e^{i(\omega t + kx)} + \mathcal{E}^*(x, t)e^{-i(\omega t + kx)}$ and $P(x, t) = \mathcal{P}(x, t)e^{i(\omega t + kx)} + \mathcal{P}^*(x, t)e^{-i(\omega t + kx)}$, then after substituting these functions into (1) and neglecting rapidly varying terms and higher-order derivatives of the field and the polarization vector amplitudes in the

resulting expression, we obtain two equations which, if we introduce complex amplitudes for the field strength and polarization of the medium, can be reduced to one equation:

$$\frac{\partial}{\partial \tau} \mathcal{E}(x, \tau) = -2\pi\mu\omega i \mathcal{P}(x, \tau). \quad (2)$$

It can be seen from the last relation that the imaginary part of the polarization vector characterizes field attenuation, i.e. absorption, while the real part characterizes dispersion. Note that in terms of its physical meaning, the magnitude of the polarization vector is proportional to the mean value of the dipole moment:

$$\mathcal{P}_a = n_0 \text{Sp}(\rho_{ab}d), \quad (3)$$

where n_0 is the particle's density and $\rho_{ab}(t)$ – is the correlation density matrix in the ab arm.

It is well known, that the evolution of density matrix is described by the Liouville equation. In the case under consideration, this equation must be considered together with equation (2) because the external field enforced on the atomic system under consideration, leads to an induction of additional polarization fields. So one can say that evolution of our system describes by the the system of the Liouville–Maxwell equations.

To perform numerical calculations in this system of equations, it would be convenient to introduce dimensionless time $\tau = t/\tau_0$, where τ_0 is the lifetime of the 2^3P state of the He atom, and the spatial variable $\kappa = x/c\tau_0$. In addition, as we continue, it would also be convenient to move from the quantities of the electric field strength to the dimensionless Rabi frequencies $(\Omega_R(\tau))_{ib} = \mathcal{E}(\tau)_{ib}\tau_0 e a_0/\hbar$ where the index i numbers the corresponding arm of the V -type scheme. In these variables, the system of the Liouville–Maxwell equations will take the form:

$$\begin{aligned} \frac{d}{d\tau} \rho_{aa}(\tau, \kappa) &= -\gamma_{aa} \rho_{aa}(\tau, \kappa) - \frac{i(\Omega_R(\tau, \kappa))_{ab}}{2} \left[\left(\frac{r_q}{a_0} \right)_{ab} \rho_{ba}(\tau, \kappa) e^{i\delta_a \tau} - \rho_{ab}(\tau, \kappa) \left(\frac{r_q}{a_0} \right)_{ab} e^{-i\delta_a \tau} \right], \\ \frac{d}{d\tau} \rho_{cc}(\tau, \kappa) &= -\gamma_{cc} \rho_{cc}(\tau, \kappa) - \frac{i(\Omega_R(\tau, \kappa))_{bc}}{2} \left[\left(\frac{r_q}{a_0} \right)_{cb} \rho_{bc}(\tau, \kappa) e^{i\delta_c \tau} - \rho_{cb}(\tau, \kappa) \left(\frac{r_q}{a_0} \right)_{bc} e^{-i\delta_c \tau} \right], \\ \frac{d}{d\tau} \rho_{bb}(\tau, \kappa) &= \gamma_{bb} \rho_{bb}(\tau, \kappa) - \frac{i(\Omega_R(\tau, \kappa))_{ab}}{2} \left[\left(\frac{r_q}{a_0} \right)_{ba} \rho_{ab}(\tau, \kappa) e^{-i\delta_c \tau} - \rho_{ba}(\tau, \kappa) \left(\frac{r_q}{a_0} \right)_{ab} e^{i\delta_c \tau} \right] \\ &\quad - \frac{i(\Omega_R(\tau, \kappa))_{bc}}{2} \left[\left(\frac{r_q}{a_0} \right)_{bc} \rho_{cb}(\tau, \kappa) e^{-i\delta_c \tau} - \rho_{bc}(\tau, \kappa) \left(\frac{r_q}{a_0} \right)_{cb} e^{i\delta_c \tau} \right], \\ \frac{d}{d\tau} \rho_{ab}(\tau, \kappa) &= \gamma_{ab} \rho_{ab}(\tau, \kappa) - \frac{i(\Omega_R(\tau, \kappa))_{ab}}{2} \left[\left(\frac{r_q}{a_0} \right)_{ab} \rho_{bb}(\tau, \kappa) e^{-i\delta_a \tau} - \rho_{aa}(\tau, \kappa) \left(\frac{r_q}{a_0} \right)_{ab} e^{i\delta_a \tau} \right] \\ &\quad + \frac{i(\Omega_R(\tau, \kappa))_{bc}}{2} \rho_{ac}(\tau, \kappa) \left(\frac{r_q}{a_0} \right)_{cb} e^{-i\delta_c \tau}, \\ \frac{d}{d\tau} \rho_{cb}(\tau, \kappa) &= \gamma_{cb} \rho_{cb}(\tau, \kappa) - \frac{i(\Omega_R(\tau, \kappa))_{bc}}{2} \left[\left(\frac{r_q}{a_0} \right)_{cb} \rho_{bb}(\tau, \kappa) e^{i\delta_c \tau} + \rho_{cc}(\tau, \kappa) \left(\frac{r_q}{a_0} \right)_{cb} e^{i\delta_c \tau} \right] \\ &\quad + \frac{i(\Omega_R(\tau, \kappa))_{ab}}{2} \rho_{ca}(\tau, \kappa) \left(\frac{r_q}{a_0} \right)_{ab} e^{i\delta_a \tau}, \\ \frac{d}{d\tau} \rho_{ac}(\tau) &= -\gamma_{ac} \rho_{ac}(\tau) - \frac{i}{2} (\Omega_R(\tau, \kappa))_{bc} \rho_{ab}(\tau, \kappa) \left(\frac{r_q}{a_0} \right)_{bc} e^{i\delta_c \tau} + \frac{i}{2} (\Omega_R(\tau, \kappa))_{ab} \left(\frac{r_q}{a_0} \right)_{bc} \rho_{bc}(\tau, \kappa) e^{-i\delta_a \tau}, \\ \frac{\partial}{\partial \tau} (\Omega_R)_i(\tau, \kappa) + \frac{\partial}{\partial \kappa} (\Omega_R)_i(\tau, \kappa) &= -i\Omega_M^2 \text{Sp}(\rho_{bi}(\tau, \kappa)) \left(\frac{r_{bi}}{a_0} \right), \quad i = a, c, \end{aligned} \quad (4)$$

where $\left(\frac{r_q}{a_0} \right)_{i,j}$ – is the matrix element of the q -th component of the operator \hat{r}/a_0 , evaluated on the eigenfunctions

of the i and j states (we assumed $q = 0$ below for simplicity), $\Omega_M = \sqrt{4\pi n_0 \hbar \omega} \frac{\tau_0 e a_0}{\hbar} \left\langle \frac{r}{a_0} \right\rangle$ – the the dimensionless value of the amplitude of the field oscillations that depends on mean value of the operator \hat{r} in the 2^3P state. Substituting the values of the corresponding fundamental constants into the last relation get $\Omega_M = 0.001132\sqrt{n_0}$, where, we recall, n_0 is the particle density expressed in inverse centimeters.

In the conclusion of this section, we note that in order to realize the process of coherent excitation in the V -type scheme, dipole moments must be first induced in the system. This can be done by a short seed pulse, which precedes the moment of the onset of excitation.

3. The variation of the phase velocity of a light wave during coherent excitation

In this section, we will consider the problem of approximate solution of system (4) under the assumption that $\Omega_{bc} \gg \Omega_{ba}$ (later we shall omit second indexes at these values), a relatively slow change in the envelopes of field strengths and correlation density matrices, and also for time intervals not spaced very far from the origin of coordinates. We will proceed from the sixth equation of system (4). If we assume that the envelope of the correlation matrix $\rho_{ab}(\tau, \kappa)$ varies rather slowly, i. e. its derivative is zero, and the population of level a is so small that it can be neglected, then it is possible to obtain a relation associating the population of level b with the matrix that distributes the coherence between levels a and c :

$$\rho_{ac}(\tau, \kappa) = \frac{e^{-i\tau(\delta_a - \delta_c)} \Omega_a(\tau, \kappa)}{\Omega_c(\tau, \kappa)} \left(\frac{r}{a_0} \right)_{ab} \rho_{bb}(\tau, \kappa) \Omega_a(\tau, \kappa) \left(\frac{r}{a_0} \right)_{cb}^{-1}. \quad (5)$$

Hence, under the assumption that the Rabi frequency Ω_a is small in comparison with Ω_c , we can obtain:

$$\rho_{ab}(\tau, \kappa) = \left(-\frac{2ie^{-i\delta_c\tau}}{\Omega_c(\tau, \kappa)} \right) \frac{\partial}{\partial\tau} \rho_{ac}(\tau, \kappa) \left(\frac{r}{a_0} \right)_{bc}^{-1}. \quad (6)$$

From the last two relations it follows that:

$$\rho_{ab}(\tau, \kappa) = \left(-\frac{2ie^{-i\tau\delta_c}}{\Omega_c(\tau, \kappa)} \right) \frac{\partial}{\partial t} \left(\frac{e^{i\tau(\delta_a - \delta_c)} \Omega_a(\tau, \kappa)}{\Omega_c(\tau, \kappa)} \left(\frac{r}{a_0} \right)_{ab} \rho_{bb}(\tau, \kappa) \left(\frac{r}{a_0} \right)_{cb}^{-1} \right) \left(\frac{r}{a_0} \right)_{bc}^{-1}. \quad (7)$$

Then, assuming $\delta_a = \delta_c$ after rather cumbersome, collations that we perform with program "Mathematica", one has the relation:

$$-i\Omega_M^2 \text{Sp} \left\{ \left[\left(-\frac{2ie^{-i\tau\delta_c}}{\Omega_c(\tau, \kappa)} \right) \frac{\partial}{\partial\tau} \left(\frac{\Omega_a(\tau, \kappa)}{\Omega_c(\tau, \kappa)} \left(\frac{r}{a_0} \right)_{ab} \rho_{bb}(\tau, \kappa) \left(\frac{r}{a_0} \right)_{cb}^{-1} \right) \left(\frac{r}{a_0} \right)_{bc}^{-1} \right] \left(\frac{r}{a_0} \right)_{ba} \right\}. \quad (8)$$

If the Rabi frequency in the arm bc is large and slowly varying, the last relation can be transformed to the form:

$$\frac{1}{v} \frac{\partial}{\partial t} \Omega_a(\kappa, \tau) + \frac{\partial}{\partial x} \Omega_a(\kappa, \tau) = 0. \quad (9)$$

Where, for the inverse phase velocity, one can write:

$$\frac{1}{v} = \frac{1}{c} \left[1 + 2\Omega_M^2 \frac{\Omega_a(\tau, \kappa)}{\Omega_c^2(\tau, \kappa)} \text{Sp} \left[\left(\frac{r}{a_0} \right)_{ab} \rho_{bb}(\tau, \kappa) \left(\frac{r}{a_0} \right)_{cb}^{-1} \left(\frac{r}{a_0} \right)_{bc}^{-1} \left(\frac{r}{a_0} \right)_{ba} \right] \right]. \quad (10)$$

According to the properties of the matrix trace, from the last relation, one can obtain the expression equitable at the first order over the ratio $\Omega_a/(\Omega_c)^2$:

$$\frac{c}{v} - 1 = 2\Omega_M^2 \frac{\Omega_a}{\Omega_c^2} \text{Sp} \left(\left\langle \left(\frac{r}{a_0} \right)_a^2 \right\rangle \rho_{bb}(\tau, \kappa) \left\langle \left(\frac{r}{a_0} \right)_c^2 \right\rangle \right), \quad (11)$$

where $\left\langle \left(\frac{r}{a_0} \right)_i^2 \right\rangle$ ($i = a, c$) denotes the mean value of square of r/a_0 value, calculated over the wave functions of states a and c . According to the fact that all values except Ω_a that are contained under the trace symbol are not negative, one can affirm that the relation between c and v depends on the sign of Ω_a : if $\Omega_a > 0$ then $c > v$ and vice versa if $\Omega_a < 0$.

On the Fig. 1 (curve 1) where for the ensemble of the helium atoms in 2^3P_j , $j = 1, 2$ state the dependence of the value $1 - v(t)/c$ on the time is represented one can see that the cure monotonically decreases over time.

In conclusion of this section, we wish to point out two things: firstly, the change in the velocity of a light wave due to the polarization of the medium during coherent excitation in the framework of the perturbation theory methods has been extensively studied and described in a large number of works (see, for example, [5]). The present study differs only in that it has been performed in a matrix form, which allows us to apply the formulas obtained herein to fine and hyperfine multiplets. Secondly, we obtained formula (11) by making rather serious assumptions, the main one of which, it seems to us, is the independence of the Rabi frequencies from time.

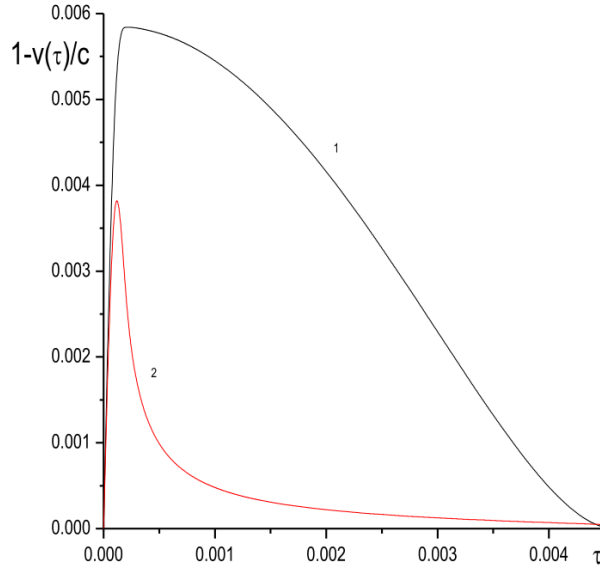


FIG. 1. Curves 1 and 2 illustrates the dependance of ratio v/c obtained with perturbation theory and numerical solution of the Liouville–Maxwell equation

4. Results of numerical calculations

Before presenting the results of numerical calculations, we recall that each of the electric fields acting in the arms ab and cb is made up of two fields – the excitation field and the polarization field that is created in the process of excitation. Below we will assume that the excitation field acting in the arm cb (“coupling field”) is strong, whereas the “probe field” acting in the arm ab is weak (one field which we examined was 100 times stronger than the other). When performing numerical calculations, we chose the values of relaxation constants according to [9].

Let us turn now to the last equation of system (4) describing the transition ba . It is known from the theory of differential equations [11] that such partial differential equation is equivalent to a system of ordinary differential equations of the type

$$\frac{dx}{c\tau_0} = \frac{d\Omega}{-i\Omega_M^2 \text{Sp} \left(\rho_{ab} \frac{r_{ab}}{a_0} \right)} = d\tau. \tag{12}$$

If we choose the dimensionless time τ as an independent variable, a general solution of last equation, can be written in the form:

$$x = (c\tau_0)\tau + C_1, \\ \Omega_a = -i\Omega_M^2 \int \text{Sp} \left(\rho_{ab} \frac{r_{ab}}{a_0} \right) d\tau + C_2. \tag{13}$$

In order to find the magnitude of Ω_a - the polarization frequency in the arm ab , we need to solve system (4), calculate the value of the correlation density matrix $\rho_{ab}(\tau)$ for each value of τ and, in parallel, use Simpsons formula to calculate the integral (13). The results of the calculations are presented in the 3D-figure (Fig. 2). From this plot one can see that the Rabi polarization frequency has the form of a rather short pulse. Similar results were obtained earlier in [3,4].

Note that when plotting Fig. 2, we assumed that spatial coordinates are linearly time-dependent, which, generally speaking, is not true even in the case under consideration, when system (4) is clearly independent of spatial coordinates. Nonlinear time dependence of spatial coordinates is explained by the fact that time dependence of these quantities is due to the correlation matrix ρ_{ab} , which is one of the solutions of system (4). In order to illustrate the effect of polarization of the medium on spatial coordinates, we numerically solved system (4), as a result of which the first two partial time derivatives of the Rabi frequency were determined. Further, if we write down formula (12) as:

$$\frac{v(\tau)}{c} = \frac{\frac{d\Omega(\tau)}{d\tau}}{-i\Omega_M^2 \text{Sp} \left(\rho_{ab} \frac{r_{ba}}{a_0} \right)}, \tag{14}$$

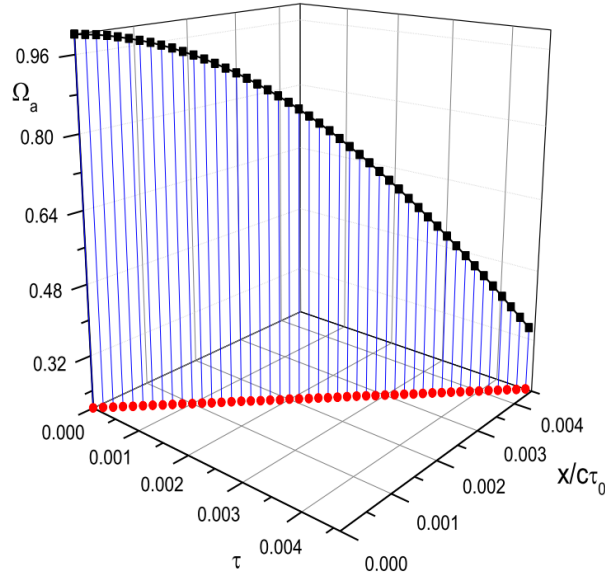


FIG. 2. Rabi frequency, in the arm tab , as a function of spatial coordinates and time

and replace the total derivative in the numerator of the last expression with its truncated Taylor series, we obtain the expression:

$$1 - \frac{v}{c} = 1 - \frac{\frac{\partial \Omega_a}{\partial \tau} + \frac{1}{2} \frac{\partial^2 \Omega_a}{\partial \tau^2} d\tau}{-i\Omega_M^2 \text{Sp}(\rho_{abd})} = \frac{\frac{1}{2} \frac{\partial^2 \Omega_a}{\partial \tau^2} d\tau}{i\Omega_M^2 \text{Sp}(\rho_{ba}d_{ab})} = -\frac{\text{Sp} \left(\frac{d}{dt} \rho_{ab} d_{ba} \right) d\tau}{2 \text{Sp}(\rho_{ba}d_{ab})}. \quad (15)$$

By using the numerical integration of the system, we calculated the right-hand side of expression (15) as a function of time. In the process, it turned out that function $1 - v(\tau)/c$ has a sharp maximum near the origin of coordinates and then decreases rapidly. The situation described is illustrated in Fig. 1 (curve 2), where, we recall, the first curve corresponds to the dependence of the relation under consideration determined by the approximate formula (11).

One of the most exciting challenges associated with the problem under consideration is the possibility of controlling the process of changing the magnitude of the group velocity of light. This problem in the framework of the approximate solution of the Liouville–Maxwell equation in theory is considered in detail in [4]. Below, we investigate this question in the framework of the approximations used in this paper.

We recall that, as noted earlier, that the sign of Ω_a determines the ratio of the group velocity to the speed of light in vacuum. From general considerations, it is clear that the possibility of manipulating the magnitude of the speed of light should depend on individual properties of emitting particles. In the present paper, the individual properties of emitting particles included both in the parameters of the energy distribution of levels, and in the magnitudes of the dipole momenta, which, in turn, determine the Rabi frequency. The elements of the dipole moment matrix depend both on the polarization direction of the exciting radiation and on the wave functions of the initial and final states. We accurately calculated the angular parts of the matrix elements of the dipole moment matrix in both arms of the V -type scheme, after which, in view of the fact that radial wave functions are not generally known, each element of the dipole moment matrix in the arm ab increased by ($\lambda = 1, 1.5, 2$) times.

We can see from Fig. 3, which presents the time dependence of the Rabi frequency generated in the arm ab for different values of λ , that this magnitude depends quite heavily on the magnitude of the dipole moment. We further note that manipulating the velocity magnitude by changing the direction of the dipole moment induced in the arms of the V -type scheme is unlikely to give the expected effect. Such a change is expressed by similarity transformation and, as follows from formula (11), owing to the invariance of the matrix trace with respect to such transformation, the ratio of the phase velocity of light to the similar magnitude in vacuum will not change.

In order to manipulate the ratio v/c , from our point of view, it is convenient to use a weak magnetic field whose direction does not coincide with the direction of polarization of the radiation acting in the arms of the V -type scheme. (It will be recalled that the excitation direction fixes the axis OZ of the laboratory coordinate system). Let us associate the axis OX of this system with the direction of the weak magnetic field. Then the

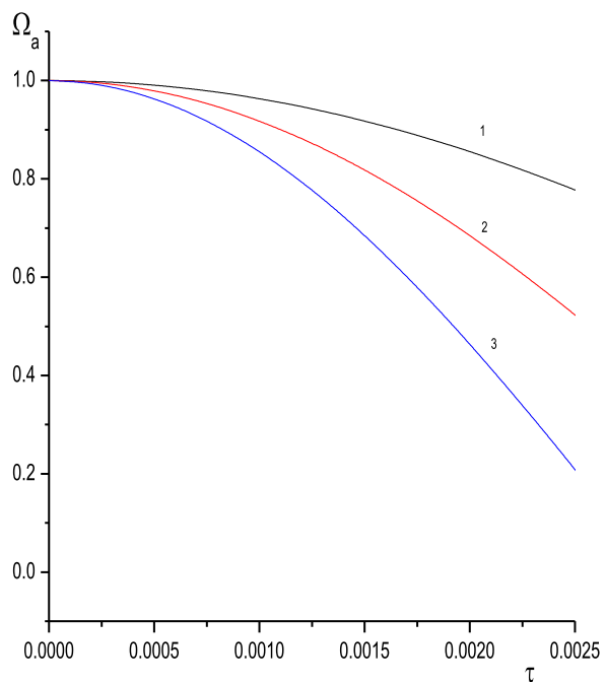


FIG. 3. Time dependence of the Rabi frequency generated in the arm ab on the values of the dipole moment. Curves 1–3 correspond to the values of $\lambda = 1, 1.5, 2$

precession of the angular momentum with respect to this direction will lead to a redistribution of the population of levels within each multiplet.

For mathematical description of the influence of a weak magnetic field along the OX axis of the laboratory frame of reference on the population of fine sublevels of the V -type scheme under consideration, a commutator $\Omega_L [\rho, j_x]_{i,j}$ should be introduced into each line of the system of the Liouville–Maxwell differential equations (4) describing a change to the density matrix $\rho(i, j)$, ($i, j = a, b, c$), where $\Omega_L = \mu_0 \mathcal{H} \tau_0 / \hbar$ is the dimensionless Larmor frequency and then, by solving the aforementioned system, we can use formula (13) to determine the values of the correlation density matrices $\rho_{ab}(\tau)$ and $\rho_{cb}(\tau)$. Knowing the time dependence of these matrices, we can use formula (13) to determine the similar dependence for the polarization frequency. The above is illustrated in Fig. 4 that shows the dependence of this polarization frequency generated in the arm cb . It can be seen from the figure that as the magnitude of the magnetic field increases, the frequency of the generated polarization field increases, whereas the magnitude of this field decreases, which agrees with the model of the angular momentum precessing in the magnetic field.

5. Conclusion

In this paper, we have considered the process of light propagation in a dispersive medium. In addition to the perturbation theory method, which was widely used earlier, in this work we performed numerical integration of the Liouville–Maxwell equations. All calculations, including analytical estimates, were performed in a matrix form, which allows for the application of the results of this paper to various fine and hyperfine multiplets.

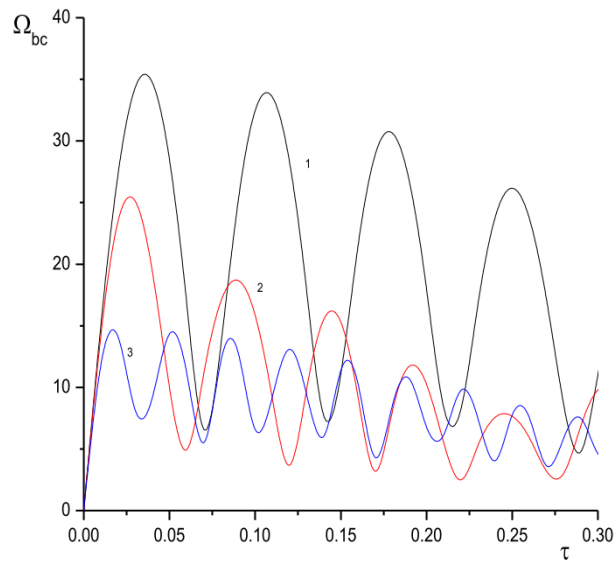


FIG. 4. Time dependence of the polarization frequency generated in the arm cb for the values of the external magnetic field $\mathcal{H} = 0, 50, 100 \text{ Gs}$

References

- [1] Harris S.E., Field J.E., Kasapi A. Disperse properties of electromagnetically induced transparency. *Phys. Rev. A*, 1992, **46** (1), P. 29–32.
- [2] Imamoglu A., Schmidt H., Woods G. Deutsch M. Strongly interacting photons in a nonlinear cavity. *Phys. Rev. Lett.*, 1997, **79**, P. 1467–1469.
- [3] Alexandrov E.B., Zapassky V.S. In the “chase” of the slow light. *Phys. Usp.*, 2006, **176** (10), P. 1093–1102.
- [4] Zelinsky I.V., Mironov V.A. The electromagnetically induced transparency. *JEPT*, 2002, **121** (5), P. 1068–1079.
- [5] Fleischhuer M., Lukin M.D. Dark-stated polarization in electromagnetically induced transparency. *Phys. Rev. Lett.*, 2000, **84** (22), P. 5094–5097.
- [6] Lukin M.D. Trapping and manipulating photon states in atomic ensembles. *Rev. Mod. Phys.*, 2003, **75**, P. 457–472.
- [7] Petrashen A.G., Sytenko N.V. Polarization characteristics of radiation of atomic ensemble under coherent excitation in the presence of the strong magnetic field. *Nanosystems: Physics, Chemistry, Mathematics*, 2015, **6** (1), P. 122–132.
- [8] Petrashen A.G., Sytenko N.V. Laser generation without inversion on the levels of the Helium atoms. *Nanosystems: Physics, Chemistry, Mathematics*, 2017, **7** (2), P. 384–393.
- [9] Frish S.E. *Optical spectra of atoms*. Moscow, 1963.
- [10] NIST Atomic Spectra Database. URL: <https://www.nist.gov/pml/atomic-spectra-database>.
- [11] Jackson J.D. *Classical electrodynamics*. Mir, Moscow, 1965, 702 p.
- [12] Stepanov V.V. *Course of differential equations*. FIZMATLIT, Moscow, 1950.

Molecular dynamics simulation of fluid viscosity in nanochannels

V. Rudyak, A. Belkin

Novosibirsk State University of Architecture and Civil Engineering,
Leningradskaya 113, Novosibirsk, 630008, Russia

valery.rudyak@mail.ru, a_belkin@ngs.ru

PACS 47.61.-k, 47.10.-g

DOI 10.17586/2220-8054-2018-9-3-349-355

The viscosity of fluids in a plane nanochannel has been studied by molecular dynamics method. The effective viscosity coefficient was determined using the fluctuation-dissipation theorem derived previously by the authors from the nonequilibrium statistical theory of fluid transport in confined conditions. It has been found that the fluid viscosity in a nanochannel is strongly dependent on the interaction potential between the fluid and channel wall molecules. In particular, increasing the depth of the potential well of this interaction leads to an increase in the viscosity. At the same time, if the depth of the potential well is small, the fluid viscosity in a nanochannel may be even lower than its viscosity in an unconfined (bulk) system. Thus, the fluid viscosity in a nanochannel and hence the channel flow resistance can be varied by changing the material of the nanochannel walls.

Keywords: nanochannel, confined system, viscosity, molecular dynamics, correlation functions, nonequilibrium statistical mechanics.

Received: 11 April 2018

1. Introduction

Interest in fluid-based transport processes (i.e. liquids and gases) in nanochannels is due to the rapid development of nanotechnologies related to power systems, medicine, the development of advanced filter elements, etc. At present, it is obvious that the properties of fluids in nanochannels and nanometer-sized pores differ fundamentally from their bulk properties. In these channels, the fluid density becomes nonuniform [1], the molecular diffusion is anisotropic [2], and other transport properties should also change. However, so far, there is no consensus about what relations should be used to describe the fluid transport coefficients, in particular viscosity, under confined conditions.

Simple models have been developed [3, 4] which consider a fluid layer with altered properties, in particular viscosity, near the channel walls. However, these models do not provide an answer to the question of how to determine the size of this layer and how the viscosity in it changes. The need to use constants that cannot be determined within the proposed theoretical model is a serious problem (see, e.g., [5, 6]). Of course, the unknown constants can be determined using experimental data; however, the available data for nanochannels are contradictory [7, 8]. Moreover, these experimental data are often unreliable as there are no direct methods for measuring physical characteristics in nanochannels and they have to be extracted from certain measured integral characteristics and interpreted using conventional macroscopic theories.

A statistical theory of transport processes under confined conditions was developed in [9, 10]. It has been established that the transport properties of fluids in nanochannels and nanopores are determined not only by the characteristics of the fluid, but also by the properties of the entire fluid – channel (pore) wall system. These transport properties are described by effective transport coefficients, which in [9, 10] are determined using fluctuation-dissipation relations between the transport coefficients and correlation functions of the corresponding microscopic fluxes. These relations extend the well-known Green-Kubo formula for fluids in bulk.

Analytically, the correlation functions can be calculated only in the simplest case of a rarefied gas (see [11–13]). In all other cases, it is necessary to use methods of molecular modeling. The purpose of the present study was to perform a molecular dynamics (MD) method to calculate the viscosity of fluids in a plane nanochannel (nanoslit) and study the factors that determine the fluid viscosity. We modeled the viscosity of argon and benzene in channels of different heights and simultaneously studied the fluid structure in these channels.

2. Method for determining the effective viscosity coefficient

In [9, 10], explicit expressions for the effective viscosity coefficient η of fluids in confined conditions were constructed using methods of nonequilibrium statistical mechanics. This coefficient is expressed in terms of time correlation functions of microscopic stress tensors. Along with the contribution from the stress tensor of the fluid,

it includes cross correlations characteristic of the fluid–wall surface system and due to the interaction between the fluid molecules and the molecules of the channel walls. The viscosity is given by the relation:

$$\eta = \eta_{ff} + \eta_{fb}, \quad (1)$$

$$\eta_{ff} = \frac{1}{5kT_f} \int_0^\tau \langle \hat{\mathbf{J}}_f(0) : \hat{\mathbf{J}}_f(t) \rangle dt,$$

$$\eta_{fb} = \frac{1}{5kT_f} \int_0^\tau \langle \hat{\mathbf{J}}_b(0) : (\hat{\mathbf{J}}_f(t) + \hat{\mathbf{J}}_{fb}(t)) + \hat{\mathbf{J}}_f(0) : \hat{\mathbf{J}}_{fb}(t) \rangle dt + \frac{1}{5kT_b} \int_0^\tau \langle \hat{\mathbf{J}}_b(0) : \hat{\mathbf{J}}_{fb}(t) \rangle dt, \quad (2)$$

where the integrands in formulas (2) are classical correlation functions [13, 14], the angular brackets denote averaging over the equilibrium distribution function, T is the temperature, k is the Boltzmann constant, and τ is the time when the viscosity reaches the so-called plateau value [15] that corresponds to the time of decay of the correlation functions. Here and below, the subscript f corresponds to the fluid molecules, and b to the molecules of the channel walls.

The time correlation functions in formulas (2) are determined by the corresponding microscopic fluxes:

$$\hat{\mathbf{J}}_\alpha = \sum_{i=1}^{N_\alpha} \frac{\mathbf{p}_i \mathbf{p}_i}{m_\alpha} + \frac{1}{2} \sum_{i=1}^{N_\alpha} \sum_{\varphi} \sum_{j=1}^{N_\varphi} (\mathbf{r}_i - \mathbf{r}_j) \mathbf{F}_{ij}, \quad \hat{\mathbf{J}}_{fb} = -\frac{1}{4} \sum_{i=1}^{N_f} \sum_{j=1}^{N_b} (\mathbf{r}_i \mathbf{r}_j) \mathbf{F}_{ij}.$$

Here \mathbf{r}_i and \mathbf{p}_i are the radius vector of the center of mass and momentum of the i -th molecule of phase α and \mathbf{F}_{ij} is the intermolecular interaction force.

In this paper, we present an investigation of fluid viscosity in a plane channel. The channel walls were modeled by two square plates, each consisting of two rows of molecules. The size of the plates was chosen so that the results remained unchanged as it increased. The molecules were located at the sites of a face-centered cubic lattice. On the channel boundaries along the walls, periodic boundary conditions were used.

The viscosity coefficient (1), (2) was calculated by the standard molecular dynamics method (see e.g., [16]). This was performed with the original SibMD software package which has previously been used to solve various nanofluid transport problems [1, 15, 17, 18]. The Newton equations were integrated by the Schofield scheme [19]. The integration step is equal to 1.09 fs. Due to the local instability and mixing of phase trajectories of the system in the molecular dynamics calculation [1, 3, 20, 21], the results should be averaged over an ensemble of independently obtained phase trajectories. In the calculations presented in this paper, averaging was carried out over five thousand independent phase trajectories.

All intermolecular interactions were described by the cutoff Lennard-Jones potential:

$$\Phi(r) = \begin{cases} 4\varepsilon_{\alpha\beta} \left(\left(\frac{\sigma_{\alpha\beta}}{r} \right)^{12} - \left(\frac{\sigma_{\alpha\beta}}{r} \right)^6 \right) - \Phi_0, & r \leq R_C; \\ 0, & r > R_C, \end{cases} \quad (3)$$

where σ is the effective diameter, ε is the depth of the potential well, R_C is the cutoff radius of the potential, and $r = |\mathbf{r}_i - \mathbf{r}_j|$ is the distance between the centers of molecules, $\alpha, \beta = f, b$. The cutoff radius of the potential was set equal to $R_C = 2.5\sigma_{ff}$, the potential shift Φ_0 was determined from the condition $\Phi(R_C) = 0$. Interaction parameters between the fluid molecules and the walls were calculated from the interaction constants of individual substances using the following combination relations $\sigma_{fb} = \sqrt{\sigma_{ff}\sigma_{bb}}$ and $\varepsilon_{fb} = \sqrt{\varepsilon_{ff}\varepsilon_{bb}}$.

The effective viscosity coefficient of a fluid in the nanochannel was compared with the viscosity coefficient of the same fluid in a bulk system, which was also simulated by the molecular dynamics method. In this case, for the simulated cubic cell filled with molecules, we used periodic boundary conditions in all directions. The comparison was carried out at the same pressure and fluid temperature. The pressure in the channel was determined from the force per unit area of the walls, and the pressure in bulk was determined by the virial theorem [14].

3. Simulation results

In formulas (2), we can distinguish three types of correlation functions ϕ which define the effective viscosity coefficient: the kinetic correlation functions, $\phi_k \sim \langle p_{ix} p_{iy}(0) \cdot p_{ix} p_{iy}(t) \rangle$, the potential correlation functions, $\phi_p \sim \langle (x_i - x_j) F_{ijy}(0) \cdot (x_i - x_j) F_{ijy}(t) \rangle$, and the cross-correlation functions, $\phi_c \sim \langle (x_i - x_j) F_{ijy}(0) \cdot p_{ix} p_{iy}(t) \rangle$. The corresponding contributions also appear when calculating the viscosity coefficient (1). The kinetic contributions are due to momentum transfer during molecular motion. It is these contributions that determine the momentum

transfer in a rarefied gas and the viscosity of the gas. The above-mentioned potential contributions are due to momentum transfer in the interaction of molecules.

Figure 1 shows the time dependences of these three components and the total correlation function for the viscosity of argon in the nanochannel considering both fluid – fluid and fluid – wall interactions. The spherically symmetric potential (3) adequately describes inert argon molecules ($\sigma_{ff} = 3.405 \text{ \AA}$, $\varepsilon_{ff}/k = 119.8 \text{ K}$). In an unconfined system, viscosity can be determined with good accuracy by the MD method, at least up to the saturation line [22]. The temperature in our MD simulation was 160 K, and the reduced concentration of molecules $n\sigma^3 = 0.4$ (here and below, $\sigma = \sigma_{ff}$). All the correlation functions are normalized to $\langle p_x^2 p_y^2 \rangle$, so that the initial value of the kinetic component is unity. The density of the system is high enough, and the potential contribution is the major one.

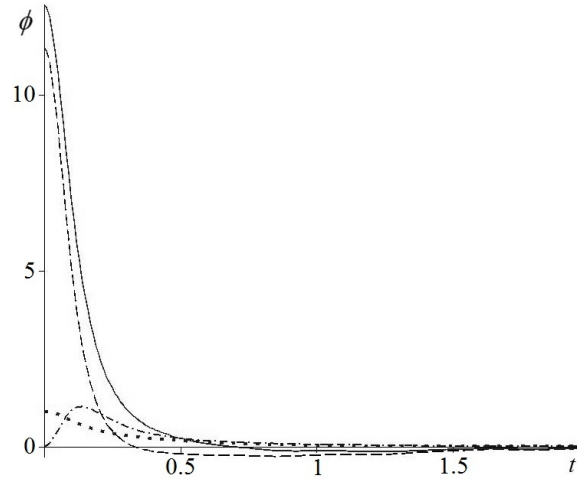


FIG. 1. Viscosity correlation function and its components versus time (in picoseconds) for argon in a nanochannel of height $h = 27.2 \text{ \AA}$ (solid line). The dashed line corresponds to the potential component, the dotted line to the kinetic component, and the dash-dotted line to the cross-correlation. The parameters of the potential of the wall molecules correspond to argon

Let us consider in more detail the relaxation of the components of the correlation functions in bulk and in the nanochannel. A comparison of the two cases is shown in Fig. 2 (the data in the figure are given on a logarithmic scale).

Two important points should be noted. First, the values of the potential component in the nanochannel far exceed those in bulk throughout its time evolution. Second, there is anisotropy in momentum transfer during collisions in the nanochannel (see curves 4 and 5 in Fig. 2). The correlation function increases more strongly in the plane perpendicular to the walls of the channel.

In contrast, the kinetic component in the nanochannel is practically isotropic and decays faster than in bulk (see curves 1 and 2 in Fig. 2), which is due, in particular, to the faster velocity relaxation of the molecules in collisions with the channel walls.

The viscosity coefficient (1), (2) is a function of the time. Its evolution for the system described above (Figs. 1 and 2) is shown in Fig. 3. The value of the viscosity coefficient is obtained only when this function reaches a plateau value in about 3 psec. The main contribution to the viscosity coefficient comes from the potential component. The viscosity coefficient in nanochannels is approximately 40 % higher than that in bulk.

To answer the question of how and which properties of the channel walls affect the viscosity, we performed a systematic simulation of fluid viscosity in channels where the interaction parameters σ_{bb} and ε_{bb} of the wall molecules (3) were varied.

It was found that the variation in the effective size of the wall molecules σ_{bb} had little effect on the effective viscosity in the channel. At the same time, the viscosity changed greatly with a change in ε_{bb} . Fig. 4 shows the relative viscosity coefficient $\eta^* = \eta/\eta_0$ in a channel of height $h = 27.2 \text{ \AA}$ normalized by the viscosity in bulk η_0 versus the parameter ε_{bb} . Increasing this parameter leads to a rapid increase in the effective viscosity coefficient.

On the logarithmic scale of Fig. 4, this increase is almost linear. For a copper wall ($\varepsilon_{ff}/k = 1247 \text{ K}$), and for a zinc wall ($\varepsilon_{ff}/k = 1040 \text{ K}$), the viscosity coefficient of argon can be expected to increase by a factor of about four. In contrast, for small values of this parameter, $\varepsilon_{bb} < \varepsilon_{ff}$, the viscosity coefficient decreases and becomes even less than η_0 .

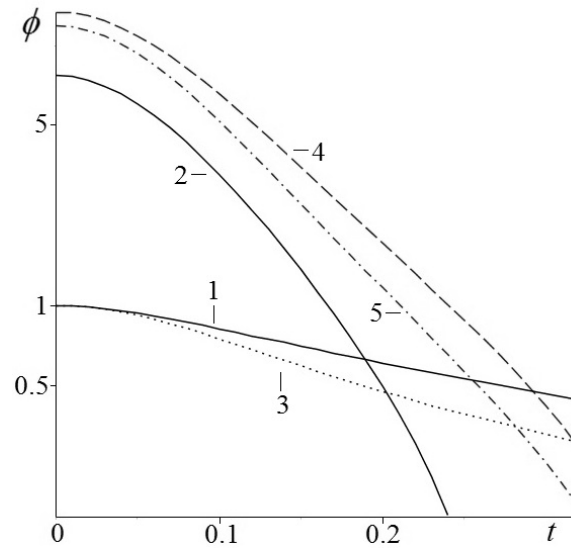


FIG. 2. Components of the correlation function of the argon viscosity coefficient versus time (in picoseconds) in bulk (the solid line 1 corresponds to the kinetic component, and the solid line 2 to the potential component) and in a nanochannel of height $h = 27.2 \text{ \AA}$ (the dotted line 3 corresponds to the kinetic component, the dashed line 4 to the potential component in the plane perpendicular to the channel walls, and the dash-dotted line 5 to the potential component in the plane of the walls)

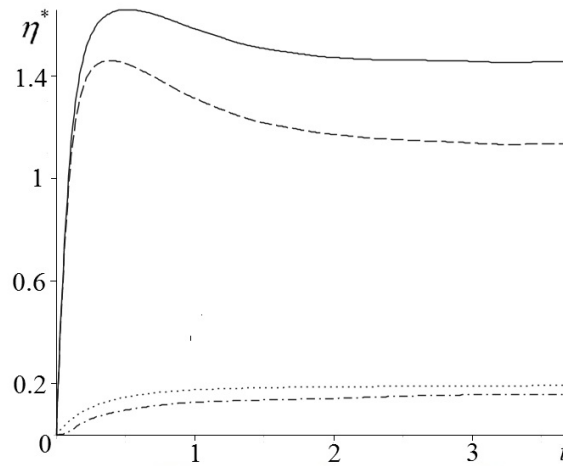


FIG. 3. Viscosity coefficient (solid line) and its components versus integration time (in picoseconds) for argon in a nanochannel of height $h = 27.2 \text{ \AA}$ (the dotted line corresponds to the kinetic component, the dashed line to the potential component, and the dot-dashed line to the cross-correlation component)

This conclusion is supported by the data in Fig. 5, which shows curves of the normalized viscosity coefficient of benzene ($\sigma_{bb} = 5.27 \text{ \AA}$, $\varepsilon_{bb}/k = 440 \text{ K}$) at room temperature versus height of channels with different wall materials. The lines in the figure correspond to the approximations of the results by the function $\eta^* = 1 \pm B/h$ (plus for higher line and minus for lower line) in which the constant B depends on the properties of the fluid and the walls. In the nanochannel with walls of carbon, whose molecules have a small value of ε ($\sigma_{bb} = 3.4 \text{ \AA}$, $\varepsilon_{bb}/k = 28 \text{ K}$), the viscosity of argon indeed decreases.

On the other hand, in the channel with aluminum walls ($\sigma_{bb} = 2.56 \text{ \AA}$, $\varepsilon_{bb}/k = 857.6 \text{ K}$), there is an increase in viscosity. It can be argued that it is the great depth of the potential well of aluminum molecules that leads to an appreciable increase in viscosity. In all cases, the differences between the viscosity coefficient in the nanochannel and the η_0 value increase monotonically with decreasing channel height.

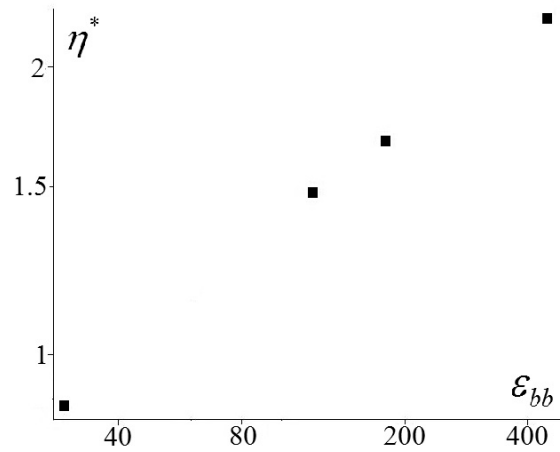


FIG. 4. Normalized viscosity coefficient of argon in a nanochannel versus potential well depth ϵ_{bb} (K), $h = 27.2 \text{ \AA}$

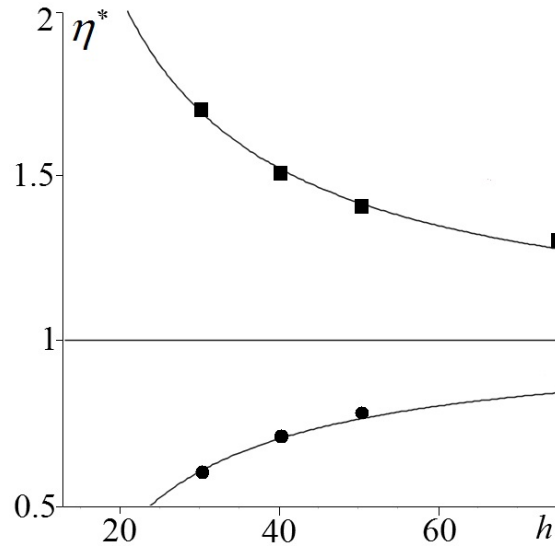


FIG. 5. Viscosity coefficient versus channel height (in angstrom units) for the following types of fluid and channel walls: C₆H₆-C (●) and C₆H₆-Al (■)

4. Conclusions

Strictly speaking, the only consistent method for nanochannel flow simulation is the molecular dynamics method [23]. However, experience has shown that conventional hydrodynamic approach is usually applicable well beyond its range of validity. Therefore, it is possible to attempt to model flows in nanochannels and small microchannels using conventional hydrodynamic methods (see, e.g., [24–26] and the reference therein). For this, however, it is necessary to have adequate data on fluid viscosity in such channels. The present study has shown that this viscosity is largely determined by the walls of the channel. This is due to the fact that the momentum redistribution process in the system depends significantly on the interaction between the fluid molecules and the channel walls, and it is this process that determines the viscosity.

The active interaction of fluid molecules with the channel walls leads to a significant change in the fluid structure near the wall. Fig. 6 shows the MD simulation data for the radial distribution function g_2 of benzene near the wall of a channel with carbon walls. Its comparison with the radial distribution function of benzene in bulk shows not only a several-fold increase in the maximum values of the radial function, but also the occurrence of a quasi-long-range order. This increase in the order of the fluid near the surface will lead to an increase in viscosity compared to its value in bulk.

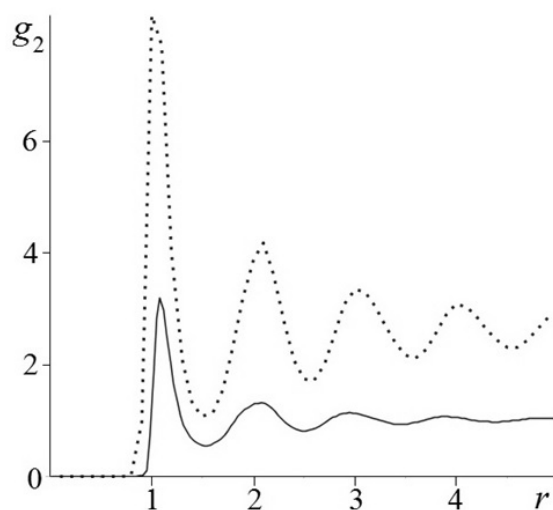


FIG. 6. Radial distribution function of benzene molecules in bulk (solid line) and in a channel with $h = 40 \text{ \AA}$ (dotted line). Intermolecular distances are in the units of σ for benzene (5.27 \AA). Values are normalized by the average concentration of the molecules

However, the contribution to the viscosity coefficient due to the interactions between the fluid molecules and the walls also plays a key role. This should be taken into account, and it should be realized that the fluid viscosity in nanochannels is not only determined by the fluid properties. In this case, it is necessary to introduce the effective viscosity (and thermal conductivity) of the entire fluid–wall system. This system is a special two-phase medium in which transport processes are in a sense similar to those in two-phase suspensions, where it is also necessary to introduce effective transport coefficients (as in the well-known Einstein’s and Maxwell’s formulas) which are determined by the interaction between base fluid molecules and nanoparticles [18].

Many experiments have demonstrated a significant reduction in flow resistance in microchannels [26,27]. This is usually associated with the slip effect in such channels [28–31]. However, as indicated above, such a reduction in flow resistance may also be due to a decrease in the effective viscosity of the fluid compared to its viscosity in bulk. In this connection, it should be noted that in this paper, we considered flow in a plane channel, in fact, in a nanoslit. However, in closed nanochannels with a circular or square cross-section, these effects will be more pronounced.

Finally, another important point should be noted. The MD simulation results show that transport processes in nanochannels are inhomogeneous, so that, generally speaking, the fluid viscosity also turns out to be inhomogeneous. Therefore, a consistent approach to the study of nanofluids’ transport properties requires the use of generalized nonlocal transport equations and nonlocal transport constitutive relations. Such approaches are well known and have been successfully used [13, 14, 32–35].

Acknowledgements

This work was supported by the Russian Science Foundation (Grants # 17-01-00040, # 17-58-45023).

References

- [1] Rudyak V.Ya., Belkin A.A., Egorov V.V., Ivanov D.A. Modeling fluid flows in nanochannels by molecular dynamics method. *Nanosystems: Physics, Chemistry, Mathematics*, 2011, **2**(4), P. 100–112.
- [2] Andryushchenko V., Rudyak V. Self-diffusion coefficient of molecular fluid in porous media. *Defect and Diffusion Forum*, 2011, **312-315**, P. 417–422.
- [3] Blake T. Slip between a liquid and a solid: D.M. Tolstoi’s (1952) theory reconsidered. *Colloids and Surfaces*, 1990, **47**, P. 135–145.
- [4] Myers T. Why are slip lengths so large in carbon nanotubes? *Microfluidics and Nanofluidics*, 2010, **10**(5), P. 1141–1145.
- [5] Popov I.Yu. Statistical derivation of modified hydrodynamic equations for nanotube flows. *Phys. Scr.*, 2011, **83**, P. 045601.
- [6] Calabro F., Lee K.P., Mattia D. Modelling flow enhancement in nanochannels: Viscosity and slippage. *Applied Mathematics Letters*, 2013, **26**, P. 991–994.
- [7] Judy J., Maynes D., Webb B.W. Characterization of frictional pressure drop for liquid flows through microchannels. *Int. J. Heat Mass Transfer*, 2002, **45**, P. 3477–3489.
- [8] Pfähler J., Harley J., Bau H., Zemel J.N. Gas and liquid flow in small channels. *Micromech. Sensors, Actuators, Syst.*, 1991, **32**, P. 49–58.
- [9] Rudyak V.Ya., Belkin A.A. Fluid viscosity under confined conditions. *Doklady Physics*, 2014, **59**(12), P. 604–606.

- [10] Rudyak V.Ya., Belkin A.A. Statistical mechanics of transport processes of fluids under confined conditions. *Nanosystems: Physics, Chemistry, Mathematics*, 2015, **6**(3), P. 366–377.
- [11] Khonkin A.D. Equations for spatial-temporal and temporal correlation functions and proof of the equivalence of the results of the Chapman-Enskog method and temporal correlation functions method. *Theoretical and Mathematical Physics*, 1970, **5**(1), P. 125–135 (in Russian).
- [12] Ernst M.H. Formal theory of transport coefficients to general order in the density. *Physica*, 1966, **32**(2), P. 209–243.
- [13] Rudyak V.Ya. *Statistical aerohydrodynamics of homogeneous and heterogeneous media*. Vol. 2. Hydromechanics. NSUACE, Novosibirsk, 2005, 468 p. (In Russian).
- [14] Zubarev D.N. *Nonequilibrium statistical thermodynamics*. Consultants Bureau, New York, 1974, 489 p.
- [15] Rudyak V.Ya., Belkin A.A., Ivanov D.A., Egorov V.V. The simulation of transport processes using the method of molecular dynamics. Self-diffusion coefficient. *High Temperature*, 2008, **46**(1), P. 30–39.
- [16] Rapaport D.C. *The Art of Molecular Dynamics Simulation*. Cambridge University Press, 1995, 549 p.
- [17] Rudyak V.Ya., Krasnolutski S.L., Ivanov D.A. Molecular dynamics simulation of nanoparticle diffusion in dense fluids. *Microfluidics and Nanofluidics*, 2011, **11**(4), P. 501–506.
- [18] Rudyak V.Ya., Krasnolutski S.L. Dependence of the viscosity of nanofluids on nanoparticle size and material. *Physics Letters A*, 2014, **378**, P. 1845–1849.
- [19] Schofield P. Computer simulation studies of the liquid state. *Comput. Phys. Comm.*, 1973, **5**(1), P. 17–23.
- [20] Norman G.E., Stegailov V.V. The classical molecular dynamics method: purpose and reality. *Nanostructures. Mathematical physics and simulation*, 2011, **4**(1), P. 31–59 (in Russian).
- [21] Norman G.E., Stegailov V.V. Stochastic Theory of the Classical Molecular Dynamics Method. *Mathematical Models and Computer Simulations*, 2013, **5**(4), P. 305–333.
- [22] Ashurst W.T., Hoover W.G. Argon shear viscosity via a Lennard-Jones Potential with equilibrium and nonequilibrium molecular dynamics. *Phys. Rev. Lett.*, 1973, **31**, P. 206–208.
- [23] Rudyak V.Ya., Minakov A.V. *Modern problems of micro- and nanofluidics*. Nauka, Novosibirsk, 2016, 298 p. (in Russian).
- [24] Belonenko M.B., Chivilikhin S.A., Gusarov V.V., Popov I.Yu., Rodygina O.A. Soliton-induced flow in carbon nanotubes. *Europhysics Letters*, **101**(6), P. 66001.
- [25] Golovina D.S., Chivilikhin S.A. Reproduction of the evolution of the liquid front profile in inhomogeneous nanoporous media. *Nanosystems: Physics, Chemistry, Mathematics*, 2017, **8**(5), P. 567–571.
- [26] Liu C., Li Z. On the validity of the Navier-Stokes equations for nanoscale liquid flows: The role of channel size. *AIP Advances*, 2011, **1**, P. 032108.
- [27] Liakopoulos A., Sofos F., Karakasidis T.E. Friction factor in nanochannel flows. *Microfluidics and Nanofluidics*, 2016, **20**(1), P. 24.
- [28] Ou J., Perot B., Rothstein P. Laminar drag reduction in microchannels using ultrahydrophobic surfaces. *Phys. Fluids*, 2004, **16**, P. 4635–4643.
- [29] Lauga E., Brenner M.P., Stone H.A. *Microfluidics: the no-slip boundary condition*. Chapter 19 in: Handbook of Experimental Fluid Dynamics, C. Tropea, A. Yarin, J. F. Foss (Eds.), Springer, 2007.
- [30] Andrienko D., Dünweg B., Vinogradova O.I. Boundary Slip as a Result of a Prewetting Transition. *J. Chem. Phys.*, 2003, **119**, P. 13106–13112.
- [31] Laturkar S.V., Mahanwa P.A. Superhydrophobic coatings using nanomaterials for anti-froth applications (review). *Nanosystems: Physics, Chemistry, Mathematics*, 2016, **7**(4), P. 650–656.
- [32] Huang Z. Formulations of nonlocal continuum mechanics based on a new definition of stress tensor. *Acta Mechanica*, 2006, **187**, P. 1127.
- [33] Eringen A.C. Nonlocal continuum mechanics based on distributions. *International J. Engineering Sci.*, 2006, **44**, P. 141147.
- [34] Meshcheryakov Yu.I., Khantuleva T.A. Nonequilibrium processes in condensed media. Part 1. Experimental studies in light of nonlocal transport theory. *Physical Mesomechanics*, 2015, **18**(3), P. 228–243.
- [35] Khantuleva T.A., Shalymov D.S. Modelling nonequilibrium thermodynamic systems from the speed-gradient principle. *Phil. Trans. R. Soc. A*, 2017, **375**, P. 20160220.

Interplay between size and stability of magnetic skyrmions

A. S. Varentsova¹, M. N. Potkina^{2,3}, S. von Malottki⁴, S. Heinze⁴, P. F. Bessarab¹

¹ITMO University, 197101 St. Petersburg, Russia

²St. Petersburg State University, 198504 St. Petersburg, Russia

³Science Institute, University of Iceland, 107 Reykjavík, Iceland

⁴Institute of Theoretical Physics and Astrophysics, University of Kiel, 24098 Kiel, Germany
varentsova.a@mail.ru, bessarab@hi.is

PACS 75.70.Ak, 75.70.Kw

DOI 10.17586/2220-8054-2018-9-3-356-363

The relationship between the size and stability of isolated skyrmions in a magnetic monolayer is analyzed based on minimum energy path calculations and atomistic spin Hamiltonian. It is demonstrated that the energy barrier protecting the skyrmion from collapse to the ferromagnetic state is not uniquely defined by the skyrmion size, although these two properties as functions of relevant material parameters follow similar trends. Stability of nanoscale skyrmions can be enhanced by a concerted adjustment of material parameters. The proposed parameter transformation conserves the skyrmion size, but does not conserve the skyrmion shape which changes from an arrow-like pattern to a profile that resembles magnetic bubbles. This transformation of the skyrmion shape is accompanied by an increase in the collapse energy barrier and thus enhancement of skyrmion stability.

Keywords: magnetic skyrmion, thermal stability, energy barrier.

Received: 1 May 2018

Revised: 10 May 2018

1. Introduction

The field of localized, topological spin textures such as magnetic skyrmions [1–3] is currently receiving a lot of attention. The interest in skyrmions is motivated by their unique properties potentially making them perfect information carriers [4–7]. Sensitivity of these spin swirls to pulses of electric current [8–10] benefits the efficient control of information flows and facilitates qualitative decrease in power consumption of data processing devices. The small size of skyrmions could increase data storage density far beyond what state-of-the-art technology offers today. For nanoscale skyrmions, thermal stability becomes an issue as thermal fluctuations can spontaneously destroy skyrmion states and, therefore, corrupt the stored data. Available experimental data on magnetic skyrmions in various materials and material combinations demonstrates inverse relationship between the skyrmion size and skyrmion stability: small skyrmions tend to be less stable compared to large ones [8, 11–21]. For example, room-temperature skyrmions in a Pt/CoFeB/MgO heterostructure are roughly 100 nm in diameter [18], which is more than an order of magnitude larger than skyrmions observed in a Pd/Fe/Ir(111) system only at low temperatures by means of spin-polarized scanning tunneling microscopy [19, 20]. The question then arises as to how general this relation between skyrmion size and skyrmion stability is and whether it is possible to design an optimal medium where magnetic skyrmions are small enough while being sufficiently stable at ambient conditions.

Equilibrium properties of skyrmions such as size and shape have intensively been studied since the very discovery of magnetic skyrmions more than twenty years ago [2–4, 22–26], but quantitative characterization of skyrmion stability has started being addressed rather recently [27–38]. Thermal stability can be quantified by calculating skyrmion lifetime using harmonic transition state theory for spins [39]. The theory predicts an Arrhenius expression for the skyrmion lifetime τ as a function of temperature T ,

$$\tau = \tau_0 e^{\Delta E/k_B T}, \quad (1)$$

where the magnitude of both the energy barrier ΔE and the pre-exponential factor τ_0 depends on the mechanism of skyrmion annihilation [38]. Theoretical calculations applied to atomistic spin Hamiltonian have previously revealed two mechanisms of skyrmion decay into a polarized, ferromagnetic configuration: Radial collapse of a skyrmion [27, 31] and escape of the skyrmion through the system boundary [32–34]. Relative contributions of these mechanisms to the skyrmion stability have been studied as a function of relevant material parameters [32], applied magnetic field [35, 38] and presence of impurities [33, 36]. The effect of long-range, frustrated exchange interaction on skyrmion stability has also been addressed using the spin Hamiltonian parametrized from density functional theory calculations [37]. It has been shown that taking exchange beyond the nearest neighbors into

account results in significant enhancement of energy barriers for the skyrmion collapse compared to what effective, nearest-neighbor models predict [37]. Overall, significant amount of knowledge on skyrmion size and skyrmion stability has been accumulated. However, these two properties have so far never been directly linked. Careful analysis of the interplay between skyrmion size and stability is of critical importance for the use of skyrmions in future information technologies.

In this article, the relationship between the size and stability of an isolated Néel skyrmion is explored using minimum energy path calculations and a two-dimensional Heisenberg exchange model. By tracing contours of constant size and collapse energy barrier on a magnetic phase diagram, it is demonstrated that there is no one-to-one correspondence between the skyrmion size and skyrmion stability, although these two properties as functions of relevant material parameters follow similar trends. The energy barrier for the skyrmion collapse into the ferromagnetic background is not a unique function of the skyrmion size, which makes it possible to adjust stability of nanoscale skyrmions. In particular, it is shown using the constant pre-exponential factor approximation that the lifetime of fixed-size skyrmions can be enhanced by several orders of magnitude by concerted modification of Dzyaloshinskii–Moriya (DM) interaction and out-of-plane magnetocrystalline anisotropy.

This article is organized as follows. In Section 2, theoretical background and details of numerical simulations are described. In Section 3, parameter dependence of an isolated skyrmion size and stability is summarized, zero-temperature stability diagram equipped with contours of constant skyrmion diameter and collapse energy barrier is obtained, and stability variation of constant-size skyrmions is quantified. Summary and outlook are presented in Section 4.

2. Methods

A two-dimensional skyrmionic system is modeled as a single monolayer of classical spins on a hexagonal lattice. The Hamiltonian of the system includes Heisenberg exchange coupling, antisymmetric DM interaction, and out-of-plane anisotropy. The energy of the system is given by the following equation:

$$E = -\frac{J}{2} \sum_{\langle i,j \rangle} \vec{m}_i \cdot \vec{m}_j - \frac{D}{2} \sum_{\langle i,j \rangle} \vec{d}_{ij} \cdot [\vec{m}_i \times \vec{m}_j] - K \sum_i (\vec{m}_i \cdot \vec{e}_K)^2. \quad (2)$$

Here, the angular brackets indicate summation over nearest neighbors only, \vec{m}_i is the unit vector defining the orientation of the magnetic moment at site i , J and D are the exchange and DM interaction parameters, respectively, K is the anisotropy constant. The unit DM vector \vec{d}_{ij} lies in the monolayer plane and points perpendicular to the bond connecting sites i and j . The unit vector \vec{e}_K defining the easy axis is normal to the monolayer plane. The Zeeman term is not included in the calculations, so as to mimic technologically relevant ambient conditions with zero applied magnetic field. Magnetostatic dipole-dipole interactions are included effectively in the anisotropy energy [3, 31, 40]. Equation (2) defines a multidimensional energy surface as a function of orientation of magnetic vectors localized on the lattice sites. Over a certain range of material parameter values, Néel-type skyrmions emerge as local energy minima. Properties of isolated skyrmions are of interest here. Therefore, only one single skyrmion is placed in the simulated system. The size of the computational domain is chosen to be large enough for the isolated, equilibrium skyrmion solution not to be affected by the boundaries. Periodic boundary conditions are applied so as to model extended two-dimensional systems.

For a given value of material parameters J , D and K , an isolated skyrmion solution is obtained by taking some rough initial guess for the skyrmion profile and then bringing that to a local minimum on the energy landscape using the velocity projection optimization method [27]. Relaxed, energy-minimum skyrmion configuration is then fitted by a two-parameter profile [20]

$$\Theta(c, w; r) = \pi + \sum_{\alpha=\pm 1} \arcsin \left[\tanh \left(\frac{-r + \alpha c}{w/2} \right) \right], \quad (3)$$

where $\Theta(c, w; r)$ is the polar angle of the spin located at the distance r from the skyrmion center and c , w are the fit parameters. Based on the obtained profile, the skyrmion radius R is evaluated using the definition of Bogdanov and Hubert [3]:

$$R = r_0 - \Theta_0 \left(\frac{d\Theta}{dr} \right)_0^{-1}, \quad (4)$$

where (r_0, Θ_0) is the steepest slope point of the profile $\Theta(c, w; r)$.

Skyrmion stability is quantified using minimum energy path (MEP) calculations applied to the skyrmion collapse into the ferromagnetic (FM) state. The highest maximum along the MEP corresponds to the first order saddle point (SP) of the energy surface representing the bottleneck of the skyrmion decay. Within the harmonic

transition state theory (HTST), the SP energy relative to the skyrmion energy minimum gives the energy barrier ΔE [39] which defines the lifetime, see Eq. (1). A Geodesic Nudged Elastic Band (GNEB) method [27,41] is used to find MEPs of skyrmion annihilation. The GNEB method involves taking the initial guess of the path represented by a discrete chain of states of the system, and systematically bringing that to the MEP by zeroing the transverse component of the gradient force at each point along the path. In order to distribute the states evenly along the path, virtual springs are introduced between adjacent states. At each state, a local tangent to the path is estimated and the GNEB force guiding the states towards the MEP is defined as the sum of the transverse component of the negative energy gradient and the component of the spring force along the tangent. The positions of states are then adjusted using some optimization algorithm, e.g. velocity projection optimization [27], so as to zero the GNEB force. In this method, both the GNEB force and the path tangent are defined in the local tangent space to the curved configuration space, which is needed to satisfy constraints on the length of magnetic moments and to properly decouple the perpendicular component of the energy gradient from the spring force. The shortest path connecting the skyrmion state and the FM state is taken to be the initial guess for the GNEB calculations. The MEPs obtained with such initial guess correspond to the radial collapse of the skyrmion. Radial collapse is likely the only mechanism of skyrmion annihilation in extended two-dimensional systems described by the Hamiltonian in Eq. (2) [29,31,41] and the only one considered here.

3. Results

Within a certain material parameter range, the atomistic model represented by Eq. (2) and its micromagnetic counterpart predict isolated skyrmion solutions as local minima of the energy functional [3, 4, 25]. Analysis involving both numerical calculations and asymptotic methods have previously revealed basic properties of isolated skyrmion solutions. In particular, it has been shown that the equilibrium size of an isolated skyrmion decreases with the anisotropy parameter but increases as the DM interaction strength increases [2, 3, 25, 43]. This behavior is consistent with analytical solutions based on ansatzes such as the one in Eq. (3) [4, 25, 44]. A representative dependence of the skyrmion diameter on K/J for two fixed values of D/J is obtained using the model given by Eq. (2) and shown in Fig. 1(a). The curves are characterized by a certain critical value of the anisotropy parameter, at which the skyrmion size diverges. Observe that confined skyrmions can demonstrate opposite trends for the skyrmion size compared to the isolated skyrmions considered here [2, 42, 43, 45].

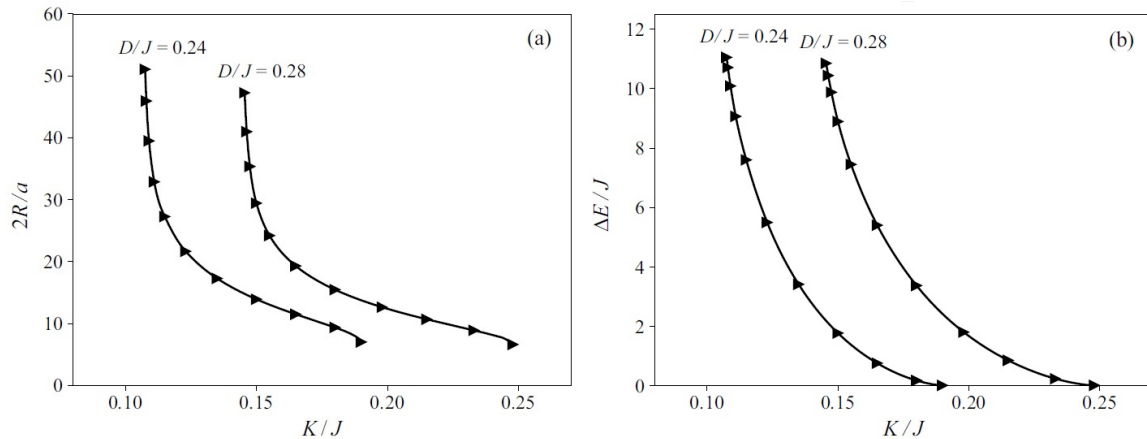


FIG. 1. (a) Skyrmion diameter in units of the lattice constant a , and (b) collapse energy barrier in units of the exchange interaction constant J as functions of the anisotropy parameter for two distinct DM interaction strengths. Triangles indicate the data points. Solid lines show the result of cubic spline interpolation between the points

Figure 1(b) shows results of GNEB calculations of the energy barrier ΔE for the skyrmion collapse into the FM background. With increasing anisotropy strength, energy barrier decreases monotonically to zero. Larger DM interaction parameter results in a larger barrier. It has also been demonstrated in previous calculations that the barrier decreases as the magnetic exchange parameter J gets larger [32]. Material parameter dependence of the collapse energy barrier thus follows the trends for the skyrmion size, as was pointed out by Stosic *et al.* [32]. This behavior is consistent with an intuitive interpretation of the skyrmion annihilation via radial collapse: The corresponding energy barrier should increase with the number of core spins that need to be flipped into the FM

state during the skyrmion collapse process and, therefore, should get larger as the skyrmion size increases. It is demonstrated below that this interpretation is actually incomplete and the collapse barrier is not uniquely defined by the skyrmion size. The barrier can be adjusted by a concerted parameter transformation preserving the skyrmion size. A trivial solution is to scale all material parameters – J , D and K – by the same factor, but such an approach gives only a limited control of the skyrmion stability. Below, the distribution of the collapse energy barriers and skyrmion diameters is superimposed on the magnetic phase diagram with the purpose of gaining more insight into the relationship between the skyrmion size and skyrmion stability.

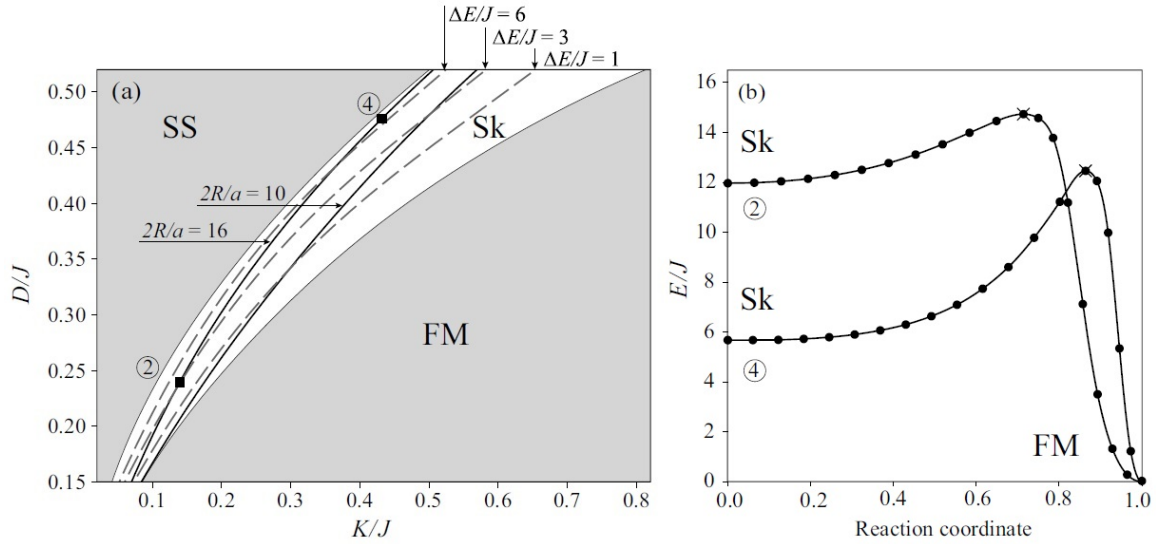


FIG. 2. (a) Zero-temperature phase diagram in reduced variables K/J and D/J for a magnetic monolayer in zero applied magnetic field. Spin spiral is the ground state of the system in the SS region, while the ferromagnetic state is the only stable configuration in the FM region. Isolated skyrmions exist in the Sk sector. Contours of equal skyrmion size are shown with solid lines. Dashed lines represent contours of constant energy barrier for the skyrmion collapse. Two points on the contour where $2R/a = 16$ are labeled with the encircled numbers. For these points, energy variation along the MEP for the skyrmion collapse is shown in the panel (b). The filled circles show position of the intermediate states along the annihilation paths, while crosses indicate energy maxima along the MEPs. The reaction coordinate is defined as the normalized displacement along the MEP. The starting- and end-points of the reaction coordinate are the skyrmion and FM states, respectively

Zero-temperature phase diagram as a function of material parameters K/J and D/J is shown in Fig. 2(a). The diagram is characterized by three regions that correspond to distinct magnetic textures emerging as minima on the energy surface of the system, see Eq. (2). In the SS region, the spin spiral is the ground state of the system. In the FM region, chiral modulations are completely suppressed and polarized ferromagnetic configuration is the only stable configuration. In between these two regions there is an Sk sector where isolated skyrmions exist as metastable states in the FM background [24, 25]. The Sk region is separated from the other two by critical lines at which skyrmion solutions become unstable. At the lower critical line, skyrmions spontaneously collapse into the FM state. Observe that the lower line is characterized by vanishing energy barrier rather than vanishing skyrmion size (see Fig. 1). The fact that skyrmions collapse with finite radii is a consequence of the discreteness of the model used here [25, 43]. At the upper critical line, isolated skyrmions strip out into spiral states [24, 25].

It is informative to trace contours of constant skyrmion diameter and collapse energy barrier in the Sk sector of the magnetic diagram. Here, the following method has been used to obtain the contours. At first, profiles of R and ΔE as functions of K/J for several values of D/J are calculated. Two profiles for $D/J = 24$ and $D/J = 28$ are presented in Fig. 1 as an example. For each profile, the value of the anisotropy parameter corresponding to a predefined skyrmion size or energy barrier is isolated by interpolation between the data points, refined using the bisection method and then placed on the K/J - D/J diagram. Finally, the points corresponding to different values of D/K are connected to trace the contour line. Contours of constant R and ΔE are shown in Fig. 2(a) with solid and dashed lines, respectively. As expected, skyrmions get both larger and more stable against transition to the FM

state in the vicinity of the strip-out critical line. However, R - and ΔE -isolines do intersect, demonstrating that the skyrmion stability is not a unique function of the skyrmion size. This result is further illustrated by a comparison of the collapse energy barriers for skyrmions of equal size. In particular, two points lying on the same constant R contour are chosen. The points labeled ② and ④ on the magnetic phase diagram correspond to parameter sets $K/J = 0.14$, $D/J = 0.24$ and $K/J = 0.44$, $D/J = 0.48$, respectively [see Fig. 2(a)]. The sets result in the same equilibrium skyrmion diameter, $2R = 16a$, with a being a lattice constant, but different collapse energy barriers, which is clear from Fig. 2(b) showing energy variation along the MEPs for the skyrmion annihilation process.

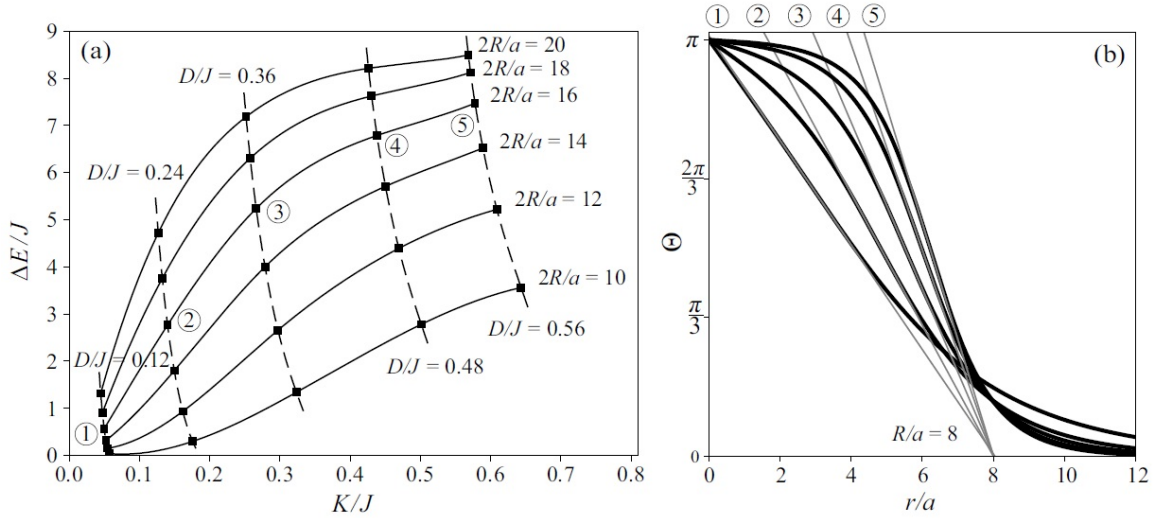


FIG. 3. (a) Energy variation along contours of equal skyrmion size (solid lines). Points corresponding to the same value of the D/J parameter are connected with dashed lines. Encircled numbers label the points for which skyrmion profiles are shown in the panel (b)

How the energy barrier changes along the contours of equal skyrmion size is summarized in Fig. 3(a). For a fixed skyrmion diameter, the collapse barrier gets larger as both K/J and D/J increase in a concerted way. The increase in the energy barrier can be rather pronounced, contributing to the enhancement of skyrmion stability. For example, the barrier for a $16a$ -diameter skyrmion varies by more than an order of magnitude within a chosen range of material parameters [see points labeled ① – ⑤ in Fig. 3(a)]. It is important to realize that the barrier enhancement is achieved by a nontrivial parameter transformation rather than simple parameter scaling since reduced values of the anisotropy parameter and DM interaction strength are used. Interestingly, this concerted parameter transformation does not conserve the skyrmion shape, although it does conserve the skyrmion size. The skyrmion profile variation along the contour where $2R = 16a$ is shown in Fig. 3(b). From Figs. 3(a), 3(b), it is clear that fixed-size skyrmions become more stable as they transform from textures with an arrow-like shape into states that resemble magnetic bubbles where more spins at the core point almost antiparallel ($\Theta \approx \pi$) to the magnetization of the FM background with $\Theta \approx 0$.

4. Conclusion

Our results demonstrate that a change in the shape of fixed-size skyrmions affects the height of the energy barrier protecting the skyrmions from collapse to the FM state. Clearly, enhanced energy barriers for the bubble-like skyrmions should have a direct impact on the skyrmion lifetime. A skyrmion's lifetime at a given temperature can be quantified using the Arrhenius law [see Eq. (1)], but the pre-exponential factor τ_0 needs to be evaluated. The prefactor incorporates the entropic and dynamical contributions to the skyrmion's stability. If skyrmion decay induced by thermal fluctuations is a rare event on the intrinsic time scale of the magnetization dynamics of the system, HTST can be used to calculate τ_0 [39]. Within the theory, the pre-exponential factor is defined by the curvature of the energy surface at the SP and at the skyrmion state minimum. For the parameter set $K/J = 0.05$, $D/J = 0.12$ (see point ① in Fig. 3), the HTST-estimate of τ_0 amounts to $7.44 \cdot 10^2 \tau_{int}$, with τ_{int} being an intrinsic precession time which can be expressed in terms of the on-site magnetic moment μ , exchange interaction parameter J and gyromagnetic ratio γ according to the following formula:

$$\tau_{int} = \frac{\mu}{J\gamma}.$$

Taking $\mu = 3$ Bohr magnetons and $J = 10$ meV, which are typical parameter values for two-dimensional magnetic systems based on transition metals [20,29], one obtains a pre-exponential factor of roughly 0.1 ns, a value which is actually often assumed in studies of thermally activated magnetic transitions [32,46,47].

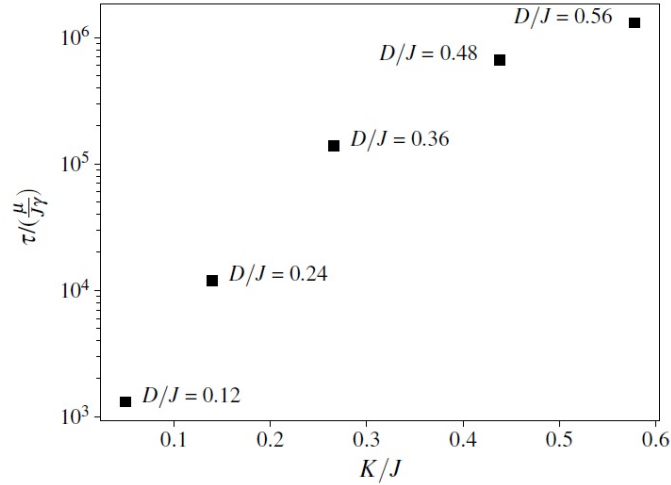


FIG. 4. Calculated skyrmion lifetime along the isoline where $2R/a = 16$. Thermal energy is taken to be $k_B T = J$. Constant Arrhenius pre-exponential factor is assumed

Assuming the constant pre-exponential factor and taking thermal energy to be $k_B T = J$, Eq. (1) can now be used to calculate the skyrmion lifetime. The calculated results of the lifetime of fixed-size skyrmions ($2R = 16a$) as a function of relevant material parameters are presented in Fig. 4. The lifetime increases significantly, by three orders of magnitude within a chosen parameter range. Obtained enhancement of the lifetime is due to the increase in the energy barrier [see Fig. 3(a)] as the constant prefactor approximation is used here. This approximation could, however, be insufficient in some cases. The Arrhenius prefactor can vary by several orders of magnitude depending on the parameters of the magnetic system, as has been demonstrated both experimentally and theoretically for Fe islands on W(110) [48,49]. Recent studies suggest that variable pre-exponential factor could be particularly relevant for magnetic skyrmions [38,50]. It remains to be seen how the prefactor changes under the variation of material parameters of a skyrmionic system and how this affects the skyrmion lifetime.

In summary, the relationship between the skyrmion size and skyrmion stability has been analyzed based on MEP calculations and atomistic spin Hamiltonian. It has been demonstrated that the energy barrier protecting the skyrmion from collapse to the FM state is not uniquely defined by the skyrmion size, which opens up the possibility to enhance the stability of nanoscale magnetic skyrmions via nontrivial, concerted adjustment of material parameters. The deduced parameter transformation conserves the skyrmion size, but does not conserve the skyrmion shape and is not reduced to a simple parameter scaling. In particular, fixed-size skyrmions transform from textures with an arrow-like shape into states that resemble magnetic bubbles as the anisotropy parameter and the DM interaction strength increase in a concerted way. This transformation of the skyrmion shape is accompanied by an increase in the collapse energy barrier and thus enhancement of skyrmion stability. The prediction that bubble-like skyrmions should be more stable than the arrow-like skyrmions of the same size could help design magnetic materials hosting nanoscale, long-lived skyrmionic bits for future digital technologies.

Acknowledgements

The authors would like to thank H. Jónsson and V.M. Uzdin for helpful discussions and useful comments. This work is supported by the Russian Science Foundation (Grant No. 17-72-10195).

References

- [1] Bogdanov A. N., Yablonsky D. A. Thermodynamically stable “vortices” in magnetically ordered crystals. The mixed state of magnets. *Sov. Phys. JETP*, 1989, **68**(1), P. 101–103.
- [2] Bogdanov A., Hubert A. Thermodynamically stable magnetic vortex states in magnetic crystals. *J. Magn. Magn. Mater.*, 1994, **138**(3), P. 255–269.
- [3] Bogdanov A., Hubert A. The properties of isolated magnetic vortices. *Phys. Stat. Sol. (b)*, 1994, **186**(2), P. 527–543.
- [4] Kiselev N. S., Bogdanov A. N., Schäfer R., Rößler U. K. Chiral skyrmions in thin magnetic films: new objects for magnetic storage technologies? *J. Phys. D: Appl. Phys.*, 2011, **44**, P. 392001.

- [5] Fert A., Cros V., Sampaio J. Skyrmions on the track. *Nat. Nanotechnol.*, 2013, **8**, P. 152–156.
- [6] Müller J. Magnetic skyrmions on a two-lane racetrack. *New J. Phys.*, 2017, **19**, P. 025002(2017).
- [7] Nagaosa N., Tokura Y. Topological properties and dynamics of magnetic skyrmions. *Nat. Nanotechnol.*, 2013, **8**, P. 899–911.
- [8] Woo S., Litzius K., Krüger B., Im M.-Y., Caretta L., Richter K., Mann M., Krone A., Reeve R. N., Weigand M., Agrawal P., Lemesh I., Mawass M.-A., Fischer P., Kläui M., Beach G. S. D. Observation of room-temperature magnetic skyrmions and their current-driven dynamics in ultrathin metallic ferromagnets. *Nat. Mater.*, 2016, **15**, P. 501–506.
- [9] Yu X. Z., Kanazawa N., Zhang W. Z., Nagai T., Hara T., Kimoto K., Matsui Y., Onose Y., Tokura Y. Skyrmion flow near room temperature in an ultralow current density. *Nat. Commun.*, 2012, **3**, P. 988.
- [10] Sampaio J., Cros V., Rohart S., Thiaville A., Fert A. Nucleation, stability and current-induced motion of isolated magnetic skyrmions in nanostructures. *Nat. Nanotechnol.*, 2013, **8**, P. 839–844.
- [11] Moreau-Lucaire C., Moutas C., Reyren N., Sampaio J., Vaz C. A. F., Van Horne N., Bouzehouane K., Garcia K., Deranlot C., Warnicke P., Wohlhüter P., George J.-M., Weigand M., Raabe J., Cros V., Fert A. Additive interfacial chiral interaction in multilayers for stabilization of small individual skyrmions at room temperature. *Nat. Nanotechnol.*, 2016, **11**, P. 444–448.
- [12] Boule O., Vogel J., Yang H., Pizzini S., de Souza Chaves D., Locatelli A., Menteş T. O., Sala A., Buda-Prejbeanu L. D., Klein O., Belmeguenai M., Roussigné Y., Stashkevich A., Chérif S. M., Aballe L., Foerster M., Chshiev M., Auffret S., Miron I. M., Gaudin G. Room-temperature chiral magnetic skyrmions in ultrathin magnetic nanostructures. *Nat. Nanotechnol.*, 2016, **11**, P. 449–454.
- [13] Yu G., Upadhyaya P., Li X., Li W., Kim S. K., Fan Y., Wong K. L., Tserkovnyak Y., Amiri P. K., Wang K. L. Room-temperature creation and spinorbit torque manipulation of skyrmions in thin films with engineered asymmetry. *Nano Lett.*, 2016, **16**(3), P. 1981–1988.
- [14] Jiang W., Upadhyaya P., Zhang W., Yu G., Jungfleisch M. B., Fradin F. Y., Pearson J. E., Tserkovnyak Y., Wang K. L., Heinonen O., te Velthuis S. G. E., Hoffmann A. Blowing magnetic skyrmion bubbles. *Science*, 2015, **17**(6245), P. 283–286.
- [15] Legrand W., Maccariello D., Reyren N., Garcia K., Moutafis C., Moreau-Lucaire C., Collin S., Bouzehouane K., Cros V., Fert A. Room-temperature current-induced generation and motion of sub-100 nm skyrmions. *Nano Lett.*, 2017, **17**(4), P. 2703–2712.
- [16] Jiang W., Zhang X., Yu G., Zhang W., Wang X., Jungfleisch M. B., Pearson J. E., Cheng X., Heinonen O., Wang K. L., Zhou Y., Hoffmann A., te Velthuis S. G. E. Direct observation of the skyrmion Hall effect. *Nat. Phys.*, 2016, **11**, P. 449–454.
- [17] Hrabec A., Sampaio J., Belmeguenai M., Gross I., Weil R., Chérif S. M., Stashkevich A., Jacques V., Thiaville A., Rohart S. Current-induced skyrmion generation and dynamics in symmetric bilayers. *Nat. Commun.*, 2017, **8**, P. 15765.
- [18] Litzius K., Lemesh I., Krüger B., Bassirian P., Caretta L., Richter K., Büttner F., Sato K., Tretiakov O. A., Förster J., Reeve R. M., Weigand M., Bykova I., Stoll H., Schütz G., Beach G. S. D., Kläui M. Skyrmion Hall effect revealed by direct time-resolved X-ray microscopy. *Nat. Phys.*, 2017, **13**, P. 170–175.
- [19] Romming N., Hanneken C., Menzel M., Bickel J. E., Wolter B., von Bergmann K., Kubetzka A., Wiesendanger R. Writing and deleting single magnetic skyrmions. *Science*, 2013, **341**(6146), P. 636–639.
- [20] Romming N., Kubetzka A., Hanneken C., von Bergmann K., Wiesendanger R. Field-dependent size and shape of single magnetic skyrmions. *Phys. Rev. Lett.*, 2015, **114**(17), P. 177203.
- [21] Hanneken C., Otte F., Kubetzka A., Dupé B., Romming N., von Bergmann K., Wiesendanger R., Heinze S. Electrical detection of magnetic skyrmions by tunnelling non-collinear magnetoresistance. *Nat. Nanotechnol.*, 2015, **10**, P. 1039–1042.
- [22] Röbber U. K., Leonov A. A., Bogdanov A. N. Chiral skyrmionic matter in non-centrosymmetric magnets. *J. Phys. Conf. Ser.*, 2011, **303**, P. 012105.
- [23] Röbber U. K., Bogdanov A. N., Pfleiderer C. Spontaneous skyrmion ground states in magnetic metals. *Nature*, 2006, **442**, P. 797–801.
- [24] Wilson M. N., Butenko A. B., Bogdanov A. N., Monchesky T. L. Chiral skyrmions in cubic helimagnet films: The role of uniaxial anisotropy. *Phys. Rev. B*, 2014, **89**, P. 094411.
- [25] Leonov A. O., Monchesky T. L., Romming N., Kubetzka A., Bogdanov A. N., Wiesendanger R. The properties of isolated chiral skyrmions in thin magnetic films. *New J. Phys.*, 2016, **18**, P. 065003.
- [26] Bogdanov A., Hubert A. The stability of vortex-like structures in uniaxial ferromagnets. *J. Magn. Magn. Mater.*, 1999, **195**(1), P. 182–192.
- [27] Bessarab P. F., Uzdin V. M., Jónsson H. Method for finding mechanism and activation energy of magnetic transitions, applied to skyrmion and antivortex annihilation. *Comput. Phys. Commun.*, 2015, **196**, P. 335–347.
- [28] Rózsa L., Simon E., Palotás K., Udvardi L., Szunyogh L. Complex magnetic phase diagram and skyrmion lifetime in an ultrathin film from atomistic simulations. *Phys. Rev. B*, 2016, **93**, P. 024417.
- [29] Rohart S., Miltat J., Thiaville A. Path to collapse for an isolated Néel skyrmion. *Phys. Rev. B*, 2016, **93**, P. 214412.
- [30] Hagemester J., Romming N., von Bergmann K., Vedmedenko E. Y., Wiesendanger R. Stability of single skyrmionic bits. *Nat. Commun.*, 2015, **6**, P. 8455.
- [31] Lobanov I. S., Jónsson H., Uzdin V. M. Mechanism and activation energy of magnetic skyrmion annihilation obtained from minimum energy path calculations. *Phys. Rev. B*, 2016, **94**, P. 174418.
- [32] Stosic D., Mulkers J., Van Waeyenberge B., Ludermit T., Milošević M. V. Paths to collapse for isolated skyrmions in few-monolayer ferromagnetic films. *Phys. Rev. B*, 2017, **95**, P. 214418.
- [33] Uzdin V. M., Potkina M. N., Lobanov I. S., Bessarab P. F., Jónsson H. The effect of confinement and defects on the thermal stability of skyrmions. *Physica B: Condens. Matter*. In press. DOI: 10.1016/j.physb.2017.09.040.
- [34] Cortés-Ortuño D., Wang W., Beg M., Pepper R. A., Bisotti M.-A., Carey R., Vousden M., Kluyver T., Hovorka O., Fangohr H. Thermal stability and topological protection of skyrmions in nanotracks. *Sci. Rep.*, 2017, **7**, P. 4060.
- [35] Uzdin V. M., Potkina M. N., Lobanov I. S., Bessarab P. F., Jónsson H. Energy surface and lifetime of magnetic skyrmions. *J. Magn. Magn. Mater.*, 2018, **459**, P. 236–240.
- [36] Stosic D., Ludermit T. B., Milošević M. V. Pinning of magnetic skyrmions in a monolayer Co film on Pt(111): Theoretical characterization and exemplified utilization. *Phys. Rev. B*, 2017, **96**, P. 214403.
- [37] von Malottki S., Dupé B., Bessarab P. F., Delin A., Heinze S. Enhanced skyrmion stability due to exchange frustration. *Sci. Rep.*, 2017, **7**, P. 12299.
- [38] Bessarab P. F., Müller G. P., Lobanov I. S., Rybakov F. N., Kiselev N. S., Jónsson H., Uzdin V. M., Blügel S., Bergqvist L., Delin A. Lifetime of racetrack skyrmions. *Sci. Rep.*, 2018, **8**, P. 3433.
- [39] Bessarab P. F., Uzdin V. M., Jónsson H. Harmonic transition-state theory of thermal spin transitions. *Phys. Rev. B*, 2012, **85**, P. 184409.

- [40] Draaisma H.J.G., de Jonge W.J.M. Surface and volume anisotropy from dipole-dipole interactions in ultrathin ferromagnetic films. *J. Appl. Phys.*, 1988, **64**(7), P. 3610–3613.
- [41] Bessarab P.F. Comment on “Path to collapse for an isolated Néel skyrmion”. *Phys. Rev. B*, 2017, **95**, P. 136401.
- [42] Butenko A. B., Leonov A. A., Bogdanov A. N., Rößler U. K. Theory of vortex states in magnetic nanodisks with induced Dzyaloshinskii-Moriya interactions. *Phys. Rev. B*, 2009, **80**, P. 134410.
- [43] Siemens A., Zhang Y., Hagemester J., Vedmedenko E. Y., Wiesendanger R. Minimal radius of magnetic skyrmions: statics and dynamics. *New J. Phys.*, 2016, **18**, P. 045021.
- [44] Büttner F., Lemesh I., Beach G. S. D. Theory of isolated magnetic skyrmions: From fundamentals to room temperature applications. *Sci. Rep.* 2018. **8**, P. 4464.
- [45] Rohart S., Thiaville A. Skyrmion confinement in ultrathin film nanostructures in the presence of Dzyaloshinskii-Moriya interaction. *Phys. Rev. B*, 2013, **88**, P. 184422.
- [46] Bedanta S., Kleemann W. Supermagnetism. *J. Phys. D*, 2008, **42**, P. 013001.
- [47] Kapaklis V., Arnalds U. B., Farhan A., Chopdekar R. V., Balan A., Scholl A., Heyderman L. J., Hjörvarsson B. Thermal fluctuations in artificial spin ice. *Nat. Nanotechnol.*, 2014, **9**, P. 514–519.
- [48] Krause S., Herzog G., Stapelfeldt T., Berbil-Bautista L., Bode M., Vedmedenko E. Y., Wiesendanger R. Magnetization reversal of nanoscale islands: How size and shape affect the Arrhenius prefactor. *Phys. Rev. Lett.*, 2009, **103**, P. 127202.
- [49] Bessarab P.F., Uzdin V.M., Jónsson H. Size and shape dependence of thermal spin transitions in nanoislands. *Phys. Rev. Lett.*, 2013, **110**, P. 020604.
- [50] Wild J., Meier T.N.G., Pöllath S., Kronseder M., Bauer A., Chacon A., Halder M., Schowalter M., Rosenauer A., Zweck J., Müller J., Rosch A., Pfleiderer C., Back C.H. Entropy-limited topological protection of skyrmions. *Sci. Adv.*, 2017, **3**(9), P. e1701704.

Scherrer formula: estimation of error in determining small nanoparticle size

A. S. Vorokh

Institute of Solid State Chemistry of the Ural Branch of the Russian Academy of Sciences,
91 Pervomaiskaya st., Ekaterinburg, Russia

vorokh@ihim.uran.ru

PACS 61.05.cc, 61.46.Df**DOI 10.17586/2220-8054-2018-9-3-364-369**

The lower limit of the applicability of the Scherrer formula has been established by calculating the diffraction patterns from model nanoparticles by the Debye formula. Particle size was calculated using the Scherrer formula for different *hkl*-peaks. The obtained data of particle sizes were compared with “real” sizes of model particles in the same *hkl*-directions. The form-factor K_{hkl} was analyzed as main correction of Scherrer formula. It was shown that the Scherrer formula error increases nonlinearly at particle sizes less than 4 nm. For any *hkl* direction, the absolute error of average particle size determination using formula does not exceed 0.3 nm. Analysis shows that average particle size can be determined by Scherrer formula from single diffraction peak of experimental pattern for center-symmetrical particles.

Keywords: Scherrer formula, nanoparticle size, Scherrer limit, Debye equation.

Received: 30 November 2017

Revised: 7 February 2018

Final revision: 3 April 2018

1. Introduction

One of the most important physical properties of nanostructured materials is particle size. Among the techniques developed for nano-scale particle size determination, the analysis of average size of coherent scattering regions from X-ray powder diffraction reflection broadening by the Scherrer formula is the simplest and most convenient [1].

Although there are numerous refinements of the formula, the question of the limits of its applicability is still unclear. The theoretical upper limit of applicability of the Scherrer formula was analyzed in detail and was found up to 600 nm for LaB₆, Si and CeO₂ [2] and 11.9 % from extinction length in general case [3]. Comparison of different experimental methods based on the Scherrer formula with TEM data for different materials showed that crystallite size values are the closest when particle sizes are less than 60 nm [4]. The Scherrer formula has no the lower limit of applicability but the question remains: what is the error of the formula when particle size decreases to zero nm? In the work [5] experimental investigation of TiO₂ anatase nanoparticles shows that absolute divergence is 0.36 nm for the crystallites smaller than 10 nm and 2.4 nm for the the crystallites larger than 15 nm.

In this work we proposed a facile theoretical analysis of the application of the Scherrer formula to diffraction reflections calculated by the Debye equation from model particles, and the contribution of the form-factor while using the Scherrer formula is evaluated. The calculation by the Debye formula is a direct result of scattering on an ensemble of atoms (irrespective of the character of ordering), which allows evaluation of the Scherrer formula accuracy. Moreover, the Debye formula was deduced in the framework of the same two assumptions that were used to derive the Scherrer formula [6]. Independence from translational symmetry allows one to use the Debye equation for investigating the non-crystalline materials [7], stacking faults [8, 9], surface relaxation [10], poorly crystalline materials [11]. Currently, the powerful software programs as DIANNA [12, 13], DEBUSSY [14] allows to apply Debye function analysis (DFA) as routine procedure for structure interpretation [15]. Nevertheless, the most material scientists uses the Scherrer formula as the simplest method of particle size determination.

The formula proposed by P. Scherrer in 1918 [16] describes the broadening of diffraction reflection peaks β as a function of the average particle size D :

$$\beta = K \frac{\lambda}{D \cos \theta}, \quad (1)$$

where λ is the X-ray wave length, θ is the Bragg reflection angle, and $K = 2\sqrt{(\ln 2)/\pi}$ is a constant. Formula (1) was deduced with two assumptions:

- 1) an X-ray wave is singly scattered on atoms of a substance (so-called kinematical approximation), and dynamic effects exert a negligibly small influence on the form of the diffraction pattern;

- 2) a material is an “ideal powder” consisting of an infinite number of identical particles located chaotically in space, which allows the powder crystallite size and shape and sample texture distribution to be neglected. The particles were supposed by P. Scherrer [16] to have a cubic shape and cubic structure.

Taking into account the above mentioned assumptions, formula (1) should presume no rigorous experimental check, and its application for the processing of experimental diffraction data has mainly an evaluative character. The error of formula (1) can be established only by comprehensive consideration of all peculiarities of the equation and by application to diffraction patterns calculated from model powder.

Let us consider the formula itself in detail. As given in [16], the formula included two ambiguous values. Firstly, the parameter β , which the author [16] designated as halfwidth in “the generally accepted sense” without specifying whether this was full width at half maximum (FWHM) or integral breadth (IB) equal to the area under the peak related to its maximal value. Secondly, the value of constant K called subsequently as the Scherrer constant or form-factor was not clear from the article. The work [16] interpreted the constant K as a relating factor between the FWHM and IB of the Gaussian function: $\text{FWHM}_G = 2\sqrt{\frac{\ln 2}{\pi}} \text{IB}_G = K \cdot \text{IB}_G$, suggesting that Scherrer supposed the diffraction peak to be approximated by the Gaussian, consequently, $\beta = \text{FWHM}_G$. Then, the Scherrer formula may be written as $\text{FWHM}_G = K \frac{\lambda}{D \cos \theta}$, where $K = 2\sqrt{\frac{\ln 2}{\pi}}$. The analogous notation $\text{IB}_G = \frac{\lambda}{D \cos \theta}$ reflects the physical meaning of the formula more clearly – the area under the diffraction curve is related with the radial distribution of atoms in the particle and, accordingly, with the size of this particle.

The factor $K = \sqrt{3/\pi} \approx 0.977$ as a necessary numerical correction appeared for the first time in work [17], where N. Selyakov presented the first detailed derivation of formula (1) for particles of trigonal structure. In the subsequent works devoted to this subject [18, 19], the values of the form-factor K were proposed for particles of different shape depending on hkl directions. According to [19], for a powder consisting of equal cubic crystallites, the coefficient K for different crystallographic indices (hkl) of the cubic crystal lattice was calculated by the formula:

$$K_{hkl} = \frac{6|h|^3}{(h^2 + k^2 + l^2)^{1/2}(6h^2 - 2|hk| + |kl| - 2|hl|)}. \quad (2)$$

In this study, cubic particles of simple cubic structure with the space group $Pm\bar{3}m$ have been chosen as model objects, since the Scherrer formula was derived exactly for such particles. We compared the particle size values calculated by equation (1) both without using the form-factor K_{hkl} and with the correction expressed by equation (2). For this purpose, we calculated the diffraction patterns from model particles by the Debye formula [20]:

$$I(q) = \sum_{j=1}^N \sum_{k=1}^N f_j(q) f_k(q) \frac{\sin(qR_{jk})}{qR_{jk}}, \quad (3)$$

where $I(q)$ is the scattering intensity, R_{jk} is the distance between the j -th and the k -th atoms; q is the modulus of the scattering vector; and $f_j(q)$ is the atomic scattering vector for the j -th atom. The scattering intensity on “ideal powder” is composed of scattering intensities on each individual powder particle and, consequently, is determined by integration over all possible positions of this particle-object in space.

The model cubic particles were set by generating the atomic coordinates with the use of a simple cubic lattice with a distance between nearest atoms equal to 0.3 nm. The atomic scattering factors $f_j(2\theta) = f_j(q)$ of model particles were calculated by approximating the tabular data for silicon atoms [21]. In the calculation of the scattering intensity measured in a real X-ray diffraction experiment by the Bragg–Brentano method, angular scattering factors should be also taken into account along with the structural factor: the geometric factor G , the Lorentz factor L and the polarization factor $P(\theta) = (1 + \cos^2 2\theta)/2$. The correction is made by multiplying the intensity by the angular factor, $LPG(\theta) = \frac{1 + \cos^2 2\theta}{4 \cdot \sin 2\theta \cdot \sin \theta}$. The diffraction patterns were calculated for $\text{CuK}\alpha$ radiation with wavelength 0.154 nm.

Diffraction peak profiles can be approximate by different methods with the highest degree of accuracy [22–24]. For accurate description of the peak shape, each diffraction peak was approximated by the pseudo-Voigt function by the formula:

$$V(\theta) = ca \left[1 + \frac{(\theta - \theta_0)^2}{\theta_L^2} \right]^{-1} + (1 - c)a \exp \left[-\frac{(\theta - \theta_0)^2}{2\theta_G^2} \right] = c \cdot l(\theta) + (1 - c) \cdot g(\theta),$$

where $l(\theta)$ is the Lorentz function; $g(\theta)$ is the Gaussian function; c is the relative contribution of the Lorentz function to the total reflection intensity; θ_L and θ_G are the Lorentz and Gaussian distribution parameters, respectively; a is the normalizing factor of intensity; and θ_0 is the position of the pseudo-Voigt function maximum. The exact FWHM_V value is determined by the solution of the nonlinear equation

$$V(\theta_h) = \frac{ac}{1 + (\theta_h/b)^2} + a(1 - c) \exp \left[-\frac{(\theta_h/b)^2}{2} \right] = \frac{a}{2},$$

which is not solved analytically, but the solution of this equation is satisfactorily described by the quadratic dependence $\theta_h = 2.355 - 0.276c - 0.079c^2$, consequently, $\text{FWHM}_V = b(2.355 - 0.276c - 0.079c^2)$. The error of such approximation is about 0.01 %. The numerical values of the parameters a , $b = \theta_L = \theta_G$, c , $2\theta_0$ of each reflection were obtained in the framework of the application program *SigmaPlot*.

Figure 1 displays the results of the calculations for the X-ray diffraction patterns. The diffraction patterns were calculated for cubic nanoparticles containing 8, 27, 64, 125, 256, 1728 or 17 576 atoms. The number of unit cell translations was 1, 2, 3, 4, 5, 11 and 25, respectively. With an increase in the nanoparticle size, the broad reflections typical for amorphous substance tend to turn into narrow peaks peculiar to coarse-crystalline material.

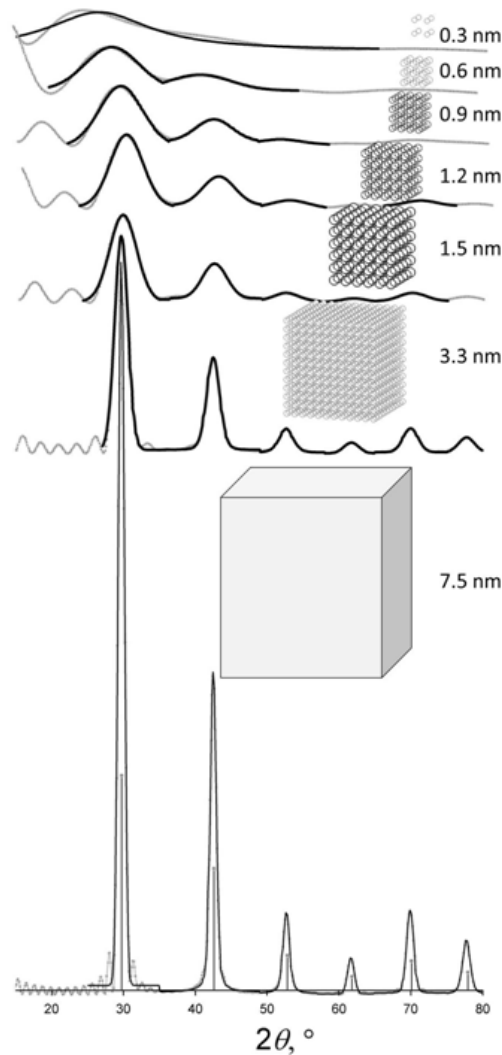


FIG. 1. Diffraction curves calculated by the Debye formula (grey) for cubic particles of the cubic unit cell structure, and approximation of reflections by the pseudo-Voigt function (black). The corresponding model particles are shown next to the diffraction patterns, the edge length is given in nm

The particle size was calculated by formula (1) $D^{Sch} = \lambda / \text{FWHM}_V \cos \theta_0$ and also with the correction for K_{hkl} : $D_{hkl}^{Sch} = K_{hkl} \lambda / \text{FWHM}_V \cos \theta_0$. The coefficient K_a for the determination of the linear size $D^{Deb} = K_a \cdot a$ of a cubic particle with edge side a in a given direction (hkl) was calculated in a similar way. For example, the linear particle size in the direction (111) is equal to the body diagonal of a cube $a\sqrt{3}$. This makes it possible to relate the sizes of a preset model cubic particle with the sizes determined by the Scherrer formula. The average size of each particle was calculated as the arithmetical mean value in all directions hkl , since the sizes of one particle depend strongly on the hkl direction. The calculated values are listed in the Table 1. In other words, the results obtained from simulated pattern can be used as the Scherrer constant [25].

The ratio $(D_{av}^{Sch} - D_{av}^{Deb}) / D_{av}^{Deb}$ characterizes the deviation between the average particle size determined by the Scherrer formula and the average size of model particle. Fig. 2 shows the error of the Scherrer formula versus the average size of model particle both with and without correction for the form-factor K_{hkl} . In both cases, the divergence of sizes determined by the Scherrer formula from the given size was 76 % for a cubic particle consisting of 8 atoms, with edge length equal to one translation. As the particle size increases, the deviation exhibited a nonlinear behavior tending to smaller values. When the particle size was more than 10 unit cell translations (~ 4 nm), the error in the calculation by the original formula (1) was up to 2 %. If the form-factor K_{hkl} is taken into account, the error is negative, which leads to a considerable particle size underestimation (over 10 %).

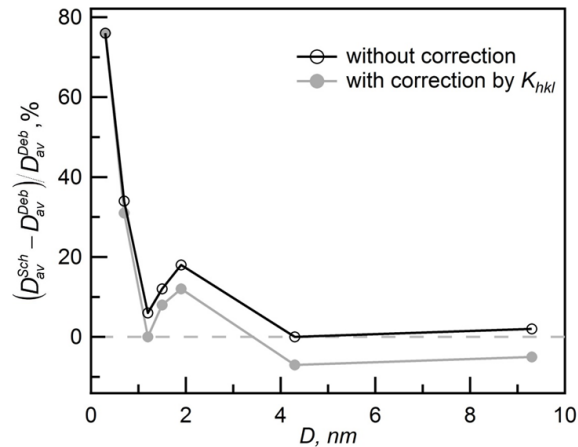


FIG. 2. The deviation of the Scherrer formula versus the size of model cubic nanoparticles determined by formula (1) and with correction for the form-factor K_{hkl} by formula (2)

The Scherrer formula implies scattering on a centrosymmetric particle (sphere, for example). The size values for different hkl -directions vary nearby the average particle size D_{av}^{Sch} (Table 1, column 3). As particle increases (Table 1, column 1), the sizes determined at any hkl -directions approach the average particle size D_{av}^{Sch} . On the other hand, the average size of the model particle D_{av}^{Deb} also demonstrates tendency to the size of centrosymmetric particle with increasing of number of atoms in the particle. Thus, the particle of 8 atoms is described by one size at one hkl -direction, and the particle of 256 atoms is described by 5 sizes at 5 hkl -directions. The more items (sizes at different hkl) in the sum the closer average particle size to a value characteristic of a centrosymmetric particle. According to this, the average particle sizes D_{av}^{Sch} and D_{av}^{Deb} approach each other as the particle sizes increase, and they become an equal at value 4.27 nm.

This implies that form-factor K_{hkl} can be ignored for estimation of particle size. The main role of the form factor K_{hkl} is to take into account the deviation of the particle size from centrosymmetry. The correction K_{hkl} strongly underestimates the size of the cubic particle body diagonal (Table 1, $hkl = 111$), so the average particle size drops sharply (Table 1, column 4). In other hkl directions, the sizes obtained with the K_{hkl} correction behave ambiguously with respect to the model particle size at the same hkl directions. The influence of the form factor is supposed to differ for particle size larger than 10 nm. Nevertheless, using form factor for the refinement procedure seems to be useless for the size range below 10 nm.

Despite the significant relative deviation of the average particle size, the absolute value of error does not exceed 0.3 nm. As a rule, this accuracy is sufficient for powder diffraction investigations. More accurate measurement requires detailed high-resolution transmission electron microscopy. In other words, the Scherrers formula can be used even for estimation of sizes of small particle. Moreover, due to the proximity of particle sizes at different

TABLE 1. The particle size versus hkl directions, and the average size \bar{D} in all directions hkl

1	2	3	4	5
Number of atoms	hkl	Particle size D^{Sch} by formula (1)	Particle size D_{hkl}^{Sch} with correction (2)	Model particle size $D^{Deb} = a \cdot K_a$
8	100	0.53	0.51	0.30
\bar{D}_8		0.53	0.51	0.30
27	100	1.02	0.99	0.60
	110	0.91	0.85	0.85
\bar{D}_{27}		0.97	0.92	0.72
64	100	1.30	1.26	0.90
	110	1.60	1.49	1.27
	111	1.05	0.95	1.56
\bar{D}_{64}		1.32	1.23	1.24
125	100	1.71	1.65	1.20
	110	1.82	1.70	1.70
	111	1.40	1.26	2.08
	210	1.99	1.63	1.20
\bar{D}_{125}		1.73	1.56	1.54
256	100	2.05	1.99	1.50
	110	2.35	2.19	2.12
	111	1.89	1.69	2.60
	200	2.31	1.99	1.50
	210	2.47	2.02	1.68
\bar{D}_{256}		2.21	1.97	1.88
1728	100	4.18	4.04	3.30
	110	4.43	4.13	4.67
	111	4.34	3.89	5.72
	200	4.13	3.54	3.30
	210	4.51	3.69	3.69
	211	4.02	3.12	4.95
\bar{D}_{1728}		4.27	3.74	4.27
17576	100	9.18	8.88	7.20
	110	9.75	9.09	10.18
	111	9.34	8.36	12.47
	200	9.30	7.98	7.20
	210	9.18	7.52	8.05
	211	10.12	7.87	10.80
\bar{D}_{17576}		9.48	8.28	9.32

hkl-directions to the average value, it is not necessary to use all peaks of diffraction pattern. The calculations show (Table 1, column 3) that applying the Scherrer formula to a single reflex of the diffraction pattern is enough to estimate the average particle size.

This is very important in cases of multiphase samples, where most reflections of different phases overlap in the experimental diffraction pattern. The possibility to use the only reflex for estimation the size of a particle with insignificant error can be great help for majority of material science researchers. Hence, in order to decrease the error of size estimation and to account the asymmetric shape of particle, the simulation of diffraction pattern by the Debye formula and high resolution electron microscopy investigation are required.

This analysis allows one to conclude that at the range below 10 nm, the Scherrer formula without K_{hkl} -correction gives more exact values. If the sizes of crystal nanoparticle are less than 4 nm, the relative error of the Scherrer formula increases appreciably. Nevertheless, the absolute error of the Scherrer formula does not exceed 0.3 nm for estimation of the average size of center-symmetrical particle.

Acknowledgements

The author thanks E. V. Shalaeva for useful discussion and A. L. Syuzumova for English translation of the article. This work was supported by the Russian Science Foundation (project No. 17-79-20165) and performed at the Institute of Solid State Chemistry UrB RAS.

References

- [1] Ingham B. X-ray scattering characterisation of nanoparticles. *Crystallography Reviews*, 2015, **21** (4), P. 229–303.
- [2] Muniz F.T.L., Miranda M.A.R., dos Santos C.M., Sasaki J.M. The Scherrer equation and the dynamical theory of X-ray diffraction. *Acta Crystallographica A: Found. & Adv.*, 2016, **72** (3), P. 385–390.
- [3] Miranda M.A.R., Sasaki J.M. The limit of application of the Scherrer equation. *Acta Crystallographica A: Found. & Adv.*, 2018, **74** (1), P. 54–65.
- [4] Uvarov V., Popov I. Metrological characterization of X-ray diffraction methods at different acquisition geometries for determination of crystallite size in nano-scale materials. *Materials Characterization*, 2013, **85**, P. 111–123.
- [5] Uvarov V., Popov I. Metrological characterization of X-ray diffraction methods for determination of crystallite size in nano-scale materials. *Mater. Charact.*, 2007, **27**, P. 883–891.
- [6] Scardi P., Billinge S.J.L., Neder R., Cervellino A. Celebrating 100 years of the Debye scattering equation. *Acta Crystallographica A: Found. & Adv.*, 2016, **72** (6), P. 589–590.
- [7] Hall B.D., Zanchet D., Ugarte D. Estimating nanoparticle size from diffraction measurements. *J. Appl. Cryst.*, 2000, **33**, P. 1335–1341.
- [8] Rempel A.A., Vorokh A.S., Neder R., Magerl A. Disordered structure of cadmium sulphide nanoparticles. *J. Surf. Investig. X-ray, Synchr. and Neutron Tech.*, 2011, **5** (6), P. 1028–1031.
- [9] Vorokh A.S., Rempel A.A. Direct-space visualization of the short and average long-range orders in the noncrystalline structure of a single cadmium sulfide nanoparticle. *JETP Letters*, 2010, **91** (2), P. 100–104.
- [10] Perez-Demydenko C., Scardi P. Diffraction peak profiles of surface relaxed spherical nanocrystals. *Philosophical Magazine*, 2017, **97** (26), P. 2317–2346.
- [11] Sestu M., Navarra G., et al. Whole-nanoparticle atomistic modeling of the schwertmannite structure from total scattering data. *J. Appl. Cryst.*, 2017, **50**, P. 1617–1626.
- [12] Tsybulya S.V., Yatsenko D.A. X-ray diffraction analysis of ultradisperse systems: The Debye formula. *J. Struct. Chem.*, 2012, **53**, S150–S165.
- [13] Yatsenko D., Tsybulya S. DIANNA (diffraction analysis of nanopowders) – a software for structural analysis of nanosized powders. *Zeitschrift Fur Kristallographie – Crystalline Materials*, 2018, **233** (1), P. 61–66.
- [14] Cervellino A., Frison R., Bertolotti F., Guagliardi A. DEBUSSY 2.0: the new release of a Debye user system for nanocrystalline and/or disordered materials. *J. Appl. Cryst.*, 2015, **48** (6), P. 2026–2032.
- [15] Nikulina O., Yatsenko D., et al. Debye function analysis of nanocrystalline gallium oxide gamma-Ga₂O₃. *Zeitschrift Fur Kristallographie – Crystalline Materials*, 2016, **231** (5), P. 261–266.
- [16] Scherrer P. Bestimmung der Größe und der inneren Struktur von Kolloidteilchen mittels Röntgenstrahlen. *Nachrichten Gesellschaft Wissenschaft Gottingen*, 1918, **2**, P. 98–100.
- [17] Seljakow N. Eine röntgenographische Methode zur Messung der absoluten Dimensionen einzelner Kristalle in Körpern von fein kristallinischem Bau. *Zeitschrift fuer Physik*, 1925, **516**, P. 439–444.
- [18] Langford J.I., Wilson A.J.C. Scherrer after Sixty Years: A Survey and Some New Results in the Determination of Crystallite Size. *J. Appl. Cryst.*, 1978, **11**, P. 102–113.
- [19] James R.W. *Optical principles of the Diffraction of X Rays*. G. Bell & Sons, 1948, 624 p.
- [20] Debye P. Zerstreuung von Röntgenstrahlen. *Annalen der Physik B*, 1915, **46**, P. 809–823.
- [21] *International Tables for X Ray crystallography IV*, Birmingham, England, 1974, 366 p.
- [22] Mitra G.B. Moments and Cumulants of Diffraction Profiles Broadened by Stacking Faults. *Journal of Crystallization Process and Technology*, 2013, **3**, P. 103–107.
- [23] Ectors D., Goetz-Neunhoeffer F., Neubauer J. Routine (an)isotropic crystallite size analysis in the double-Voigt approximation done right? *Powder Diffraction*, 2017, **32**, S27–S34.
- [24] Ida T. New measures of sharpness for symmetric powder diffraction peak profiles. *J. Appl. Cryst.*, 2008, **41**, P. 393–401.
- [25] Li Z. Characterization of Different Shaped Nanocrystallites using X-ray Diffraction Line Profiles. *Particle & Particle Systems Characterization*, 2011, **28** (1–2), P. 19–24.

Possibility of drug delivery due to hydrogen bonds formation in nanodiamonds and doxorubicin: molecular modeling

A. N. Bokarev, I. L. Plastun

Saratov State Technical University named after Yuri Gagarin, Saratov, Russia

andreybokarev@mail.ru, inna_pls@mail.ru

PACS 36.40.Mr

DOI 10.17586/2220-8054-2018-9-3-370-377

The possibility of drug delivery and retention in cells due to hydrogen bond formation between enriched nanodiamonds and highly toxic drugs (for example doxorubicin), is investigated by numerical simulation. Using molecular modeling by the density functional theory method with the B3LYP functional and the 6-31G(d) basic set, we analyze hydrogen bond formation and their influence on IR-spectra and structure of molecular complex which is formed due to interaction between doxorubicin and nanodiamonds enriched by carboxylic groups. Numerical modeling of carboxylated nanodiamonds and doxorubicin interaction is based on nanodiamond representation by a diamond-like nanoparticle with simpler structure. Enriched adamantane (1,3,5,7-adamantanetetracarboxylic acid) is used as an example of carboxylated diamond-like nanoparticle. Combined IR spectrum as imposing of IR spectra for doxorubicin and 1,3,5,7-adamantanetetracarboxylic acid various interaction positions is obtained. The combined IR spectrum demonstrates good agreement with experimental data. The obtained results demonstrate that there can be strong hydrogen bonds between doxorubicin and nanodiamond as one of basic mechanism for drug delivery and retention in cells.

Keywords: doxorubicin, nanodiamond, drug delivery, 1,3,5,7-adamantanetetracarboxylic acid, molecular complex, hydrogen bond, molecular modeling, density functional theory, IR spectrum.

Received: 23 December 2017

Revised: 15 March 2018

Final revision: 20 March 2018

1. Introduction

Detonation nanodiamond (ND) is one of most promising materials for targeted drug delivery [1–3] – one of rapidly developing areas of modern chemistry, pharmacology and medicine. Wide possibilities for surface modification and advantageous dimensions make nanodiamonds very attractive objects for use in the drug delivery process. Many experimental studies are devoted to increasing the efficiency of tumor treatment by using drugs in combination with nanodiamonds [4–12]. It is nontoxic, biocompatible and able to overcome biological barriers, penetrating into the cells [10]. For the immobilization of drugs on ND surface are commonly used an adsorption [11] and covalent grafting [8, 12] methods.

A number of studies have shown that therapeutic efficacy of drugs is enhanced and their toxicities may be attenuated with immobilization on ND. Such studies are: investigation of amikacin-immobilized ND antibacterial activity [8], enhance of drug retention in cancer cells due to ND-mitoxantrone molecular complexes [13], flavonoids transport due to diamond-like nanoparticles [14], enhance therapeutic efficacy of doxorubicin due to ND [9, 15] and many other studies (see, for example, reviews [4] and [6]).

As noted above, the most popular methods of drug immobilization on ND surface are adsorption and covalent grafting, but also there is one more simple immobilization method – creation of molecular complex due to hydrogen bond formation, that is due to electrostatic interaction. One of example for drug and ND electrostatic interaction analysis is doxorubicin (DOX) ($C_{27}H_{29}NO_{11}$). It is one of the most well-known and widely used drugs for the treatment of cancer. Unfortunately, DOX, like most anticancer drugs, is toxic. Doctors must limit the dose administered since doxorubicin can cause major side effects such as hair loss, nausea [16], and weakening of the heart muscle over time (cardiomyopathy) [17]. Significant reduction in side effects can be achieved by increasing the efficiency of the mechanism for drug delivery to tumor cells.

Theoretical investigation of DOX and ND electrostatic interaction and analysis of DOX–ND molecular dynamic depending on a pH-factor was conducted in [15], where in modeling process used a bare ND. However, in real nature experiments usually used an enriched ND, containing various functional groups as $-COOH$, $-CONH$, $-OH$, $-CO$, $-NH_2$, $-SH$, $-CH_2$, $-H$, etc. (see, for example, [6]). The enriched ND surface promotes strengthening of the intermolecular interactions that, as a result, causes increase in the drug delivery efficacy.

Experimental studies of DOX and enriched ND molecular complexes, formed as a result of electrostatic interaction, demonstrate a significant enhancement of DOX therapeutic efficacy [9]. In this article conclusion, it is

said that the effect of DOX enhancement is found, but the mechanism of its emergence is not explained. Theoretical studies of DOX and ND intermolecular interaction will be able to offer an explanation for this mechanism, but now investigation of DOX and ND electrostatic interaction and analysis of hydrogen bonds formation in DOX–ND molecular complex have not been carried out. For this reason, such study is quite relevant as attempt of an explanation of DOX efficacy enhancement mechanisms.

Thus, the aim of present work is investigation of hydrogen bond formation between DOX and COOH-enriched ND by analysis of calculated IR spectra and optimized structures of formed molecular complexes. ND are a means of drug retention in cancer cells. Energy of formed hydrogen bonds will define a use possibility for ND as tool of drug delivery and retention in cells due to electrostatic interaction mechanism.

2. Molecular modeling

Molecular modeling was executed by numerical simulation based on the density functional theory [18], in particular, on the B3LYP functional method [19]. In B3LYP method there is representation of the molecular orbital as a linear combination of linearly independent functions, which are called basis functions. For numerical simulations, we used split-valence basis sets. These sets are characterized by high accuracy, which is achieved by the valence orbital representation by two sets of functions. The notation for the split-valence basis sets is typically M -NPG, where M denotes the number of primitive Gaussian functions which are included in the basis function of atomic orbital (M takes values from 3 to 6), the N and P show that the valence orbital are composed of two basis functions each, the first one composed of a linear combination of N primitive Gaussian functions (N is typically equal to 2 or 3), the other composed of a linear combination of P primitive Gaussian functions. In present work we use the split-valence 6-31G(d) basis set. Obviously, the atomic orbital of the inner electron shell is approximated by six Gaussian functions. Orbital of the valence shell is described, respectively, three and one Gaussian functions. For numerical modeling of intermolecular interaction in molecular compound we used the Gaussian 09 program complex [20], which is traditionally applied for investigations in various areas of computational physics and chemistry and approved by the authors in [14] and other investigations.

Procedures of molecular modeling and spectra calculations require a large amount of computational resources and time depending on the structure complexity of molecules, which form the compound, and on the total number of atoms in the complex. The typical ND has diameter of ~ 4 to 40 nm [4,6] and includes more than 1000 atoms. Therefore, the modeling of real ND and DOX interaction at the level of studying the possibility of intermolecular bond formation is very difficult for personal computers. For this reason, the question arises concerning the possibility of using small size diamond-like nanoparticles, which would be similar to large size nanodiamonds in their characteristics and intermolecular interaction capabilities.

In the process of molecular modeling by numerical simulations, we used a model based on the simplest diamondoid, adamantane. Adamantane ($C_{10}H_{16}$) is the smallest diamond-like hydrocarbon particle. The spatial arrangement of carbon atoms in adamantane molecule is the same as in the diamond crystal. This structure is the basic “building” block for larger diamond-like structures [21]. In present work, we consider the modified adamantane, named 1,3,5,7-adamantantetracarboxylic acid (AdTCA) ($C_{14}H_{16}O_8$), which contains 4 carboxylic ($-\text{COOH}$) groups [22]. The modified structure is resulted from the substitution of 4 hydrogen atoms for carboxylic groups in original adamantane. To assess the possibility of using AdTCA as an object that approximates a large-size carboxylated ND, we also calculated IR spectra for 1 nm diameter ND ($C_{88}H_{64}O_8$) enriched by 4 carboxylic groups. The chemical structures of adamantane, AdTCA and 1 nm diameter ND are presented on Fig. 1.

In order to account for anharmonicity in intermolecular interactions, we used the following scaling factors for resulted vibrational modes: 0.9713 (range 0 – 1000 cm^{-1}); 0.9744 (range 1000 – 2000 cm^{-1}); 0.956 (range above 2000 cm^{-1}). These factors are used to decrease the divergence between calculated and experimental data, which is caused by using the harmonic approximation in numerical simulations.

3. Results and discussion

In our investigations, we based our work on experimental results obtained in [9]. In this work, the ND–DOX molecular complex was obtained using a novel adsorption technique developed with a pH 8.5 coupling buffer. Follow the experimental results [9], we consider a ND–DOX molecular complex in crystal phase. As is shown in our preliminary calculation results, all hydrogen bonds are present in an aqueous phase, but their energy becomes a little less than in a crystal phase, and their investigation is not a subject for research in this article.

The structure of DOX molecule and the calculated IR spectrum of DOX in comparison with the experimental IR spectrum of DOX, taken from work [9], are shown in Figs. 2a and 2b, respectively. Peaks in the high-frequency region of the calculated IR spectrum (1 – 5 on Fig. 2b) correspond to stretching vibrations of O–H bonds in DOX

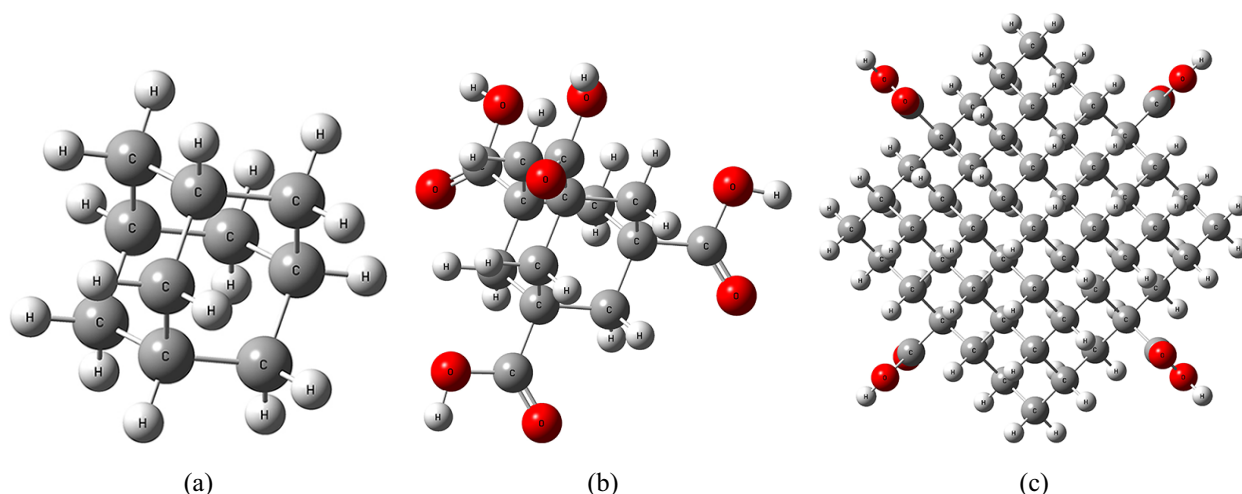


FIG. 1. Structure of adamantane (a), 1,3,5,7-adamantanetetracarboxylic acid $C_{14}H_{16}O_8$ (b) and 1 nm diameter nanodiamond $C_{88}H_{64}O_8$, enriched by 4 carboxylic ($-COOH$) groups (c)

(1 – 5 on Fig. 2a). After carrying out the frequencies scaling, the calculated spectrum is in good agreement with the experimental data.

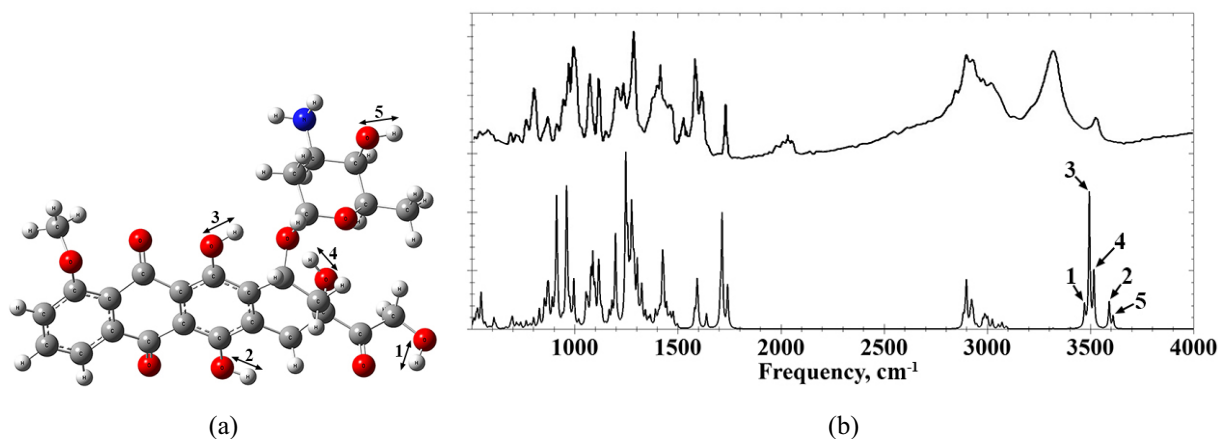


FIG. 2. Structure (a) and experimental (upper) and calculated (lower) IR spectra (b) of doxorubicin with designated 1–5 O–H bonds

The calculated frequencies of stretching vibrations for O–H bonds in DOX, which can participate in the formation of hydrogen bonds, are: 1 – 3472 cm^{-1} , 2 – 3591 cm^{-1} , 3 – 3495 cm^{-1} , 4 – 3517 cm^{-1} , 5 – 3610 cm^{-1} . The lengths of all O–H bonds are on the order of 0.97 \AA .

Let us consider the possibility of using AdTCA as an object that approximates a large-size carboxylated ND. In Fig. 3, we can compare calculated IR spectra of 1 nm diameter ND enriched by 4 $-COOH$ groups and AdTCA with experimental IR spectrum of carboxylated ND provided by the Laboratory of laser spectroscopy of solutions of supramolecular compounds and nanostructures (headed by T. A. Dolenko, Physics Department of Moscow State University).

In the calculated IR spectrum of AdTCA (Fig. 3, lower), there are four characteristic regions which correspond to stretching vibrations of C–O and C–C bonds ($1000 - 1200\text{ cm}^{-1}$), C=O bonds ($1780 - 1800\text{ cm}^{-1}$), C–H bonds ($2915 - 2995\text{ cm}^{-1}$) and stretching vibrations of O–H bonds (3523 cm^{-1}). The frequencies of the most intense peaks in the considered regions are 1144 cm^{-1} , 1795 cm^{-1} , 2917 cm^{-1} and 3523 cm^{-1} , respectively. The considered characteristic regions in the obtained IR spectra of AdTCA are in good agreement with the corresponding regions in the calculated IR spectrum of 1 nm diameter ND, enriched by 4 carboxylic groups (Fig. 3, center) and the experimental IR spectrum of carboxylated ND (Fig. 3, upper). However, the procedures of structure optimization and spectra calculations AdTCA require much less computational time than the calculation of 1 nm diameter ND.

Thus, the high level of consistency of the characteristic regions in considered spectra and a smaller amount of the required computational time allows the use of AdTCA as an object that approximates a large-size carboxylated ND at the level that allows qualitative estimation of compound formation during molecular modeling.

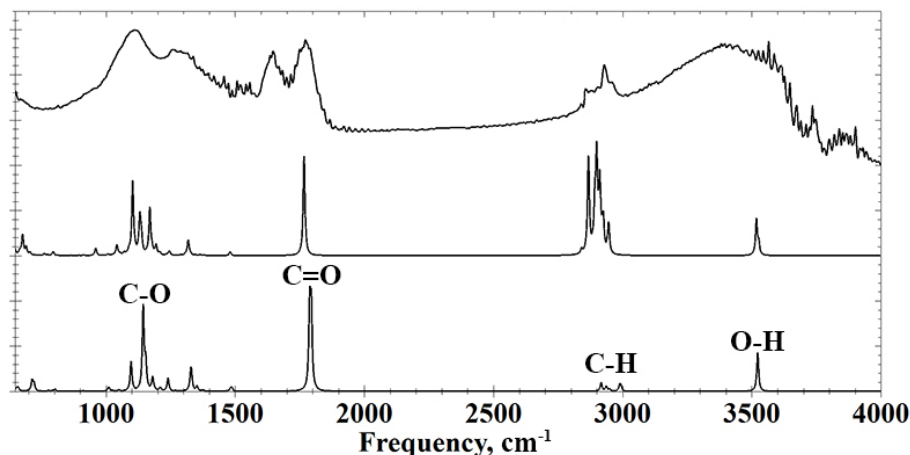


FIG. 3. Experimental IR spectrum of carboxylated nanodiamond (upper), calculated IR spectra of 1 nm diameter nanodiamond (central) and 1,3,5,7-adamantanetetracarboxylic acid (lower)

As we spoke above, the sizes of NDs, which are used in scientific experiments with DOX, are from 4 nm and higher [9], and the width of the DOX molecule is about 1.5 nm, therefore we can assume that the DOX molecule can be attached to the ND at several points simultaneously. The doxorubicin molecule includes five O–H bonds (1 – 5 on Fig. 2a) and two N–H bonds, whose hydrogen atoms can theoretically participate in the formation of hydrogen bonds as a donor, as well as eleven oxygen atoms and one nitrogen atom that can participate in the formation of hydrogen bonds as an acceptor. In our studies, we considered possible variants of interaction with all these atoms, but due to the limitations of molecular modeling caused by the structural features of AdTCA and ND and computation mechanism of energy optimization, only six variants of the complexes were obtained. Thus, in our calculations we investigate the parameters of hydrogen bonds, which are formed between AdTCA and DOX at all possible interaction positions. As a result of numerical simulation, we obtained optimized structures and the IR spectra of the six formed molecular complexes (Figs. 4 and 5) and analyzed the energy of intermolecular hydrogen bonds (H-bonds).

The energy of H-bonds is investigated by analysis of such parameters as length of a hydrogen bridge and the frequency shift. The energy of hydrogen bonds was estimated using empirical Iogansen formula [23]: $-\Delta H = 0.3(\Delta\nu - 40)^{1/2}$, where $\Delta\nu$ – frequency shift of the stretching vibration of O–H bond (ΔH in kcal/mol, $\Delta\nu$ – cm^{-1}).

According to the optimized structures and calculated IR spectra for six cases of molecular compound (Fig. 4 and Fig. 5), it can be noted that in all interaction positions the one H-bond or two H-bonds are formed between AdTCA and DOX.

Two peaks (1 and 2 in Fig. 4a and in Fig. 5c) at 3207 cm^{-1} and at 3376 cm^{-1} for case 1 (Fig. 4a) and for case 6 – at 3187 cm^{-1} and at 3362 cm^{-1} (Fig. 5c) correspond to stretching vibrations of O–H bond in AdTCA, which participates in the H-bond formation with DOX, and in DOX, which participates in the H-bond formation with AdTCA, respectively. In case 2, there are two formed intermolecular H-bonds between AdTCA and DOX which participate in intermolecular H-bond formation, occur at the same frequency of 3350 cm^{-1} (1 and 2 in Fig. 4b).

In interaction positions named as cases 3, 4 and 5 (Fig. 4c and Fig. 5a,b), only one intermolecular H-bond is formed between AdTCA and DOX. Peaks at 3314 cm^{-1} for case 3 (1 in Fig. 4c) and at 3251 cm^{-1} for case 4 (1 in Fig. 5a) corresponds to stretching vibrations of O–H bond in AdTCA, which participates in hydrogen bond formation with DOX. Let's note that peak at 2797 cm^{-1} for case 5 (1 in Fig. 5b) which corresponds to H-bond formation with nitrogen atom in DOX.

We analyze the H-bonds parameters in six cases of AdTCA–DOX molecular complex to estimate the strength of the formed H-bonds. The calculated parameters, whose analysis provides the estimation of a hydrogen bond's influence on the structure and the IR spectrum, are presented in Table 1. In the first column, the case numbers of molecular complex and H-bonds numbers are given; in the second – lengths of O–H bond in them; in the third – lengths of O–H...O and O–H...N hydrogen bridges; in the fourth – frequencies of stretching vibrations of O–H

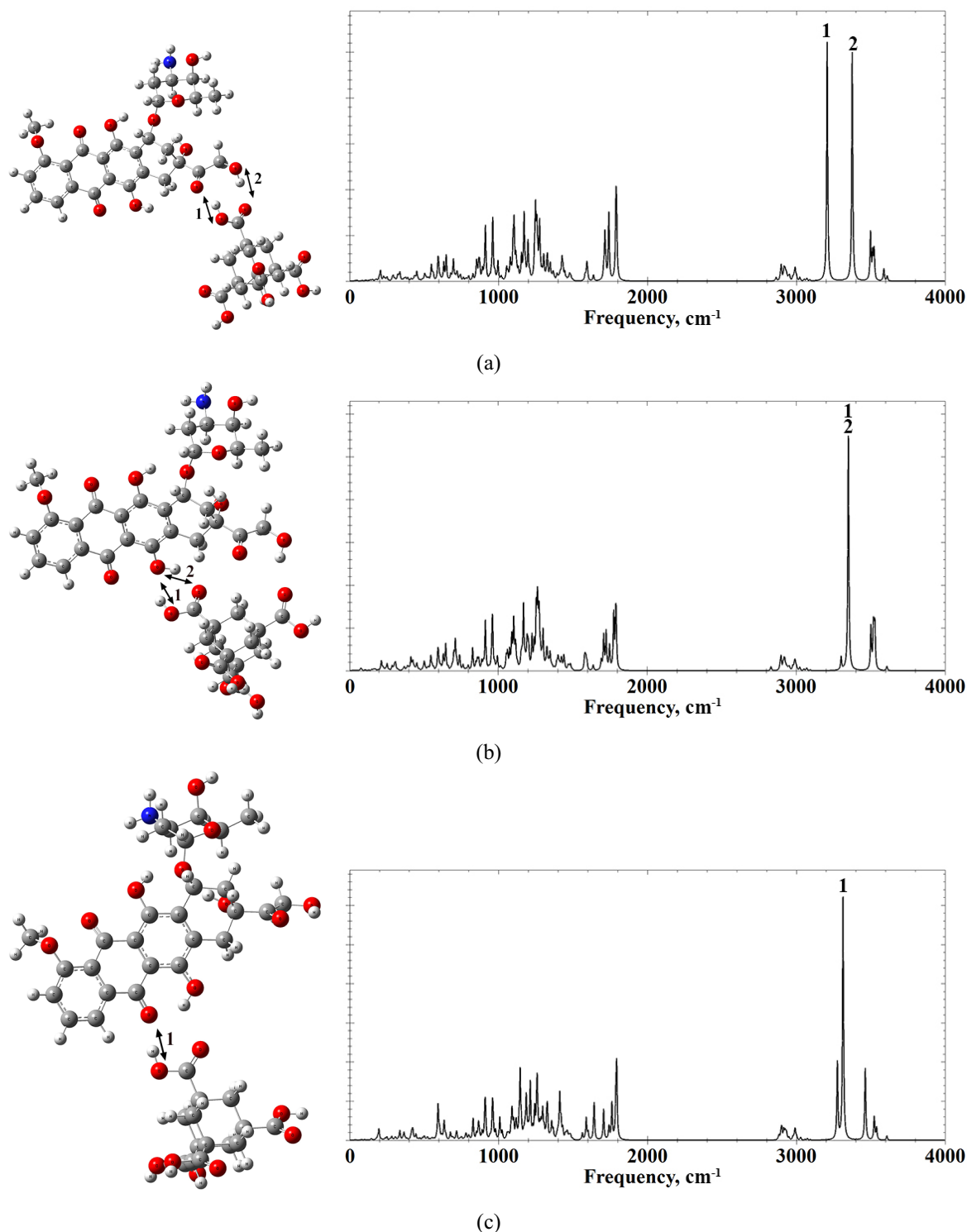


FIG. 4. Structures (left) and calculated IR spectra (right) for three cases of the molecular compound AdTCA and DOX: case 1 (a), case 2 (b), case 3 (c)

bonds; in the fifth – splitting and shifts of these frequencies in complex formation; in the sixth – formation energies of hydrogen bonds.

According to the data, presented in Table 1, it should be noted that the strongest hydrogen bond between AdTCA and DOX is formed with participation of O–H bond in AdTCA and nitrogen atom in DOX (case 5), which is expressed in the big frequency shift on 726 cm^{-1} to the long-wavelength region. The length of the formed

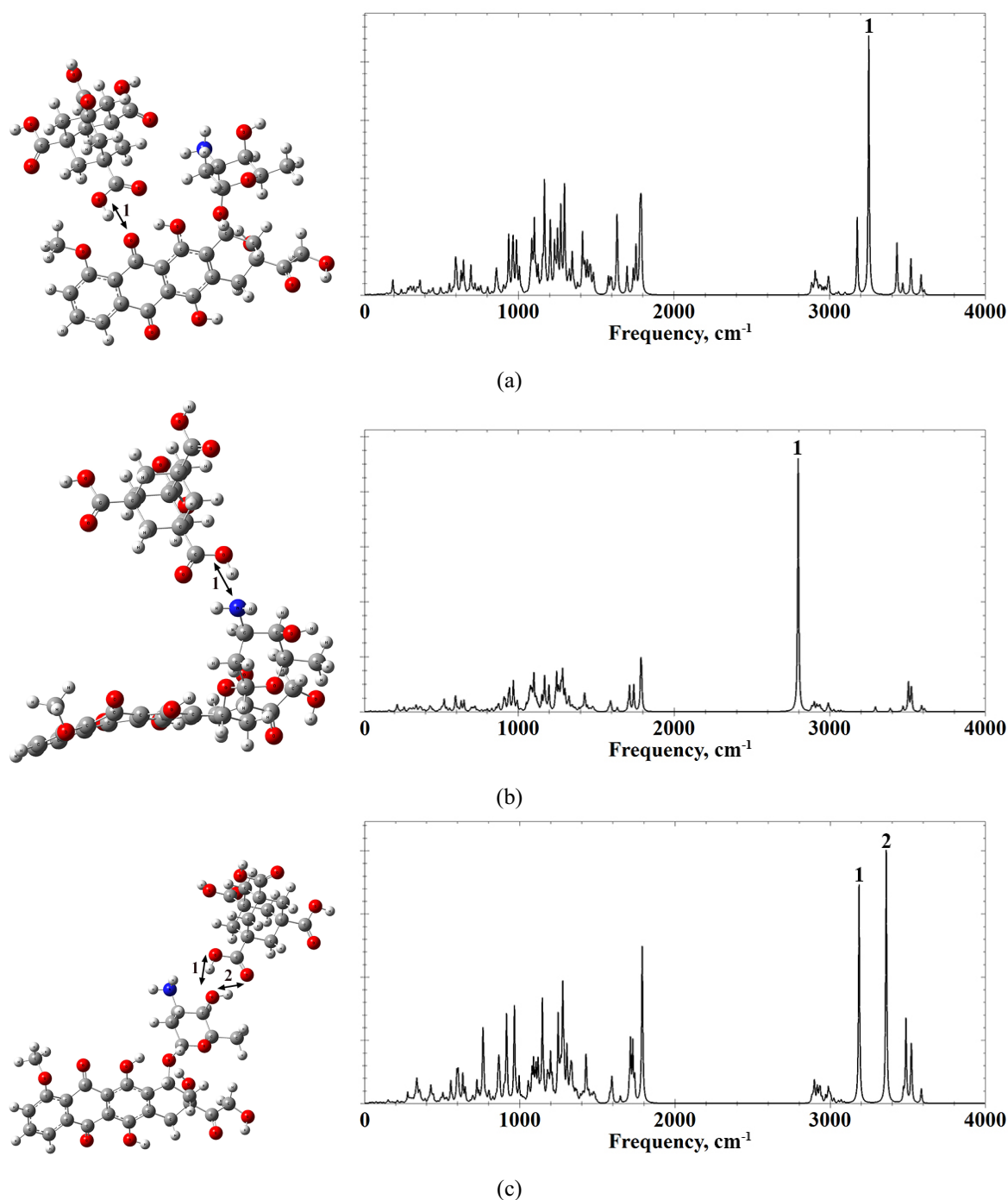


FIG. 5. Structures (left) and calculated IR spectra (right) for three cases of the molecular compound AdTCA and DOX: case 4 (a), case 5 (b), case 6 (c)

hydrogen bridge is 2.76 \AA – the shortest length among all cases of connection AdTCA–DOX. The H-bond energy is 7.857 kcal/mol , which demonstrates the existence of a strong hydrogen bond.

The hydrogen bonds for the majority of AdTCA–DOX molecular complex cases can be characterized as bonds of average force as the frequency shift for them makes size from 173 cm^{-1} in case 2 to 336 cm^{-1} in case 6 and bond energy does not exceed 5 kcal/mol . The second H-bond in case 1 can be characterized as weak bond as the frequency shift for it makes 96 cm^{-1} and the bond energy is 2.245 kcal/mol .

TABLE 1. Calculated H-bonds parameters in six cases of AdTCA–DOX molecular complexes

Case number/ bond number	OH length R_{OH} , Å	Hydrogen bridge length R_{OH-O} , Å	Frequency ν , cm^{-1}	Frequency shift $\Delta\nu$, cm^{-1}	Bond energy $-\Delta H$, kcal/mol
1/1	0.99	2.78	3207	316	4.984
1/2	0.98	2.78	3376	96	2.245
2/1	0.99	2.95	3350	173	3.46
2/2	0.98	2.8	3350	241	4.253
3/1	0.99	2.76	3314	209	3.9
4/1	0.99	2.8	3251	272	4.57
5/1	1.02	2.76 (OH–N)	2797	726	7.857
6/1	0.99	2.82	3187	336	5.161
6/2	0.98	2.86	3362	248	4.327

Thus, it is possible to note that in AdTCA–DOX molecular complex there can be seven H-bonds of average force, one strong and one weak hydrogen bond what proves existence of the rather strong electrostatic interaction between nanodiamond and DOX.

We compare our results with the experimental IR spectrum of the powder of the nanodiamond-doxorubicin complex taken from [9]. For comparison, we created the combined IR spectrum as imposing of calculated IR spectra for six cases of molecular complexes, corresponded to six interaction positions between AdTCA and DOX (Fig. 6).

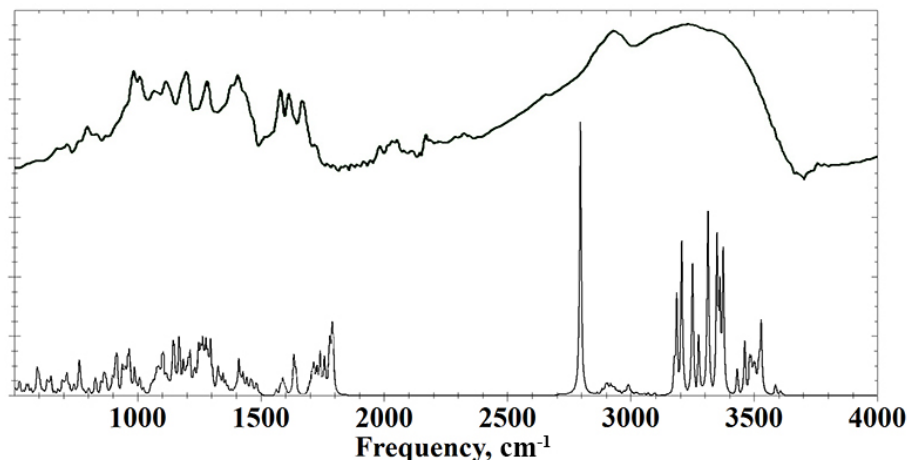


FIG. 6. Experimental IR spectrum of ND–DOX molecular complex (upper) and combined IR spectrum of six variants of AdTCA–DOX molecular complexes (lower)

As can be seen on Fig. 6, there is the good agreement of the characteristic regions in the experimental and combined IR spectra, in particular, the wide area of stretching vibrations of O–H bonds, which participate in the hydrogen bonds formation (3150 to 3600 cm^{-1}) and the peak on 2797 cm^{-1} , corresponded to stretching vibrations of O–H bond in AdTCA, which participates in hydrogen bond formation with nitrogen atom in DOX. Wide boundaries of the region, which corresponds to stretching vibrations of O–H bonds, indicate a large number of formed hydrogen bonds of various configurations in the experimental nanodiamond-doxorubicin complex, including the considered interaction variants.

4. Conclusions

During molecular modeling, it was established that AdTCA–DOX molecular complex can occur due to nine hydrogen bonds formed in six various cases for the molecular compound. One of H-bond is strong and seven

H-bonds are bonds of average force. Since the sizes of NDs, which are used in scientific experiments with DOX, are from 5 nm and higher, and the width of the DOX molecule is about 1.5 nm, it can be assumed that the DOX molecule can be attached to the ND on several points simultaneously. The combined IR spectrum, with imposing of calculated IR spectra for six cases of molecular complexes, corresponded to six interaction positions between AdTCA and DOX and was created for comparison with experimental IR spectra of ND–DOX molecular complex [9]. We can observe a good agreement between the calculated and the experimental IR spectra, especially in the high-frequency area corresponding to stretching vibrations of O–H bonds, which participate in the intermolecular hydrogen bond formation. This indicates a large number of formed hydrogen bonds in the experimental ND–DOX complex and the stability of compound as a result of electrostatic interaction.

The obtained results demonstrate that there can be strong electrostatic interaction between doxorubicin and carboxylated detonation nanodiamonds. The formed hydrogen bonds can be considered as one of main mechanisms for targeted drug delivery and for drug retention in cells and, thus, for enhancement of doxorubicin therapeutic efficacy, as observed in experiment [9].

References

- [1] *Nanotherapeutics: Drug Delivery Concepts in Nanoscience*. Ed. by Lamprecht A. CRC Press, Taylor and Francis Group, Boca Raton, 2008, 292 p.
- [2] Gupta R.B., Kompella U.B. *Nanoparticles Technology for Drug Delivery*. N.-Y. Taylor & Francis Group, 2006, 403 p.
- [3] Popova N.R., Popov A.L., Shcherbakov A.B., Ivanov V.K. Layer-by-layer capsules as smart delivery systems of CeO₂ nanoparticle based theranostic agents. *Nanosystems: physics, chemistry, mathematics*, 2017, **8** (2), P. 282–289.
- [4] Yakovlev R.Y., Solomatin A.S., et al. Detonation diamond – a perspective carrier for drug delivery systems. *Rus. J. Gen. Chem.*, 2014, **84** (2), P. 379–390.
- [5] Ho D., Wang C-H.K., Chow E.K-H. Nanodiamonds: The intersection of nanotechnology, drug development, and personalized medicine. *Science Advances*, 2015, **1** (7), P. 1500439.
- [6] Shenderova O.A., McGuire G.E. Science and engineering of nanodiamond particle surfaces for biological applications (Review). *Biointerphases*, 2015, **10** (3), P. 030802.
- [7] Schrand A.M., Ciftan H.S.A., Shenderova O.A. Nanodiamond particles: properties and perspectives for bioapplications. *Crit. Rev. Solid State Mater. Sci.*, 2009, **34**, P. 18–74.
- [8] Solomatin A.S., Yakovlev R.Yu., et al. Antibacterial activity of Amikacin-immobilized detonation nanodiamond. *Nanosystems: physics, chemistry, mathematics*, 2017, **8** (4), P. 531–534.
- [9] Salaam A.D., Hwang P.T.J., et al. Nanodiamonds enhance therapeutic efficacy of doxorubicin in treating metastatic hormone-refractory prostate cancer. *Nanotechnology*, 2014, **25** (42), P. 425103.
- [10] Zhang X., Hu W., et al. A comparative study of cellular uptake and cytotoxicity of multiwalled carbon nanotubes, graphene oxide, and nanodiamond. *Toxicol. Res.*, 2012, **1**, P. 62–68.
- [11] Shugalei I.V., Voznyakovskii A.P., et al. Biological activity of detonation nanodiamond and prospects in its medical and biological applications. *Russ. J. Gen. Chem.*, 2013, **83** (5), P. 851–883.
- [12] Liu K.K., Zheng W.W., et al. Covalent linkage of nanodiamondpaclitaxel for drug delivery and cancer therapy. *Nanotechnology*, 2010, **21**, P. 1–14.
- [13] Toh T.-B., Lee D.-K., et al. Nanodiamondmitoxantrone complexes enhance drug retention in chemoresistant breast cancer cells. *Mol. Pharmaceutics*, 2014, **11**, P. 2683–2691.
- [14] Plastun I.L., Agandeeva K.E., Bokarev A.N., Zenkin N.S. Diamond-like nanoparticles influence on flavonoids transport: molecular modeling. *Proc. SPIE*, 2017, 103360K.
- [15] Adnan A., Lam R., et al. Atomistic simulation and measurement of pH dependent cancer therapeutic interactions with nanodiamond carrier. *Mol. Pharmaceutics*, 2011, **8**, P. 368–374.
- [16] Petrioli R., Fiaschi A.I., et al. The role of doxorubicin and epirubicin in the treatment of patients with metastatic hormone refractory prostate cancer. *Cancer Treat. Rev.*, 2008, **34**, P. 710–8.
- [17] Saltiel E., McGuire W. Doxorubicin (adriamycin) cardiomyopathy – a critical review. *West J. Med.*, 1983, **139**, P. 332–341.
- [18] Kohn W. Nobel Lecture: Electronic structure of matterwave functions and density functionals. *Reviews of Modern Physics*, 1999, **71** (5), P. 1253–1266.
- [19] Pople J. Nobel Lecture: Quantum chemical models. *Reviews of Modern Physics*, 1999, **71** (5), P. 1267–1274.
- [20] Frisch M.J., Trucks G.W., et al. *Gaussian 09, Revision A.02*. Wallingford CT, Gaussian Inc., 2009.
- [21] Fort R.C.Jr., Schleyers P. von R. Adamantane: Consequences of diamondoid structure. *Chem. Rev.*, 1964, **64** (3) P. 277–300.
- [22] Ermer . Five-fold diamond structure of adamantane-1,3,5,7-tetracarboxylic acid. *Journal of American Chemical Society*, 1988, **110** (12), P. 3747–3754.
- [23] Iogansen A.V. *IR Spectroscopy and Hydrogen Bond Energy Determination*. Hydrogen Bond, Nauka, Moscow, 1981, P. 112–155 (in Russian).

Phase composition and photoluminescence correlations in nanocrystalline $\text{ZrO}_2\text{:Eu}^{3+}$ phosphors synthesized under hydrothermal conditions

A. N. Bugrov^{1,2}, R. Yu. Smyslov^{1,3}, A. Yu. Zavialova^{2,4}, D. A. Kirilenko^{5,6}, D. V. Pankin⁷

¹Institute of macromolecular compounds RAS, Bolshoy pr. 31, 199004, St. Petersburg, Russia

²Saint Petersburg Electrotechnical University “LETI”, ul. Professora Popova 5, 197376, St. Petersburg, Russia

³Petersburg Nuclear Physics Institute, NRC KI, Orlova roscha mcr. 1, 188300, Gatchina, Leningrad region, Russia

⁴Saint Petersburg State Institute of Technology (Technical University),
Moskovsky pr. 26, 190013, St. Petersburg, Russia

⁵Ioffe Institute RAS, Politekhnicheskaya ul. 26, 194021, St. Petersburg, Russia

⁶ITMO University, Kronverskii av. 49, 197101, St. Petersburg, Russia

⁷Research park SPbU, Ulianovskaya 5, 198504, St. Petersburg, Russia

alexander.n.bugrov@gmail.com

PACS 78.67. n; 78.67.Bf

DOI 10.17586/2220-8054-2018-9-3-378-388

Luminescent zirconia nanoparticles with europium ion content 1 and 10 mol.% were synthesized under hydrothermal conditions. Annealing of ZrO_2 : 1 mol. Eu^{3+} nanoparticles made it possible to obtain a sample with a high monoclinic phase content up to 92 %. An increase in the concentration of Eu^{3+} ions introduced into the zirconia crystal lattice has made it possible to almost completely convert its monoclinic and tetragonal phases into cubic modification. The phase composition of the synthesized samples was determined by powder X-ray diffraction, electron microdiffraction, and Raman spectroscopy. Analysis of the crystallographic data and the luminescent spectra helped to reveal correlations between the $\text{ZrO}_2\text{:Eu}^{3+}$ nanoporphor structure and the energy redistribution of Eu^{3+} optical transitions at 614 – 626 nm and 606 – 633 nm wavelengths. In addition, a relationship was established between the phase composition of nanoparticles based on zirconia and the luminescence lifetime of Eu^{3+} ions.

Keywords: hydrothermal synthesis, solid solutions, zirconia, europium, phase transitions, nanoparticles, photoluminescence, fluorescence lifetime.

Received: 4 April 2018

Revised: 14 April 2018

1. Introduction

Zirconia and its solid solutions have some non-trivial physico-chemical properties. It is worth mentioning mechanical strength [1,2], hardness [3,4], wear and crack resistance [5,6], high thermal expansion [7], low thermal conductivity [8], and photocatalytic activity [9]. Zirconia transparency is in a broad spectral range from mid-wavelength IR ($\lambda < 8 \mu\text{m}$) to near UV ($\lambda > 300 \text{ nm}$) [10]. Chemical and photochemical stability [11,12], along with a high refractive index [13], low phonon energy [14] and large band gap [15] make zirconia an ideal matrix for obtaining highly effective luminescent materials [16].

Zirconia is found in the form of three main polymorphic modifications. A thermodynamically stable monoclinic modification of zirconia ($m\text{-ZrO}_2$) occurs naturally in the form of baddeleyite minerals. Monoclinic (α) zirconia P21/c [17] exists at room temperature and up to 1170 °C; above this temperature, its transition into a denser tetragonal (β) form occurs. The tetragonal phase P42/nmc [18] is stable in the temperature range 1170 – 2370 °C, whose upper limit determines the formation of the cubic (γ) modification of ZrO_2 belonging to the structural type of fluorite Fm3m [19].

The highest performance indicators have metastable high-temperature modifications of ZrO_2 (cubic and tetragonal), which are stabilized by the introduction of Mg, Ca, Sc and rare earth elements (REE) ions. Substitutional solid solutions based on zirconia are obtained by introducing the trivalent ions of II and III groups in the periodic system or REE ions (in particular lanthanides) into the ZrO_2 crystal lattice [20–23].

Oxygen vacancies play a significant role in the formation of the tetragonal and cubic phases of zirconia. Phase stabilization using only oxygen vacancies was confirmed by theoretical calculations [24]. In addition to phase stabilization, oxygen vacancies also strongly affect the luminescence intensity of the Ln^{3+} ions and the Stark splitting of the spectral terms [25,26]. The change in the luminescence intensity and the phase transition from ZrO_2 equilibrium modification to metastable tetragonal and even cubic occurs with an increase of the lanthanide content in its crystal lattice. For stabilizing the tetragonal phase, it is usually necessary to add up to 6 mol.% of the

trivalent ions, whereas the required concentration to achieve the cubic phase is 10 – 12 mol.% [27]. The tetragonal with or separately from the monoclinic phase of ZrO_2 are formed depending on the synthesis method at a low concentration of Ln^{3+} ions. High annealing temperatures lead to the formation of large grains, thereby reducing the effect of surface defects on nonradiative recombination of excitations. Both defects (volume and surface defects) and structure have a significant effect on the intensity of luminescence [28].

Lanthanide ions are widely used as local probes to identify the crystalline structure of materials. The trivalent europium ion is well known as a red-emitting activator due to its $^5\text{D}_0\text{--}^7\text{F}_j$ ($j = 0, 1, 2, 3, 4$). These transitions are very sensitive to structural changes and depend on the local symmetry of the crystal field around the Eu^{3+} ions in different oxide matrix [29]. Europium is preferable as a luminescent structural probe for determining the number, location, and symmetry of the metal ions in the compound, as well as the population of their levels because of its non-degenerate emission state $^5\text{D}_0$. Other lanthanide ions have transitions, which are usually a mixture of magnetic (MDT, $^5\text{D}_0\text{--}^7\text{F}_1$) and dielectric (EDT, $^5\text{D}_0\text{--}^7\text{F}_2$) dipole transitions, and the symmetry effects in them are less pronounced [30].

Today in the literature there are several papers on the luminescence of zirconia nanoparticles doped with europium ions [31–35]. They provide information on changes in the splitting of EDT and MDT for Eu^{3+} ions in various crystal structures of ZrO_2 . Moreover, the researchers consider aspects of the crystal structure effect of zirconia on the luminescence lifetime of Eu^{3+} ions in order to increase the productivity of optical devices based on them. It is critical from a fundamental point of view to identify correlations between the zirconia crystalline structure and the europium luminescence properties in the $\text{ZrO}_2:\text{Eu}^{3+}$ nanoparticles, and also the nature of their changes as a function of temperature and dopant concentration. Also, the combination of the physico-chemical properties of ZrO_2 matrix acting as an oscillator with the europium optical characteristics gives a considerable potential in the field of photonic applications, such as solid-state lasers, sensors, optical amplifiers, scintillators, phosphors and lamps [36].

In this regard, this work aimed to obtain $\text{ZrO}_2:\text{Eu}^{3+}$ nanoparticles under hydrothermal conditions and to vary their phase composition due to annealing at high temperature, as well as changing the lanthanide concentration in the zirconia lattice with subsequent analysis of the structure influence on the europium luminescent properties.

2. Experimental methods

The compositions with 1 and 10 mol.% of europium ions which make it possible to obtain zirconia mainly in tetragonal and cubic polymorphous modifications were selected for the synthesis of luminescent nanoparticles according to the $\text{ZrO}_2\text{--Eu}_2\text{O}_3$ phase diagram [37]. $\text{ZrO}_2:\text{Eu}^{3+}$ nanoparticles were synthesized by coprecipitation of zirconium and europium hydroxides from 0.5 M chloride solutions, followed by dehydration of the resulting mixtures under hydrothermal conditions. Coprecipitation of hydroxides was performed using NH_4OH solution (25 %) at room temperature and continuous mechanical stirring to pH = 8. The resulting white precipitates were washed with distilled water until a negative reaction to chloride ions and neutral pH, using the decantation method. Then, the $\text{ZrO}(\text{OH})_2\text{--Eu}(\text{OH})_3$ compositions were dried in air at 100 °C. Hydrothermal treatment of coprecipitated hydroxides was performed in steel autoclaves according to the procedure given in [38].

Wide angle X-ray diffraction analysis of synthesized nanoparticles and annealed samples were obtained at scattering angles varying from 10 ° to 100 ° with 0.02 ° step using a Rigaku SmartLab diffractometer (Tokyo, Japan). $\text{Cu-K}\alpha$ radiation (40 kV, 40 mA) was used. The identification of ZrO_2 crystalline phases was performed in Crystallographica Search-Match software by comparing our experimental data with powder diffraction files from the ICDD (International Centre for Diffraction Data) database. The crystallite size was estimated from the broadening of X-ray diffraction (XRD) lines of the $\text{ZrO}_2:\text{Eu}^{3+}$ nanopowders in the PD-Win 4.0 program complex using the Scherrer formula. The ReX software [39] with the Crystallography Open Database (COD) was used for quantitative X-ray phase analysis and calculation of lattice parameters from WAXD data.

The size, shape and phase composition of the $\text{ZrO}_2:\text{Eu}^{3+}$ nanoparticles were determined using a transmission electron microscope JEM-2100F (JEOL microscope, Tokyo, Japan) at an acceleration voltage of 90 kV. Bright-field images and electron diffraction patterns were obtained. Sample preparation included dispersing of $\text{ZrO}_2:\text{Eu}^{3+}$ nanoparticles in ethanol by ultrasonic bath and subsequent dipping of the graphene foil grids in the resulting slurry.

Raman measurements were performed using LabRAM HR800 (Horiba Jobin Yvon, Japan) with 1800 gr/mm diffraction grade in backscattering geometry. Raman spectra were recorded with excitation by a 488 nm of Ar^+ laser. Before measurement, the spectrometer was calibrated using 520.7 cm^{-1} line of silicon standard.

The elemental composition of nanoparticles was controlled by the microanalysis system INCA (Oxford Instruments, UK) using a Zeiss SUPRA 55VP field-emission from Carl Zeiss AG (Germany).

The emission spectra and the luminescence lifetime of $\text{ZrO}_2:\text{Eu}^{3+}$ nanoparticles were recorded with a spectrophotometer LS-100 BASE (PTI Lasers INC, Canada). The geometric width of the output slit of the excitation

monochromator was 1.25 mm, and that of the entrance slit of the fluorescence monochromator was 0.5 mm. The wavelength interval for the emission spectra of nanophosphors was set at 560 – 770 nm, and photoluminescence was excited in the range of 205 – 315 nm. The xenon lamp in the pulsed mode was used as a source of excitation. The integration window of the signal was 100 – 2000 μ s.

The luminescence lifetimes for nanophosphors containing Eu^{3+} were determined from the emission intensity decay using pulse xenon lamp mode. The luminescence was excited at 247 nm, and it was observed at 606 and 614 nm. The values of lifetimes were calculated with an iterative fitting procedure using QtiPlot software [40]. The reliability of coincidence of the experimental signal with that calculated was monitored by the statistical parameter χ_2 , which characterizes the extent to which the experimental data coincide with the theoretical model.

3. Results and discussion

A mixture of coprecipitated zirconium and europium hydroxides prepared for the synthesis of ZrO_2 :1 mol.% Eu^{3+} nanoparticles is amorphous according to XRD data. Its hydrothermal treatment over 4 hours at 250 °C and 15 MPa led to the formation of ZrO_2 : Eu^{3+} nanocrystals with an average size of 15 ± 3 nm consisting of monoclinic and tetragonal polymorphous modifications in the 22:78 ratio (Fig. 1(a)). ZrO_2 :1 mol.% Eu^{3+} nanoparticles were annealed in air at 1200 °C for 2 hours and slowly cooled to room temperature together with the furnace in order to increase the monoclinic phase content. During the heating process at the temperature of the equilibrium phase transition ($T = 1170$ °C), the existing monoclinic zirconia ($m\text{-ZrO}_2$) transforms into a tetragonal polymorphic modification. Since this phase transition is reversible, zirconia is transformed into an equilibrium modification $m\text{-ZrO}_2$ with slow cooling. The quantitative X-ray phase analysis performed in the ReX program using the cards of the diffraction standards for monoclinic [41] and tetragonal [42] zirconia showed that phase ratio is 92:8 after annealing of ZrO_2 :1 mol.% Eu^{3+} nanoparticles (Fig. 1(b)). The Eu^{3+} ions introduced into the crystal lattice of zirconia nanoparticles stabilize the metastable tetragonal phase ($t\text{-ZrO}_2$) and do not entirely transfer it to equilibrium upon cooling. The average crystallite size calculated from the broadening of the X-ray diffraction maxima for both the monoclinic and tetragonal phases after annealing was 29 ± 5 nm. Eu^{3+} ions in an amount of 10 mol.% were introduced into the zirconia crystalline structure to stabilize its cubic phase ($c\text{-ZrO}_2$) and reduce the monoclinic content to a minimum. In this case, the ZrO_2 :10 mol.% Eu^{3+} nanoparticles consisted of 98 % of the zirconia cubic phase, and the remaining 2 vol.% corresponded to its monoclinic polymorphic modification (Fig. 1(c)). $c\text{-ZrO}_2$ [43] and $m\text{-ZrO}_2$ cards [41] from the COD database were used to calculate the phase composition of nanoparticles. The size of the coherent scattering regions for ZrO_2 :10 mol.% Eu^{3+} nanoparticles, calculated from the Scherrer equation, was 12 ± 2 nm. The portions of m -, t -, and $c\text{-ZrO}_2$ phases, calculated using intensities of Raman shifts, are correlated with those obtained with Rietveld refinement (Table 1). The parameters of the unit cell for the monoclinic, tetragonal, and cubic phases refined by the Rietveld method from X-ray diffractograms of ZrO_2 : Eu^{3+} nanoparticles (Table 1) are comparable with the literature data [44].

TABLE 1. Structural parameters of ZrO_2 : Eu^{3+} nanoparticles

Sample	Phase composition	Unit cell parameters	$\frac{I_{m/(t,c)}}{I_m + I_{t,c}}$ ¹⁾
ZrO_2 :1 mol.% Eu^{3+}	22 vol.% $m\text{-ZrO}_2$	–	0.209
	78 vol.% $t\text{-ZrO}_2$	$a = 3.6102$; $b = 3.6102$; $c = 5.1847$ $\alpha = 90^\circ$; $\beta = 90^\circ$; $\gamma = 90^\circ$	0.791
ZrO_2 :1 mol.% Eu^{3+} (annealing 1200 °C)	92 vol.% $m\text{-ZrO}_2$	$a = 5.1575$; $b = 5.2055$; $c = 5.3115$ $\alpha = 90^\circ$; $\beta = 99.03^\circ$; $\gamma = 90^\circ$	0.867
	8 vol.% $t\text{-ZrO}_2$	$a = 3.6003$; $b = 3.6003$; $c = 5.1787$ $\alpha = 90^\circ$; $\beta = 90^\circ$; $\gamma = 90^\circ$	0.133
ZrO_2 :10 mol.% Eu^{3+}	2 vol.% $m\text{-ZrO}_2$	–	0.114
	98 vol.% $c\text{-ZrO}_2$	$a = 5.1548$; $b = 5.1548$; $c = 5.1548$ $\alpha = 90^\circ$; $\beta = 90^\circ$; $\gamma = 90^\circ$	–

Note: ¹⁾Portions of m -, t -, and $c\text{-ZrO}_2$ phases were calculated using intensities of Raman shifts I_m , at 177.7 cm^{-1} and $I_{t,c}$ at 146 cm^{-1} in Fig. 4.

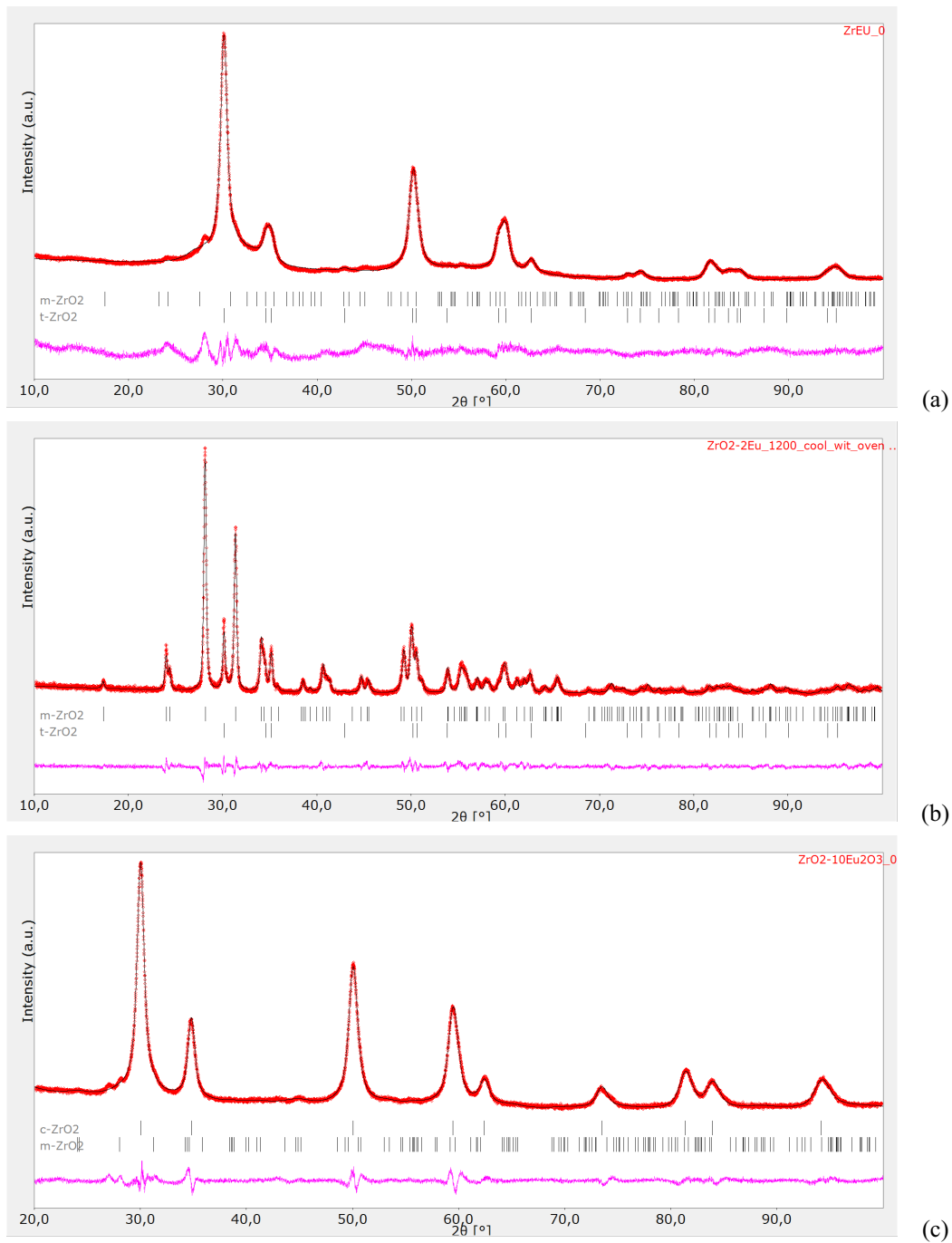


FIG. 1. Line profile analysis in the Rietveld method of powder X-ray diffractograms for nanoparticles: a – $\text{ZrO}_2: 1 \text{ mol.}\% \text{Eu}^{3+}$; b – $\text{ZrO}_2: 1 \text{ mol.}\% \text{Eu}^{3+}$ annealed at $1200 \text{ }^\circ\text{C}$; c – $\text{ZrO}_2: 10 \text{ mol.}\% \text{Eu}^{3+}$

The diameter of the $\text{ZrO}_2:1 \text{ mol.}\% \text{Eu}^{3+}$ nanoparticles from the TEM micrographs (Fig. 2(1a)) correlates with the average crystallite size calculated from the X-ray diffractogram (Fig. 1a). Annealing the sample at $1200 \text{ }^\circ\text{C}$ leads to the fusion of nanocrystals to submicron dimensions (Fig. 2(1b)). In the case of zirconia stabilized with 10 mol.% europium ions, microphotographs contain both spherical particles 10 nm in diameter and cubical with an average size of 13 nm (Fig. 2(1c)). According to electron microdiffraction data, the $\text{ZrO}_2:1 \text{ mol.}\% \text{Eu}^{3+}$ nanoparticles in native form and after thermal treatment contain the monoclinic and tetragonal phases (Fig. 2(2a,2b)), and with the increase in the concentration of europium ions only the fluorite-like structure stabilizes (Fig. 2(2c)).

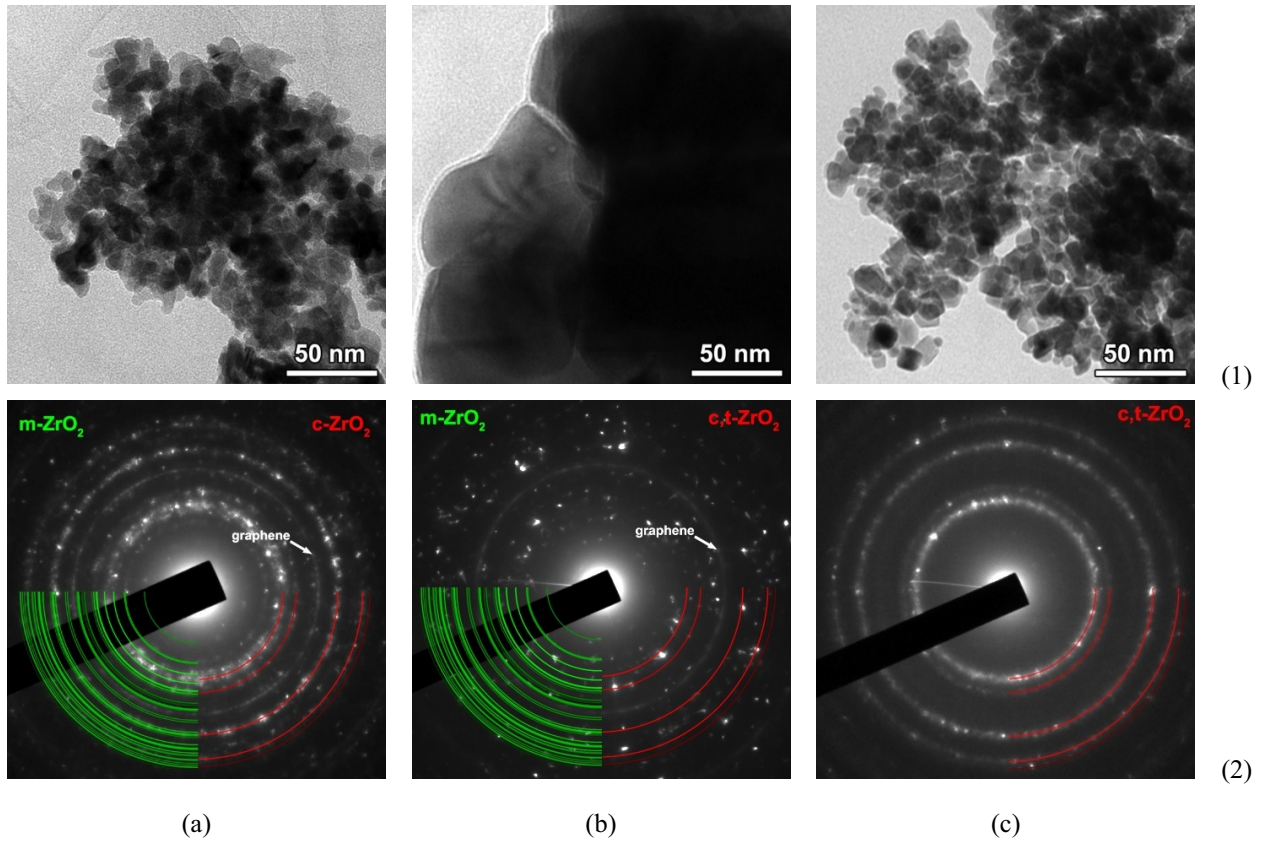


FIG. 2. TEM micrographs (1) and electronic diffraction patterns (2) of nanoparticles: a – $\text{ZrO}_2:1 \text{ mol.}\% \text{Eu}^{3+}$; b – $\text{ZrO}_2:1 \text{ mol.}\% \text{Eu}^{3+}$ annealed at $1200 \text{ }^\circ\text{C}$; c – $\text{ZrO}_2:10 \text{ mol.}\% \text{Eu}^{3+}$

The data of the Energy Dispersive X-ray Spectrometry (EDS) analysis, shown in Fig. 3 and Table 2, confirm the compliance of europium content (mol.%) in ZrO_2 -based nanophosphors to the values determined by synthesis.

TABLE 2. EDS analysis of $\text{ZrO}_2:\text{Eu}^{3+}$ nanoparticles

Sample	Zr	Eu	O
	wt. %		
$\text{ZrO}_2:1 \text{ mol.}\% \text{Eu}^{3+}$	67.2 ± 0.9	1.6 ± 0.5	31.2 ± 0.8
$\text{ZrO}_2:10 \text{ mol.}\% \text{Eu}^{3+}$	61.9 ± 0.9	12.1 ± 0.5	26 ± 0.8

The differences between *t*-, *c*- ZrO_2 and *m*- ZrO_2 phases are reflected in the normalized Raman spectra (Fig. 4). For the nanoparticles with 1 mol% Eu^{3+} subjected to subsequent annealing at $1200 \text{ }^\circ\text{C}$, the Raman shifts indicate that the sample preferably consists of the *m*- ZrO_2 phase (curve 1). The strong peaks are at 183 , 335 , and 474 cm^{-1} [45,46]. Besides, the small number of bands observed for the sample with 1 mol.% Eu^{3+} allows identifying the *t*- ZrO_2 phase considerably easily with the peaks shown at 149 , 224 , 292 , 324 , 407 , 456 , and 636 cm^{-1} (curve 2) [47]. In the Raman spectra of $\text{ZrO}_2:10 \text{ mol.}\% \text{Eu}^{3+}$ nanoparticles, there are mainly hard-to-separate bands of the high-temperature metastable *c*-zirconia phases with a narrow band at 145 cm^{-1} and broad bands $230 - 290 \text{ cm}^{-1}$, $400 - 430 \text{ cm}^{-1}$, $530 - 670 \text{ cm}^{-1}$ and a shoulder at 301 cm^{-1} (curve 3) [48]. Some peaks of the monoclinic modification are likely to appear at this. The phase ratio in the samples of $\text{ZrO}_2:\text{Eu}^{3+}$ nanoparticles, calculated from the Raman spectra, correlates with the XRD data refined by the Rietveld method (Table 1).

Figure 5 shows the photoluminescence spectra of nanophosphors containing Eu^{3+} ions in the ZrO_2 matrix for the three cases studied. The emission band represents a quasilinear spectrum and consists of characteristic

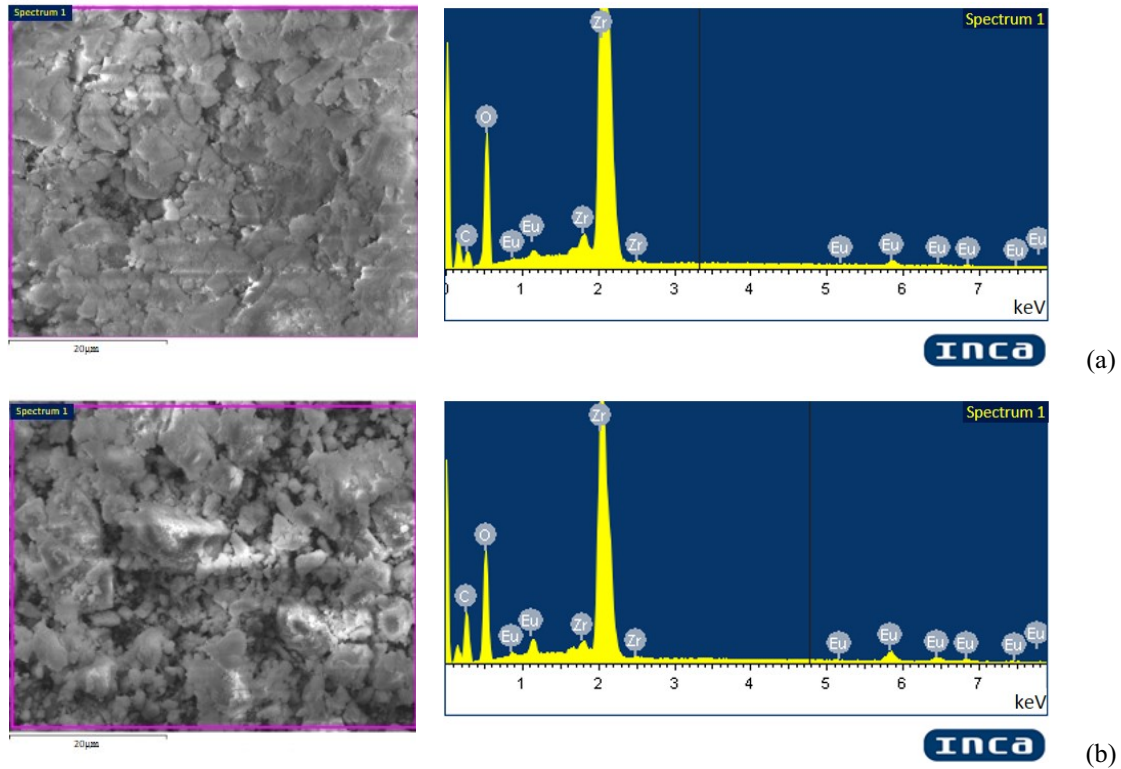


FIG. 3. SEM selected area image and EDS spectrum of ZrO_2 nanoparticles with 1 mol.% (a) and 10 mol.% Eu^{3+} (b)

luminescence peaks corresponding to optical transitions between the spectral terms of the ion Eu^{3+} : ${}^5D_0 \rightarrow {}^7F_J$ ($0 \leq J \leq 6$) 581, 592, 614, 655 and 712 nm [49]. The optical transition of ${}^5D_0 \rightarrow {}^7F_2$ splits into 4 peaks in a zirconia crystal field with maxima at 606, 614, 625, 633 nm and different contributions, depending on the ratio of ZrO_2 polymorphous modifications. The more significant is a less symmetrical m -phase as compared with t - or c - ZrO_2 phases, the higher is the contribution of the peak at 614 nm compared to the peak at 606 nm (compare curve 1 with curves 2 and 3). In the optical transition ${}^5D_0 \rightarrow {}^7F_4$, it is also seen that the higher symmetry of the prevailing phase is, the stronger the Stark effect is, i.e., this peak is more shifted into the long-wavelength region. So, the maximum for the m -phase is at 712 nm, for t - or c - ZrO_2 it is already at 715.3 nm.

Figure 6 shows the luminescence intensity decays $I_{lum}(t)$ of Eu^{3+} in the ZrO_2 matrix. The table includes the calculated parameters of the curves using the stretched exponential function first used by A. Werner in 1907 to describe the complex luminescence decay, and then by Theodor Förster in 1949 to describe the fluorescence decay of electron energy donors [50–52]:

$$I_{lum}(t) = I_{lum}(0) \exp \left[- \left(\frac{t - t_0}{\tau_{PL}} \right)^\beta \right], \quad (1)$$

where t is decay time; $I_{lum}(0)$ is the luminescence intensity at $t = 0$; τ_{PL} is the photoluminescence lifetime; t_0 is the time shift in the observation channels; β is the width of luminescence lifetime spectrum in the excited states ($0 \leq \beta \leq 1$).

Analysis of the luminescence decay data for the three studied systems showed (Table 3) that the more homogeneous system regarding the polymorphic modification content (m -phase of ZrO_2) is, the narrower lifetime spectrum range of the excited state, characterized by the value $D_f = 2 - \beta$, we observe [52–54]. The less symmetrical m -phase has the shortest luminescence lifetime – 0.57 ms, versus 2.39 ms for the t - ZrO_2 . The decrease in the luminescence lifetime for nanoparticles with a stabilized cubic phase of zirconia (10 mol% Eu^{3+}), in comparison with the $ZrO_2:1$ mol.% Eu^{3+} sample which contains a mixture of m/t -phases may indicate the occurrence of concentration quenching at a high europium concentration.

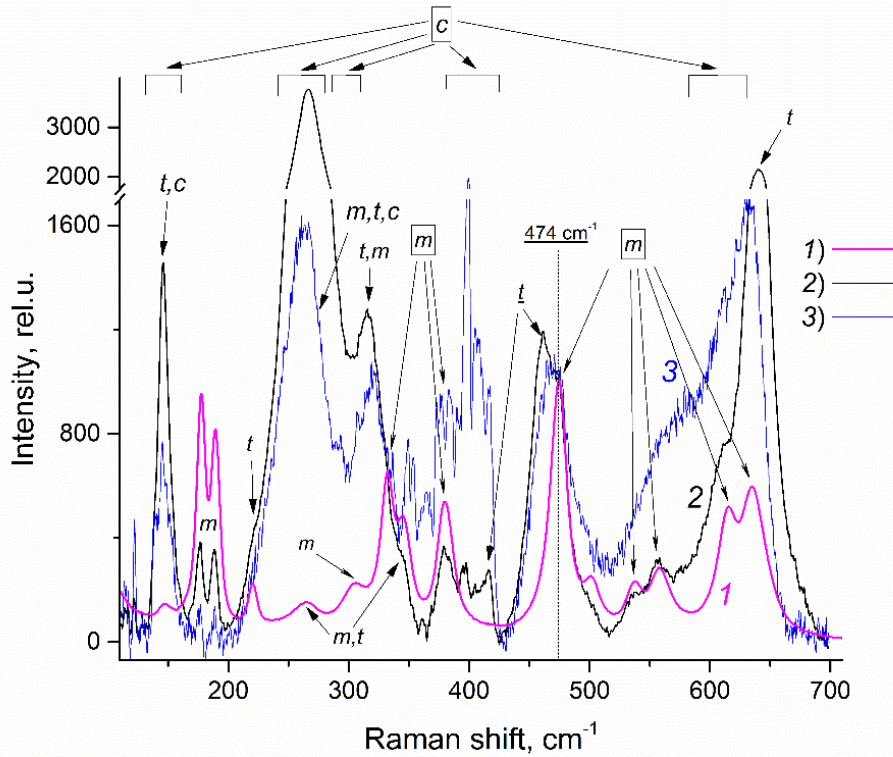


FIG. 4. Normalized Raman spectra of nanoparticles: 1 – ZrO_2 :1 mol.% Eu^{3+} annealed at 1200 °C; 2 – ZrO_2 :1 mol.% Eu^{3+} ; 3 – ZrO_2 :10 mol.% Eu^{3+} . Spectra were normalized at 474 cm^{-1}

TABLE 3. Analysis of the luminescence decay for ZrO_2 : Eu^{3+} nanoparticles

No.	Sample	Phase composition, mol.%			τ_{PL} , ms	β	$D_f = 2 - \beta$	$I_{lum}(0)$	χ_{red}^2
		<i>m</i>	<i>t</i>	<i>c</i>					
1	ZrO_2 :1 mol.% Eu^{3+} (annealing 1200 °C)	92	8	–	0.57 ± 0.02	0.898(12)	1.102	318.0 ± 35.2	2.08
2	ZrO_2 :1 mol.% Eu^{3+}	22	78	–	2.39 ± 0.03	0.872(7)	1.128	188.6 ± 1.7	1.84
3	ZrO_2 :10 mol.% Eu^{3+}	2	–	98	1.18 ± 0.01	0.749(5)	1.251	187.1 ± 1.1	1.28

Note: the luminescence decay was observed at 606 nm for ZrO_2 nanoparticles with 1 and 10 mol.% Eu^{3+} and at 614 nm for the annealed sample using the excitation wavelength of 247 nm.

4. Conclusions

The ZrO_2 :1 mol.% Eu^{3+} nanophosphors represented by a mixture of monoclinic and tetragonal phases with a set of interconfiguration $4f^{n-1}5d-4f^n$ optical transitions in the red region of the emission spectrum, and quasilinear bands distinctive for europium ions were obtained under hydrothermal conditions. Samples, where europium ions were predominantly in the crystal lattice of either the metastable or the equilibrium zirconia phase, were obtained by increasing the concentration of the stabilizer ions to 10 mol.% and annealing the synthesized nanoparticles at a temperature of 1200 °C. It was shown that the luminescent properties of Eu^{3+} ions in the zirconia crystal lattice are very sensitive to the phase composition of the nanoparticles. The Stark splitting of the dielectric (${}^5D_0 \rightarrow {}^7F_1$) and magnetic (${}^5D_0 \rightarrow {}^7F_1$) dipole transitions of Eu^{3+} ions with maxima at 590 and 606 nm is observed for ZrO_2 cubic phase with a more symmetric structure. The contribution of the peaks at 596 and 614 nm significantly

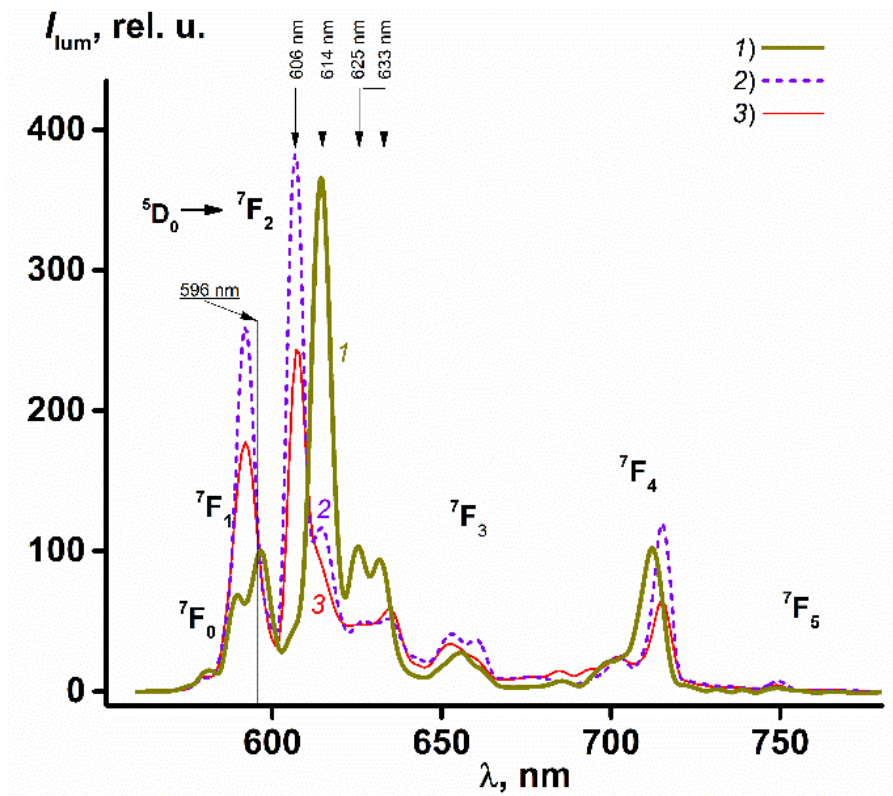


FIG. 5. Normalized luminescence spectra of nanoparticles: 1 – $\text{ZrO}_2:1 \text{ mol.}\% \text{Eu}^{3+}$ annealed at $1200 \text{ }^\circ\text{C}$; 2 – $\text{ZrO}_2:1 \text{ mol.}\% \text{Eu}^{3+}$; 3 – $\text{ZrO}_2:10 \text{ mol.}\% \text{Eu}^{3+}$. Excitation is at 247 nm . Photoluminescence spectra are normalized at 596 nm

increases in the case of a sample in which the zirconia monoclinic modification predominates. The luminescence lifetime of Eu^{3+} ions also correlates with the symmetry of the crystal field, a more extended 2.39 ms refers to $t\text{-ZrO}_2$, and a short 0.57 ms is characteristic of the monoclinic phase. Thus, Eu^{3+} ions, given their sensitivity to the environment, can be used as a structural probe, and the method of luminescence spectroscopy serves to identify the phase composition of the oscillator matrix.

Acknowledgements

Dr. A.N. Bugrov thanks the Russian Foundation for Basic Research (grant number 16-33-60227) for financial support. The work was performed with the use of the equipment of the Joint Research Center “Material science and characterization in advanced technology” (Ioffe Institute, St. Petersburg, Russia). The experimental work was facilitated by the Engineering Center equipment of the St. Petersburg State Technological Institute (Technical University). The Raman spectrum measurements were performed at the Center for Optical and Laser Materials Research, St. Petersburg State University.

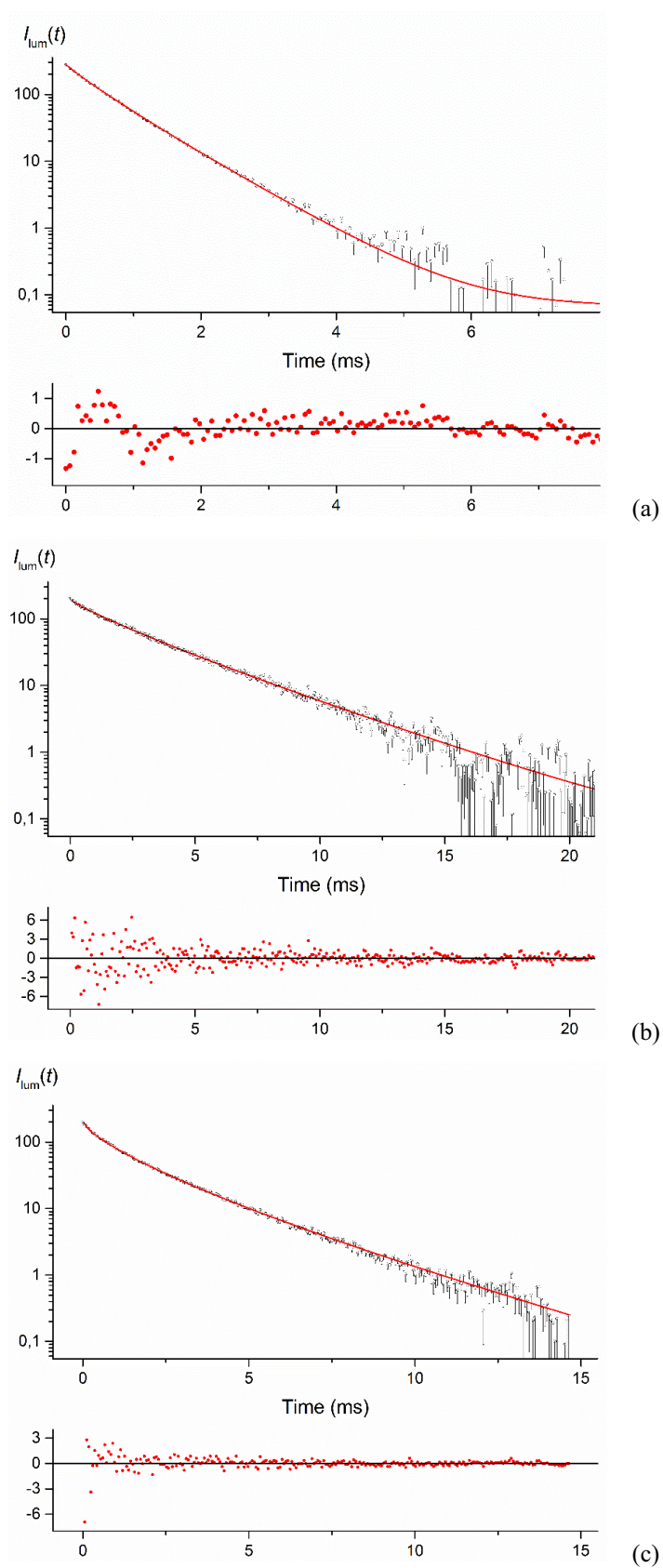


FIG. 6. Luminescence intensity decay of europium ions for nanoparticles: a – ZrO_2 :1 mol.% Eu^{3+} annealed at 1200 °C; b – ZrO_2 :1 mol.% Eu^{3+} ; c – ZrO_2 :10 mol.% Eu^{3+}

References

- [1] Eichler J., Eisele U., Rodel J. Mechanical properties of monoclinic zirconia. *J. Am. Ceram. Soc.*, 2004, **87** (7), P. 1401–1403.
- [2] Aktasa B., Tekelib S., Salman S. Improvements in microstructural and mechanical properties of ZrO_2 ceramics after addition of BaO. *Ceramics International*, 2016, **42**, P. 3849–3854.
- [3] Borik M.A., Bublik V.T., Vilkova M.Yu., et al. Structure, phase composition and mechanical properties of ZrO_2 partially stabilized with Y_2O_3 . *Modern Electronic Materials*, 2015, **1** (1), P. 26–31.
- [4] Lyapunova E.A., Uvarov S.V., Grigoriev M.V., et al. Modification of the mechanical properties of zirconium dioxide ceramics by means of multiwalled carbon nanotubes. *Nanosystems: physics, chemistry and mathematics*, 2016, **7** (1), P. 198–203.
- [5] Ramachandra M., Abhishek A., Siddeshwar P., Bharathi V. Hardness and wear resistance of ZrO_2 nanoparticle reinforced Al nanocomposites produced by powder metallurgy. *Procedia Materials Science*, 2015, **10**, P. 212–219.
- [6] Grathwohl G., Liu T. Crack resistance and fatigue of transforming ceramics: II, CeOs-stabilized tetragonal ZrO_2 . *J. Am. Ceram. Soc.*, 1991, **74** (12), P. 3028–3034.
- [7] Hayashi H., Saitou T., Maruyama N., et al. Thermal expansion coefficient of yttria-stabilized zirconia for various yttria contents. *Solid State Ionics*, 2005, **176** (5–6), P. 613–619.
- [8] Leclercq B., Mevrel N., Liedtke V., Hohenauer W. Thermal conductivity of zirconia-based ceramics for thermal barrier coating. *Hohenauer Mat.-wiss. u. Werkstofftech*, 2003, **34**, P. 406–409.
- [9] Bugrov A.N., Rodionov I.A., Smyslov R.Yu., et al. Photocatalytic activity and luminescent properties of Y, Eu, Tb, Sm and Er-doped ZrO_2 nanoparticles obtained by hydrothermal method. *Int. J. Nanotechnology*, 2016, **13** (1/2/3), P. 147–157.
- [10] Klimke J., Trunc M., Krell A. Transparent tetragonal yttria-stabilized zirconia ceramics: influence of scattering caused by birefringence. *J. Am. Ceram. Soc.*, 2011, **94** (6), P. 1850–1858.
- [11] Shojai F., Mantyla T.A. Chemical stability of yttria-doped zirconia membranes in acid and basic aqueous solutions: chemical properties, effect of annealing and aging time. *Ceramics International*, 2001, **27** (3), P. 299–307.
- [12] Reisfeld R., Zelner M., Patra A. Fluorescence study of zirconia films doped by Eu, Tb and Sm and their comparison with silica films. *Journal of Alloys and Compounds*, 2000, **300–301**, P. 147–151.
- [13] Jerman M., Qiao Z., Mergel D. Refractive index of thin films of SiO_2 , ZrO_2 , and HfO_2 as a function of the films mass density. *Applied Optics*, 2005, **44** (15), P. 3006–3012.
- [14] Soares M.R.N., Nico C., Peres M., et al. Structural and optical properties of europium doped zirconia single crystals fibers grown by laser floating zone. *Journal of Applied Physics*, 2011, **109** (1), P. 013516.
- [15] Sinhamahapatra A., Jeon J.-P., Kang J., et al. Oxygen-deficient zirconia (ZrO_{2-x}): A new material for solar light absorption. *Sci. Rep.*, 2016, **6**, P. 27218.
- [16] Chen X., Liu Y., Tu D. *Lanthanide-doped luminescent nanomaterials: from fundamentals to bioapplications*. Springer-Verlag Berlin Heidelberg, 2014, 208 p.
- [17] Stefanic G., Music S. Factors influencing the stability of low temperature tetragonal ZrO_2 . *Croatica Chemica Acta*, 2002, **75** (3), P. 727–767.
- [18] Vasilevskaya A., Almjasheva O.V., Gusarov V.V. Peculiarities of structural transformations in zirconia nanocrystals. *Journal of Nanoparticle Research*, 2016, **18** (188), 11 p.
- [19] Kurapova O.Yu., Konakov V.G. Phase evolution in zirconia-based systems. *Rev. Adv. Mater. Sci.*, 2014, **36**, P. 177–190.
- [20] Sahina O., Demirkola H., Gocmez M., et al. Mechanical properties of nanocrystalline tetragonal zirconia stabilized with CaO, MgO and Y_2O_3 . *Acta Physica Polonica A*, 2013, **123** (2), P. 296–298.
- [21] Romer V.H., Rosa E., Lopez-Luke T., et al. Brilliant blue, green and orange-red emission band on Tm^{3+} -, Tb^{3+} - and Eu^{3+} -doped ZrO_2 nanocrystals. *Journal of Physics D: Applied Physics*, 2010, **43**, P. 465105.
- [22] Almjasheva O.V., Smirnov A.V., Fedorov B.A., et al. Structural features of $\text{ZrO}_2\text{-Y}_2\text{O}_3$ and $\text{ZrO}_2\text{-Gd}_2\text{O}_3$ nanoparticles formed under hydrothermal conditions. *Russian Journal of General Chemistry*, 2014, **84** (5), P. 804–809.
- [23] Almjasheva O.V., Garabadzhiu A.V., Kozina Yu.V., et al. Biological effect of zirconium dioxide-based nanoparticles. *Nanosystems: physics, chemistry and mathematics*, 2017, **8** (3), P. 391–396.
- [24] Fabris S. A stabilization mechanism of zirconia based on oxygen vacancies only. *Acta Mater.*, 2002, **50**, P. 5171–5178.
- [25] Smits K., Grigorjeva L., Millers D., et al. Europium doped zirconia luminescence. *Opt. Mater. (Amst)*, 2010, **32**, P. 827–831.
- [26] Meetei S.D., Singh S.D. Hydrothermal synthesis and white light emission of cubic $\text{ZrO}_2:\text{Eu}^{3+}$ nanocrystals. *Journal of Alloys and Compounds*, 2014, **587**, P. 143–147.
- [27] Smits K., Olsteins D., Zolotarjovs A., et al. Doped zirconia phase and luminescence dependence on the nature of charge compensation. *Scientific Reports*, 2017, **7**, P. 444–453.
- [28] Tiseanu C., Cojocaru B., Parvulescu V.I., et al. Order and disorder effects in nano- ZrO_2 investigated by micro-Raman and spectrally and temporarily resolved photoluminescence. *Phys. Chem. Chem. Phys.*, 2012, **14**, P. 12970–12981.
- [29] Liu Y., Tu D., Zhu H., Chen X. Lanthanide-doped luminescent nanoprobe: controlled synthesis, optical spectroscopy, and bioapplications. *Chem. Soc. Rev.*, 2013, **42**, P. 6924–6958.
- [30] Gupta S.K., Natarajan V. Synthesis, characterization and photoluminescence spectroscopy of lanthanide ion doped oxide materials. *BARC Newsletter*, 2015, P. 14–21.
- [31] Bugrov A.N., Zavialova A.Yu., Smyslov R.Yu., et al. Luminescence of Eu^{3+} ions in hybrid polymer-inorganic composites based on poly(methyl methacrylate) and zirconia nanoparticles. *Luminescence*, 2018, P. 1–13.
- [32] Mon A., Ram S. Enhanced phase stability and photoluminescence of Eu^{3+} modified t- ZrO_2 nanoparticles. *J. Am. Ceram. Soc.*, 2008, **91** (1), P. 329–332.
- [33] Vidya Y.S., Anantharaju K.S., Nagabhushana H., et al. Combustion synthesized tetragonal $\text{ZrO}_2:\text{Eu}^{3+}$ nanophosphors: Structural and photoluminescence studies. *Spectrochimica Acta Part A: Molecular and Biomolecular Spectroscopy*, 2015, **135**, P. 241–251.
- [34] Ghosh P., Patra A. Role of surface coating in $\text{ZrO}_2/\text{Eu}^{3+}$ nanocrystals. *Langmuir*, 2006, **22**, P. 6321–6327.
- [35] Ninjbadgar T., Gamweiner G., Borger A., et al. Synthesis of luminescent $\text{ZrO}_2:\text{Eu}^{3+}$ nanoparticles and their holographic sub-micrometer patterning in polymer composites. *Adv. Funct. Mater.*, 2009, **19**, P. 1819–1825.

- [36] Hobbs H., Briddon S., Lester E. The synthesis and fluorescent properties of nanoparticulate ZrO_2 doped with Eu using continuous hydrothermal synthesis. *Green Chem.*, 2009, **11**, P. 484–491.
- [37] Lopato L.M., Andrievskaya E.R., Shevchenko A.V., Red'ko V.P. Phase relations in the ZrO_2 – Eu_2O_3 system. *Russian Journal of Inorganic Chemistry*, 1997, **42** (10), P. 1588–1591.
- [38] Bugrov A.N., Almjasheva O.V. Effect of hydrothermal synthesis conditions on the morphology of ZrO_2 nanoparticles. *Nanosystems: physics, chemistry and mathematics*, 2013, **4** (6), P. 810–815.
- [39] Bortolotti M., Lutterotti L., Lonardelli I. ReX: a computer program for structural analysis using powder diffraction data. *J. Appl. Cryst.*, 2009, **42** (3), P. 538–539.
- [40] Vasilef I. *QTIPLLOT, Data Analysis and Scientific Visualisation*. Universiteit Utrecht, Utrecht, Nederlande, 2011.
- [41] Smith D.K., Newkirk H.W. The crystal structure of baddeleyite (monoclinic ZrO_2) and its relation to the polymorphism of ZrO_2 . *Acta Crystallographica*, 1965, **18**, P. 983–991.
- [42] Igawa N., Ishii Y. Crystal structure of metastable tetragonal zirconia up to 1473 K. *J. Am. Ceram. Soc.*, 2001, **84** (5), P. 1169–1171.
- [43] Martin U., Boysen H., Frey F. Neutron powder investigation of tetragonal and cubic stabilized zirconia, TZP and CSZ, at temperatures up to 1400 K. *Acta Crystallographica Section B*, 1993, **49** (3), P. 403–413.
- [44] Meetei S.D., Singh S.D., Singh N.S., et al. Crystal structure and photoluminescence correlations in white emitting nanocrystalline $ZrO_2:Eu^{3+}$ phosphor: Effect of doping and annealing. *Journal of Luminescence*, 2012, **132**, P. 537–544.
- [45] Basahel S.N., Ali T.T., Mokhtar M., Narasimharao K. Influence of crystal structure of nanosized ZrO_2 on photocatalytic degradation of methyl orange. *Nanoscale Research Letters*, 2015, **10** (73), 13 p.
- [46] Adamski A., Jakubus P., Sojka Z. Synthesis of nanostructured tetragonal ZrO_2 of enhanced thermal stability. *Nukleonika*, 2006, **51**, P. 27–33.
- [47] Bersani D., Lottici P.P., Rangel G., et al. Micro-Raman study of indium doped zirconia obtained by sol-gel. *J Non-Crystalline Solids*, 2004, **345–346**, P. 116–119.
- [48] Gazzoli D., Mattei G., Valigi M. Raman and X-ray investigations of the incorporation of Ca^{2+} and Cd^{2+} in the ZrO_2 structure. *J Raman Spectrosc.*, 2007, **38** (7), P. 824–831.
- [49] Kerbellec N., Catala L., Daigebonne C., et al. Luminescent coordination nanoparticles. *New J. Chem.*, 2008, **32**, P. 584–587.
- [50] Lakowicz J. *Principles of Fluorescence Spectroscopy*, 3rd ed. Springer, New York, 2006.
- [51] Ishida H., Bunzli J.-C., Beeby A. Guidelines for measurement of luminescence spectra and quantum yields of inorganic and organometallic compounds in solution and solid state (IUPAC Technical Report). *Pure Appl. Chem.*, 2016, **88** (7), P. 701–711.
- [52] Novikov E.G., Hoek A., Visser A., Hofstraat J.W. Linear algorithms for stretched exponential decay analysis. *Optics Communications*, 1999, **166**, P. 189–198.
- [53] Klatt J., Gerich C., Grobe A., et al. Fractal dimension of time-resolved autofluorescence discriminates tumour from healthy tissues in the oral cavity. *Journal of Cranio-Maxillo-Facial Surgery*, 2014, **42** (6), P. 852–854.
- [54] Lianos P., Duportail G. Time-resolved fluorescence fractal analysis in lipid aggregates. *Biophys. Chem.*, 1993, **48**, P. 293–299.

Study of glucose concentration influence on blood optical properties in THz frequency range

S. I. Gusev¹, P. S. Demchenko¹, E. A. Litvinov¹,
O. P. Cherkasova^{2,3}, I. V. Meglinski⁴, M. K. Khodzitskiy¹

¹Terahertz Biomedicine laboratory, ITMO University,
Kronverkskiy Ave, 49, St. Petersburg, 197101, Russia

²Biophysics laboratory, Institute of Laser Physics of SB RAS,
Ac. Lavrentiev Ave, 13, Novosibirsk, 630090, Russia

³Novosibirsk State Technical University,
K. Marksa Ave, 20, Novosibirsk, 630073, Russia

⁴University of Oulu, P.O. Box 4500, FI-90015, Oulu, Finland
mail@gusev-spb.ru, khodzitskiy@yandex.ru

PACS 78.47.D-, 42.25.Gy, 87.50.U-

DOI 10.17586/2220-8054-2018-9-3-389-400

The optical properties of whole human blood with the different glucose level were studied by terahertz time-domain spectroscopy at frequencies ranging from 0.3 – 0.5 THz. The increasing of refractive index of blood at the glucose level growth was shown for series of experiments. The dispersion of complex refractive index of human nails was obtained. Based on these data, the non-invasive glucose measuring technique was proposed which utilizes the reflection of the THz pulse from nail plate/nail bed interface.

Keywords: spectroscopy, THz frequency range, blood, glucose, diabetes.

Received: 7 April 2018

Revised: 14 May 2018

1. Introduction

Currently, terahertz time-domain spectroscopy (THz TDS) and imaging techniques are applied in various fields such as astronomy, security screening, communications, genetic engineering, pharmaceutical quality control, medical imaging and biomedical engineering [1–4].

Several unique features make THz-based technology very suitable for medical applications. The main feature of THz spectroscopy which is really important for biophotonics is that the characteristic energies of molecules rotational and vibrational motions lay in THz frequency region, so many chemical and biological molecules can be identified by their characteristic resonant peaks [5]. Also THz radiation is very sensitive to water [6], so it could provide a great contrast of samples with different water content. In addition, THz radiation is non-ionizing due to it has very low photon energy. As a result, it might be safely applied to *in vivo* diagnostics. This fact is a significant advantage for biological structure investigation, because there does not appear to be any tissue damage during the procedure [7, 8].

Delayed diagnostics of diabetes mellitus as well as insufficient control on patient are the general reasons of complications, which lead to invalidation and higher mortality. It should be noted that a large number of patients have macrovascular complications due to unnormal blood glucose level: hyperglycemia, hypoglycemia, variability of glycemia. Statistics shows that growth of glycated hemoglobin (HbA1c) index from 6 % to 9 % leads to a four-fold increased risk of microvascular complications and twice the risk of myocardial infarction [9]. Hypoglycemia (even in subclinical situations) is associated with a 2 – 2.5-fold increased risk of mortality from cardiovascular complications and a four-fold increase in the number of cardiovascular cases in [10]. Variability of glycemia is another risk factor, as variability of glucose level by more than 60 mg/dl is a predictor of coronary atherosclerosis (2.6-fold increased risk) even more accurate than HbA1c [11]. In addition, glycemia variability on an empty stomach is an independent predictor of cardiovascular lethal cases for senior patients with diabetes mellitus type 2 [12], urgent patients [13] and patients with myocardial infarction [14].

The present clinical methods of glucose level sensing include the following: opto-chemical (Accu-Chek Active) and electro-chemical (Bayer Contour TS, Abbott Freestyle, OneTouch Select) glucometers, continuous glucose monitoring sensors (Medtronic MiniMed, Freestyle Libre), electro-chemistry for labs (EKF Biosen C), all of which require fresh blood sampling. At the same time, there is still lack of non-invasive methods of glucose measuring: some are out of production due to drawbacks [15], while other are only at experimental stages [16, 17],

or slowly coming to market [18, 19]. Some papers show great skepticism about the possibility of completely non-invasive glucose measuring techniques [20].

Despite these facts and opinions, this paper is part of a series of works [21–23], the goal of which is non-invasive glucose measuring technique which can use benefits of THz radiation for biomedical diagnostics purposes.

This work presents both transmission and reflection spectroscopic methods in THz frequency range to analyze glucose level in blood samples. The transmission mode is simpler to maintain and it was used to make *in vitro* analysis of blood and nail samples. Collected data was used for modeling of *in vivo* non-invasive experiment in CST Microwave Studio software.

2. Experimental setup

The optical properties of blood samples were experimentally studied at frequencies ranging from 0.3–0.5 THz using THz TDS in transmission mode [24]. The scheme of the setup is shown in Fig. 1.

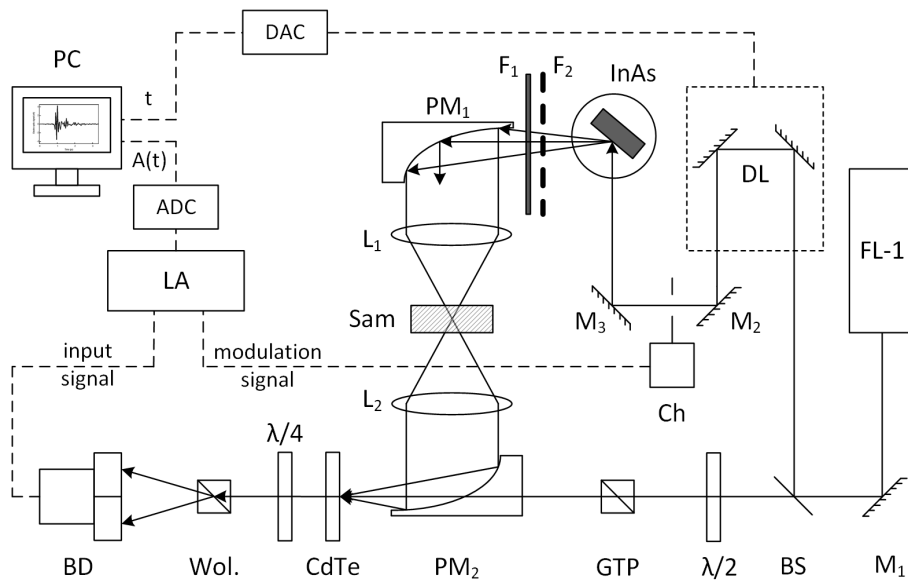


FIG. 1. Experimental THz TDS setup in transmission mode (FL-1 – femtosecond laser based on potassium-yttrium tungstate crystal activated with ytterbium (Yb: KYW), generating femtosecond pulses; F1,2 – a set of teflon filters for IR wavelength range cutting off, BS – beamsplitter, DL – optical delay line, M1,2,3 – mirrors, Sam – investigated sample, Wol. – Wollaston prism, CdTe – electro-optical cadmium-telluride crystal, BD – balanced detector, LA – lock-in amplifier, PC – personal computer, GTP – Glan-Taylor prism, PM1,2 – parabolic mirrors, Ch – chopper, DAC – digital to analog converter, ADC – analog to digital converter)

Broadband pulsed THz radiation is generated by means of an InAs semiconductor in a 2.0 T magnetic field by irradiating it with femtosecond pulses of an Yb: KYW laser (wavelength of 1040 nm, at a pulse duration of 120 fs, the pulse repetition frequency of 75 MHz, the power of 1 W). THz radiation has the following output characteristics: the pulse duration of 2.7 ps, the main power is concentrated at the frequency range from 0.3 to 0.5 THz with an average power up to 30 μ W, which was measured by a Golay cell. The typical transmission spectrum of air for this THz TDS is shown in Fig. 2 (Spectral resolution is 1 GHz). THz radiation passes through a teflon filter (which omits wavelengths shorter than 50 μ m). After that, the THz radiation passes through the sample fixed in a focal plane perpendicular to the beam. The existence of the THz field changes the birefringence of the electrooptical crystal, i.e. causing the refractive index difference for polarizations along different axes of the crystal. The electric field-induced birefringence changes the probe beam's polarization [25]. As a result, the THz pulse induces birefringence of the probe beam in the crystal due to the electrooptical effect. The birefringence magnitude is directly proportional to the amplitude of terahertz radiation electric field in the time point $E(t)$. These data are required to calculate $E(\omega)$ using the Fourier transform.

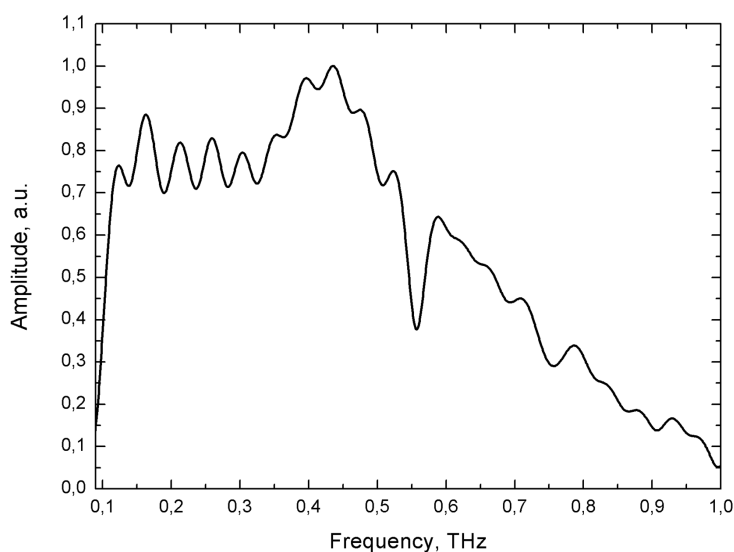


FIG. 2. Transmission spectrum of air

3. Sample preparation

In the experiment, 8 blood samples were used, each with a different glucose concentration. The samples under study were obtained from the same person over a short time period (about 2 hours). The patient had no significant diseases other than diabetes mellitus. The patient had an increased levels of: glycated hemoglobin (7,9 %); LD cholesterol (4.60 mmol/l); uric acid (9,1 mmol/l). Other blood components levels were normal. This fact helped us to provide the stable concentration of blood components (excluding glucose concentration) to avoid multiple dependences within the time of experiment. The study was performed in accordance with Good Clinical Practice (GCP) and with the 1964 Helsinki declaration and its later amendments. All measurements were performed with assistance and control of the staff of the Institute of Endocrinology of Federal Almazov North-West Medical Research Center (St.Petersburg, Russia).

The first step of sample preparation was increasing glucose level of the diabetic patient up to hyperglycemia level. It is quite a fast process so samples were obtained during the time of decreasing glucose level after insulin injection. This experiment contained samples with the following glucose concentrations shown in Table 1. The glucose concentrations in the blood were measured twice per a sample using Abbott Freestyle Optium [26] glucometer. This instrument shows concentration in values of mmol/l standard, which can be converted to mg/dl by multiplication by 18. This model of electro-chemical glucometer model is widely used in clinical research [27]. The glucose concentration measurement and THz test happened simultaneously.

The blood drops were located inside a special polymethyl methacrylate (PMMA) container (Figs. 3,4). In the middle this container was a recess with a depth of 75 μm . This type of blood holder provides keeping stable thickness of a sample and protects biological fluid from drying.

TABLE 1. The list of the glucose concentrations of samples used in experiment.

Sample #	mmol/l	mg/dl
1	3.0	54.0
2	3.8	68.4
3	6.2	111.6
4	9.2	165.6
5	11.0	198.0
6	14.9	268.2
7	18.0	324.0
8	19.0	342.0

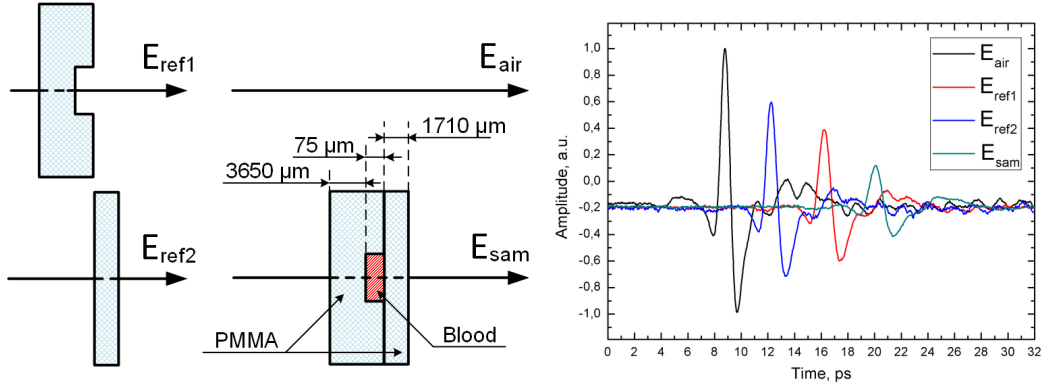


FIG. 3. The scheme of sample preparation and experimental THz waveforms

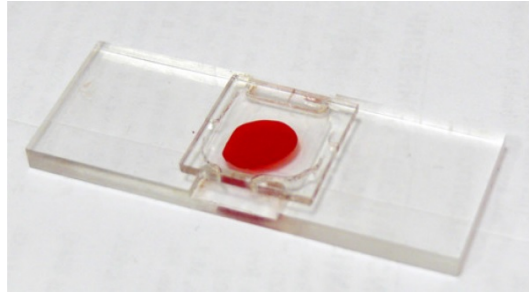


FIG. 4. Polymethyl methacrylate (PMMA) container with blood

4. Data acquisition

For each sample, a time-amplitude transmission waveform was taken 100 times and averaged for each time-point. In addition, transmission waveforms of air, bottom and top parts of container were measured. All the acquired waveforms were converted to the frequency domain $\hat{E}(\omega)$ using Fourier transform. Then, the THz electric field is:

$$\hat{E}(\omega) = \frac{1}{\sqrt{2\pi}} \int_{-\infty}^{+\infty} f(t) \exp(-i\omega t) dt = E_0(\omega) \exp(-i\varphi(\omega)), \quad (1)$$

where $f(t)$ is the time-amplitude waveform, ω is the angular frequency, $E_0(\omega)$ is the amplitude data, $\varphi(\omega)$ is the phase data.

At the first step, $E_{ref1}(t)$, $E_{ref2}(t)$, THz waveforms were used to obtain the phase delay dispersions for the bottom part and the top part of container, $\Delta\varphi_1(f)$ and $\Delta\varphi_2(f)$ correspondingly, where $\Delta\varphi_1(f) = \varphi_{ref1}(f) - \varphi_{air}(f)$, $\Delta\varphi_2(f) = \varphi_{ref2}(f) - \varphi_{air}(f)$. At the second step $E_{sam}(t)$ THz waveform was used to obtain the phase dispersion for the container with blood $\varphi_{sam}(f)$. Then the phase delay dispersion for blood was calculated as: $\Delta\varphi_{blood}(f) = \varphi_{sam}(f) - \varphi_{ref}(f)$, where $\varphi_{ref}(f) = \varphi_{air}(f) + \Delta\varphi_1(f) + \Delta\varphi_2(f)$. The phase delay dispersion for blood $\Delta\varphi_{blood}(f)$ was used to calculate complex refractive index and complex permittivity.

As a result, the refractive index n can be calculated for a sample inside the container. The real part of the blood refractive index $n_{real\ blood}$ is calculated as:

$$n_{real\ blood}(f) = 1 + \frac{c(\varphi_{sam}(f) - \varphi_{ref}(f))}{2\pi f d_{blood}}, \quad (2)$$

where c is the speed of light in vacuum, d_{blood} is the thickness of blood layer, f is the frequency, ref and sam indices mean values attitude to reference and sample signals correspondingly.

The absorption coefficients α are calculated using the electric field amplitude data:

$$d_{sam} = d_{ref1} + d_{ref2} + d_{blood}, \quad (3)$$

$$\alpha(f)_{ref1} = \frac{1}{d_{ref1}} \ln \left(\frac{E_{air}(f)}{E_{ref1}(f)} \right)^2, \quad (4)$$

$$\alpha(f)_{ref2} = \frac{1}{d_{ref2}} \ln \left(\frac{E_{air}(f)}{E_{ref2}(f)} \right)^2, \quad (5)$$

$$\alpha(f)_{sam} = \frac{1}{d_{sam}} \ln \left(\frac{E_{air}(f)}{E_{sam}(f)} \right)^2, \quad (6)$$

$$\alpha_{blood}(f) = \frac{d_{sam} \alpha_{sam}(f) - d_{ref1} \alpha_{ref1}(f) - d_{ref2} \alpha_{ref2}(f)}{d_{blood}}. \quad (7)$$

In addition, the blood penetration depth L_{blood} is the reverse function to the blood absorption coefficient α_{blood} :

$$L_{blood}(f) = \frac{1}{\alpha_{blood}(f)}, \quad (8)$$

The imaginary part of the refractive index $n_{imag\ blood}(f)$ requires data about the blood absorption coefficient α_{blood} :

$$n_{imag\ blood}(f) = \frac{\alpha_{blood}(f) c}{4 \pi f}, \quad (9)$$

Both parts of the blood permittivity ε_{blood} use both parts of the complex refractive index n_{blood} :

$$\varepsilon_{real\ blood}(f) = n_{real\ blood}^2(f) - n_{imag\ blood}^2(f), \quad (10)$$

$$\varepsilon_{imag\ blood}(f) = 2 n_{real\ blood}(f) n_{imag\ blood}(f). \quad (11)$$

All of these optical properties are available as results of Spectrnia software [21], to obtain the dispersion of optical properties of materials (complex refractive index, complex permittivity, complex conductivity); the spectral characteristics (transmission, reflection, absorption spectra) in transmission and reflection modes.

5. Transmission experiment results

Based on 8 biosamples, we have investigated the frequency dispersions of n_{real} , α , ε_{real} , ε_{imag} in the THz frequency range (Fig. 5).

After data acquisition, the next step is finding dependencies between glucose concentrations and optical properties. To determine the dependence of blood optical properties upon glucose concentration we selected the experimental data at 0.30, 0.35, 0.40, 0.45 THz. These frequencies were chosen due to maximal THz electric field amplitude and minimal absorption of water vapor [28]. Fig. 6 shows the dependences of glucose concentration on the real part of the refractive index and on the real part of the permittivity. The dependence is not linear with blood glucose concentrations above 16 mmol/l. This may be due to the change in physico-chemical properties of blood components with high glucose concentration [29,30]. As known hyperglycemia caused by insulin deficiency is accompanied by a large loss of electrolytes, dehydration of tissues and osmolality increase of blood plasma.

In a week we repeated these experiments to check the type of dependence of glucose level on the blood optical properties. The comparison of data of two experiments is shown in Fig. 6. We observe the shift of the calibration curves but the shape of the curves was similar. This shift may be caused by the variation of the concentrations of the patient blood components (cholesterol, uric acid, etc.) in another experiment.

The dependences of glucose concentration on the real part of the refractive index and the real part of the permittivity were approximated by all OriginPro embedded functions to find the most suitable one. The Gompertz function (formula 12) fitted these dependences better than other ones.

$$y = A \exp \left(- \exp(-C(x - B)) \right). \quad (12)$$

These dependencies indicate that quantitative blood glucose levels analysis is feasible by using TDS in the THz frequency range. According to these data, we can simulate glucose level analysis by performing numerical modeling in the reflective mode.

Often, during the process of mixing, analysis the model of effective medium is used. It means the following case: if we mix few media with known optical parameters and proportions, we can calculate optical parameters as the sum of multiplication products of medium concentrations and its optical parameters. In our case, the results

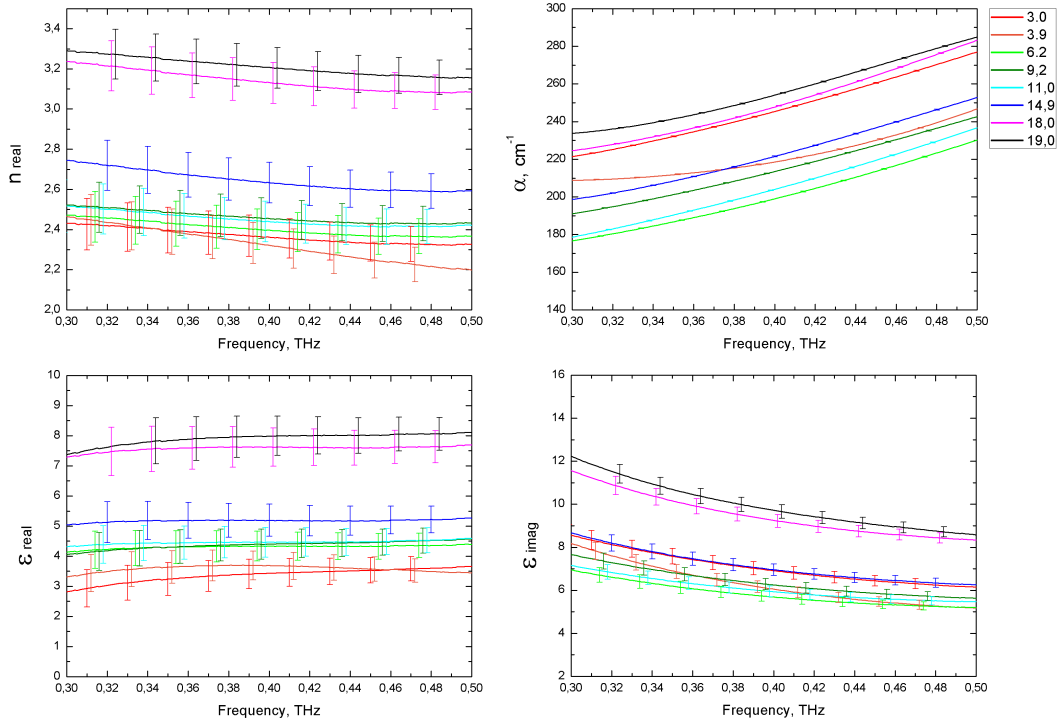


FIG. 5. Dispersions of optical parameters of samples with different glucose concentration $C_{glucose}$: subgraph *a* shows the real part of refractive index $n_{real}(f)$, *b* – the absorption coefficient $\alpha(f)$, *c* – the real part of permittivity $\epsilon_{real}(f)$, *d* – the imaginary part of permittivity $\epsilon_{imag}(f)$

TABLE 2. The coefficients of Gompertz fitting for dependence of glucose concentration $C_{glucose}$ on real parts of refractive index n_{real} (left tab) and of permittivity ϵ_{real} (right tab) at the frequencies of 0.30, 0.35, 0.40, 0.45 THz

Frequency	Coefficient A		Coefficient B		Coefficient C	
	Ex.1	Ex.2	Ex.1	Ex.2	Ex.1	Ex.2
0.30 THz	19.0	16.2	2.49	2.17	4.14	16.98
0.35 THz	19.0	16.2	2.44	2.13	4.21	14.59
0.40 THz	19.0	16.2	2.40	2.12	4.24	12.71
0.45 THz	19.0	16.2	2.36	2.11	4.23	11.65

Frequency	Coefficient A		Coefficient B		Coefficient C	
	Ex.1	Ex.2	Ex.1	Ex.2	Ex.1	Ex.2
0.30 THz	19.0	16.2	3.73	2.73	0.84	1.86
0.35 THz	19.0	16.2	3.99	3.17	0.85	4.54
0.40 THz	19.0	16.2	4.07	3.21	0.87	4.30
0.45 THz	19.0	16.2	4.07	3.18	0.87	3.52

cannot be fitted into a model of effective medium theory due to the model being developed for noninteracting components, thus the biochemical interaction of components cannot be fitted into this model [31].

6. Reflective THz time-domain spectroscopy

Terahertz radiation is highly absorbed by water and biological tissues, so signal transmission through a biotissue for non-invasive measurements is not possible practically at THz frequencies. At the same time, it's possible to use THz time domain spectroscopy in the reflective mode, which allows to study a layered structure [32]. Fig. 7 shows a sketch of THz spectrometer for this case. The nail may be used as a reference sample for non-invasive glucose level sensing.

The typical reflected THz waveform obtained at the interaction of THz pulse with a nail layered structure is shown in Fig. 8.

The time domain of the resulting pulse train detected in the reflection measurements consists of a reference pulse, a pulse reflected from the front of the nail plate, and a sample pulse, a delayed pulse reflected from the nail plate/nail bed interface. The optical properties of the nail bed may be retrieved from the ratio between the sample and reference electric fields obtained experimentally.

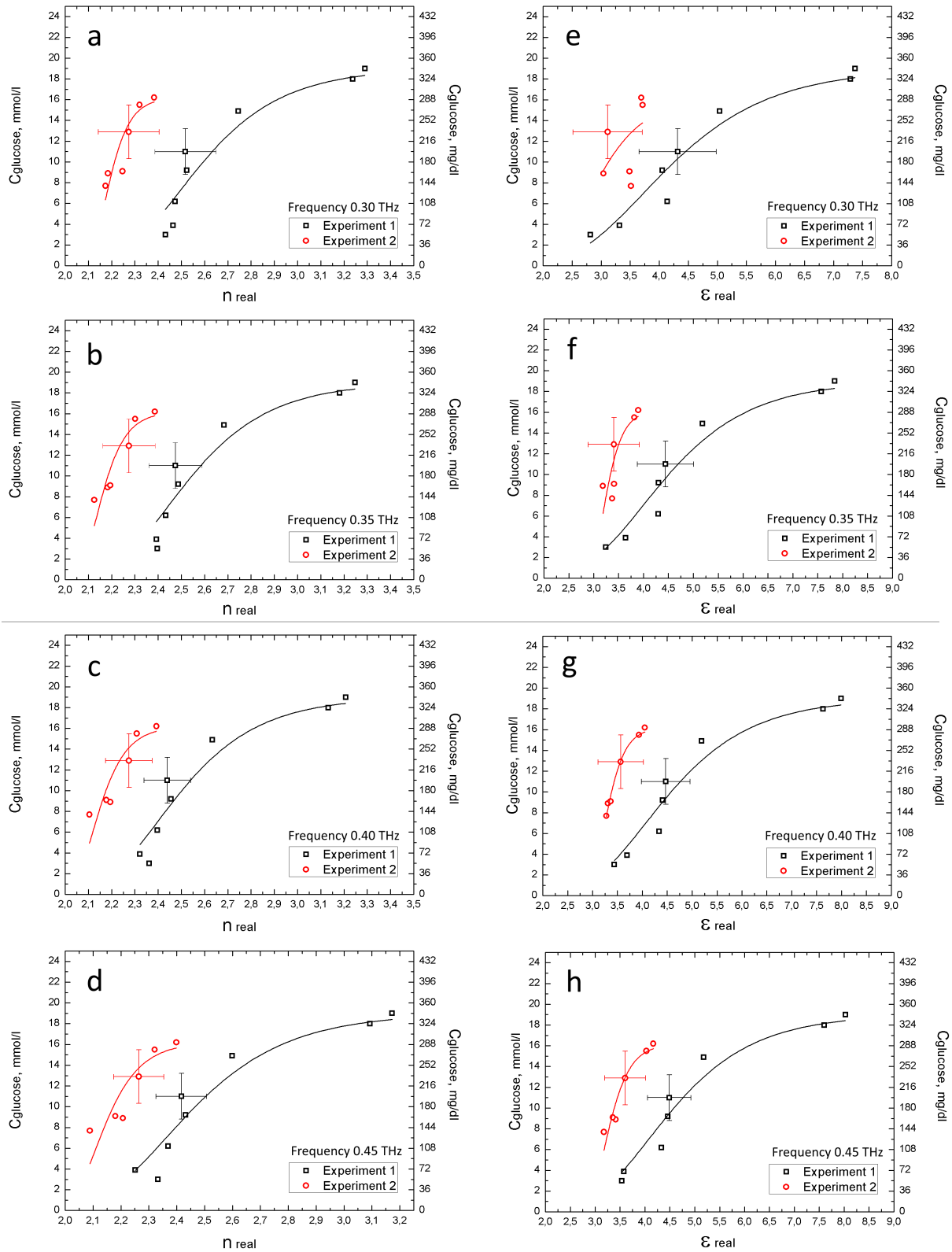


FIG. 6. Dependencies of glucose concentration on the real part of refractive index $C_{glucose}(n_{real})$ (a,b,c,d) and real part of permittivity $C_{glucose}(\epsilon_{real})$ (e,f,g,h) at the frequencies of 0.30, 0.35, 0.40, 0.45 THz. Gompertz function is used to perform fitting line. Comparison of results of two experiments.

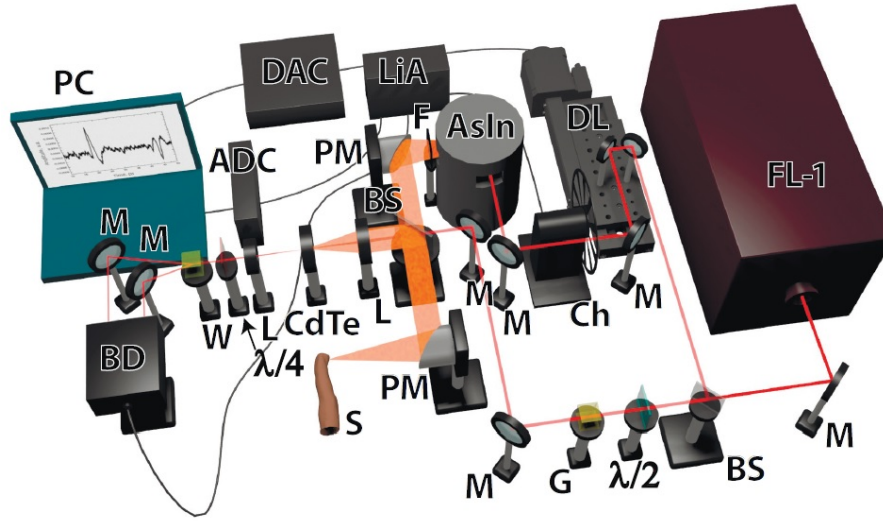


FIG. 7. Sketch of THz TDS spectrometer in reflection mode for glucose level sensing (FL-1 – femtosecond laser based on potassium-yttrium tungstate crystal activated with ytterbium (Yb: KYW), generating femtosecond pulses; F – a set of teflon filters for IR wavelength range cutting off, BS – beamsplitter, DL – optical delay line, M – mirrors, S – investigated sample, W – Wollaston prism, CdTe – electro-optical cadmium-telluric crystal, BD – balanced detector, LiA – lock-in amplifier, PC – personal computer, G – Glan-Taylor prism, PM – parabolic mirrors, Ch – chopper, DAC – digital to analog converter, ADC – analog to digital converter)

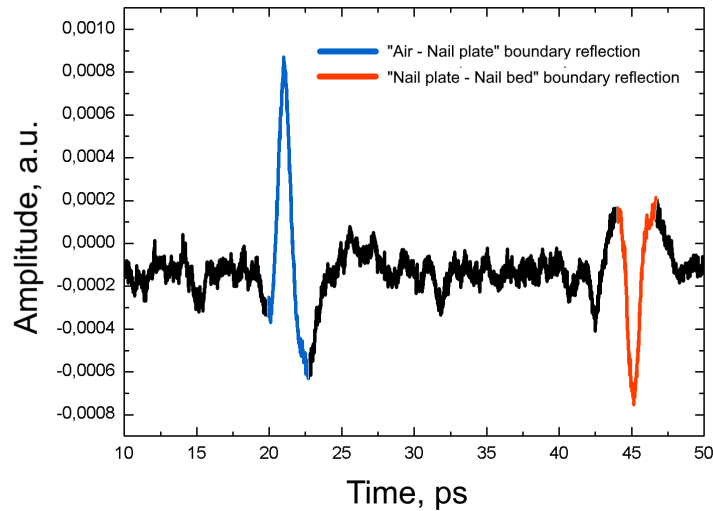


FIG. 8. Typical reflected signal from a human nail

So the nail is a type of layered structure, which has quasi-homogenous layers with defined boundaries: nail plate and nail bed. Moreover, the nail bed contains significant part of capillaries, the optical properties of which strongly depend on the glucose level in blood. Therefore such structure may be simply simulated using the finite difference time domain (FDTD) solver by CST. The simulated nail is shown in Fig. 9.

A waveguide port simulated a TE plane wave propagating through a medium. The port works as an emitter and detector. The THz bipolar waveform of the source was experimentally recorded and was fitted by the formula for a THz surface field emitter:

$$E(t) = \frac{2A}{\tau^2} \exp\left(\frac{-(t + \Delta t)^2}{\tau^2}\right) - 4A \frac{(t + \Delta t)^2}{\tau^4} \exp\left(\frac{-(t + \Delta t)^2}{\tau^2}\right), \quad (13)$$

where τ is 0.765 ps, A is 0.41 and Δt is -5.8 ps. The experimental and theoretical ones are shown in Fig. 10.

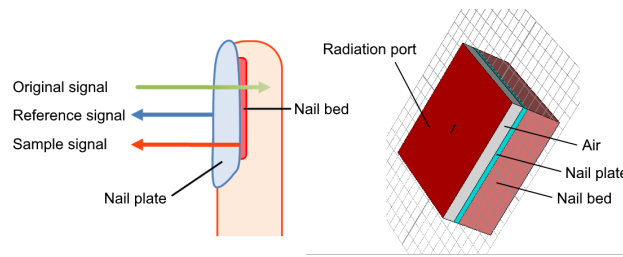


FIG. 9. Principal scheme of the reflecting nail structure (left) and its realization in CST Microwave Studio (right)

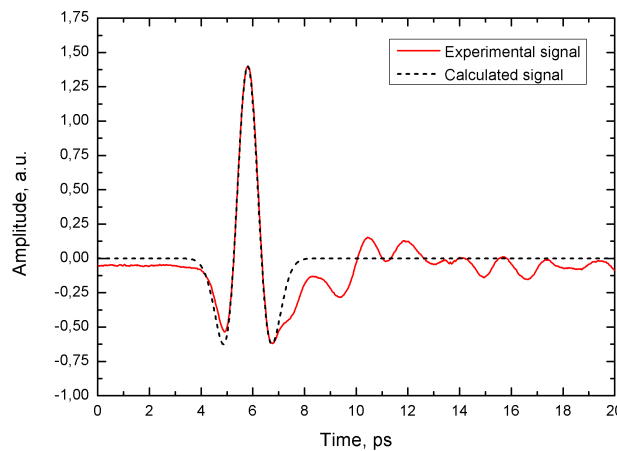


FIG. 10. THz source signal: experimental (solid line) and theoretical (dotted line)

In the model we used the experimental data for the human nails [23] (Fig. 11). The thickness of the nail plate was 0.58 mm.



FIG. 11. The nail samples under study

The experimental dispersions of the real and imaginary parts of the nail plate permittivity are shown in Fig. 12.

The thickness of the nail bed layer was chosen as 3 mm due to the fact, that we observed only the reflective signal from the structure. It was assumed that the dispersions of nail bed permittivity for the different glucose concentrations can be replaced by the dispersions of the permittivity of blood samples with the different glucose levels. The assumption was made due to the nail bed containing blood-filled capillaries [33] and the main reason the nail bed's optical properties change is due to varying blood glucose concentrations.

Modeled THz waveforms of reflected signals from the nail for different glucose levels are shown in Fig. 13. As seen from the figure, the peak-to-peak amplitude of the sample pulse reflected from the nail plate/nail bed

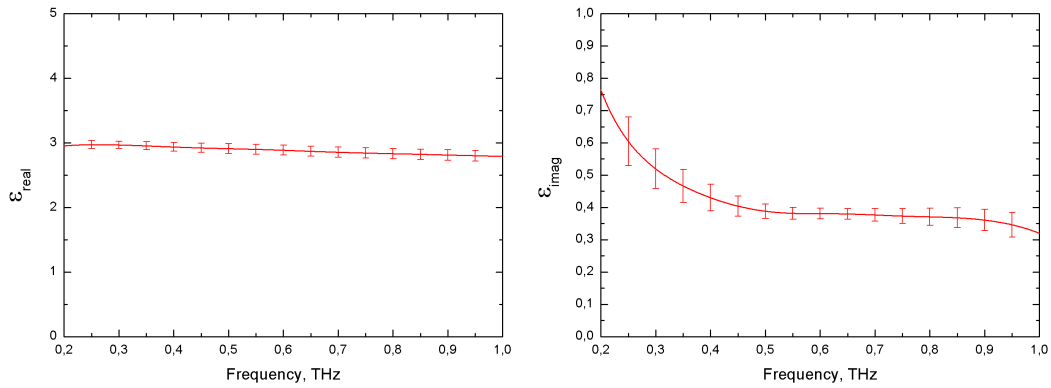


FIG. 12. The dispersion of the real and imaginary parts of the permittivity of the nails. Spectral resolution is 1 GHz.

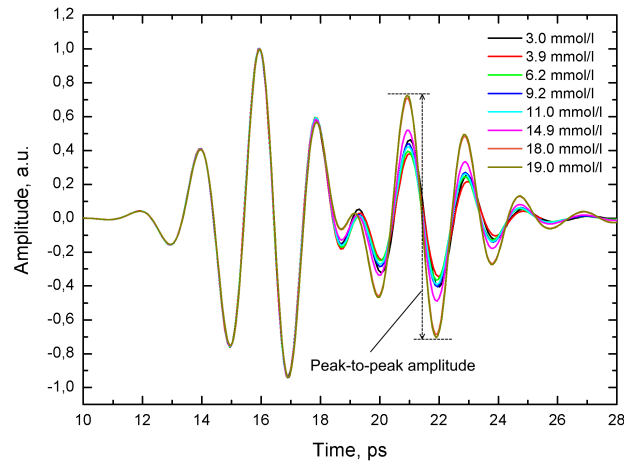


FIG. 13. THz waveforms for the different glucose levels in blood

interface changes with varying glucose levels. The increasing the blood glucose level results in an increase in the amplitude of the pulse reflected from the nail bed (Fig. 14). So the reflection mode of THz TDS may be used as non-invasive technique for glucose level control.

7. Conclusion

This work shows the application of THz time domain spectroscopy in the field of glucose sensing. Based on the refractive index dispersion for whole human blood, we demonstrate that different blood glucose levels have individual refractive index dispersions in frequencies ranging from 0.3–0.5 THz and the relationships between the refractive index and glucose concentration at the single THz frequencies are described by the Gompertz function. Additionally, the dispersion of complex refractive index of human nails in the transmission mode was obtained. Based on these data we proved the possibility of non-invasive glucose level sensing in reflective mode using reflection of THz pulse from nail plate/nail bed interface. This research may provide a quick, accurate, and continuous method to measure glucose concentration in human blood, which has wide potential application in clinical practice.

Acknowledgements

This work was financially supported by the Government of Russian Federation, Grant 074-U01.

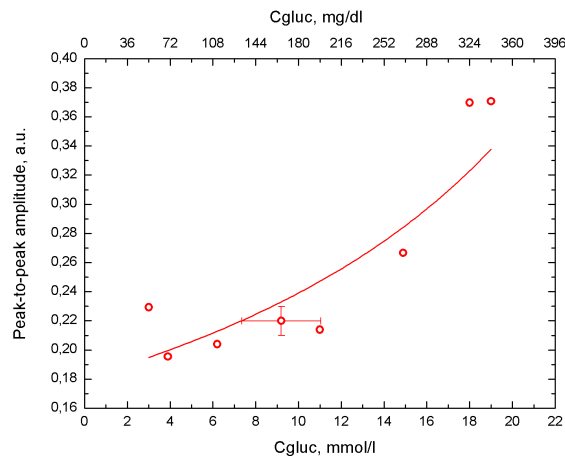


FIG. 14. The dependence of the peak-to-peak amplitude of THz reflected signal on the glucose level in blood

References

- [1] Shur M. Terahertz technology: devices and applications. *Proceedings of ESSDERC*, 2005, **35**, P. 13–21.
- [2] Consolino, L., Bartalini S., and De Natale P. Terahertz Frequency Metrology for Spectroscopic Applications: a Review. *Journal of Infrared, Millimeter, and Terahertz Waves*, 2017, **38** (11), P. 1289–1315.
- [3] Al-Naib, I., Withawat W. Recent Progress in Terahertz Metasurfaces. *Journal of Infrared, Millimeter, and Terahertz Waves*, 2017, **38** (9), P. 1067–1084.
- [4] Reid C.B., Reese G., Gibson A.P., Wallace V.P. Terahertz time-domain spectroscopy of human blood. *IEEE Transactions on Terahertz Science and Technology*, 2013, **3** (4), P. 363–367.
- [5] Yang X., Zhao X., Yang K., Liu Y., Liu Y., Fu W., Luo Y. Biomedical applications of terahertz spectroscopy and imaging. *Trends in biotechnology*, 2016, **34** (10), P. 810–824.
- [6] Thrane L., Jacobsen R. H., Jepsen P. U., Keiding S. THz reflection spectroscopy of liquid water. *Chemical Physics Letters*, 1995, **240** (4), P. 330–333.
- [7] Fitzgerald, A. J., Berry, E., Zinovev, N. N., Walker, G. C., Smith, M. A., Chamberlain, J. M. An introduction to medical imaging with coherent terahertz frequency radiation. *Physics in Medicine & Biology*, 2002, **47** (7), P. R67.
- [8] Wang, K., Da-Wen S., Hongbin P. Emerging non-destructive terahertz spectroscopic imaging technique: Principle and applications in the agri-food industry. *Trends in Food Science & Technology*, 2017, **67**, P. 93–105.
- [9] Stratton I. M., Adler A. I., Neil H. A. W., Matthews D. R., Manley S. E., Cull C. A., Hadden D., Turner R. C., Holman R. R. Association of glycaemia with macrovascular and microvascular complications of type 2 diabetes (UKPDS 35): prospective observational study. *British Medical Journal*, 2000, **321** (7258), P. 405–412.
- [10] Zoungas S., Patel A., Chalmers J., de Galan B. E., Li Q., Billot L., Woodward M., Ninomiya T., Neal B., MacMahon S. et al. Severe hypoglycemia and risks of vascular events and death. *New England Journal of Medicine*, 2010, **363** (15), P. 1410–1418.
- [11] Su G., Mi S., Tao H., Li Z., Yang H., Zheng H., Zhou Y., Ma C. Association of glycemic variability and the presence and severity of coronary artery disease in patients with type 2 diabetes. *Cardiovascular Diabetology*, 2011, **10** (1), P. 19.
- [12] Muggeo M., Verlato G., Bonora E., Zoppini G., Corbellini M., De Marco R. Long-term instability of fasting plasma glucose, a novel predictor of cardiovascular mortality in elderly patients with noninsulin-dependent diabetes mellitus: the verona diabetes study. *Circulation*, 1997, **96** (6), P. 1750–1754.
- [13] Krinsley J. S. Glycemic variability: a strong independent predictor of mortality in critically ill patients. *Critical Care Medicine*, 2008, **36** (11), P. 3008–3013.
- [14] Wang X., Zhao X., Dorje T., Yan H., Qian J., Ge J. Glycemic variability predicts cardiovascular complications in acute myocardial infarction patients with type 2 diabetes mellitus. *International Journal of Cardiology*, 2014, **172** (2), P. 498–500.
- [15] Tierney M. J., Tamada J. A., Potts R. O., Jovanovic L., Garg S., Team C. R. et al. Clinical evaluation of the Glucowatch® Biographer: a continual, non-invasive glucose monitor for patients with diabetes. *Biosensors and Bioelectronics*, 2001, **16** (9-12), P. 621–629.
- [16] Larin K. V., Eledrisi M. S., Motamedi M., Esenaliev R. O. Noninvasive blood glucose monitoring with optical coherence tomography: A pilot study in human subjects. *Diabetes Care*, 2002, **25** (12), P. 2263–2267.
- [17] Cherkasova O. P., Nazarov M. M., Smirnova I. N., Angeluts A. A., Shkurinov A. P. Application of time-domain THz spectroscopy for studying blood plasma of rats with experimental diabetes. *Physics of Wave Phenomena*, 2014, **22** (3), P. 185–188.
- [18] Segman Y. New method for computing optical hemodynamic blood pressure. *Journal of Clinical and Experimental Cardiology*, 2016, **7** (12), P. 1–7.
- [19] Chen, Hua, et al. Quantify Glucose Level in Freshly Diabetics Blood by Terahertz Time-Domain Spectroscopy. *Journal of Infrared, Millimeter, and Terahertz Waves*, 2018, **39** (4), P. 399–408.
- [20] Smith J. The Pursuit of Noninvasive Glucose: Hunting the Deceitful. Turkey, 5th Edition. 2017.
URL: <http://nivglucose.com/The%20Pursuit%20of%20Noninvasive%20Glucose%205th%20Edition.pdf>.

- [21] Gusev S. I., Borovkova M. A., Strepitov M. A., Khodzitsky M. K. Blood optical properties at various glucose level values in THz frequency range. *Proceedings of the SPIE-OSA*, 2015, **9537**, P. 95372.
- [22] Gusev S. I., Balbekin N. S., Sedykh E. A., Kononova Yu. A., Litvinenko E. V., Goryachuk A. A., Begaeva V. A., Goryachuk A. A., Babenko A. Yu., Khodzitsky M. K. Influence of creatinine and triglycerides concentrations on blood optical properties of diabetics in THz frequency range. *Journal of Physics: Conference Series*, 2016, **735** (1), P. 012088.
- [23] Guseva V. A., Gusev S. I., Demchenko P. S., Sedykh E. A., Khodzitsky M. K. Optical properties of human nails in THz frequency range. *Journal of Biomedical Photonics & Engineering*, 2016, **2** (4), P. 040306.
- [24] Bespalov V. G., Gorodetskiĭ A. A., Denisyuk I. Yu., Kozlov S. A., Krylov V. N., Lukomskĭ G. V., Petrov N. V., Putilin S. E. Methods of generating superbroadband terahertz pulses with femtosecond lasers. *Journal of Optical Technology*, 2008, **75** (10), P. 636–642.
- [25] Zhang, Xi-Cheng, Jingzhou Xu. *Introduction to THz wave photonics*. Springer, New York, 2010., P. 40–43.
- [26] Sheffield C. A., Kane M. P., Bakst G., Busch R. S., Abelseh J. M., Hamilton R. A. Accuracy and precision of four value-added blood glucose meters: the Abbott Optium, the DDI Prodigy, the HDI True Track, and the HypoGuard Assure Pro. *Diabetes Technology & Therapeutics*, 2009, **11** (9), P. 587–592.
- [27] Biester T., Danne T., Bläsig S., Remus K., Aschemeier B., Kordonouri O., Bardtrum L., Haahr H. Pharmacokinetic and prandial pharmacodynamic properties of insulin degludec/insulin aspart in children, adolescents, and adults with type 1 diabetes. *Pediatric Diabetes*, 2016, **17** (8), P. 642–649.
- [28] Van Exter M., Fattinger C., Grischkowsky D. Terahertz timedomain spectroscopy of water vapor. *Optics letters*, 1989, **14** (20), P. 1128–1130.
- [29] Bogner P., Sipos K., Ludany A., Somogyi B., Miseta A. Steadystate volumes and metabolism-independent osmotic adaptation in mammalian erythrocytes. *European Biophysics Journal*, 2002, **31** (2), P. 145–152.
- [30] Jain S. K. Hyperglycemia can cause membrane lipid peroxidation and osmotic fragility in human red blood cells. *Journal of Biological Chemistry*, 1989, **264** (35), P. 21340–21345.
- [31] Son J.-H. *Terahertz Biomedical Science and Technology*. CRC Press, Boca Raton., 2014. P. 347–350.
- [32] Němec H., Kadlec F., Kužel P., Duvillaret L., Coutaz L. Independent determination of the complex refractive index and wave impedance by time-domain terahertz spectroscopy. *Optics communications*, 2006, **260** (1), P. 175–183.
- [33] Hasegawa K., Pereira B. P. The microvasculature of the nail bed, nail matrix, and nail fold of a normal human fingertip. *Journal of Hand Surgery*, 2001, **26** (2), P. 283–290.

Optical properties and photocatalytic activity of nanocrystalline TiO₂ doped by 3d-metal ions

I. V. Kolesnik^{1,2}, V. A. Lebedev¹, A. V. Garshev^{1,3}

¹Lomonosov Moscow State University, Leninskie Hills, 1, Moscow, 119992, Russia

²Institute of General and Inorganic Chemistry, Leninsky avenue, 31, Moscow, 119991, Russia

³Institute of Metallurgy, Leninsky avenue, 49, Moscow, 119334, Russia

kolesnik.iv@gmail.com, vasya_lebedev@mail.ru, garshev@inorg.chem.msu.ru

PACS 61.46.+w, 61.46.-w, 71.55.-I, 78.20.-e, 78.40.Fy, 81.05.-t, 81.07.Bc, 82.50.Hp

DOI 10.17586/2220-8054-2018-9-3-401-409

The influence of impurities on optical and photocatalytic properties was studied in a series of nanocrystalline TiO₂ with similar coherent scattering region sizes, phase compositions, surface areas and lattice parameters doped by Fe, Cr, Mn and V ions. Doping leads to an increase of absorption in the visible part of the spectrum due to the formation of additional levels in the band gap. In the case of Fe and Cr ions, d-d transitions are observed, whereas in the case of Mn and V ions, an additional band is associated with the transition from impurity level to E_c . The presence of impurities effectively suppresses photocatalytic activity in the methyl orange decoloration reaction.

Keywords: titanium oxide, nanocrystalline, doped TiO₂, photocatalysis, band gap, Urbach tail, impurity levels.

Received: 11 November 2017

1. Introduction

Tuning of photocatalytic properties of titanium dioxide is important for many practical applications of this material. One of the approaches to modify the photocatalytic activity of TiO₂ is doping by metal and non-metal ions. Different dopants such as metal ions: iron, chromium, nickel, manganese, niobium, cerium and other lanthanides, and non-metal atoms have been studied in detail [1–15].

In the case of TiO₂ doped with metal ions, which substitute Ti⁴⁺, or non-metals which substitute O²⁻ or sit in interstitial positions the material absorbs light with higher wavelengths in comparison with undoped TiO₂. Some authors associate this observation with the change of the band gap [16, 17]. Other authors suggest that the change of optical properties can be explained by the formation of additional energy levels in the band gap [18–20]. Such levels not only change optical properties but also may exert influence on the dynamics of the charge carriers.

For instance, it was observed [1, 14] that doping in titanium positions in TiO₂ lattice leads to the suppression of photocatalytic activity of TiO₂ because of the formation of defects such as oxygen vacancies, which may trap the electrons and form color centers. It is obvious that the type and concentration of defects partially determine photocatalytic activity of TiO₂ and should lead to the decrease of photocatalytic activity because of recombination processes. However many other works mentioned above demonstrate that doping leads to the increase of photocatalytic activity.

One can explain these contradictory tendencies by the influence of other factors which influence on photocatalytic activity of TiO₂: crystallinity, particle size, phase composition and surface [21–23]. Introduction of impurity with subsequent calcinations at relatively high temperature lead to the situation when several characteristics within the same series of the samples change. For example, optical properties, grain size and crystallinity may change with the increase of dopant concentration because impurities influence on TiO₂ crystallization process.

In present study we used an approach which allowed us to distinguish the effects of the change of optical properties from microstructure and phase composition effects on the photocatalytic properties of metal doped TiO₂. We prepared nanocrystalline TiO₂ with different concentrations of iron, chromium, vanadium and manganese impurities and with other characteristics such as phase composition, surface area, porosity and coherent scattering region sizes which were close to the parameters of non-doped samples. Their optical properties were studied by means of UV-Vis spectroscopy. The deconvolution of the spectra allowed us to find the positions of energy levels in the band gaps and to assign them to certain impurities, color centers and other processes. We also measured the photocatalytic properties of pure and doped nanocrystalline TiO₂ in the methyl orange decoloration reaction to find correlation between optical properties and photocatalytic activity.

2. Experimental

The synthesis of nanocrystalline TiO_2 was performed by hydrolysis of $\text{Ti}(\text{O}^i\text{C}_3\text{H}_7)_4$ (Aldrich, 97 %) in presence of triblock copolymer Pluronic (Aldrich, 95 %) in aqueous media. Titanium isopropoxide was added to the solution of the polymer, NH_4F (Sigma-Aldrich, 98 %) and HNO_3 at pH=2 under vigorous stirring. The final composition of the reaction mixture was: 1 $\text{Ti}(\text{O}^i\text{C}_3\text{H}_7)_4$: 0.016 P123 : 14.8 HNO_3 : 0.01 NH_4F : 164 H_2O . The suspension was stirred for 72 hours at room temperature; the precipitate was collected and washed several times by centrifugation. To prepare doped TiO_2 proper amount of the corresponding salt ($\text{Mn}(\text{NO}_3)_2 \cdot 4\text{H}_2\text{O}$ (Aldrich, 95 %), $\text{Fe}(\text{NO}_3)_3 \cdot 9\text{H}_2\text{O}$ (Fluka, 95 %), $\text{Cr}(\text{NO}_3)_3 \cdot 9\text{H}_2\text{O}$ (Sigma-Aldrich, 98 %), NH_4VO_3 (Sigma-Aldrich, 99 %)) was added to the reaction mixture before the addition of $\text{Ti}(\text{O}^i\text{C}_3\text{H}_7)_4$. The following molar ratios of impurity to titanium were put into reaction mixtures: 0.05 %, 0.1 %, 0.5 %, 1 % and 3 %.

Characterization of pure and doped TiO_2 was carried out by powder x-ray diffraction. X-ray diffraction patterns were acquired using a Rigaku D/MAX 2500 diffractometer equipped with $\theta - 2\theta$ Bragg-Brentano reflection goniometer, Cu-rotating anode (40 kV, 250 mA), curved graphite monochromator placed at the reflected beam and a scintillation counter. Diffraction data were collected in the 0.5 – 60 2θ range with a 0.01 step and a fixation time of 2 s/step. The ICDD PDF-2 base was used to identify crystalline phases. The fitting of XRD profile was performed by means of Jana 2006 software [24]. Transmission electron microscopy (TEM) studies were performed at the Zeiss Libra 200 at 200 kV. Bright field TEM and selected area electron diffraction (SAED) images were collected using a CCD Gatan Ultrascan 4000 at $2k \times 2k$ resolution. Adsorption and desorption isotherms of nitrogen were obtained at 77 K on a Quantachrome NOVA 4200e. The samples were outgassed at 473 K for 5 h before measurements were performed. The concentration of impurities was determined by mean of mass-spectrometry with inductively-coupled plasma (ICP MS) using ELAN DRC II Perkin Elmer spectrometer. Optical properties were analyzed by a UV-visible diffuse reflectance spectrometer Lambda 950 (Perkin Elmer) in the range 200 – 1100 nm.

Photocatalytic activity was measured by the decoloration of methyl orange in aqueous solution under UV illumination by high-pressure Hg bulb (5 W) in a cylindrical quartz IceGlass reactor with a thermostating contour.

3. Results and discussion

The concentrations of impurity ions in doped TiO_2 samples were determined by ICP-MS (Table 1). One can see that molar ratio of impurity content to TiO_2 is lower than in reaction mixture during the synthesis but systematically increases with increase of the concentration of metal salt in the reaction mixtures. The concentration of impurity changes had the following ranges: 0.03 to 1.63 mol. % for Fe-doped TiO_2 ; 0.02 to 1.22 mol. % for Cr-doped TiO_2 ; 0.03 to 1.44 mol. % for V-doped TiO_2 ; 0.02 to 1.24 mol. % for Mn-doped TiO_2 .

The structure and phase composition of pure and doped titanium oxide samples were characterized by low temperature nitrogen sorption, powder X-Ray diffraction and transmission electron microscopy. The parameters of the porous and crystalline structure as well as phase composition for all samples are similar (Table 1). All samples have high specific surface area (230 – 290 m^2/g) and consist of the mixture of anatase (80 – 90 %) and brookite (10 – 20 %) with the sizes of coherent scattering regions ranging from 4 – 6 nm. The formation of anatase phase during hydrolysis and relatively low temperature treatment is in good agreement with literature data [25]. Any other phases containing iron, chromium, vanadium and manganese have not been detected by X-Ray diffraction. The unit cell parameters were determined for anatase phase ($a = 3.78 \pm 0.02 \text{ \AA}$, $c = 9.48 \pm 0.09 \text{ \AA}$) and seem to be the same for all samples in the range of calculation uncertainty (Table 1) unlike Nb-doped samples in the same concentration range [26].

Typical TEM image of Cr-doped sample is presented on Fig. 1. The sample consists of the primary particles with diameters in the range 4 – 6 nm. This result is in good agreement with the result of calculation of coherent scattering region size for this sample. The other samples have the same microstructure according TRM data.

The electron diffraction pattern consists of concentric circles which are typical for polycrystalline samples. The values of d correspond to the anatase phase. The reflections for brookite phase are not clearly seen because of low brookite content, small particle size and because the most of the reflections of brookite phase overlap with the reflections of anatase.

Optical properties of pure and doped titanium oxide were studied by diffuse reflectance UV-Vis spectroscopy. The spectra are presented on the Fig. 2. All doped samples demonstrate the increase of absorption in visible region in comparison with pure TiO_2 . Also, the intensity of visible light absorption increases with the increase of dopant concentration. The intensity of optical absorption depends not only on the concentration but also on the nature of the dopant. In the case of Fe- and Mn-doped TiO_2 , we observe a shoulder near the absorption edge. Whereas in

TABLE 1. Impurity concentrations, specific surface areas, CSR sizes and unit cell parameters of anatase phases for pure and doped nanocrystalline TiO₂

Impurity to titanium ratios ion reaction mixture (mol. %)	Impurity concentration (mol. %) determined by ICP MS	Specific surface area (m ² /g)	CSR size (nm) and phase content (%)			Unit cell parameters of anatase, Å	
			anatase	5	90	a	3.78±0.02
Pure TiO ₂	–	270	brookite	6	10	c	9.48±0.09
			anatase	6	90	a	3.79±0.02
0.05 (Fe)	0.03	250	brookite	4	10	c	9.49±0.04
			anatase	6	90	a	3.80±0.01
0.1 (Fe)	0.09	240	brookite	4	10	c	9.51±0.06
			anatase	6	90	a	3.80±0.04
0.5 (Fe)	0.25	230	brookite	5	10	c	9.48±0.09
			anatase	6	90	a	3.79±0.02
1 (Fe)	0.53	270	brookite	4	10	c	9.53±0.07
			anatase	5	90	a	3.78±0.02
3 (Fe)	1.63	250	brookite	4	10	c	9.49±0.07
			anatase	5	90	a	3.81±0.02
0.05 (Cr)	0.02	230	brookite	4	10	c	9.53±0.06
			anatase	5	90	a	3.80±0.02
0.1 (Cr)	0.05	230	brookite	4	10	c	9.49±0.07
			anatase	5	90	a	3.81±0.03
0.5 (Cr)	0.24	230	brookite	5	10	c	9.48±0.07
			anatase	6	90	a	3.78±0.02
1 (Cr)	0.50	270	brookite	5	10	c	9.45±0.05
			anatase	5	90	a	3.90±0.01
3 (Cr)	1.22	250	brookite	4	10	c	9.49±0.02
			anatase	5	90	a	3.80±0.02
0.05 (Mn)	0.03	270	brookite	5	10	c	9.51±0.06
			anatase	6	80	a	3.80±0.02
0.1 (Mn)	0.07	290	brookite	5	20	c	9.50±0.06
			anatase	4	80	a	3.81±0.03
0.5 (Mn)	0.27	260	brookite	5	20	c	9.52±0.05
			anatase	5	90	a	3.78±0.02
1 (Mn)	0.35	290	brookite	5	10	c	9.49±0.05
			anatase	5	90	a	3.80±0.03
3 (Mn)	1.44	280	brookite	4	10	c	9.50±0.03
			anatase	5	90	a	3.81±0.01
0.05 (V)	0.02	260	brookite	5	10	c	9.52±0.08
			anatase	5	90	a	3.80±0.01
0.1 (V)	0.03	250	brookite	5	10	c	9.47±0.05
			anatase	5	90	a	3.81±0.02
0.5 (V)	0.18	280	brookite	4	10	c	9.50±0.05
			anatase	5	80	a	3.79±0.01
1 (V)	0.36	280	brookite	5	20	c	9.46±0.07
			anatase	5	80	a	3.81±0.02
3 (V)	1.24	250	brookite	4	20	c	9.49±0.04

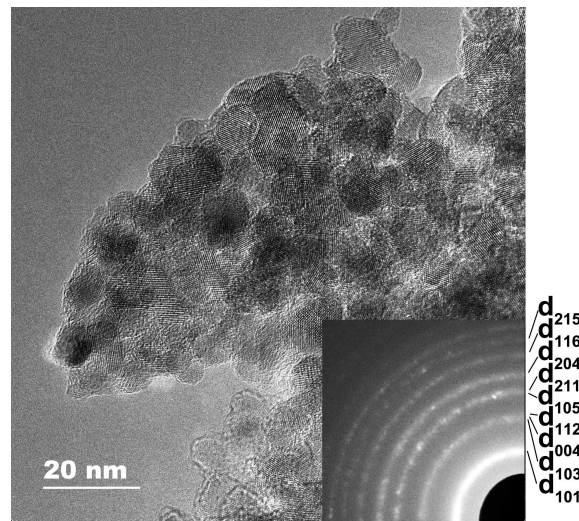


FIG. 1. Typical TEM image of Cr-doped nanocrystalline TiO_2 (1.22 mol.% of Cr)

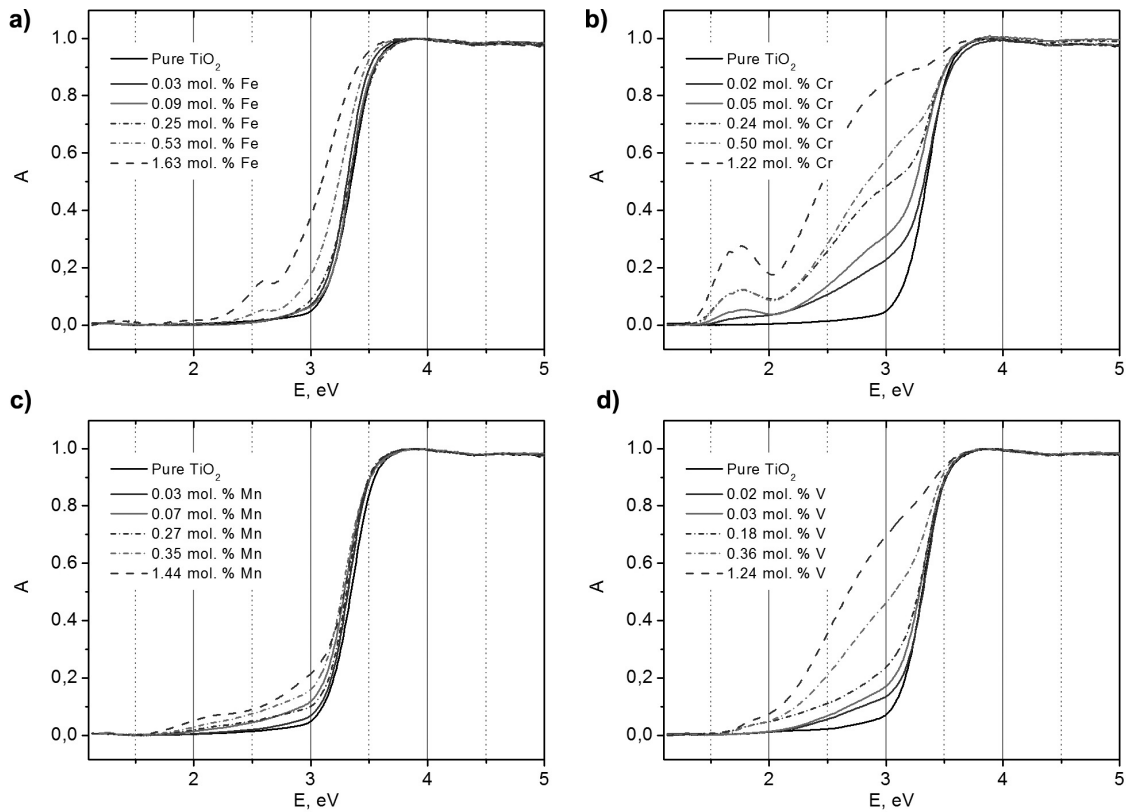


FIG. 2. UV-Vis spectra of nanocrystalline TiO_2 and nanocrystalline TiO_2 doped by Fe (a), Cr (b), Mn (c) and V (d) ions

case of V- and Cr- doped TiO_2 the intensity of absorption which is associated with impurity is comparable with the intensity of TiO_2 absorption edge.

It was mentioned before that all samples have similar nanocrystalline structure, coherent scattering region size and phase composition. The unit cell parameters for pure and doped samples also do not change significantly. Thus, one can assume that the physical band gap is also constant and the change of optical properties occurs due to the formation of new energy levels in the band gap. The value of the band gap and the positions of impurity-associated levels were determined by mathematical processing of UV-Vis spectra.

Anatase is the main component of the nanocrystalline TiO₂ sample according XRD data and it is an indirect semiconductor. The procedure of band gap determination for indirect semiconductors involves plotting of the absorption spectrum in coordinates $\sqrt{\alpha}$ vs. $h\nu$ and finding of the interceptions of the linear parts of the curve with the abscissa axis [27]. The values which are found by this approach correspond to phonon-assisted transitions. However there are no linear parts of the absorption curve in case of anatase (Fig. 3). Similar absorption spectrum was observed in anatase single crystals [31]. It was concluded that anatase absorption edge follows Urbach rule because the excitons are self-trapped. In case when the absorption edge is Urbach type, the absorption depends on photon energy as:

$$\alpha(E) = \alpha_0 \exp\left(-\sigma \frac{E_0 - E}{kT}\right),$$

where $\alpha(E)$ is absorption coefficient, σ is the steepness parameter, E_0 is optical gap value and E is photon energy. We estimated optical gap value E_0 using this equation as the slope of the absorption curve in logarithmic coordinates and obtained the value of 3.35 eV which is in good agreement with the data provided in [28]. On the other hand there is significant discrepancy with the other literature data [29] where the band gap value of anatase was found to be only 3.05 eV. The authors of this work did not provide the details about the band gap calculation procedure and did not mention Urbach nature of anatase absorption edge.

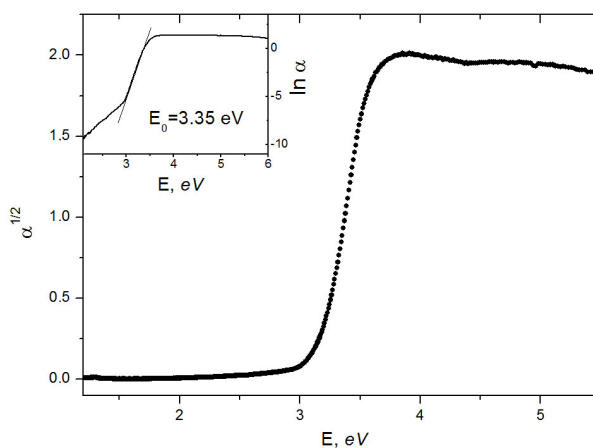
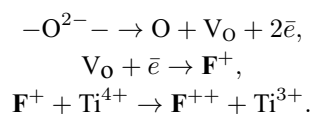


FIG. 3. UV-Vis spectrum of nanocrystalline TiO₂ $\sqrt{\alpha}$ vs. $h\nu$ and calculation of optical bang gap assuming Urbach tail (inset)

Further deconvolution of the spectra allowed us to determine the transition energies associated with defect levels in the band gap. The approach was suggested by Serpone, Kuznetsov, Rybchuk and Emeline for oxygen-deficient and nitrogen-doped titanium oxide [18–20,30]. In our work, the spectrum of undoped TiO₂ was subtracted from the spectra of doped samples and the residual spectrum was deconvoluted by Gaussian functions. The positions of maxima of Gaussian peaks were associated with different types of transitions. Some of these transitions are observed in all doped samples and there are the transitions which are characteristic for certain dopant. The deconvolution of the spectra of doped samples which Fig. 4. contain the highest concentrations of impurity are presented on Fig. 4 and the schematic representation of the transitions is presented on the Fig. 4.

Two bands, at approximately 2.7 eV and 2.9 eV, are present in the spectra of all doped samples. According to the data of Serpone and Emeline [18–20] they can be attributed to d-d transitions of Ti³⁺ or may be associated with oxygen vacancy level in the band gap [31]. The formation of Ti³⁺ ions in the lattice of TiO₂, vacancies in anionic positions and color centers may occur due to partial reduction during decomposition of organic residuals during calcination:



The bands at 3.2 – 3.3 eV may be attributed to the transitions to exciton levels near the band gap edges.

All other bands differ in the spectra of the samples with different type of dopant and were associated with d-d transitions of impurity ions or with transitions from impurity level to E_c . The positions of impurity levels in nanocrystalline anatase TiO₂ were taken the same as experimental values for rutile single crystal [32]. The levels of Fe³⁺, Cr³⁺, V⁴⁺ and Mn³⁺ lie at 3.0, 2.7, 1.9 and 2.1 eV below E_c respectively.

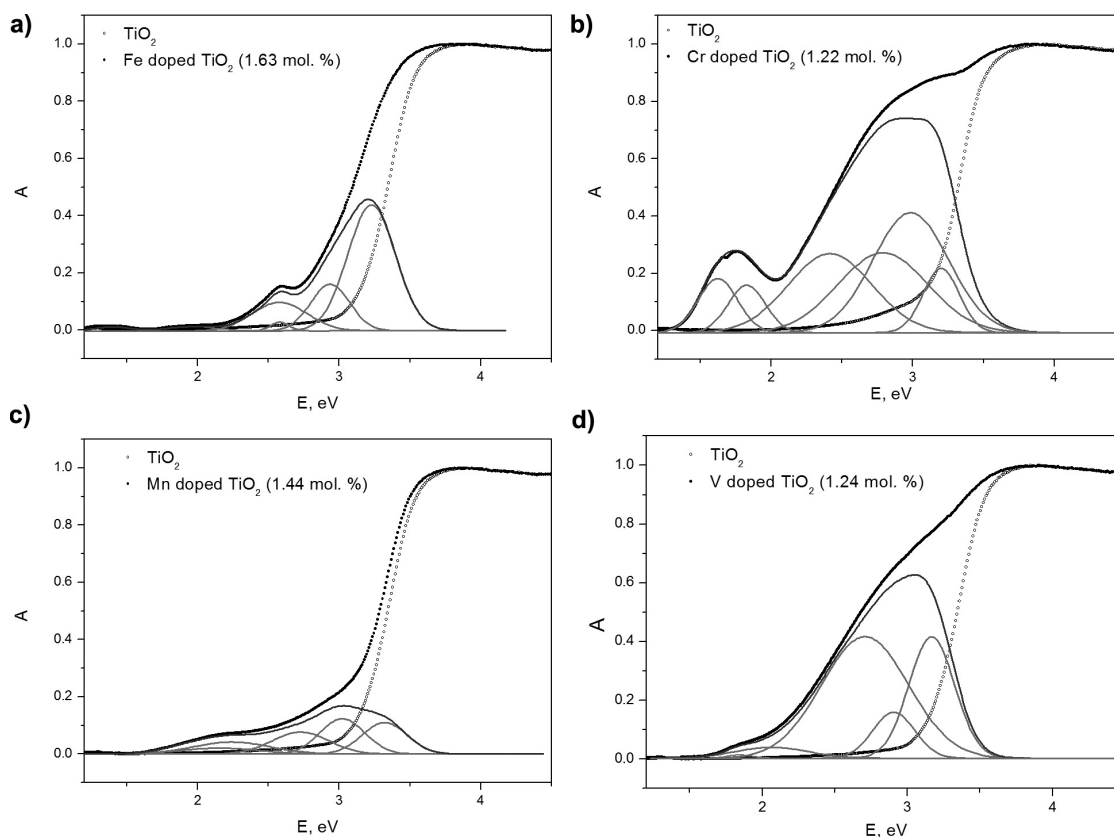


FIG. 4. Deconvolution of UV-Vis spectra of nanocrystalline TiO_2 doped by Fe (a), Cr (b), Mn (c) and V (d) ions

In the case of Cr-doped TiO_2 , we observe 3 bands with the energies 2.4, 1.8 and 1.6 eV. These energies are very close to the energies of d-d transitions of Cr^{3+} ions observed in Cr-doped spinel and ruby [33,34]. In both cases Cr^{3+} ion is in octahedral coordination and the crystal field of oxygen atoms which surround it may be assumed as similar. So, we conclude that these bands correspond to the d-d transitions of Cr^{3+} ions in anatase lattice.

The same approach can be used for interpreting the spectra of Fe-doped samples. The bands which are present in the spectra of Fe-doped samples at 1.4, 1.9 and 2.6 eV are very close to the bands of Fe^{3+} in spinel [35]. So, these bands correspond to d-d transitions of Fe^{3+} ions in anatase lattice.

The situation for V-doped and Mn-doped samples is different. The bands of d-d transitions of Mn^{3+} ion in spinel lattice and V^{4+} in garnet lattice in octahedral coordinations have energies of 2.9 and 2.4 eV respectively [36,37]. But according to the work of Mitsushima et al. the levels of V^{4+} and Mn^{3+} are sitting 2.1 and 1.9 eV below E_c . So, it is not possible to observe d-d transitions for these ions and the bands which are observed in the spectra of V- and Mn-doped samples can be attributed to the transition from the impurity level to E_c . The experimental values which have been observed in this work are 1.8 eV for V-doped anatase and 1.9 eV for Mn-doped anatase. The positions of the levels in the band gap of nanocrystalline TiO_2 are provided on the Fig. 5.

The band at approximately 2.1 – 2.2 eV is also present in the spectra of all samples. It can be attributed to the transition associated with the color center: $\text{F}^+ \rightarrow \text{F}^{+*}$ [18]. Sekiya et. al associates this band with Ti^{3+} d-d transition [31]. And Mitsushima attributes this transition to intrinsic defect states in TiO_2 [32]. So this band may be assumed as one more defect-associated band in spectra of Mn- and V-doped samples.

The influence of doping on the photocatalytic properties of nanocrystalline TiO_2 was studied in the reaction of methyl orange decoloration. The first order constants of the decoloration reaction for pure and doped samples are presented on the Fig. 6. We observe a significant decrease in the photocatalytic activity for all doped samples. Chromium and vanadium are the dopants which most effectively suppress photocatalytic activity.

Also, photocatalytic activity decreases in presence of Mn and Fe-impurities. Photocatalytic activity sharply drops in presence of very small impurity concentrations and then slightly increases in the Mn-doped series and

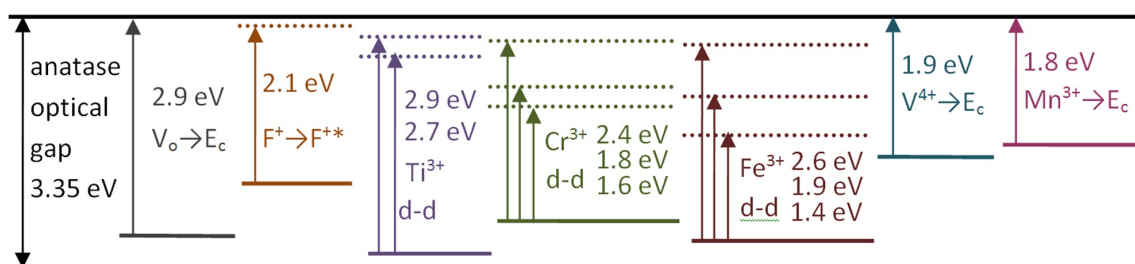


FIG. 5. The positions of energy levels in the band gap of nanocrystalline TiO₂ doped by ions of 3d-elements

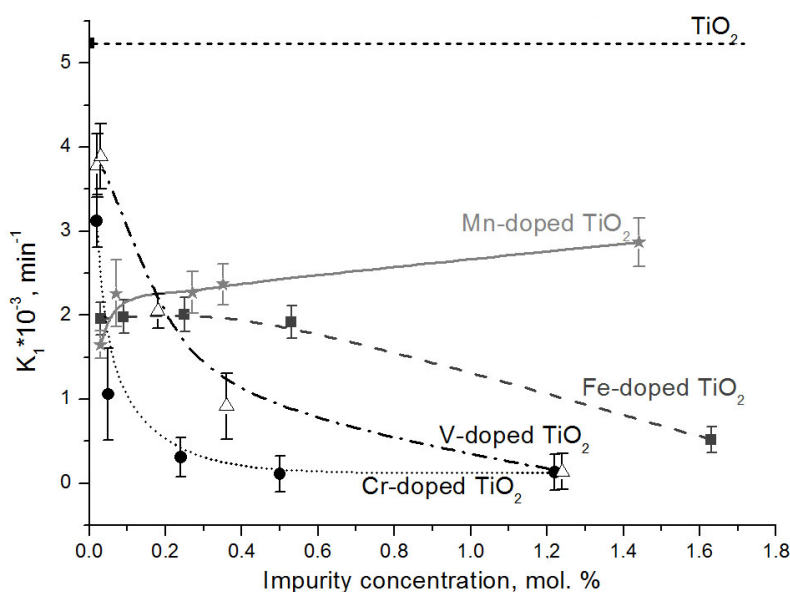


FIG. 6. First order reaction constants of the decoloration of methyl orange for nanocrystalline TiO₂ doped by ions of 3d-elements

decreases in the Fe-doped series. The absorption curves of Fe- and Mn- doped samples with low dopant concentrations are very close to the absorption curve of undoped sample. One can conclude that there may be the factors which influence photocatalytic activity in addition to the particle size, phase composition and optical properties.

So, if the structure and phase composition of doped by d-metal ions does not change in comparison with undoped samples, photocatalytic activity is effectively suppressed due to defect levels. Thus, doping by cations seems to be ineffective for developing materials with enhanced photocatalytic activity. Conversely, titanium oxide with small defect concentration is the most promising photocatalyst. The modification of its properties by preparing composites with metal particles and semiconductors indeed leads to the growth of photocatalytic activity [38,39].

On the other hand, the ability of 3d-metal ions to suppress photocatalytic activity may be also useful for some applications. For example, photocatalytic activity is not useful and even harmful in cosmetic pigments, paints, plastic fillers. In this case reactive oxygen species, which are generated due to photocatalytic reactions damage organic components of cosmetic, paint or plastic and doping by metal cations is effective way to prevent these adverse effects. Iron as non-toxic impurity may be used in TiO₂ cosmetic pigments to suppress their ability to generate reactive oxygen species under sunlight. Such pigments may provide a non-toxic alternative to known pigments like nanocrystalline cerium oxide doped by gadolinium [40].

4. Conclusions

The influence of doping on photocatalytic activity and in association with optical properties without interference with the other factors was studied on the series of the samples of nanocrystalline TiO₂ doped by Cr, Fe, V and Mn with similar phase composition, surface area and coherent scattering region sizes. The impurities effectively suppress photocatalytic activity of TiO₂. TiO₂-based materials with suppressed photocatalytic activity can be used

as plastic fillers and cosmetic pigments because they will not generate active radicals under solar irradiation. UV-Vis spectral analysis of the samples allowed us to determine the nature of the levels, which are formed in the band gap. In case of all samples, we observe d-d transitions of Ti^{3+} ion and a transition from the color center to E_c . In case of Cr- and Fe-doped samples, we observe d-d transitions of these ions and in the spectra of Mn- and V-doped TiO_2 the transitions from metal impurity level to E_c are present.

Acknowledgements

This work was supported by Russian Science Foundation (research project 17-73-10493). The measurements on Rigaku D/MAX 2500 diffractometer and Zeiss Libra 200 electron microscope were have been done due to the Program of Development of M. V. Lomonosov State University.

References

- [1] Herrmann J.-M. Detrimental cationic doping of titania in photocatalysis: why chromium Cr^{3+} -doping is a catastrophe for photocatalysis, both under UV- and visible irradiations. *New J. Chem.*, 2012, **36**, P. 883–890.
- [2] Bettinelli M., Speghini A., Falcomer D., Daldosso M., Dallacasa V., Romano V. Photocatalytic, spectroscopic and transport properties of lanthanide-doped TiO_2 nanocrystals. *J. Phys.: Condens. Matter*, 2006, **18**, P. S2149–S2160.
- [3] Cui L., Wang Yu., Niu M., Chen G., Cheng Y. Synthesis and visible light photocatalysis of Fe-doped TiO_2 mesoporous layers deposited on hollow glassmicrobeads. *Journal of Solid State Chemistry*, 2009, **182**, P. 2785–2790.
- [4] Karvinen S., Lamminmäk R.-J. Preparation and characterization of mesoporous visible-light-active anatase. *Solid State Sciences*, 2003, **5**, P. 1159–1166.
- [5] Kumbhar A., Chumanov G. Synthesis of iron(III)-doped titania nanoparticles and its application for photodegradation of sulforhodamine-B pollutant. *Journal of Nanoparticle Research*, 2005, **7**, P. 489–498.
- [6] Li G., Liu C., Liu Yu. Different effects of cerium ions doping on properties of anatase and rutile TiO_2 . *Applied Surface Science*, 2006, **253**, P. 2481–2486.
- [7] Liu B., Wanga X., Caia G., Wen L., Song Y., Zhao X. Low temperature fabrication of V-doped TiO_2 nanoparticles, structure and photocatalytic studies. *Journal of Hazardous Materials*, 2009, **169**, P. 1112–1118.
- [8] Liu S., Xie T., Chen Z., Wu J. Highly active V- TiO_2 for photocatalytic degradation of methyl orange. *Applied Surface Science*, 2009, **255**, P. 8587–8592.
- [9] Andreas Mattsson A., Leideborg M., Karin Larsson, Westin G., Osterlund L. Adsorption and Solar Light Decomposition of Acetone on Anatase TiO_2 and Niobium Doped TiO_2 Thin Films. *J. Phys. Chem. B*, 2006, **110**, P. 1210–1220.
- [10] Ranjit K.T., Willner I., Bossmann S.H., Braun A.M. Lanthanide Oxide Doped Titanium Dioxide Photocatalysts: Effective Photocatalysts for the Enhanced Degradation of Salicylic Acid and t-Cinnamic Acid. *Journal of Catalysis*, 2001, **204**(2), P. 305–313.
- [11] Xiao J., Peng T., Li R., Peng Z., Yan C. Preparation, phase transformation and photocatalytic activities of cerium-doped mesoporous titania nanoparticles. *Journal of Solid State Chemistry*, 2006, **179**, P. 1161–1170.
- [12] Xin B., Ren Z., Wang P., Liu J., Jing L., Fu H. Study on the mechanisms of photoinduced carriers separation and recombination for Fe^{3+} - TiO_2 photocatalysts. *Applied Surface Science*, 2007, **253**, P. 4390–4395.
- [13] Silva A.M.T., Silva C.G., Drazic G., Faria J.L. Ce-doped TiO_2 for photocatalytic degradation of chlorophenol. *Catalysis Today*, 2009, **144**, P. 13–18.
- [14] Kemp T.J., McIntyre R.A., Transition metal-doped titanium(IV) dioxide: Characterisation and influence on photodegradation of poly(vinyl chloride). *Polymer Degradation and Stability*, 2006, **91**, P. 165–194.
- [15] Kolesnik I.V., Chebotaeva G.S., Yashina L.V., Konstantinova E.A., Eliseev A.A., Lukashin A.V., Tretyakov Yu.D. Preparation of nanocrystalline nitrogen-doped mesoporous titanium dioxide. *Mendeleev Communications*, 2012, **23**(1), P. 11–13.
- [16] Savio A.K.P.D., Fletcher J., Robles Hernandez F.C. Sonosynthesis of nanostructured TiO_2 doped with transition metals having variable bandgap. *Ceramics International*, 2013, **39**, P. 2753–2765.
- [17] Di Paola A., Marci G., Palmisano L., Schiavello M., Uosaki K., Ikeda S., B. Ohtani B. Preparation of Polycrystalline TiO_2 Photocatalysts Impregnated with Various Transition Metal Ions: Characterization and Photocatalytic Activity for the Degradation of 4-Nitrophenol. *J. Phys. Chem. B*, 2002, **106**, P. 637–645.
- [18] Serpone N. Is the Band Gap of Pristine TiO_2 Narrowed by Anion- and Cation-Doping of Titanium Dioxide in Second-Generation Photocatalysts? *J. Phys. Chem. B*, 2006, **110**, P. 24287–24293.
- [19] Kuznetsov V.N., Serpone N. Visible Light Absorption by Various Titanium Dioxide Specimens. *J. Phys. Chem. B*, 2006, **110**, P. 25203–25209.
- [20] Kuznetsov V.N., Serpone N. On the Origin of the Spectral Bands in the Visible Absorption Spectra of Visible-Light-Active TiO_2 Specimens Analysis and Assignments. *J. Phys. Chem. C*, 2009, **113**, P. 15110–15123.
- [21] Lebedev V.A., Kozlov D.A., Kolesnik I.V., Poluboyarinov A.S., Becerikli A.E., Grnert W., Garshev A.V. The amorphous phase in titania and its influence on photocatalytic properties. *Applied Catalysis B: Environmental*, 2016, **195**, P. 39–47.
- [22] Di Paola A., Bellardita M., Palmisano L., Barbierikova Z., Brezova V. Influence of crystallinity and OH surface density on the photocatalytic activity of TiO_2 powders. *Journal of Photochemistry and Photobiology A: Chemistry*, 2013, **273**, P. 59–67.
- [23] Sakatani Y., Grosso D., Nicole L., Boissiere C., Soler-Illia G.J. de A.A., Sanchez C.J. Optimised photocatalytic activity of grid-like mesoporous TiO_2 films: effect of crystallinity, pore size distribution, and pore accessibility. *Mater. Chem.*, 2006, **16**, P. 77–82.
- [24] Petricek X.V., Dusek M., Palatinus L. Crystallographic Computing System JANA2006: General features. *Zeitschrift für Kristallographie - Crystalline Materials*, 2014, **229**, P. 345352–34356.
- [25] Almjasheva O.V. Formation and structural transformations of nanoparticles in the TiO_2 - H_2O system. *Nanosystems: physics, chemistry, mathematics*, 2016, **7**(6), P. 1031–1049.

- [26] Vildanova M.F., Kozlov S.S., Nikolskaia A.B., Shevaleevskiy O.I., Tsvetkov N.A., Alexeeva O.V., Larina L.L. Niobium-doped titanium dioxide nanoparticles for electron transport layers in perovskite solar cells. *Nanosystems: physics, chemistry, mathematics*, 2017, **8**(4), P. 540–545.
- [27] Pankove J.I. *Optical Processes in Semiconductors*. Dover Publications, Inc., New York, 1975, 343 p.
- [28] Tang H., Levy F., Berger H., Schmid P.E. Urbach tail of anatase TiO₂. *Physical Review B*, 1995, **52**(11), P. 7771–7774.
- [29] Di Paola A., Bellardita M., Palmisano L., Parrino F. Junction Effect on the Photocatalytic Activity of Mixed-Phase TiO₂ Nanoparticles. *ECS Transactions*, 2010, **25**(42), P. 29-35.
- [30] Emeline A.V., Kuznetsov V.N., Rybchuk V.K., Serpone N. Visible-Light-Active Titania Photocatalysts: The Case of N-Doped TiO₂ - Properties and Some Fundamental Issues. *International Journal of Photoenergy*, 2008, P. 1-19.
- [31] Sekiya T., Ichimura K., Igarashi M., Kurita S. Absorption spectra of anatase TiO₂ single crystals heat-treated under oxygen atmosphere. *Journal of Physics and Chemistry of Solids*, 2000, **61**, P. 1237–1242.
- [32] Mizushima K., Tanaka M., Asai A., Iida S., Goodenough J.B. Impurity Levels Of Iron-Group Ions In TiO₂. *J Phys. Chem. Solids*, 1979, **10**, P. 1129–1140
- [33] Wood D.L., Imbusch G.F., Macfarlane R.M., Kisliuk P., and Larkin D.M. Optical Spectrum of Cr³⁺ Ions in Spinels. *The Journal of Chemical Physics*, 1968, **48**, P. 5255–5263.
- [34] Low W. Absorption Lines of Cr³⁺ in Ruby. *The Journal of Chemical Physics*, 1960, **33**, P. 1162–1163.
- [35] Reddy B.J., Frost R.L. Spectroscopic characterization of chromite from the Moa-Baracoa Ophiolitic Massif, Cuba. *Spectrochimica Acta Part A*, 2005, **61**, P. 1721–1728.
- [36] Bosi F., Hälenius U., Andreozzi G.B., Skogby H., Lucchesin S. Structural refinement and crystal chemistry of Mn-doped spinel: A case for tetrahedrally coordinated Mn³⁺ in an oxygen-based structure. *American Mineralogist*, 2007, **92**, P. 27–33.
- [37] Brenier A., Madej C., Pedrini C., Boulon G. Crystal growth and luminescence properties of calcium- and vanadium-doped gadolinium gallium garnet. *Chemical Physics Letters*, 1991, **177**(6), P. 590–592.
- [38] Karthikeyan N., Narayanan V., Stephen A. Visible light degradation of textile effluent using nanostructured TiO₂/Ag/CuO photocatalysts. *Nanosystems: Physics, Chemistry, Mathematics*, 2016, **7**(4), P. 695–698.
- [39] Kozlov D.A., Lebedev V.A., Polyakov A.Yu, Khazova K.M., Garshev A.V. The microstructure effect on the Au/TiO₂ and Ag/TiO₂ nanocomposites photocatalytic activity. *Nanosystems: Physics, Chemistry, Mathematics*, 2018, **9**(2), P. 266–278.
- [40] Popov A.L, Savintseva I.V., Mysina E.A., Shcherbakov A.B., Popova N.R., Ivanova O.S., Ivanov V.K. Cytotoxicity analysis of gadolinium doped cerium oxide nanoparticles on human mesenchymal stem cells. *Nanosystems: Physics, Chemistry, Mathematics*, 2018, **9**(3), P. 18–25.

On an adsorption/photocatalytic performance of nanotubular $\text{Mg}_3\text{Si}_2\text{O}_5(\text{OH})_4/\text{TiO}_2$ composite

A. A. Krasilin^{1,2}, I. S. Bodalyov³, A. A. Malkov³, E. K. Khrapova², T. P. Maslennikova⁴, A. A. Malygin³

¹Kurnakov Institute of General and Inorganic Chemistry of the Russian Academy of Sciences,
31 Leninsky prospect, Moscow 119991, Russia

²Ioffe Institute, 26 Politekhnikeskaya street, St. Petersburg, 194021, Russia

³Saint-Petersburg State Institute of Technology, 26 Moskovskiy Prospekt, St. Petersburg 190013, Russia

⁴Institute of Silicate Chemistry, Russian Academy of Sciences,
2 Naberezhnaya Admirala Makarova, St. Petersburg 199034, Russia

ikrasilin@gmail.com

PACS 68.43.Mn, 82.65.+r

DOI 10.17586/2220-8054-2018-9-3-410-416

Here, we study a performance of nanotubular $\text{Mg}_3\text{Si}_2\text{O}_5(\text{OH})_4/\text{TiO}_2$ hybrid adsorbent/photocatalyst in the process of decolorizing an aqueous solution of crystal violet. The composite material was produced by hydrothermal treatment with one or more subsequent cycles of TiCl_4 treatment and vapor-phase hydrolysis according to the molecular layering technique. Decolorization was observed in situ by UV-VIS spectroscopy. It was found that TiO_2 deposition yields 2 to 3 times improvement of decolorization performance. Depending on TiO_2 phase type – amorphous or crystalline – this rise is related with either enhancement of adsorption rate either appearance of photocatalytic activity. Finally, fitting procedure issues in case of complex decolorization process were discussed.

Keywords: chrysotile nanotubes, titanium tetrachloride, titanium oxide, crystal violet dye, adsorption, photocatalysis, water remediation.

Received: 1 April 2018

Revised: 8 May 2018

1. Introduction

In the last few decades, wastewater remediation becomes an important problem, the disregard of which accelerates depletion of fresh water resources and ocean contamination. Heavy and textile industries provide various contaminants like heavy metal ions, organic dyes, and diverse organics [1–3]. In order to prevent the overspread of hazardous materials, a number of techniques based on adsorption (separation) [4–7] and catalytic alteration [8–12] can be applied. The problem is that several pollutants can be present in the wastewater simultaneously, and a remediating agent which possesses only one instrument for purification, will not always be capable of handling them simultaneously.

Here, we study a combination of adsorption performance of synthetic $\text{Mg}_3\text{Si}_2\text{O}_5(\text{OH})_4$ chrysotile nanotubes with photocatalytic action of TiO_2 . The nanotubes can be synthesized by hydrothermal method using various crystalline and amorphous initial components [13–17]. Flexible capabilities of chemical composition tuning – for example, by introducing various d-elements like Ni [18–20], Co [21], Fe [22–24] – and synthesis conditions allows to control surface properties (active sites) and area [25]. Hydroxyl groups reached surface together with the inner channel make chrysotile nanotubes favorable for adsorption and immobilization of various molecules [26–28] and heavy metal ions of Pb, Cd, Sr, and Nd [29–32].

In turn, TiO_2 is a well-known and widely used photocatalysis for water purification and splitting [33–35]. Its photocatalytic activity can be further enhanced by creating various types of composite materials with metals [12,34], sulfides [36–39], oxides and clays [40–42], or by varying the shape of TiO_2 nanoparticles [43–45]. In our present study, we used molecular layer deposition technique [46,47] with subsequent hydrolysis to obtain TiO_2 phase on $\text{Mg}_3\text{Si}_2\text{O}_5(\text{OH})_4$ nanotubes.

2. Experimental

Chrysotile nanotubes were synthesized hydrothermally using a procedure described in detail elsewhere [48,49]. Stoichiometric (with Mg:Si molar ratio as 3:2) mixture of MgO and SiO_2 were taken as initial compounds. Hydrothermal treatment was carried out in stainless-steel high-pressure vessels at 350 °C, 70 MPa during 24 h using 1 wt.% NaOH water solution as hydrothermal medium.

$Mg_3Si_2O_5(OH)_4/TiO_2$ composite synthesis was carried by sequential treatment of the nanotubes by $TiCl_4$ and H_2O vapors in a flow-through reactor equipped with a McBain balance (see [49] for details). Initially, as-synthesized nanotubes were annealed at 400 °C for 5 h on air and then exposed to dry N_2 for 2 hours in order to remove adsorbed water molecules and stabilize surface hydroxyl content. On a chemisorption step, chrysotile nanotubes were treated by $TiCl_4$ at 150 °C and 400 °C during 5 – 6 h. Generally, this time is enough to saturate the nanotubes by $TiCl_4$, what was controlled by McBain balance. After that, the reaction zone was purged with dry nitrogen. For the hydrolysis step, the sample was exposed to a stream of air passed at 20 °C through a bubbler filled with distilled water and at temperature in the reactor starting from 150 °C to 400 °C. A final step was purging the reactor with dry N_2 at 400 °C. Four full cycles (chemisorption–purge–hydrolysis–purge) were carried out for the sample treated by $TiCl_4$ at 150 °C in order to increase TiO_2 content.

Thus, 3 samples were prepared for further study: as-synthesized chrysotile nanotubes; nanotubes treated with $TiCl_4$ and H_2O for 4 times (cycles) at the chemisorption temperature of 150 °C; and nanotubes treated once at 400 °C.

X-ray powder diffraction (XRPD) patterns of as-synthesized chrysotile nanotubes and the products of their treatment were acquired by a Rigaku Smartlab SE powder diffractometer with a Cu anode ($\lambda_{Cu}=0.15406$ nm) in the 5 – 70 ° 2θ range with 0.01 ° steps. A PDF-2 database was used for phase identification and peak indexing.

Specific surface area was calculated involving the Braunauer–Emmett–Teller theory. 9-points N_2 adsorption isotherms were acquired using Micromeritics ASAP 2020 analyzer. Prior the measurement, the samples were annealed at 400° until a constant weight was obtained.

Scanning electron microscopy (SEM) was performed on A Carl Zeiss NVision 40 SEM/EDS workstation.

In situ studies of decolorization performance were carried out on a modular system consisting of a Xe light source (Mikropack HPX-2000), temperature-controlled cuvette holder with magnetic stirrer (Quantum Northwest TC 125), attenuator, optical fiber connectors (Ocean Optics QP600-1-SR), and a UV-VIS spectrometer (Ocean Optics QE 65000). 1.5 ± 0.1 mg of the sample was mixed with 1.9 ml of deionized water in 4 ml PMMA cuvettes. The suspensions obtained were magnetically stirred at 25 °C throughout the experiment. First, the spectrum of each suspension was recorded in the 300 – 800 nm range and stored as the reference. Then, 0.1 ml of 400 mg/l crystal violet aqueous solution was added to the suspension. Absorbance spectra were recorded for every minute during more than 4 hours starting right after the dye addition. Here and subsequently, this regime is called measurement “on light”. To exclude action of light, the same batch of kinetics experiment were performed “in dark” by blocking off the beam. The cuvette with the sample was lighted up for 1 – 2 seconds only to acquire the spectra. For 4 hours run, 9 to 10 measurements were made.

Solution decolorization P_t at time t was calculated as follows:

$$P_t = \frac{I_0 - I_t}{I_0} 100 \%, \quad (1)$$

where I_0 is initial (maximal) absorbance intensity, and I_t is intensity at time t .

3. Results and discussion

Figure 1a shows XRPD patterns of initial sample and its treatment products. According to phase analysis, hydrothermal synthesis yields chrysotile (card #10-381) nanotubes together with some amount of platy lizardite (#82-1837). Principal reflections of chrysotile and lizardite overlap, so only specific lizardite reflections are marked on the XRPD pattern. The presence of the platy lizardite phase could be caused by Al cations presence in starting mixture [48] because Al doping of nanotubular chrysotile strongly effects on its morphology [50]. However, crystallinity of platy lizardite is significantly better than that of tubular chrysotile. The fact that the intensities of reflections at around 35° 2θ are comparable means that the lizardite phase content is negligibly low.

Low-temperature (150 °C) treatment with $TiCl_4$ and H_2O vapors does not lead to formation of new essential crystalline phases except NaCl as a byproduct. Ti element presence with concentration around 0.3 mmol per 1 g of $Mg_3Si_2O_5(OH)_4$ in case of low-temperature treatment was confirmed in [49] by SEM/EDS and chemical analysis, so we can assume that TiO_2 stays mostly in amorphous phase bounded with the chrysotile nanotube surface. High-temperature treatment with $TiCl_4$ and H_2O (400 °C) results in the formation of a mixture of anatase and rutile with predomination of the latter (Ti content around 2.9 mmol/g [49]). Chrysotile phase, in general, withstands the heat exposure, and its XRPD pattern remains the same.

Figure 1b demonstrates specific surface area decrease during the treatment of chrysotile nanotubes with $TiCl_4$ and H_2O vapors. The observable drop is caused both by heat effect (partial chrysotile dehydroxylation and shrinkage of its interlayer space) and, mainly, by mass increase due to $TiCl_4$ deposition and hydrolysis.

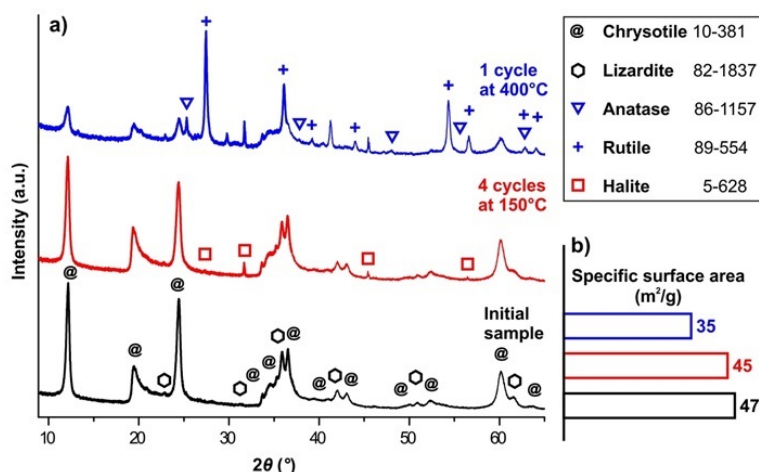


FIG. 1. XRPD patterns of initial sample and samples after treatment with TiCl_4 and H_2O vapors (see experimental part for details). Cards numbers are given according to the PDF-2 database; b) Specific (BET) surface area of initial sample and its treatment products

Figure 2 shows SEM-images of the samples obtained in SE (morphological contrast) and BSE modes (phase contrast). As-synthesized chrysotile nanotubes have diameters in the range of 30 – 50 nm and length varying from hundreds of nm up to 1 – 2 μm (Fig. 2a). Chrysotile nanotubes form various morphologies including cylinder, cylinder-in-cylinder, and cone. General nanotubular form preserves during TiCl_4 and H_2O vapors treatment, that correlates with the XRPD data. In particular, SEM-images on Fig. 2b (low-temperature treatment) reveal the absence morphology and phase which would differ from the nanotubular one. In contrast, high-temperature treatment (Fig. 2c) leads to the formation of highly crystalline – and more atomically dense in comparison to chrysotile nanotubes – particles which obviously consist of TiO_2 . The average size of the particle is around 100 nm, but there is also a fraction of them with the sizes under tens of nm.

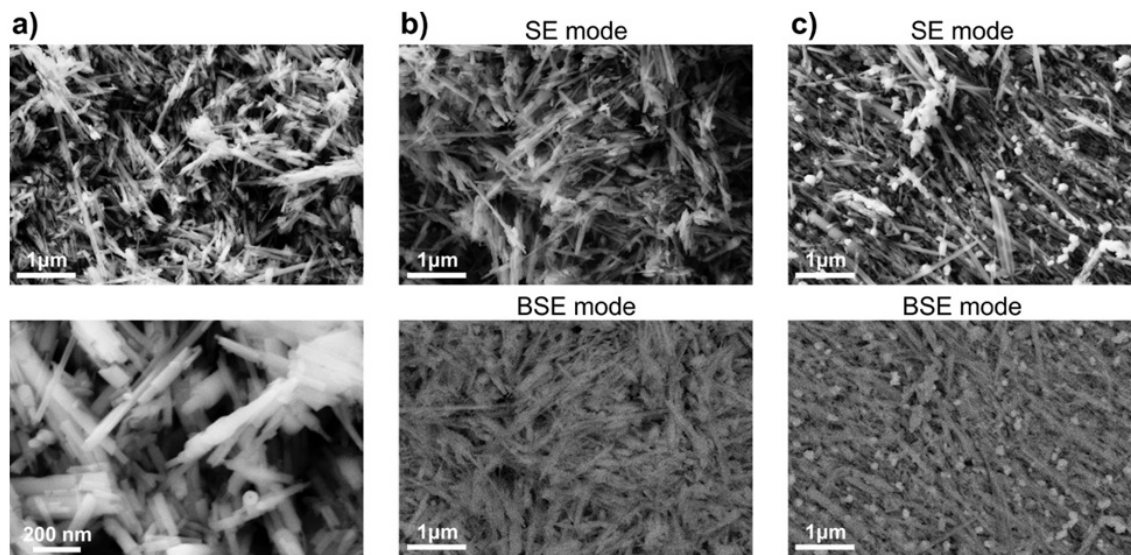


FIG. 2. SEM-images of a) initial sample, b) product of 4 cycles treatment at 150 °C, c) product of 1 cycle treatment at 400 °C. BSE mode gives phase contrast (see text for details)

Figure 3a demonstrates an example of change in crystal violet solution absorbance spectra during $\text{Mg}_3\text{Si}_2\text{O}_5(\text{OH})_4/\text{TiO}_2$ composite-promoted decolorization. A common situation for all samples studied is that the majority of the decolorization effect is achieved during the first hour of solution contact with the solid phase. After that time, the decolorization rate decreases gradually. In accordance with Fig. 3, none of the samples was able

to reach 100% decolorization degree, which could be related both with general solid/liquid ratio and the sample's individual performance. And the latter changes drastically.

Comparative analysis of decolorization kinetic curves reveals several following features: 1) decolorization performance of untreated sample (as-synthesized chrysotile nanotubes) is the lowest among the samples tested; 2) there is an increase in decolorization depending on how the measurements were carried out (on light or in dark, see experimental part for details); 3) there is a divergence (at the initial time of the experiment) and then convergence of kinetic curves on Fig. 3c. The initial sample, as we suppose, possesses only adsorption performance, whereas the samples treated by $TiCl_4$ and H_2O vapors can have both adsorption and photocatalytic potential, so it should be primarily compared with the samples investigated in dark. This comparison shows that the chrysotile nanotubes treated by 4 cycles at 150 °C have the highest adsorption performance. Assuming equal measurement conditions (temperature, pH, dye concentration, solid phase mass, stirring), two key factors govern adsorption performance: specific surface area and surface properties. Treatment with $TiCl_4$ and H_2O vapors leads to decrease of the former (Fig. 1b), so the increase of adsorption performance is caused by advantageous change of surface properties, in other words, a number and/or a type (force) of active sites. It is most probably that after low-temperature treatment TiO_2 , while it does not form crystalline phase, distributes in an optimal way on the nanotube's surface and forms a large number of active sites, thus increasing total adsorption performance. High-temperature treatment strongly decreases the surface area and forces TiO_2 to form autonomous crystalline phase. Note that the general forms of the kinetic curves on Fig. 3b and Fig. 3d (measured in dark) are highly similar. This fact can be related to partial reduction of chrysotile nanotubes surface properties after crystalline TiO_2 phase formation.

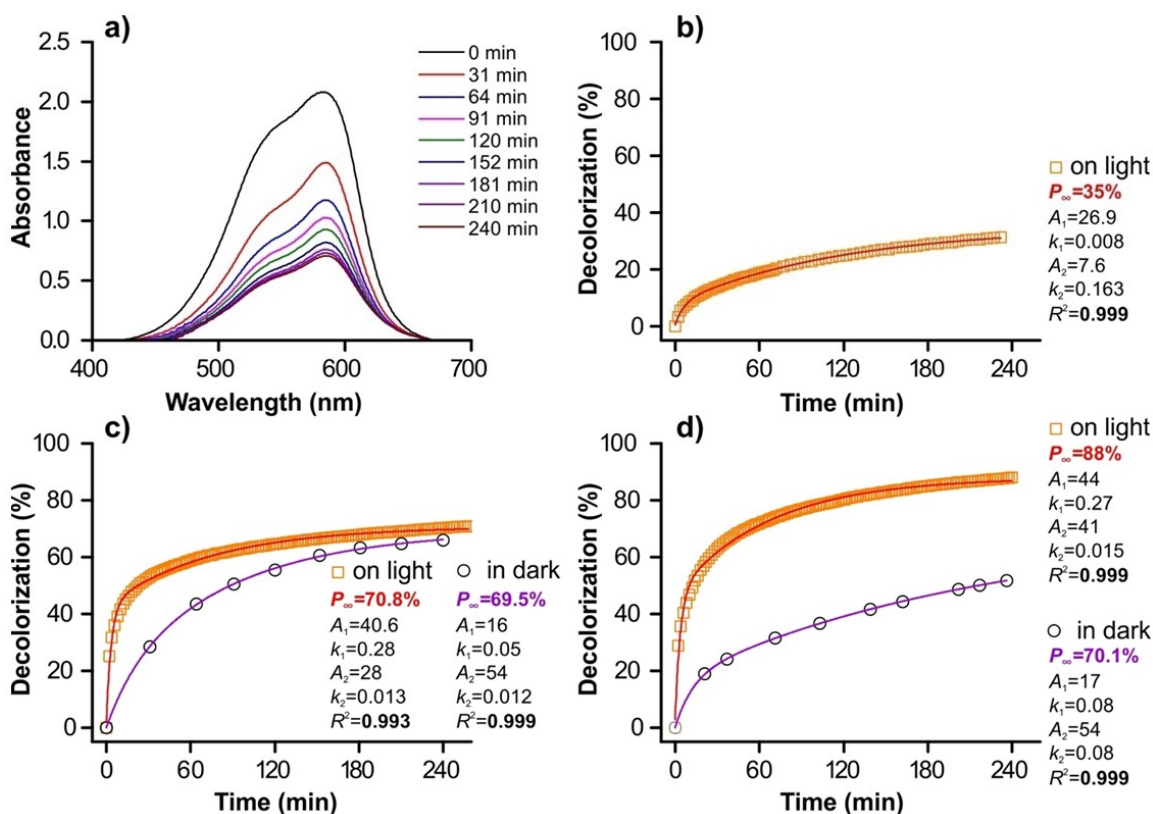


FIG. 3. a) Change in UV-VIS absorbance spectra of crystal violet solution during the decolorization experiment performed in dark (for the 4 treatment cycles at 150 °C). Decolorization curves for b) initial sample, c) sample after 4 treatment cycles at 150 °C, and d) sample after 1 treatment cycle at 400 °C. Points denote experimental data, and solid lines represent the results of fitting procedure (see text for details). Text insets contain information on fitting parameters

The most probable origin of the second feature (Fig. 3c,d) is photocatalytic action of TiO_2 . A common condition for the photocatalysis is an existence of sufficiently wide bandgap, which can be realized in crystalline solid. According to that, there is an essential increase of decolorization performance when measured on light

only in case crystalline TiO₂ is present in the system. Interaction with light grants 2 – 3 times increase of decolorization performance (Fig. 3d). After 4 hours of the experiment, the divergence of the curves decreases slightly. In case of amorphous TiO₂ there is also a light-induced decolorization, which can be seen at the very initial time of the process (Fig. 3c), the effect of which vanishes during the experiment. After 4 hours, the two curves become very similar. It is interesting to note that the maximum difference between the curves obtained on light and in dark for both samples achieves after around 15 – 20 minutes of exposure, but crystalline TiO₂ phase provide long-term constant shift of decolorization performance. Most likely this contribution should be related to photocatalytic activity. The Mg₃Si₂O₅(OH)₄/TiO₂ composite material obtained by 1 treatment cycle at 400 °C is the most appropriate one in the case of combined adsorption and interaction with light is utilized for water remediation. Considering complex interaction process of pollutant with decontaminating agent, there is often a problem of choosing the appropriate kinetic model. Here, we tried to adopt so-called double-exponential model used for description of heavy metal ions adsorption kinetics [51,52]. The main reason for the use of this model is that it accounts for two ongoing processes, which, in our case, are adsorption and light-induced decolorization. Model equation is written as follows:

$$P_t = P_\infty - A_1 \exp(-k_1 t) - A_2 \exp(-k_2 t), \quad (2)$$

where P_t is decolorization at time t , P_∞ is decolorization at infinitely long time of the experiment, A_1 , k_1 , A_2 , k_2 are model parameters. The main objective of this fit is to estimate the P_∞ value which determines the performance of the studied material. Nonlinear fitting procedure was applied.

Text insets on Fig. 3b,c,d demonstrate fitting results for the decolorization curves. All cases show high value of adjacent R^2 criterion, which is, does not speak well for applicability and physical consistency of the chosen model. However, we can consider a number of features regarding P_∞ value obtained.

First, for some samples (measured on light) the P_∞ value can be underestimated by the fitting procedure. This is a typical situation for the case of kinetic data approximation [53]. In our case, it especially can be seen on Fig. 3d: there is deviation of the fitted curve at the end of the experiment. In addition, adsorption phenomena are considered to be equilibrium processes (in terms of adsorption and desorption speeds), whereas photocatalysis either occurs continuously either fades out because of photocatalyst degradation, and this can bring additional error to the P_∞ value.

Second, double-exponential model was originally applied solely to the adsorption process, and the parts of the model equation (2) were rather related to certain adsorption stages. This complicates discussion of model parameter values in the case when adsorption is combined with other types of processes promoting decolorization. Nevertheless, we should note the proximity of model parameters for the samples obtained by low- and high-temperature treatment and measured in dark (Fig. 3c,d): treatment regime influences on adsorption rate stronger than on an adsorption capacity (proportional to observed decolorization). Finally, according to fitting results on Fig. 3d, the light-induced process which granted the highest performance of the composite with crystalline TiO₂ will lose its influence at long-term exposure lying beyond the current experiment time.

4. Conclusion

Here, we report on the application of Mg₃Si₂O₅(OH)₄ chrysotile nanotubes / TiO₂ composite as an adsorbent and photocatalyst for the process of decolorization of crystal violet. The composite material was obtained by hydrothermal synthesis of nanotubes with subsequent treatment with TiCl₄ and H₂O vapors according to the molecular layering technique. This treatment allows control of the TiO₂ content and phase state. Chrysotile nanotube treatment results in a 2- to 3-fold increase of their decolorization potential, depending on TiO₂ phase type. If it forms amorphous phase on the nanotubes surface, then the increase is caused mostly by favorable change of the active sites type. If it forms crystal phase, then decolorization is a combined action of adsorption and photocatalysis. The latter affords the highest decolorization rates.

Although the proposed composites are promising for the cases where combined remediation action is needed, there is still a number of hindrances regarding quantitative description (modeling) of the overall process kinetics. This is crucial for both in-depth understanding of relations between adsorption and photocatalysis, and design of an appropriate apparatus.

Acknowledgements

The research was supported by Russian Science Foundation grant 17-73-10426. The SEM research was performed using the equipment of the JRC PMR IGIC RAS. The XRPD study was performed using the equipment of the Engineering Centre of Saint Petersburg State Technological Institute (Technical University).

References

- [1] Burakov A.E., Galunin E.V., Burakova I.V., Kucherova A.E., Agarwal S., Tkachev A.G., Gupta V.K. Adsorption of heavy metals on conventional and nanostructured materials for wastewater treatment purposes: A review. *Ecotoxicol. Environ. Saf.*, 2018, **148**, P. 702–712.
- [2] Khin M.M., Nair A.S., Babu V.J., Murugan R., Ramakrishna S. A review on nanomaterials for environmental remediation. *Energy Environ. Sci.*, 2012, **5** (8), P. 8075.
- [3] Cai Z., Sun Y., Liu W., Pan F., Sun P., Fu J. An overview of nanomaterials applied for removing dyes from wastewater. *Environ. Sci. Pollut. Res.*, 2017, **24** (19), P. 15882–15904.
- [4] Ali I., Gupta V.K. Advances in water treatment by adsorption technology. *Nat. Protoc.*, 2007, **1** (6), P. 2661–2667.
- [5] Kamaruddin M.A., Yusoff M.S., Aziz H.A., Akinbile C.O. Recent developments of textile waste water treatment by adsorption process: a review. *Int. J. Sci. Res. Knowl*, 2013, P. 60–73.
- [6] Mittal A., Mittal J., Malviya A., Kaur D., Gupta V.K. Adsorption of hazardous dye crystal violet from wastewater by waste materials. *J. Colloid Interface Sci.*, 2010, **343** (2), P. 463–473.
- [7] Gupta V.K., Kumar R., Nayak A., Saleh T.A., Barakat M.A. Adsorptive removal of dyes from aqueous solution onto carbon nanotubes: A review. *Adv. Colloid Interface Sci.*, 2013, **193–194**, P. 24–34.
- [8] Peter A., Mihaly-Cozmuta A., Nicula C., Mihaly-Cozmuta L., Jastrzbska A., Olszyna A., Baia L. UV light-assisted degradation of methyl orange, methylene blue, phenol, salicylic acid, and rhodamine B: photolysis versus photocatalysis. *Water, Air, Soil Pollut.*, 2017, **228** (1), P. 41.
- [9] Mohmood I., Lopes C.B., Lopes I., Ahmad I., Duarte A.C., Pereira E. Nanoscale materials and their use in water contaminants removal – a review. *Environ. Sci. Pollut. Res.*, 2013, **20** (3), P. 1239–1260.
- [10] Chakma S., Moholkar V.S. Investigation in mechanistic issues of sonocatalysis and sonophotocatalysis using pure and doped photocatalysts. *Ultrason. Sonochem.*, 2015, **22**, P. 287–299.
- [11] Chu K.H., Al-Hamadani Y.A.J., Park C.M., Lee G., Jang M., Jang A., Her N., Son A., Yoon Y. Ultrasonic treatment of endocrine disrupting compounds, pharmaceuticals, and personal care products in water: A review. *Chem. Eng. J.*, 2017, **327**, P. 629–647.
- [12] Kozlov D.A., Lebedev V.A., Polyakov A.Y., Khazova K.M., Garshev A.V. The microstructure effect on the Au/TiO₂ and Ag/TiO₂ nanocomposites photocatalytic activity. *Nanosyst.: Phys. Chem. Math.*, 2018, **9** (2), P. 266–278.
- [13] Korytkova E.N., Maslov A.V., Pivovarova L.N., Drozdova I.A., Gusarov V.V. Formation of Mg₃Si₂O₅(OH)₄ nanotubes under hydrothermal conditions. *Glas. Phys. Chem.*, 2004, **30** (1), P. 51–55.
- [14] Falini G., Foresti E., Gazzano M., Gualtieri A.F., Leoni M., Lesci I.G., Roveri N. Tubular-shaped stoichiometric chrysotile nanocrystals. *Chem. Eur. J.*, 2004, **10** (12), P. 3043–3049.
- [15] Bloise A., Belluso E., Catalano M., Barrese E., Miriello D., Apollaro C. Hydrothermal alteration of glass to chrysotile. *J. Am. Ceram. Soc.*, 2012, **95** (10), P. 3050–3055.
- [16] Lafay R., Montes-Hernandez G., Janots E., Chiriac R., Findling N., Toche F. Nucleation and growth of chrysotile nanotubes in H₂SiO₃/MgCl₂/NaOH medium at 90 to 300 °C. *Chem. Eur. J.*, 2013, **19** (17), P. 5417–5424.
- [17] Krasilin A.A., Nevedomsky V.N., Gusarov V.V. Comparative energy modeling of multiwalled Mg₃Si₂O₅(OH)₄ and Ni₃Si₂O₅(OH)₄ nanoscroll growth. *J. Phys. Chem. C.*, 2017, **121** (22), P. 12495–12502.
- [18] Bloise A., Belluso E., Fornero E., Rinaudo C., Barrese E., Capella S. Influence of synthesis conditions on growth of Ni-doped chrysotile. *Microp. Mesop. Mater.*, 2010, **132** (1–2), P. 239–245.
- [19] McDonald A., Scott B., Villemure G. Hydrothermal preparation of nanotubular particles of a 1:1 nickel phyllosilicate. *Microp. Mesop. Mater.*, 2009, **120** (3), P. 263–266.
- [20] Krasilin A.A., Gusarov V.V. Redistribution of Mg and Ni cations in crystal lattice of conical nanotube with chrysotile structure. *Nanosyst.: Phys. Chem. Math.*, 2017, **8** (5), P. 620–627.
- [21] Korytkova E.N., Pivovarova L.N. Hydrothermal synthesis of nanotubes based on (Mg,Fe,Co,Ni)₃Si₂O₅(OH)₄ hydrosilicates. *Glas. Phys. Chem.*, 2010, **36** (1), P. 53–60.
- [22] Piperno S. et al. Characterization of geoinspired and synthetic chrysotile nanotubes by atomic force microscopy and transmission electron microscopy. *Adv. Funct. Mater.*, 2007, **17** (16), P. 3332–3338.
- [23] Korytkova E.N., Pivovarova L.N., Semenova O.E., Drozdova I.A., Povnich V.F., Gusarov V.V. Hydrothermal synthesis of nanotubular Mg-Fe hydrosilicate. *Russ. J. Inorg. Chem.*, 2007, **52** (3), P. 338–344.
- [24] Krasilin A.A., Panchuk V.V., Semenov V.G., Gusarov V.V. Formation of variable-composition iron(III) hydrosilicates with the chrysotile structure. *Russ. J. Gen. Chem.*, 2016, **86** (12), P. 2581–2588.
- [25] White R.D., Bavykin D. V., Walsh F.C. Morphological control of synthetic Ni₃Si₂O₅(OH)₄ nanotubes in an alkaline hydrothermal environment. *J. Mater. Chem. A.*, 2013, **1** (3), P. 548–556.
- [26] Artali R., Del Pra A., Foresti E., Lesci I.G., Roveri N., Sabatino P. Adsorption of human serum albumin on the chrysotile surface: a molecular dynamics and spectroscopic investigation. *J. R. Soc. Interface*, 2008, **5** (20), P. 273–283.
- [27] Valentim I.B., Joekes I. Adsorption of sodium dodecylsulfate on chrysotile. *Coll. Surf., A: Physicochem., Eng. Aspects*, 2006, **290** (1–3), P. 106–111.
- [28] Teixeira A.P.C., Purceno A.D., de Paula C.C.A., da Silva J.C.C., Ardisson J.D., Lago R.M. Efficient and versatile fibrous adsorbent based on magnetic amphiphilic composites of chrysotile/carbon nanostructures for the removal of ethynilestradiol. *J. Hazard. Mater.*, 2013, **248–249**, P. 295–302.
- [29] Cheng L.L., Wei X.D., Hao X.L., Ruan D., Yu S.M. The removal of strontium(II) and neodymium(III) from their aqueous solutions on chrysotile nanotubes. *Adv. Mater. Res.*, 2014, **881–883**, P. 519–524.
- [30] Yu S., Zhai L., Wang Y., Liu X., Xu L., Cheng L. Synthesis of magnetic chrysotile nanotubes for adsorption of Pb(II), Cd(II) and Cr(III) ions from aqueous solution. *J. Environ. Chem. Eng.*, 2015, **3** (2), 752–762.
- [31] Cheng L., Ren X., Wei X., Sun X., Yu S. Facile synthesis and characterization of chrysotile nanotubes and their application for lead(II) removal from aqueous solution. *Sep. Sci. Technol.*, 2014, **50** (5), P. 700–709.
- [32] Golubeva O.Y., Maslennikova T.P., Ulyanova N.Y., Dyakina M.P. Sorption of lead(II) ions and water vapors by synthetic hydro- and aluminosilicates with layered, framework, and nanotube morphology. *Glas. Phys. Chem.*, 2014, **40** (2), P. 250–255.

- [33] Chong M.N., Jin B., Chow C.W.K., Saint C. Recent developments in photocatalytic water treatment technology: A review. *Water Res.*, 2010, **44** (10), P. 2997–3027.
- [34] Karthikeyan N., Narayanan V., Stephen A. Visible light degradation of textile effluent using nanostructured TiO₂/Ag/CuO photocatalysts. *Nanosyst.: Phys. Chem. Math.*, 2016, **7** (4), P. 695–698.
- [35] Subramanian V.R., Sarker S., Yu B., Kar A., Sun X., Dey S.K. TiO₂ nanotubes and its composites: Photocatalytic and other photo-driven applications. *J. Mater. Res.*, 2013, **28** (3), P. 280–293.
- [36] Zhukovskiy M.A., Smirnova N.P., Rusetsky I.A., Kolbasov G.Y., Eremenko A.M. Physical and chemical properties and photocatalytic activity of nanostructured TiO₂/CdS Films. *J. Appl. Spectrosc.*, 2014, **81** (2), P. 238–243.
- [37] Kozlova E.A., Kozhevnikova N.S., Cherepanova S.V., Lyubina T.P., Gerasimov E.Y., Kaichev V.V., Vorontsov A.V., Tsybulya S.V., Rempel A.A., Parmon V.N. Photocatalytic oxidation of ethanol vapors under visible light on CdS–TiO₂ nanocatalyst. *J. Photochem. Photobiol. A Chem.*, 2012, **250**, P. 103–109.
- [38] Kozlova E.A., Rempel' A.A., Valeeva A.A., Gorbunova T.I., Kozhevnikova N.S., Cherepanova S.V., Gerasimov E.Yu., Saraev A.A., Korovin E.Yu., Parmon V.N. Photoactivity of TiO₂/CdS and SiO₂/CdS hybrid nanostructured systems in the partial oxidation of ethanol under irradiation with visible light. *Kinet. Catal.*, 2015, **56** (4), P. 515–522.
- [39] Zheng L., Han S., Liu H., Yu P., Fang X. Hierarchical MoS₂ nanosheet@TiO₂ nanotube array composites with enhanced photocatalytic and photocurrent performances. *Small*, 2016, **12** (11), P. 1527–1536.
- [40] Chen J.-Z., Chen T.-H., Lai L.-W., Li P.-Y., Liu H.-W., Hong Y.-Y., Liu D.-S. Preparation and characterization of surface photocatalytic activity with NiO/TiO₂ nanocomposite structure. *Materials (Basel)*, 2015, **8** (7), P. 4273–4286.
- [41] Wang Y.-F., Hsieh M.-C., Lee J.-F., Yang C.-M. Nonaqueous synthesis of CoO_x/TiO₂ nanocomposites showing high photocatalytic activity of hydrogen generation. *Appl. Catal. B Environ.*, 2013, **142**, P. 626–632.
- [42] Szczepanik B. Photocatalytic degradation of organic contaminants over clay-TiO₂ nanocomposites: A review. *Appl. Clay Sci.*, 2017, **141**, P. 227–239.
- [43] Maksimov V.D., Shaporev A.S., Ivanov V.K., Churagulov B.R., Tret'yakov Y.D. Hydrothermal synthesis of nanocrystalline anatase from aqueous solutions of titanyl sulfate for photocatalytic applications. *Theor. Found. Chem. Eng.*, 2009, **43** (5), P. 713–718.
- [44] Meskin P.E., Gavrilov A.I., Maksimov V.D., Ivanov V.K., Churagulov B.P. Hydrothermal/microwave and hydrothermal/ultrasonic synthesis of nanocrystalline titania, zirconia, and hafnia. *Russ. J. Inorg. Chem.*, 2007, **52** (11), P. 1648–1656.
- [45] Sadovnikov A.A., Baranchikov A.E., Zubavichus Y.V., Ivanova O.S., Murzin V.Y., Kozik V.V., Ivanov V.K. Photocatalytically active fluorinated nano-titania synthesized by microwave-assisted hydrothermal treatment. *J. Photochem. Photobiol. A Chem.*, 2015, **303**, P. 36–43.
- [46] Malygin A.A., Malkov A.A., Sosnov E.A. Structural-dimensional effects and their application in the “core–nanoshell” systems synthesized by molecular layering. *Russ. Chem. Bull., Int. Ed.*, 2017, **66** (11), P. 1939–1962.
- [47] Abdulagatov A.I., Hall R.A., Sutherland J.L., Lee B.H., Cavanagh A.S., George S.M. Molecular layer deposition of titaniconic films using TiCl₄ and ethylene glycol or glycerol: growth and properties. *Chem. Mater.*, 2012, **24** (15), P. 2854–2863.
- [48] Maslennikova T.P., Korytkova E.N. Regularities of the filling of Mg₃Si₂O₅(OH)₄ hydrosilicate nanotubes with solutions of sodium hydroxide and sodium chloride. *Glas. Phys. Chem.*, 2011, **37** (4), P. 418–425.
- [49] Bodalyov I.S., Malkov A.A., Korytkova E.N., Maslennikova T.P., Malygin A.A. Temperature factor in interaction of nanotubular magnesium hydrosilicate, Mg₃Si₂O₅(OH)₄, with titanium tetrachloride and water vapors. *Russ. J. Appl. Chem.*, 2014, **87** (2), P. 151–159.
- [50] Krasilin A.A., Gusarov V.V. Control over morphology of magnesium-aluminum hydrosilicate nanoscrolls. *Russ. J. Appl. Chem.*, 2015, **88** (12), P. 1928–1935.
- [51] Chiron N., Guilet R., Deydier E. Adsorption of Cu(II) and Pb(II) onto a grafted silica: isotherms and kinetic models. *Water Res.*, 2003, **37** (13), P. 3079–3086.
- [52] Wilczak A., Keinath T.M. Kinetics of sorption and desorption of copper(II) and lead (II) on activated carbon. *Water Environ. Res.*, 1993, **65** (3), P. 238–244.
- [53] Plazinski W., Rudzinski W., Plazinska A. Theoretical models of sorption kinetics including a surface reaction mechanism: A review. *Adv. Colloid Interface Sci.*, 2009, **152** (1-2), P. 2–13.

Synthesis and properties of nanoscale films of the Y_2O_3 – Fe_2O_3 system on silicon

I. A. Milyaeva¹, N. S. Perov², V. V. Bessalova², M. V. Berezhnaya¹, V. O. Mittova³,
Anh Tien Nguyen⁴, I. Ya. Mittova¹

¹Voronezh State University, Voronezh, 394018 Russia

²Lomonosov Moscow State University, Moscow, 119991 Russia

³Burdenko Voronezh State Medical University, Voronezh, 394036 Russia

⁴Ho Chi Min City University of Education, Ho Chi Min City, Viet Nam

cnurova2010@yandex.ru

PACS 75.50.Cc, 81.07.Wx

DOI 10.17586/2220-8054-2018-9-3-417-423

Thin films of the Y_2O_3 – Fe_2O_3 /Si system with nanometer-scale thicknesses were synthesized by centrifugation with application of sol and gel of $YFeO_3$. It was found that the samples formed from the gel are characterized by the following composition: Fe_2O_3 , Fe_3O_4 , and Y_2O_3 , $YFeO_3$, which is not consistent with the data, obtained for powder products, and can indicate that the thermal annealing conditions were insufficient for the formation of a single-phase product. For the first time, the magnetic properties of thin ferrite films of yttrium on the surface of the silicon formed from the gel were measured. The nature of the hysteresis loop of nanofilms of yttrium ferrite with different parameters of time and speed of centrifugation suggests that the samples exhibit soft magnetic properties of a ferromagnet. The correlation between the value of specific magnetization and thickness of nanofilms was established.

Keywords: sol-gel synthesis, nanofilms, centrifugation, yttrium orthoferrite, magnetic properties.

Received: 9 February 2018

Revised: 20 March 2018

1. Introduction

The wide application of multiferroics is due to the fact that these materials have two kinds of orderings – ferromagnetic and ferroelectric – which have utility in microelectronics, recording devices, and the storage and reading of information [1–7]. According to the study [8], yttrium orthoferrite also shows multiferroic properties.

There are various methods of producing films of semiconducting metal oxides. The sol-gel method is most promising for the formation of nanofilms of ferrites involving the deposition of metal hydroxides, their conversion into a colloidal state, the colloidal solution applied on the substrate and crystallization of oxide phases during thermal dehydration [9].

The popularity of this technology is associated, primarily, with high chemical homogeneity of the products, which in turn reduces the temperature and duration of final thermal treatment. Despite the large number of studies devoted to the sol-gel technology, the synthesis of specific samples requires an individual approach, providing the precipitation of highly dispersed, easily translatable in a colloidal state [10–12].

The goal of this study was the formation and investigation of magnetic properties of nanodimensional Y_2O_3 – Fe_2O_3 films, synthesized by the sol-gel method on a surface of Si.

2. Materials and methods

2.1. Initial substances

For the formation of thin films, the sol-gel synthesis of $YFeO_3$ technique was used [13]. The following reagents were used as original reactants: nitrate iron (III) 9-water, $Fe(NO_3)_3 \cdot 9H_2O$ (h), yttrium nitrate 6-aqueous $Y(NO_3)_3 \cdot 6H_2O$ (H. h), distilled water.

2.2. The synthesis of Y_2O_3 – Fe_2O_3 films

The substances were taken in stoichiometric ratio, concentration of the solutions was 0.008 M, the total volume of solution was 100 ml. Solutions of nitrates of iron (III) and yttrium in distilled water was boiled prior to gel formation, and then applied on the silicon substrate by centrifugation, at a speed of 2000 – 5000 rpm within 1 – 15 min. The films were annealed in a muffle furnace for one hour at 750 °C. Such thermal annealing parameters were chosen based on the results of [13] for the synthesis of $YFeO_3$ nanopowders.

2.3. Methods of investigation

The thickness of the synthesized films was determined by spectroscopic ellipsometry (Ellipse 1891).

Determination of sample compositions was conducted by x-ray diffraction (XRD, x-ray diffractometer Thermo ARL X'tra) and infrared spectroscopy (X-ray, ft-IR spectrometer Vertex 70).

The surface morphology of the formed films was investigated by atomic force microscopy (AFM, Solver P47 Pro Corporation NT-MDT).

The study of the magnetic characteristics (magnetization J , the coercive force H_C) of films on silicon synthesized from the gel was performed at room temperature using vibrating magnetometer sample (VSM, "Lakeshore", model 7404).

3. Results and discussion

The results of determination of film thickness, confirming the nanometer range, are presented in Table 1.

TABLE 1. The thickness of the films synthesized from the gel on the Si surface after annealing at 750 °C, defined by spectral ellipsometry

No.	τ rotation speed, min.	ν rotation speed, rpm	thickness, nm
1	5	2000	17
2	15	2000	19
3	5	4000	20
4	5	5000	15
5	15	5000	15
6	1	5000	49
7	15	5000	38

The qualitative picture of the concentration of components in the film was established by x-ray diffraction analysis conducted by x-ray diffractometer Thermo ARL X'tra in a small angle range. This was necessary to ensure that the high-intensity peaks of the substrate do not overlap the peaks of the film. The data obtained (Figs. 1, 2 and Tables 2, 3) demonstrated that samples no. 6 and no. 7 showed in Table 1 contain following phases: Fe_2O_3 , Fe_3O_4 , Y_2O_3 , YFeO_3 .

TABLE 2. The results of digital processing of diffraction pattern of sample No. 6

The angle of incidence of the x-ray beam	D_{hkl} (Å)	Phase
25.47	3.32	Fe_2O_3
49.38	1.84	Fe_2O_3
37.47	2.40	Fe_3O_4
57.98	1.59	Fe_3O_4
40.80	2.21	Y_2O_3
49.38	1.84	Y_2O_3
51.91	1.76	Y_2O_3
23.37	3.80	YFeO_3
51.91	1.76	YFeO_3

It should be noted that the most intensive peaks were peaks corresponding to the substrate at all diffractograms. This fact suggests that the thickness of the film grown on the surface did not exceed a few hundred nanometers and it was confirmed by the studies of thickness using spectroscopic ellipsometry.

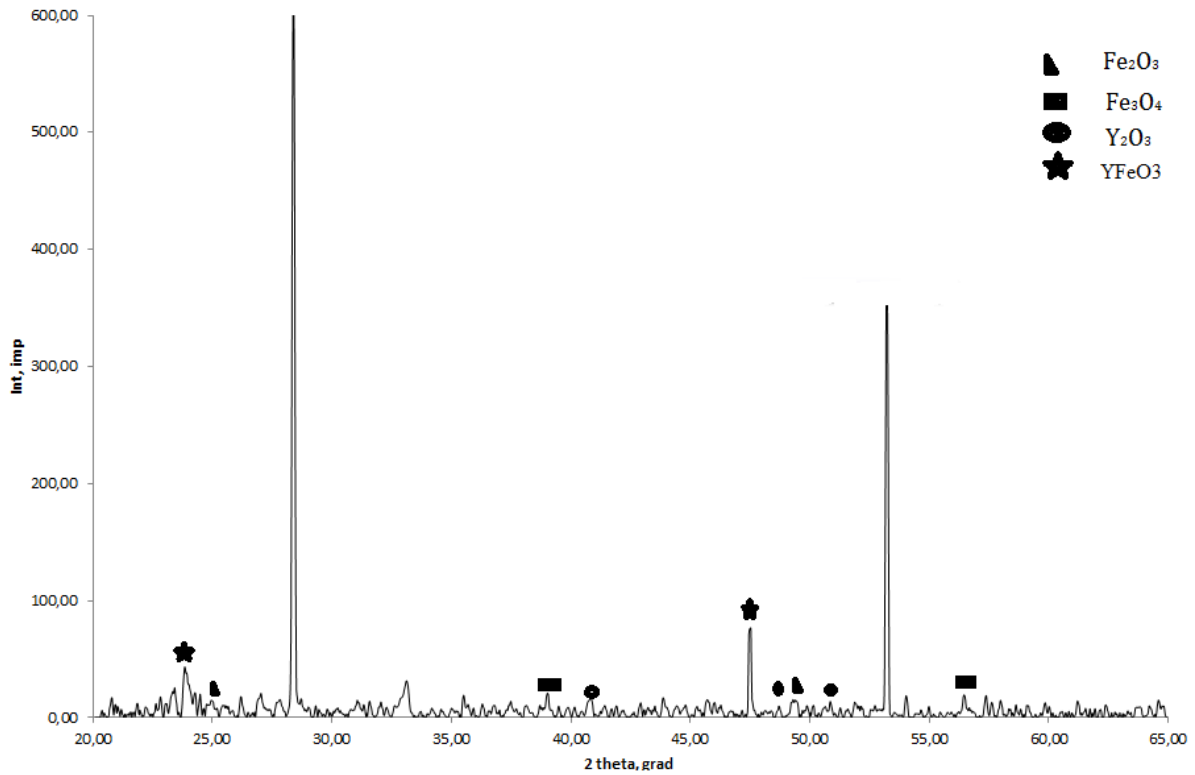


FIG. 1. X-ray powder diffraction patterns of sample No. 6 ($\tau = 1$ min, $\nu = 5000$ rev./min.), synthesized from the gel on the surface of Si

TABLE 3. The results of digital processing of diffraction pattern of sample No. 7

The angle of incidence of the x-ray beam	D_{hkl} (Å)	Phase
40.23	2.24	Fe_2O_3
60.18	1.53	Fe_2O_3
59.20	1.56	Fe_3O_4
33.15	2.70	Y_2O_3
34.91	2.57	Y_2O_3
56.92	1.61	Y_2O_3
26.13	3.41	$YFeO_3$
53.22	1.72	$YFeO_3$
56.92	1.61	$YFeO_3$

IR absorption spectra of the samples were recorded for establishing the correlation with XRD data.

According to IR spectroscopy data (Fig. 3), the composition of the films included: Y_2O_3 ($\nu = 480\text{ cm}^{-1}$), Fe_2O_3 ($\nu = 620\text{ cm}^{-1}$), Fe_3O_4 ($\nu = 1160\text{ cm}^{-1}$), $YFeO_3$ ($\nu = 1300\text{ cm}^{-1}$) and these data correlated with the results of XRD.

The surfaces of the synthesized samples had a developed structure with a pronounced wavy nature (the AFM data). Comparison of the images detected the decrease of the grain surface with increasing size of the individual nanocrystallites.

The observed result indicates the significant effect of centrifugation parameters on the nature and structure of the resulting films. Increasing the speed and time of rotation contributed to the smoothing of film topography. For

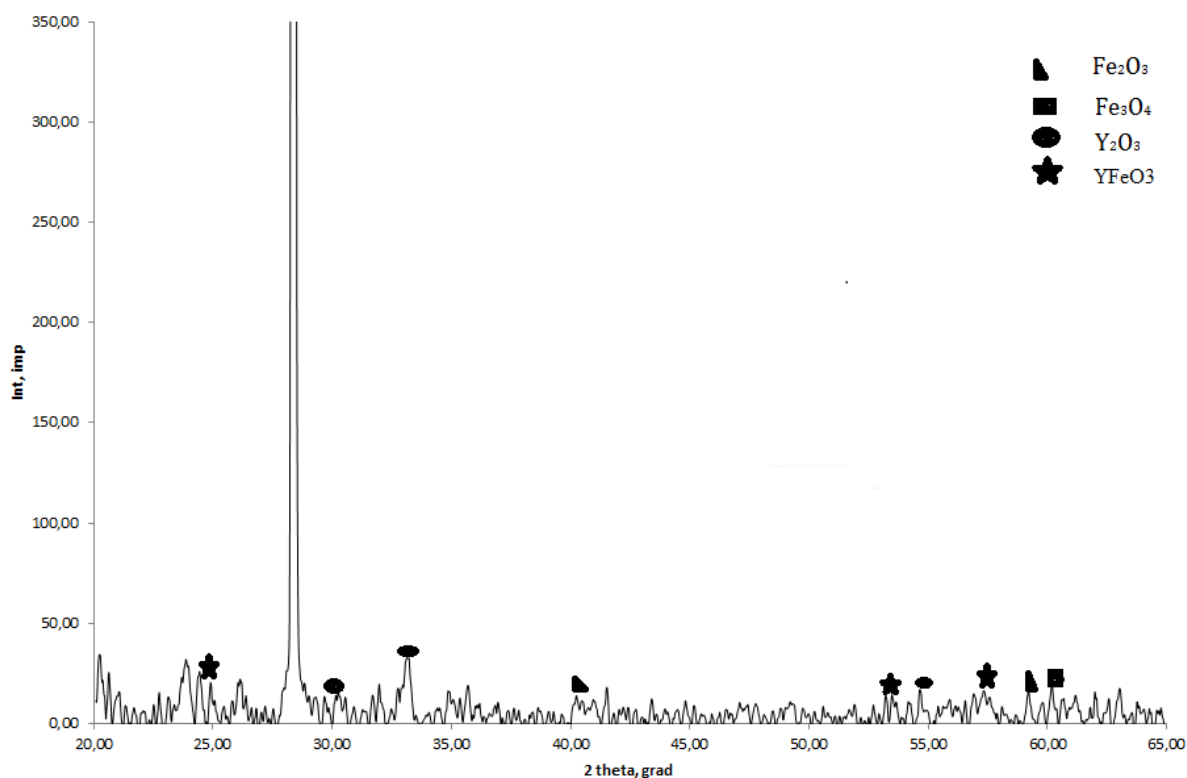


FIG. 2. X-ray diffraction pattern of sample No. 7 ($\tau = 15$ min., $y = 5000$ ob./min). Synthesized from the gel on the surface of Si

example, by increasing the centrifugation time (Figs. 4 and 5) during film formation from the gel decreased the difference in height of the terrain from 8 to 6 nm.

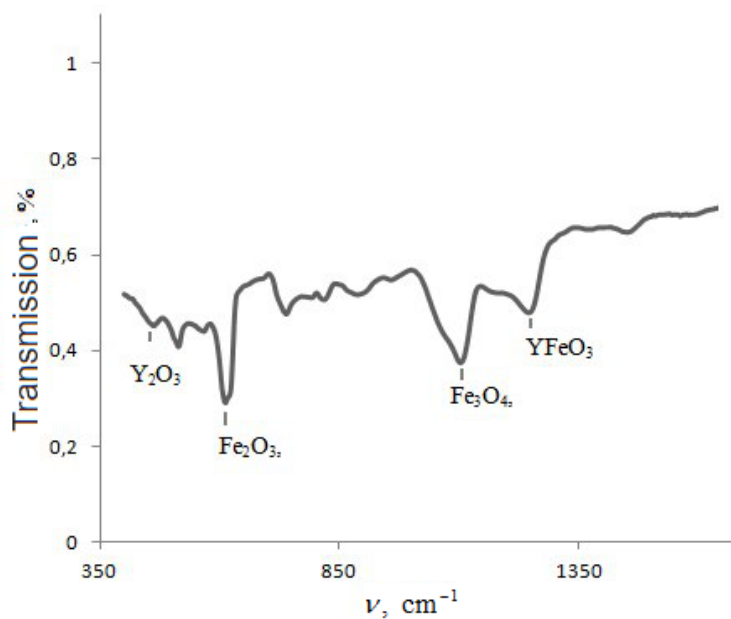


FIG. 3. The IR absorption spectrum of the sample No. 6, synthesized from the gel on the surface of Si

Increasing the centrifugation speed from 4000 rpm to 5000 rpm also caused surface smoothing, the height of the terrain decreased from 12 nm to 10 nm.

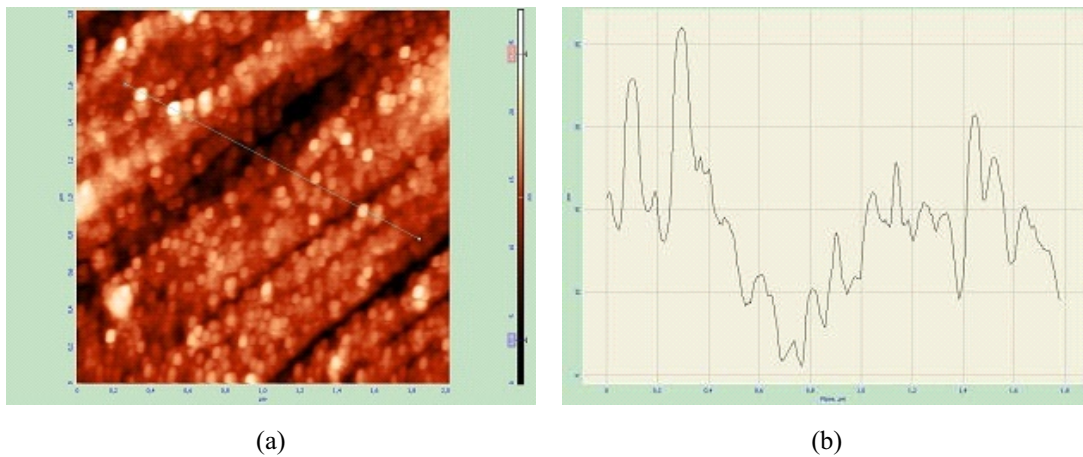


FIG. 4. AFM image (a) and surface profile (b) of sample No. 1 ($\tau = 5$ min, $v = 2000$ rpm), synthesized from the gel on the surface of Si

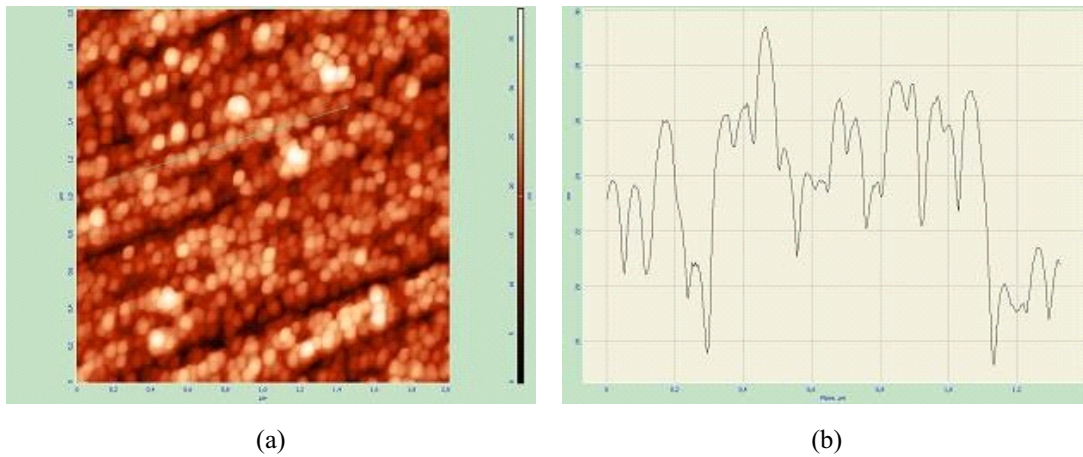


FIG. 5. AFM image (a) and surface profile (b) of sample No. 2 ($\tau = 15$ min, $v = 2000$ rpm), synthesized from the gel on the surface of Si

Thus, by varying the process parameters, it is possible to achieve the formation of films with a given structure and morphology.

Determination of the magnetic characteristics (magnetization J , the coercive force H_C) of the synthesized gel film was carried out using a VSM ("Lakeshore", model 7404) at room temperature. The magnetic field was directed in the film plane.

The field dependence of the magnetic moment of the sample with nanofilm on Si (smooth curve obtained by interpolation of the original data of Langevin curve by least square method) deposited by centrifugation of the gel for 1 min at a speed of 5000 rpm./min (sample no. 6 of Table 1) is shown in Fig. 6. The specific magnetization in a field of 1250 kA/m was 47 A·m²/kg. The determination of coercive force of the sample was not possible due to the low magnetic moment and high noise signal. According to estimates, the coercive force of yttrium ferrite nanofilms was not more than 100 Oe, which indicates magnetically soft ferromagnet. On the other hand, the magnitude of the saturation field exceeded 500 kA/m, which shows high magnetic anisotropy. We can assume that the axis of easy magnetization of magnetic anisotropy is oriented perpendicular to the film's plane.

Figure 7 shows the dependence of the magnetic moment of the thin film sample on the Si surface, deposited by centrifugation of the gel for 15 min. at a speed 5000 rev./min (sample no. 7) from the intensity of the applied field. The sample reached magnetic saturation in a field of 450 kA/m, $J = 37.5$ A·m²/kg. The shape of the hysteresis loop was similar to the previous dependence also indicates the ferromagnetic character of the nanoscale films.

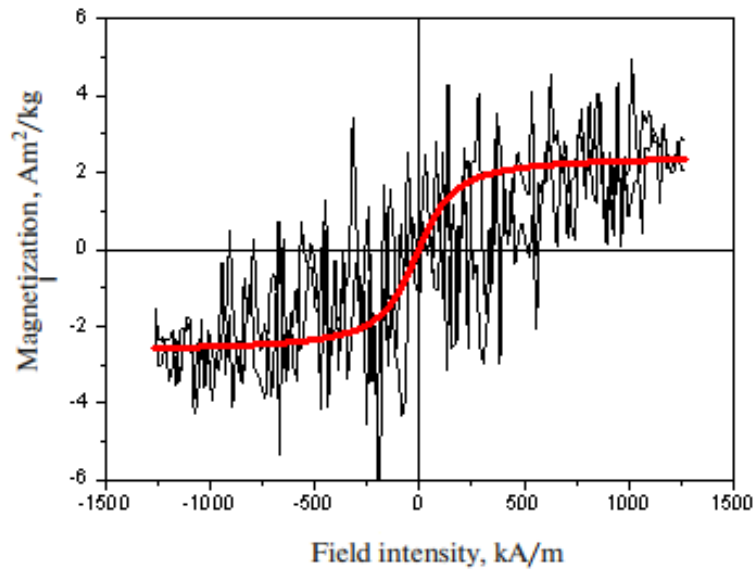


FIG. 6. Field dependence of the magnetization of the sample No. 6 YFeO_3/Si ($\tau = 5$ min, $\nu = 2000$ rpm), synthesized from the gel after annealing at 750°C , 60 min. Smooth curve is obtained by interpolation of the original data curve Langevin least squares

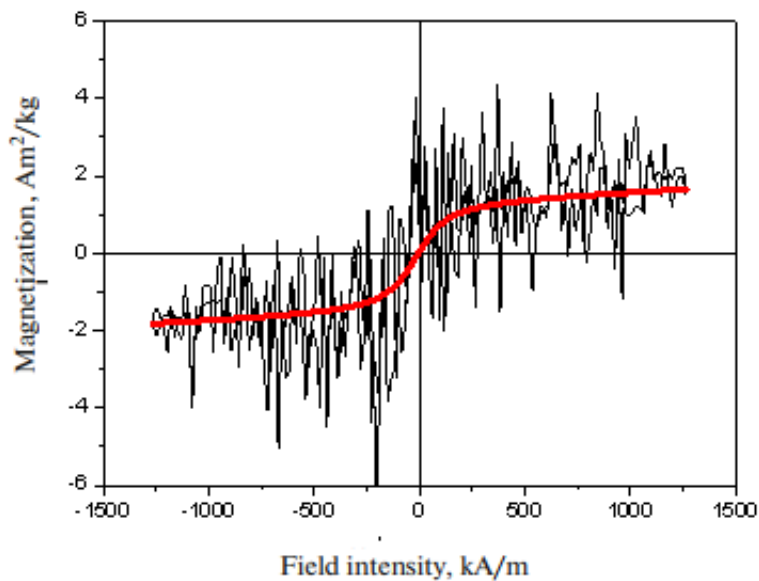


FIG. 7. Field dependence of the magnetization of the sample No. 7 YFeO_3/Si ($\tau = 15$ min, $\nu = 5000$ rpm), synthesized from the gel after annealing at 750°C , 60 min. Smooth curve was obtained by interpolation of the original data of the Langevin curve by the least square method

Thus, with the decrease in thickness of the YFeO_3 films from 49 to 38 nm (Table 1) a decrease of the specific magnetization in a field of 1250 kA/m $47 \text{ A}\cdot\text{m}^2/\text{kg}$ to $37.5 \text{ A}\cdot\text{m}^2/\text{kg}$ was observed. The values of the saturation field of both samples were close, indicating the magnetocrystalline nature of the magnetic anisotropy. For yttrium ferrite nanopowders, synthesized by the sol-gel method, $J = 0.242 \text{ A}\cdot\text{m}^2/\text{kg}$ [13]. The relatively high value of specific magnetization of the synthesized samples was due to the presence of impurity Fe_2O_3 , Fe_3O_4 phases with a pronounced ferromagnetism [14, 15].

The results can be used to produce bulk composite materials, as well as for the manufacture of devices requiring a rapid remagnetization using minimal energy, for example, transformer coils [16, 17]. The synthesized films, along with other oxides of transition metals [18, 19] can act as catalysts for the formation of functional layers by thermal oxidation of binary semiconductor compounds A_3B_5 .

4. Conclusions

Samples of the Y_2O_3 - Fe_2O_3 /Si system with the application of $YFeO_3$ gel were synthesized by centrifugation. These samples were thin films on silicon with nanometer range thickness. The samples formed from the gel were characterized by the following composition: Fe_2O_3 , Fe_3O_4 , Y_2O_3 , $YFeO_3$, which is not consistent with the data obtained for powder products [13], and may indicate that thermal annealing is insufficient for the formation of a single-phase product.

The generated samples had a developed surface morphology with a pronounced wavy structure. The average surface elevation for the samples synthesized from the gel ranged from 8 to 10 nm. Surface morphology of synthesized samples was smoother with increasing time and speed of the centrifugation of the substrate.

Nanofilms of yttrium ferrite are magnetically soft ferromagnets, the specific magnetization increased with increasing film thickness in the range of 38 – 49 nm from 37.5 to 47 $A \cdot m^2/kg$ in field 1250 kA/m. The presence of impurity phases of iron oxides in the samples increases the magnetization value and increases the range of application of the formed heterostructures.

Acknowledgements

The study was supported by RFBR grant (no. 18-03-00354a).

This work was performed using the equipment of the Scientific Equipment Sharing Centre, Voronezh State University, Voronezh, Russia, and the Department of Magnetism, Lomonosov Moscow State University, Moscow, Russia; the equipment that was used at the Department of Magnetism was purchased out of the funds of the Moscow State University Development Program.

References

- [1] Nguyen A.T., Phan Ph.H.Nh., et al. The characterization of nanosized $ZnFe_2O_4$ material prepared by coprecipitation. *Nanosystems: Physics, Chemistry, Mathematics*, 2016, **7** (3), P. 459–463.
- [2] Almjasheva O.V., Gusarov V.V. Prenucleation formations in control over synthesis of $CoFe_2O_4$ nanocrystalline powders. *Russian Journal of Applied Chemistry*, 2016, **89** (6), P. 851–856.
- [3] Gubin S.P., Koksharov Yu.A., Khomutov G.B., Yurkov G.Yu. Magnetic nanoparticles: preparation, structure and properties. *Russian Chemical Reviews*, 2005, **74** (6), P. 489–520.
- [4] Chithralekha P., Murugeswari C., Ramachandran K., Srinivasan R. The study on ultrasonic velocities of $Co_xFe_{3-x}O_4$ nanoferrofluid prepared by co-precipitation method. *Nanosystems: Physics, Chemistry, Mathematics*, 2016, **7** (3), P. 558–560.
- [5] Lomanova N.A., Gusarov V.V. Influence of synthesis temperature on $BiFeO_3$ nanoparticles formation. *Nanosystems: Physics, Chemistry, Mathematics*, 2013, **4** (5), P. 696–705.
- [6] Khlopov B.V. Magnetic properties of thin-film materials of the modern hard magnetic disks in case of influence of an external constant magnetic field. *Electronic Magazine 'MAI'*, 2012, **57**, P. 316–321.
- [7] Belyaev B.A. Study of thin magnetic films and microstrip devices on their basis. *Izvestiya Vuzov. Physics*, 2010, **53** (9/2), P. 163–165.
- [8] Shang M., Zhang Ch., et al. The multiferroic perovskite $YFeO_3$. *Applied Physics Letters*, 2013, **102**, 062903(1–3).
- [9] Sharygin L.M. *Sol-gel technology for producing nanomaterials*. UrO RAN, Yekaterinburg, 2011, 46 p.
- [10] Brinker C.J. *Sol-Gel Science: The Physics and Chemistry of Sol-Gel Processing*. Academic Press, London, 2013, 912 p.
- [11] Shabanova N.A., Sarkisov P.D. *Sol-gel Technology. Nanodispersed Silica. Binomial*. Laboratory of Knowledge, Moscow, 2012, 309 p.
- [12] Maksimov A.I. *Fundamentals of Sol-Gel Technology of Nanocomposites*. 'Elmore', Saint-Petersburg, 2007, 255 p.
- [13] Nguen A.T., Mittova I.Ya., Almiasheva O.V. Synthesis and magnetic properties of $YFeO_3$ nanocrystals. *Journal of Applied Chemistry*, 2009, **82** (11), P. 1766–1769.
- [14] Sharma S. Magnetic behaviour of solgel driven $BiFeO_3$ thin films with different grain size distribution. *Journal of Magnetism and Magnetic Materials*, 2016, **401**, P. 180–187.
- [15] Kotsikau D., Pankov V., et al. Structural, magnetic and hyperfine characterization of $Zn_xFe_{3-x}O_4$ nanoparticles prepared by sol-gel approach via inorganic precursors. *Journal of Physics and Chemistry of Solids*, 2018, **114**, P. 64–70.
- [16] Salikhov S.V. Regularities of formation of structure and magnetic properties of nanosized and nanostructured powders based on iron oxides. PhD Thesis, National Research Technological University 'MISIS', Moscow, 2016, 205 p.
- [17] Kalinkin A.N., Kozhbakhteev E.M., Poliakov A.E., Skorikov V.M. The application of $BiFeO_3$ and $Bi_4Ti_3O_{12}$ in ferroelectric memory, phase shifters of the phased array and microwave transistors NEMT. *Inorganic material*, 2013, **49** (10), P. 1113–1125.
- [18] Mittova I.Ya., Tomina E.V., Sladkopevtsev B.V. Effect of the mild method of formation VXOY/InP structures using V_2O_5 gel on the process of their oxidation and composition of nanosized oxide films. *Nanosystems: Physics, Chemistry, Mathematics*, 2014, **5** (2), P. 307–314.
- [19] Mittova I.Ya., Tomina E.V., et al. Effect of modification of an InP surface by $(V_2O_5 + PbO)$ and $(NiO + PbO)$ oxide mixtures of different compositions on the thermal oxidation process and the characteristics of the formed oxide films. *Russian Physics Journal*, 2015, **57** (12), P. 1691–1696.

Structural and magnetic properties of $\text{YFe}_{1-x}\text{Co}_x\text{O}_3$ ($0.1 \leq x \leq 0.5$) perovskite nanomaterials synthesized by co-precipitation method

Nguyen Anh Tien¹, Chau Hong Diem¹, Nguyen Thi Truc Linh¹, V. O. Mittova², Do Tra Huong³, I. Ya. Mittova⁴

¹Ho Chi Minh City University of Education, Ho Chi Minh City, Vietnam

²Burdenko Voronezh State Medical University, Voronezh, 394036, Russia

³Thai Nguyen University of Education, Thai Nguyen University, Vietnam

⁴Voronezh State University, Voronezh, 394018, Russia

anhvienhcmup@gmail.com, hongdiem.chau@gmail.com, linhttn2811@gmail.com, vmittova@mail.ru, dotrahuong@gmail.com, imittova@mail.ru

PACS 75.50.Cc, 81.07.Wx

DOI 10.17586/2220-8054-2018-9-3-424-429

$\text{YFe}_{1-x}\text{Co}_x\text{O}_3$ ($0.1 \leq x \leq 0.5$) perovskite-type nanomaterials were successfully synthesized by the chemical co-precipitation method via the hydrolysis of Y(III), Fe(III) and Co(II) cations in boiling water using 5 % aqueous KOH solution as a precipitating agent. Along with the increase of cobalt ion concentration (x values, from 0.1 to 0.5), there was an decrease in the crystallite size nanomaterials (from 25.68 to 22.89 nm), as well as in the lattice constants ($a = 5.5781 - 5.5217 \text{ \AA}$; $b = 5.2732 - 5.2177 \text{ \AA}$, $c = 7.5902 - 7.5009 \text{ \AA}$; $V = 223.26 - 216.11 \text{ \AA}^3$), but there was an increase in the magnetic parameters including coercive force ($H_c = 88.86 \text{ Oe}$), remnant magnetization ($M_r = 0.031 - 0.268 \text{ emu/g}$), saturation magnetization ($M_s = 0.413 - 1.006 \text{ emu/g}$) and maximum energy product ($(\text{BH})_{\text{max}} = 0.413 - 1.006 \text{ emu/g}$).

Keywords: nanomaterial, co-doped YFeO_3 , perovskite, co-precipitation.

Received: 15 March 2018

Revised: 27 March 2018

1. Introduction

In general, ABO_3 perovskite-type materials are dielectric antiferromagnetic, which can be changed to ferromagnetic by doping it with impurity ions [1–4], especially, in the case of the perovskite-type materials that have rare-earth elements (R) at A sites and Fe(III) ions at the B sites. The reason is the magnetic moment of iron in RFeO_3 is shifted slightly. When transition metals, which have the changed ionic radius at the variable oxidation states, are doped in the structure of RFeO_3 , it may cause an exchange interaction and indirectly lead to ferromagnetic properties. As a ferromagnetic material, perovskites can have interesting properties such as thermoelectric effect, giant magneto-caloric effect (GMCE), giant magneto-resistance (GMR) or spin glass state at low temperature. Thus, perovskite-type materials, particularly at the nano scale, can be applied in the fields of catalysts, solid-oxide fuel cells (SOFCs), chemical sensors, semiconductors, etc. [5–7]. Recently, Co-doped YFeO_3 materials have attracted extensively studying thanks to their interesting magnetic properties that may be changed because of the variable oxidation and spin states of cobalt, as well as its concentration in the solid solution [8].

There are numerous methods to synthesize RFeO_3 nanomaterials such as sol-gel combustion, sol-gel citrate or thermal hydrolysis, etc. [2–4, 9–11]. However, the preparation of the nanomaterials having RFeO_3 single phase by the mentioned methods requires the investigation of many factors including heating temperature and retention time, pH, stoichiometric ratio between the components, etc. As a result, the optimal conditions were difficult to be determined, and the formation of impurity phases such as Fe_3O_4 , YFe_2O_4 or $\text{Y}_3\text{Fe}_5\text{O}_{12}$ [12, 13] might have a negative impact on the quality of the obtained materials. In our previous research [14–16], the perovskite nanomaterials were successfully synthesized by co-precipitation method via the hydrolysis of transition metal ions in boiling water. This paper presents the results of the structural and magnetic properties of Co-doped YFeO_3 nanomaterials prepared by co-precipitation method via the hydrolysis of Y(III), Fe(III) and Co(II) cations in boiling water using 5 % aqueous KOH solution as a precipitating agent.

2. Materials and methods

2.1. Materials

In this research, $\text{Y}(\text{NO}_3)_3 \cdot 6\text{H}_2\text{O}$ (Merck, > 99 %), $\text{Fe}(\text{NO}_3)_3 \cdot 9\text{H}_2\text{O}$ (Merck, ≥ 99 %), $\text{Co}(\text{NO}_3)_2 \cdot 6\text{H}_2\text{O}$ (Merck, ≥ 99 %), KOH (Merck, 99 %) were used for the synthesis of $\text{YFe}_{1-x}\text{Co}_x\text{O}_3$ ($0.1 \leq x \leq 0.5$) perovskite-type nanomaterials.

2.2. Methods

Co-doped $YFeO_3$ were prepared via the process shown in Fig. 1. A mixture of $Y(NO_3)_3 \cdot 6H_2O$, $Fe(NO_3)_3 \cdot 9H_2O$ and $Co(NO_3)_2 \cdot 6H_2O$ salts with the stoichiometric ratio of Y(III) : Fe(III) : Co(II) = 1 : (1 - x) : x ($x = 0.1; 0.15; 0.2; 0.25; 0.3$ and 0.5) was dissolved in distilled water. This solution was added to a glass vessel containing hot water ($t^\circ > 90^\circ C$) and stirred continuously. And then, the obtained mixture was cooled down to the room temperature ($25 - 30^\circ C$), slowly added an excess KOH 5 % solution until the pH greater than 7. The mixture was stirred continuously for 30 mins, and settled for 15 mins. The precipitate was separated from the solution by filtration, washed with distilled water, left to dry at the room temperature and ground into powder.

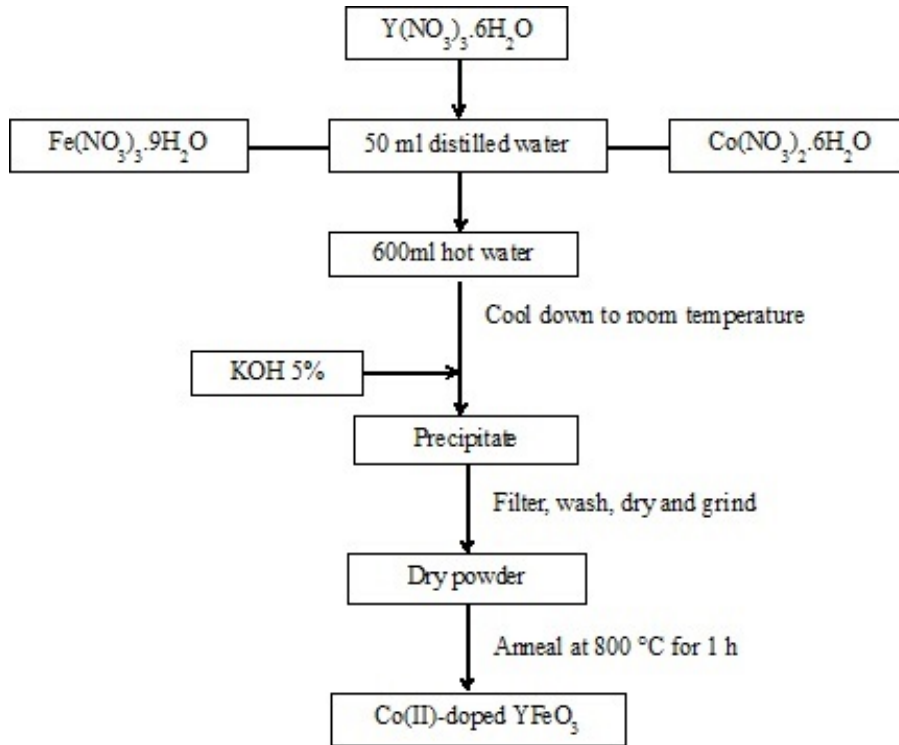


FIG. 1. Flow chart for synthesis of Co-doped $YFeO_3$ by co-precipitation method

All precipitates were converted to perovskite-type materials by annealing at $800^\circ C$ for 1 hour with a heating rate of $10 K/min$. The annealing condition was determined according to the previous results [14, 17].

Phase composition of the synthesized samples was identified by powder X-ray diffraction (XRD) with a D8-ADVANCE diffractometer (Germany) using $CuK\alpha$ radiation ($\lambda = 0.154056 nm$), $2\theta = 20 - 80^\circ$, a scan rate of $0.02^\circ s^{-1}$. Average size (nm) of crystal phase was calculated by Debye-Scherrer formula:

$$D_{XRD} = \frac{k\lambda}{\beta \cos \theta}, \quad (1)$$

where k is the shape factor (for the orthorhombic structure, $k = 0.9$); λ is the X-ray wavelength (nm); β is the full width at half maximum (rad) and θ is the position of the diffraction peak.

Lattice constants a , b , c and the unit cell volume V were determined thanks to the X'pert High Score Plus 2.2b software.

Particle size and morphology of $YFe_{1-x}Co_xO_3$ nanomaterials were determined by transmission electron microscopy (TEM) with a JEOL-1400 microscope (Japan). Elemental composition of the samples was determined by energy-dispersive X-ray spectroscopy (EDX) with a FESEM S-4800 spectrometer (Japan). Magnetic parameters of the samples (coercive force H_c , remnant magnetization M_r , saturation magnetization M_s) were carried out at room temperature by a vibrating sample magnetometer (VSM) MICROSENE EV11 (Japan).

3. Results and discussion

3.1. Crystal structure

Figure 2 presented the XRD patterns of $\text{YFe}_{0.8}\text{Co}_{0.2}\text{O}_3$ nanomaterial and component oxides which were prepared via the process shown in Fig. 1 (after annealing at $800\text{ }^\circ\text{C}$ for 1 hour). The results showed that $\text{YFe}_{0.8}\text{Co}_{0.2}\text{O}_3$ nanomaterial was pure perovskite-type, particularly, the peaks of YFeO_3 and Co-doped YFeO_3 were coincident with those of YFeO_3 orthoferrite phase (Card no. 00-039-1489 [18]). The diffraction peaks of oxide impurities cannot be identified in the XRD results. Noticeably, Co_3O_4 oxide was obtained instead of CoO because $\text{Co}(\text{OH})_2$ hydroxide can be oxidized and decomposed after annealing at high temperature [19]:

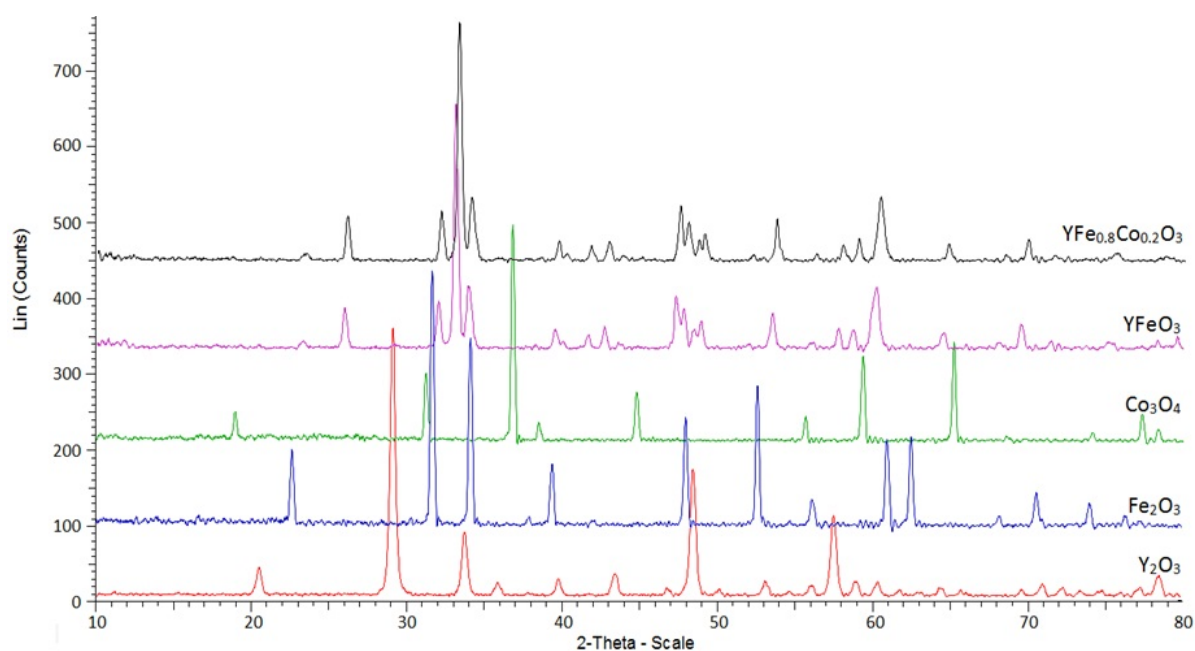
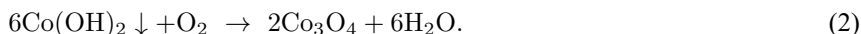


FIG. 2. XRD patterns of $\text{YFe}_{0.8}\text{Co}_{0.2}\text{O}_3$, YFeO_3 and Y_2O_3 , Fe_2O_3 , Co_3O_4 oxides annealed at $800\text{ }^\circ\text{C}$ for 1 hour

This result indicated that Co ions existed in both (II) and (III) oxidation states in the crystal lattice of YFeO_3 .

The XRD patterns of $\text{YFe}_{1-x}\text{Co}_x\text{O}_3$ ($0.1 \leq x \leq 0.5$) samples (Fig. 3) showed the structures of the samples were single-phase perovskites, particularly, they were in the orthorhombic structure with space group $Pnma$, No. 62. This proved that Fe(III) was partly substituted by Co(II)/Co(III). When the concentration of Co ions increased, XRD peaks shifted toward a higher 2θ (right shift) and gradually broadened while the intensity of peaks decreased. Consequently, there was a decrease of lattice parameters and crystal size (Fig. 4A and Table 1). The similar results were published in the previous researches [1, 16, 17].

The results shown in Table 1 showed that lattice parameters of $\text{YFe}_{1-x}\text{Co}_x\text{O}_{3\pm\delta}$ samples decreased in parallel of the increase of the dopant concentration. The substitution of Fe^{3+} ions ($r_{\text{Fe}^{3+}} = 0.65\text{ \AA}$ [19]) by smaller Co^{3+} ions ($r_{\text{Co}^{3+}} = 0.55\text{ \AA}$ [19]) led to the reduction of unit cell parameters following to Vergard's law for ideal solid solution.

Crystal sizes of $\text{YFe}_{1-x}\text{Co}_x\text{O}_{3\pm\delta}$ samples calculated by Debye-Scherrer formula (1) were in the range of 22 to 26 nm. The decrease in the values of crystal size in parallel of the increase of Co concentration can be explained by the substitution of Fe^{3+} ions by Co^{3+} ions, which led to the lattice distortion, the higher internal stress and the limitation of growing of crystalline.

3.2. Elemental composition

EDX spectra showed that the compositions of $\text{YFe}_{1-x}\text{Co}_x\text{O}_3$ samples included Y, Fe, Co and O, without impurity element. The empirical formulas obtained from the elemental analysis were in excellent agreement with the suggested formulas (Table 2).

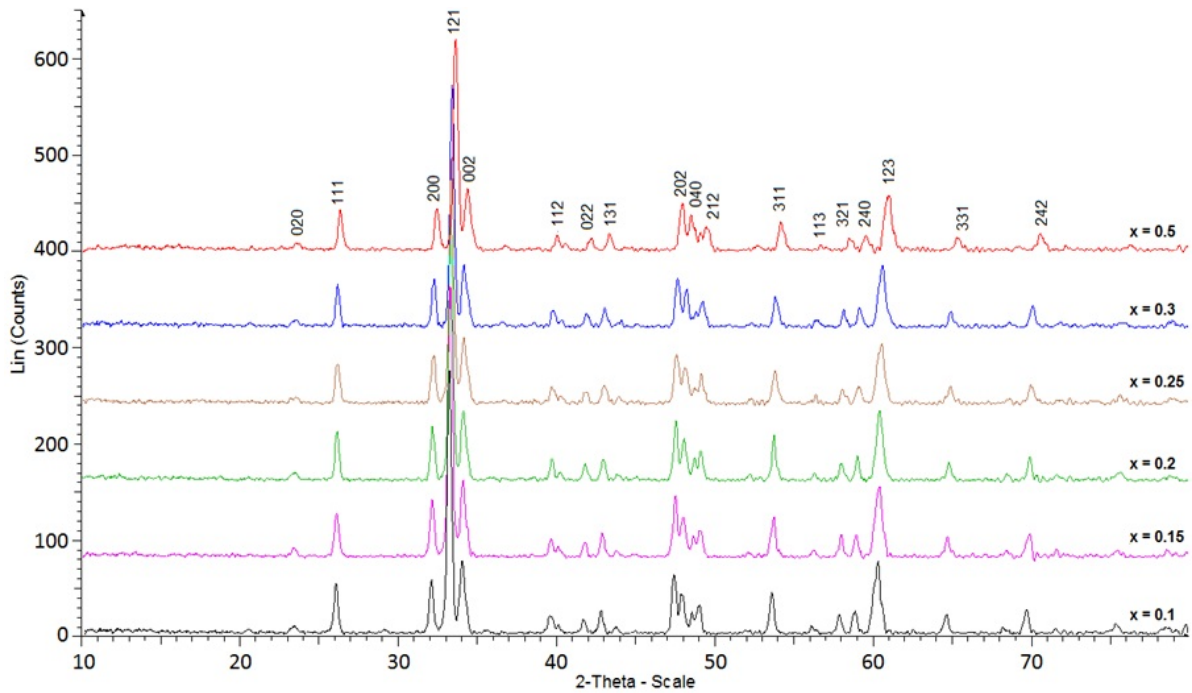


FIG. 3. XRD patterns of $YFe_{1-x}Co_xO_3$ samples annealed at $800\text{ }^\circ\text{C}$ for 1 hour

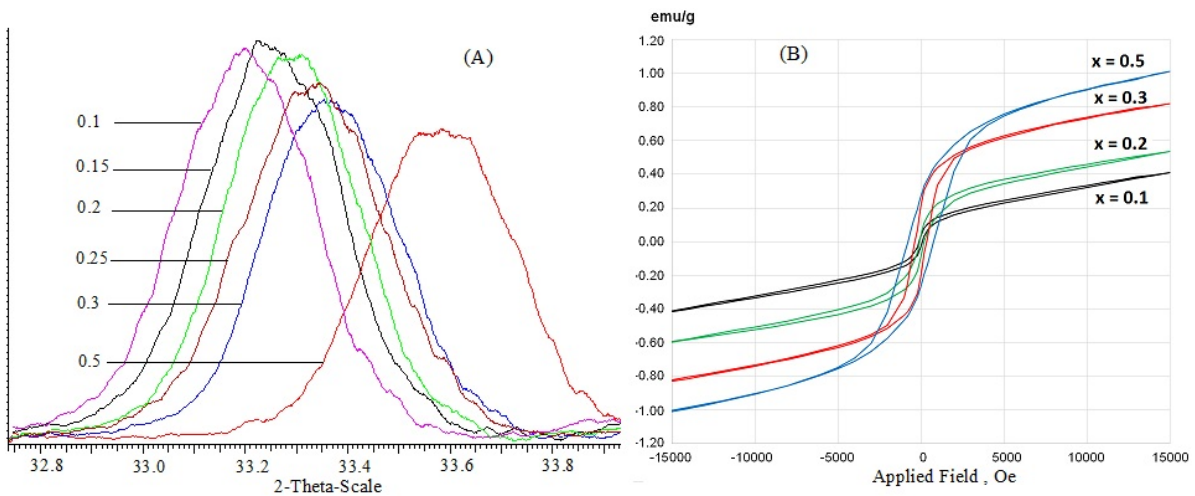


FIG. 4. Slow-scan XRD patterns of peak (121) (A) and field dependence of the magnetization (B) of $YFe_{1-x}Co_xO_3$ nanomaterials annealed at $800\text{ }^\circ\text{C}$ for 1 h

3.3. Morphology

TEM images of $YFe_{1-x}Co_xO_3$ samples ($x = 0.1$; 0.3 and 0.5) (Fig. 5) showed that the shape and size of nanoparticles synthesized were quite homogeneous. Particularly, the particles were in spherical or slightly angular shapes, with an average size of $30 - 50\text{ nm}$.

3.4. Magnetic properties

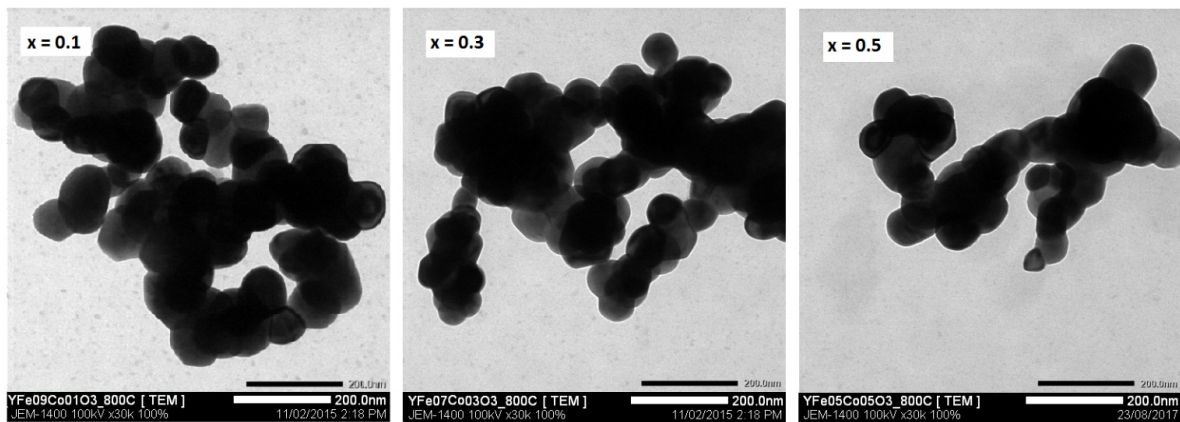
The magnetic parameters of the samples proved that Co substitution impacted not only on the structure but also on magnetic properties of the nanoparticles synthesized (Fig. 5B and Table 2). When the amount of Co ions in $YFeO_3$ crystal lattice increased, the magnetic parameters including H_c , M_r and M_s increased, and were significantly higher than those of the original $YFeO_3$ material [14, 17]. This can be explained by the increase of magnetocrystalline anisotropy because the substitution of Co into the sites of Fe. Besides, Co substitution also

TABLE 1. Lattice parameters and the values of crystal size of $\text{YFe}_{1-x}\text{Co}_x\text{O}_3 \pm \delta$ nanomaterials

$\text{YFe}_{1-x}\text{Co}_x\text{O}_3$	2θ (121), °	D_{XRD} , nm	a , Å	b , Å	c , Å	V , Å ³
$x = 0.1$	33.1913	25.68	5.5781	5.2732	7.5902	223.26
$x = 0.15$	33.2616	25.67	5.5694	5.2625	7.5758	222.04
$x = 0.2$	33.2792	24.44	5.5648	5.2619	7.5708	221.68
$x = 0.25$	33.3330	24.18	5.5575	5.2580	7.5551	220.77
$x = 0.3$	33.3668	23.96	5.5524	5.2505	7.5482	220.05
$x = 0.5$	33.5797	22.89	5.5217	5.2177	7.5009	216.11

TABLE 2. EDX results and magnetic properties of $\text{YFe}_{1-x}\text{Co}_x\text{O}_3$ materials

$\text{YFe}_{1-x}\text{Co}_x\text{O}_3$	Nominal composition	Actual composition	H_c , Oe	M_r , emu/g	M_s , emu/g	$(\text{BH})_{\text{max}}$, emu/g
$x = 0$	YFeO_3 [15]	$\text{YFe}_{1.02}\text{O}_{3.32}$	53.36	0.019	0.390	0.390
$x = 0.1$	$\text{YFe}_{0.9}\text{Co}_{0.1}\text{O}_3$	$\text{YFe}_{0.88}\text{Co}_{0.11}\text{O}_{3.37}$	88.86	0.031	0.413	0.413
$x = 0.2$	$\text{YFe}_{0.8}\text{Co}_{0.2}\text{O}_3$	$\text{YFe}_{0.79}\text{Co}_{0.21}\text{O}_{3.28}$	132.66	0.075	0.569	0.569
$x = 0.3$	$\text{YFe}_{0.7}\text{Co}_{0.3}\text{O}_3$	$\text{YFe}_{0.69}\text{Co}_{0.28}\text{O}_{3.67}$	352.16	0.207	0.825	0.825
$x = 0.5$	$\text{YFe}_{0.5}\text{Co}_{0.5}\text{O}_3$	$\text{YFe}_{0.51}\text{Co}_{0.51}\text{O}_{3.43}$	781.46	0.268	1.006	1.006

FIG. 5. TEM images of $\text{YFe}_{1-x}\text{Co}_x\text{O}_3$ nanomaterials annealed at 800 °C for 1 h

led to a change in Fe–O–Fe angles, as well as an oxidation of a small amount of Fe^{3+} ions to Fe^{4+} ions to compensate the charge caused by the appearance of Co^{2+} at the sites of Fe^{3+} . Similar results were mentioned by other authors [16, 17, 20].

Noticeably, with $x \geq 0.2$, YFeO_3 changed gradually from a soft magnetic material ($H_c < 100$ Oe) to a hard magnetic material with high coercive force ($H_c \gg 100$ Oe, especially with $x = 0.5$). This proved that magnetic properties of YFeO_3 material can be changed by doping Co, thus the applicability of this material can be extended in many devices requiring the soft magnetic material (cores of transformers, electromagnets, magnetic conductors) and also the ones requiring the hard magnetic material (permanent magnets or recorders).

4. Conclusions

$\text{YFe}_{1-x}\text{Co}_x\text{O}_3$ ($0.1 \leq x \leq 0.5$) perovskite-type nanomaterials were successfully prepared by the chemical coprecipitation method via the hydrolysis of cations in hot water ($t^\circ \geq 90$ °C) with KOH 5 % as a precipitating agent. Along with the increase of Co doping, the values of crystal size and unit cell volume decreased from 26 nm to 22

nm, from 224 \AA^3 to 216 \AA^3 , respectively, while those of the coercive force (H_c), remnant magnetization (M_r), saturation magnetization (M_s) and maximum energy product (BH_{max}) increased from 88.86 to 781.46 Oe, from 0.031 to 0.268 emu/g, from 0.413 to 1.006 emu/g and from 0.413 to 1.006 emu/g, respectively. The substitution of Co into the sites of Fe led to a change of the crystal lattice, which affected the magnetic properties of $YFeO_3$ perovskite-type nanomaterials.

References

- [1] Nishiyama Sh., Asako I., Iwadate Ya., Hattori T. Preparation of $Y(Mn_{1-x}Fe_x)O_3$ and Electrical Properties of the Sintered Bodies. *Open Journal of Inorganic Chemistry*, 2015, **5**, P. 7–11.
- [2] Gimaztdinova M.M., Tugova E.A., Tomkovich M.V., Popkov V.I. Synthesis of $GdFeO_3$ nanocrystals. *Condensed Matter and Interfaces*, 2016, **18** (3), P. 422–431.
- [3] Bachina A., Ivanov V.A., Popkov V.I. Peculiarities of $LaFeO_3$ nanocrystals formation via glycine-nitrate combustion. *Nanosystems: Physics, Chemistry, Mathematics*, 2017, **8** (5), P. 647–653.
- [4] Martinson K.D., Kondrashkova I.S., Popkov V.I. Synthesis of $EuFeO_3$ nanocrystals by glycine-nitrate combustion method. *Russian Journal of Applied Chemistry*, 2017, **90** (8), P. 980–985.
- [5] Lee J., Kim S., Tak Y., Yoon Y.S. Study on the LLT solid electrolyte thin film with LiPON interlayer intervening between LLT and electrodes. *Journal of Power Sources*, 2006, **163**, P. 173–179.
- [6] Oemar U., Ang P.S., Hidajat K., Kawi S. Promotional effect of Fe on perovskite $LaNi_xFe_{1-x}O_3$ catalyst for hydrogen production via steam reforming of toluence. *International Journal of Hydrogen Energy*, 2013, **38**, P. 5525–5534.
- [7] Jeffrey W.F. Perovskite oxides for semiconductor-based gas sensors. *Sensors and Actuators B: Chemical*, 2007, **123**, P. 1169–1179.
- [8] Karpinsky D.V., Troyanchuk I.O., et al. Crystal structure and magnetic properties of the $LaCo_{0.5}Fe_{0.5}O_3$ perovskite. *Crystallography Report*, 2006, **51** (4), P. 596–600.
- [9] Maiti R., Basu S., Chakravorty D. Synthesis of nanocrystalline $YFeO_3$ and its magnetic properties. *Journal of Magnetism And Magnetic Materials*, 2009, **321**, P. 3274–3277.
- [10] Lomanova N.A., Gusarov V.V. Influence of synthesis temperature on $BiFeO_3$ nanoparticles formation. *Nanosystems: Physics, Chemistry, Mathematics*, 2013, **4** (5), P. 696–705.
- [11] Feng C., Ruan Sh., et al. Ethanol sensing properties of $LaCo_xFe_{1-x}O_3$ nanoparticles: Effects of calcination temperature, Co-doping, and carbon nanotube-treatment. *Sensors and Actuators B*, 2011, **155** (1), P. 232–238.
- [12] Chithralekha P., Murugeswari C., Ramachandran K., Srinivasan R. The study on ultrasonic velocities of $Co_xFe_{3-x}O_4$ nanoferrofluid prepared by co-precipitation method. *Nanosystems: Physics, Chemistry, Mathematics*, 2016, **7** (3), P. 558–560.
- [13] Jacob K.T., Rajitha G. Nonstoichiometry, defects and thermodynamic properties of $YFeO_3$, YFe_2O_4 , $Y_3Fe_5O_{12}$. *Solid State Ionics*, 2012, **224**, P. 32–40.
- [14] Nguyen A.T., Almjashaeva O.V., et al. Synthesis and magnetic properties of $YFeO_3$ nanocrystals. *Inorganic Materials*, 2009, **45** (11), P. 1304–1308.
- [15] Nguyen A.T., Mittova I.Ya., et al. Influence of the preparation conditions on the size and morphology of nanocrystalline lanthanum orthoferrite. *Glass Physics and Chemistry*, 2008, **34** (6), P. 756–761.
- [16] Knurova M.V., Mittova I.Ya., et al. Effect of the degree of doping on the size and magnetic properties of nanocrystals $La_{1-x}Zn_xFeO_3$ synthesized by the sol-gel method. *Russian Journal of Inorganic Chemistry*, 2017, **62** (3), P. 281–287.
- [17] Nguyen A.T., Hap M.C. Study on synthesis of modified $Y_{1-x}Cd_xFeO_3$ nanosized material by co-precipitation method. *Vietnam Journal of Chemistry*, 2016, **54** (5e 1, 2), P. 237–241.
- [18] JCPDC PCPDFWIN: A Windows Retrieval/Display program for Accessing the ICDD PDF - 2 Data base, International Centre for Diffraction Data, 1997.
- [19] Housecroft C.E., Sharpe A.G. *Inorganic Chemistry*, 2nd ed. Pearson Prentice Hall, USA, 2005, 949 p.
- [20] Nguyen A.T., Mittova I.Ya., et al. Sol-gel formation and properties of nanocrystals of solid solution $Y_{1-x}Ca_xFeO_3$. *Russian Journal of Inorganic Chemistry*, 2014, **59** (2), P. 40–45.

Cytotoxicity analysis of gadolinium doped cerium oxide nanoparticles on human mesenchymal stem cells

A. L. Popov¹, I. V. Savintseva¹, E. A. Mysina¹, A. B. Shcherbakov², N. R. Popova¹,
O. S. Ivanova³, D. D. Kolmanovich⁴, V. K. Ivanov^{3,5,*}

¹Institute of Theoretical and Experimental Biophysics, Russian Academy of Sciences,
Pushchino, Moscow region, 142290, Russia

²Zabolotny Institute of Microbiology and Virology, National Academy of Sciences of Ukraine,
Kyiv D0368, Ukraine

³Kurnakov Institute of General and Inorganic Chemistry of Russian Academy of Sciences,
Moscow 119991, Russia

⁴Kabardino-Balkarian State University, Nalchik, 360004, Russia

⁵Moscow Technological University, Institute of Fine Chemical Technologies, Moscow 119991, Russia

*van@igic.ras.ru

PACS 87.55.ne, 87.85.Rs, 81.07.Bc

DOI 10.17586/2220-8054-2018-9-3-430-438

A complex analysis of cytotoxicity was performed for a nanodispersed sol of cerium dioxide doped with gadolinium ($\text{Ce}_{0.8}\text{Gd}_{0.2}\text{O}_{2-x}$) using a culture of mesenchymal stem cells. The absence of cyto- and genotoxicity over a wide range of concentrations (10^{-5} – 10^{-9} M) was demonstrated. At that, the highest concentration of $\text{Ce}_{0.8}\text{Gd}_{0.2}\text{O}_{2-x}$ nanoparticles (10^{-4} M) was found to slightly reduce the activity of intracellular dehydrogenase, yet not leading to the development of apoptosis and further cell death. The obtained results confirm a high degree of $\text{Ce}_{0.8}\text{Gd}_{0.2}\text{O}_{2-x}$ nanoparticle biocompatibility, which opens prospects for their safe application as a contrasting agent in the magnetic resonance tomography.

Keywords: ceria, gadolinium, nanomaterials, cytotoxicity, mesenchymal stem cells.

Received: 22 March 2018

1. Introduction

The modern level of nanotechnology development allows for the design of new polyfunctional materials possessing unique physicochemical properties that find wide application in the manufacturing of sensors [1, 2], catalysts [3, 4] hybrid functional coatings [5, 6] and biomedical products [7]. At that, nanocrystalline cerium dioxide is considered to be one of the most promising materials for biomedical purposes [8–16]. To date, a broad variety of techniques and synthetic schemes is reported for the preparation of nanocrystalline cerium dioxide and for its surface modification, conferring it a variety of functional properties [17–20].

Previously, we proposed a new method for obtaining aqueous sols of nanodisperse solid solutions of cerium dioxide doped with gadolinium ions, with a potential for use in biomedicine [21]. The Gd^{3+} ion, having 7 unpaired electrons ($^8S_{7/2}$), is known to possess an exceptionally high magnetic moment ($7.94 \mu_B$), which makes it possible to use gadolinium-containing compounds as contrast agents in the magnetic resonance imaging (MRI) [22]. It is believed that nanocrystalline gadolinium oxide is one of the most promising contrast agents for MRI, since it is characterized by a higher value of the longitudinal relaxation constants compared to the Gd^{3+} chelate complexes [23]. Meanwhile gadolinium does not participate in the human biochemical cycle and is highly toxic in its ionic form, which eliminates the possibility of its direct biomedical application without additional modification [24]. In existing clinically approved gadolinium-based contrasting preparations, the biological inertness of gadolinium ion is achieved by encapsulating it in macrocyclic complexes [25].

In light of this, the present study aimed to carry out a comprehensive assessment of the cytotoxic properties of a new type of citrate-stabilized cerium dioxide nanoparticles doped with gadolinium on the culture of human mesenchymal stem cells.

2. Materials and methods

2.1. Synthesis of $\text{Ce}_{0.8}\text{Gd}_{0.2}\text{O}_{2-x}$ nanoparticles

For the preparation of colloidal solutions of cerium dioxide nanoparticles doped with gadolinium, assuming the sum of rare-earth elements per liter of solvent equal to 0.01 mole, 0.347 g of $\text{Ce}(\text{NO}_3)_3 \cdot 6\text{H}_2\text{O}$ and 0.087 g of $\text{Gd}(\text{NO}_3)_3 \cdot 5\text{H}_2\text{O}$ (molar ratio Ce:Gd = 4:1) were dissolved in 100 ml of distilled water, and a preliminarily transformed to the OH-form anion exchange resin Amberlite IRA 410 CL was added to the resulting solution until a pH = 10.0. The formed sols were separated from the resin by filtration, immediately transferred to 100 ml polytetrafluoroethylene autoclaves (filling degree ~50 %) and exposed to hydrothermal microwave treatment for 1 hour at 150 °C. After the completion of experiments the autoclaves were removed from the oven and cooled to room temperature in air. Citric acid was added to the resulting aqueous sols of the solid solution of rare-earth oxides to achieve the concentration of 0.01 M. According to the X-ray diffraction analysis, the crystal cell parameter for the sample $\text{Ce}_{0.8}\text{Gd}_{0.2}\text{O}_{2-x}$, determined upon refinement of the crystal structure, is 0.54174(4) nm.

2.2. Preparation of aqueous sols of $\text{Ce}_{0.8}\text{Gd}_{0.2}\text{O}_{2-x}$ nanoparticles and analysis of physico-chemical parameters

The 0.01 M solution of sol (1 ml) was mixed with 2 ml of isopropyl alcohol (70 %) and stirred for 30 minutes at ~80 °C. The resulting solution was then centrifuged (9.000 g) for 10 minutes at 20 °C, the supernatant was removed and the obtained precipitate was redispersed in 500 μl of isopropyl alcohol. This sequence was repeated three times. The resulting precipitate was dried at 50 °C in an oven and then redispersed in 500 μl of deionized water. The obtained sol was diluted to pH 7.2 with 10 % aqueous ammonia.

The size distribution of nanoparticles in sols was assessed by a dynamic light scattering method using a Beckman Coulter N5 Submicron Particle Size Analyzer (USA). The size distribution was studied for $\text{Ce}_{0.8}\text{Gd}_{0.2}\text{O}_{2-x}$ nanoparticle dispersions in deionized water, F12 culture medium (HEPES) and F12 culture medium containing 5 % of serum. The micromorphology of nanoparticles was analyzed with the transmission electron microscopy using a Leo912 AB Omega electron microscope at acceleration voltage of 100 kV (magnification up to $\times 500000$), the phase composition of the samples was determined by electron diffraction.

2.3. Cell culture

Dental pulp stem cells (DPSC) were isolated from the third molar germ extracted for orthodontic indications from a healthy 16-year-old patient. The cells were extracted with DMEM ("PanEko", Russia) containing 200 U/ml penicillin and 200 $\mu\text{g}/\text{ml}$ streptomycin ("Life Technologies", USA) with a syringe inserted into the dental apex and further treated with 0.25 % trypsin – 0.02 % EDTA ("Life Technologies", USA) for 30 min at 37 °C. The isolated cells were centrifuged for 2 min at 1500 rpm and resuspended to a single cell state in the culture medium consisting of DMEM/F-12 (1:1; Life Technologies) with the addition of 10 % fetal calf serum (FCS). The obtained solution was transferred into 25 ml vials and cultured in the 5 % CO_2 atmosphere at 37 °C with the addition of 10 % FCS (HyClone), 100 U/ml penicillin/streptomycin, 2 mM L-glutamine in DMEM ("PanEko", Russia). When the subconfluent cells state was achieved, the cultured cells were treated with 0.25 % EDTA-trypsin solution, and added to 75 cm^3 vials in a ratio of 1:3. Cells were cultured in DMEM/F-12 ("PanEko", Russia) with the addition of 10 % FCS, 100 U/ml penicillin/streptomycin and 2 mM L-glutamine. In our study, cell cultures of 3–5 passages were used.

2.4. MTT assay

The determination of mitochondrial and cytoplasmic dehydrogenases activity in living cells was carried out using a MTT assay based on the reduction of the colorless tetrazolium salt (3-[4,5-dimethylthiazol-2-yl]-2,5-diphenyltetrazolium bromide, MTT). [26]. After 24 and 72 hours of culturing cells 0.5 mg/ml of MTT reagent was introduced into the wells by replacing the culture medium, followed by a standard MTT assay.

2.5. The differentiated fluorescent staining method

Assessment of viability of cells cultured in the presence of $\text{Ce}_{0.8}\text{Gd}_{0.2}\text{O}_{2-x}$ nanoparticles was performed on a Carl Zeiss Axiovert 200 microscope. An L-7007 LIVE/DEAD BacLight Bacterial Viability Kit (Invitrogen) was used for the assay, which includes SYTO 9 fluorescent dye (absorption – 420 nm, emission – 580 nm) and propidium iodide (PI) (absorption – 488 nm, emission 640 nm). The morphological analysis of the nuclear apparatus after incubation with nanoparticles was performed using a nuclear dye Hoechst 33342 (absorption – 361 nm, emission – 486 nm) (Invitrogen). The dyes were added to the medium (1 $\mu\text{g}/\text{ml}$) and the plate was placed

in a CO₂ incubator for 15 minutes. Microphotography was performed after washing the cells of the dye with a phosphate-buffered saline.

2.6. Assessment of the free lactate dehydrogenase level

The method allows estimation of the cytoplasmic enzyme concentration – lactate dehydrogenase, which is found in the culture medium in case of cell membrane damage. The cells were seeded into 96-wells microplates and cultured for 24 h in an atmosphere of 5 % CO₂ in air at 37 °C. Six hours after seeding the culture medium was replaced with a medium containing Ce_{0.8}Gd_{0.2}O_{2-x} nanoparticles with concentrations from 10⁻⁴ M to 10⁻⁹ M. Cells with added medium, which did not contain Ce_{0.8}Gd_{0.2}O_{2-x} nanoparticles, were used as a positive control. Wells with cells containing 10 μl of Triton X-100 were used as a negative control. The level of lactate dehydrogenase in the culture medium was determined 24 hours after the introduction of the Ce_{0.8}Gd_{0.2}O_{2-x} nanoparticles in accordance with the manufacturer's protocol (Thermo Scientific™ Pierce™ LDH Cytotoxicity Assay Kit). The optical density of the solutions was determined at wavelengths λ = 490 nm and λ = 640 nm using a Microplate Reader Thermo Multiskan Ascent 96 & 384 photocolormeter (Thermo Fisher Scientific, United Kingdom).

2.7. Analysis of proliferative activity of human MSC

The cells were seeded into 96-wells microplates (Corning Costar, USA) at a density of 10⁴/cm² and cultured for 12 h in an atmosphere of 5 % CO₂ in air at 37 °C, followed by introduction of Ce_{0.8}Gd_{0.2}O_{2-x} nanoparticles solutions with various concentration (10⁻⁴ M – 10⁻¹¹ M) by replacing the culture medium. The proliferative activity was analyzed and the number of cells in each well was counted daily for 4 days using a Molecular Devices CloneSelect Imager System Plate Reader.

2.8. Statistical data analysis

The experiments were carried out in 3 – 4 replicates, analytical determinations for each sample were performed in duplicate. The results of the experiments were compared with the control experiment. The methods of variation statistics were applied to estimate the reliability of results. To assess the statistical significance, the Mann–Whitney U test was used (p ≤ 0.05). The obtained data was processed using the GraphPad 5.0 and Microsoft Excel 2007 programs.

3. Results and discussion

3.1. Physico-chemical parameters of the studied samples

According to TEM data, the synthesized Ce_{0.8}Gd_{0.2}O_{2-x} nanoparticles have an ultra-small size, on the order of 3 – 5 nm (Fig. 1a).

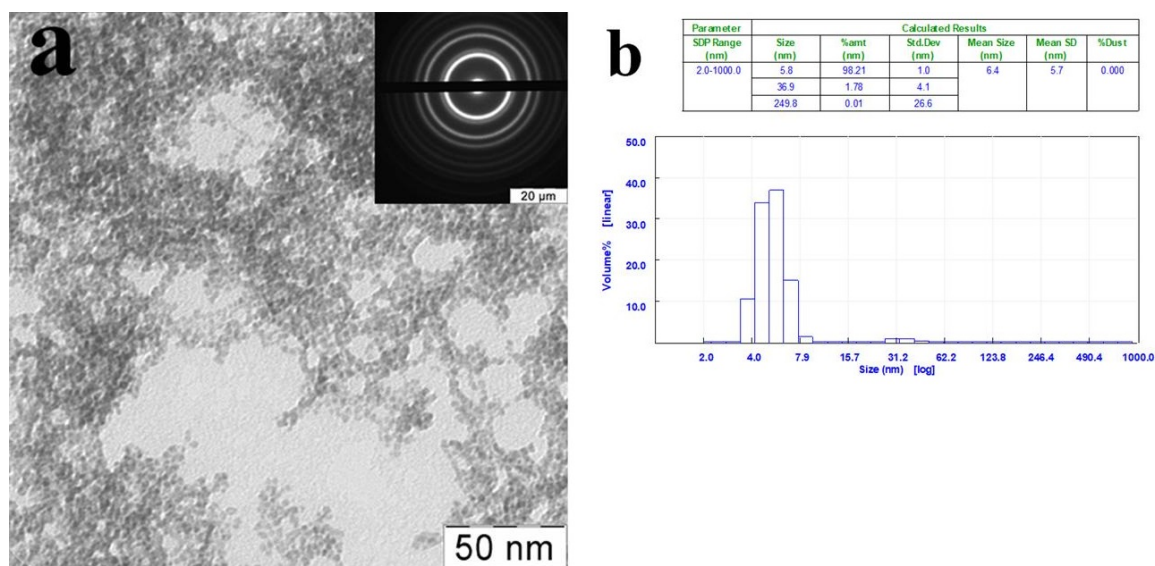


FIG. 1. (a) TEM image of Ce_{0.8}Gd_{0.2}O_{2-x} nanoparticles; (b) A size distribution histogram of Ce_{0.8}Gd_{0.2}O_{2-x} nanoparticles upon dilution in a culture medium containing 5 % serum

Next, the size distribution of the nanoparticles was determined by forming suspensions in deionized water, F12 culture medium (HEPES) and F12 culture medium (HEPES) containing 5 % fetal calf serum. To prepare the suspensions, the sol of $Ce_{0.8}Gd_{0.2}O_{2-x}$ nanoparticles was diluted 20-fold by adding a predetermined amount of each solvent. The hydrodynamic radius of nanoparticles in deionized water suspensions was 5.0 – 7.0 nm, which amounts 95 – 99 % of the total volume of the suspension. The analysis of the hydrodynamic radius of $Ce_{0.8}Gd_{0.2}O_{2-x}$ nanoparticles in F12 serum-free medium showed that the mean size of nanoparticle is 12 nm (65.8 %), while in the colloidal solution the micron-size aggregates (34.1 %) are present.

The dilution of $Ce_{0.8}Gd_{0.2}O_{2-x}$ nanoparticles in F12 medium containing FCS provides the monodispersity of the system and the mean hydrodynamic radius of the particles amounts about 6.0 nm, which is 97 – 100 % of the total volume of the suspension. Earlier it was shown that the negative zeta-potential of nanoparticles surface results in minimal adsorption of proteins (or complete absence of adsorption) on the surface of nanoparticles [27]. Since the layer of citrate ions covering the surface of the nanoparticle provides a negative zeta-potential for the surface, it can be assumed that serum proteins that are partially adsorbed on the surface of nanoparticle, i.e. not forming a “protein corona” of considerable scale, are the size-stabilizing factor for nanoparticles. On the basis of these results, it can be concluded that an interaction with serum proteins does not lead to significant aggregation of nanoparticles, which may allow one to maintain the hydrodynamic radius close to the initial one, for example, after the introduction of nanoparticles into the bloodstream.

TABLE 1. Size distribution analysis of $Ce_{0.8}Gd_{0.2}O_{2-x}$ nanoparticles after dilution in various biological media

Solvent	Size of nanoparticles, nm	% of the total number in the sample	error, %
Deionized water	5.0	99.5	0.000
	51.2	0.19	
	987.5	0.26	
Culture medium F12	12.1	69.21	8.097
	149.3	0.59	
	2248.4	30.20	
Culture medium F12 +5% serum	5,8	98,77	8,851
	61,0	0,83	
	228,5	0,21	
	907,3	0,19	

3.2. Study of cytotoxicity of $Ce_{0.8}Gd_{0.2}O_{2-x}$ nanoparticles

The MTT test was used to assess the viability of human MSCs cultured in the presence of $Ce_{0.8}Gd_{0.2}O_{2-x}$ nanoparticles. Fig. 2 shows that incubation of human MSCs with $Ce_{0.8}Gd_{0.2}O_{2-x}$ nanoparticles in the range of concentration from 10^{-5} M to 10^{-9} M does not lead to a decrease in the level of dehydrogenase activity after 24 hours and 72 hours of cultivation. It is worth noting that MTT signal tends to increase in the experiments with micro- and nanomolar concentrations of nanoparticles, which might be associated with the promotion of MSC proliferation in the presence of cerium dioxide nanoparticles doped with gadolinium. An increase in the level of dehydrogenase activity indirectly denotes an increase in the number of viable cells. This confirms the more active proliferation of cells in the presence of $Ce_{0.8}Gd_{0.2}O_{2-x}$ nanoparticles, which may be due to the effect of nanoparticles on the level of intracellular ROS and, consequently, intracellular signaling pathways. Indeed, our recent publications show that nanoparticles of undoped cerium dioxide are capable of accelerating the proliferation of cells in culture [28–30]. Presumably, one of the mechanisms underlying the stimulation of proliferative activity is the ability of cerium dioxide nanoparticles to act as an effective antioxidant and to reduce the level of intracellular ROS that is slightly elevated under *in vitro* culture conditions [31].

The analysis of free lactate dehydrogenase level (Fig. 3) in culture of human MSC after co-cultivation of cells with $Ce_{0.8}Gd_{0.2}O_{2-x}$ nanoparticles did not reveal a significant increase both after 24 hours and after 72 hours, which confirms the absence of cytotoxic effect of nanoparticles over the whole studied range of concentrations.

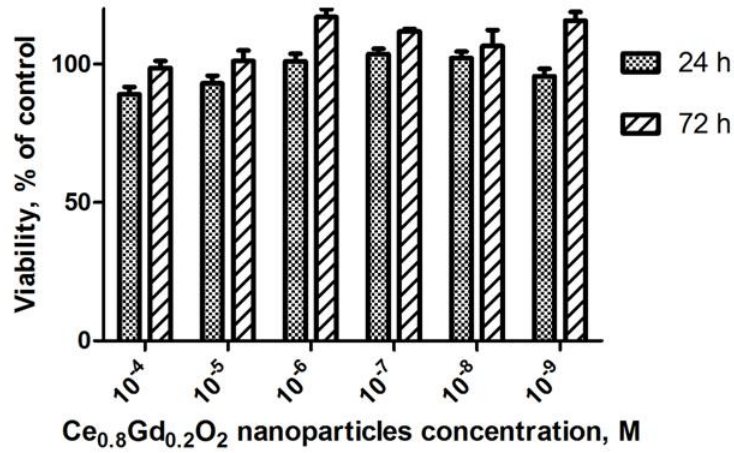


FIG. 2. The analysis of human MSC dehydrogenase activity (in % of control) according to the MTT test when incubated with Ce_{0.8}Gd_{0.2}O_{2-x} nanoparticles (10⁻⁴ – 10⁻⁹ M) after 24 and 72 hours of culture

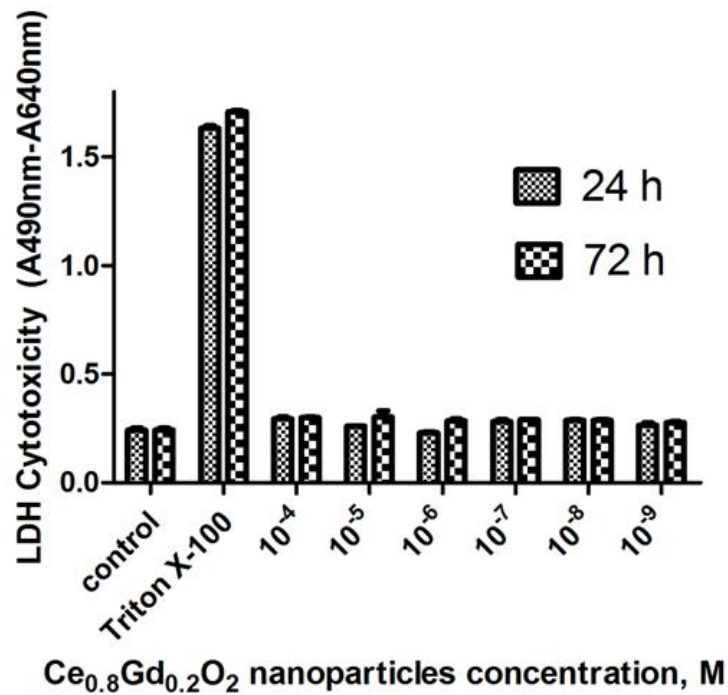


FIG. 3. The analysis of free lactate dehydrogenase level in culture of human MSC after 24 hours and 72 hours of co-cultivation of cells with Ce_{0.8}Gd_{0.2}O_{2-x} nanoparticles (10⁻⁴ M – 10⁻⁹ M)

To estimate the ratio of dead and living cells in the culture of MSC after culturing with the $\text{Ce}_{0.8}\text{Gd}_{0.2}\text{O}_{2-x}$ nanoparticles, the method of differentiated fluorescent staining was used (Fig. 4). The method is based on the monitoring of viable cells depending on the integrity of their membranes. The SYTO 9 dye stains all the cells in the culture (green staining), while a breach of the integrity of the membrane ensures its permeability to the selective propidium iodide DNA dye (red staining of dead nuclei).

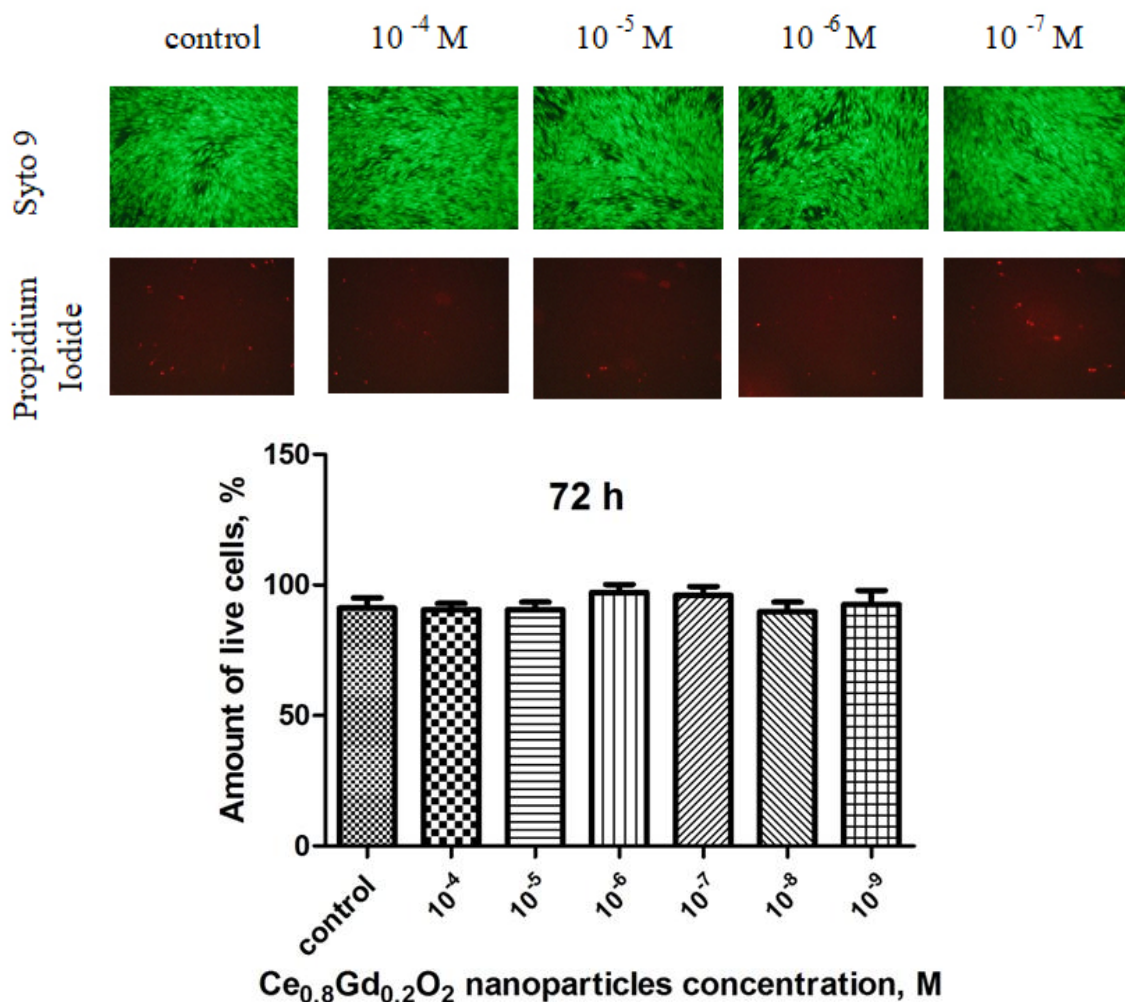


FIG. 4. Microphotographs and a graph of the quantitative estimation of the proportion of viable human MSCs after 72 hours of cultivation with $\text{Ce}_{0.8}\text{Gd}_{0.2}\text{O}_{2-x}$ nanoparticles (10^{-4} M – 10^{-9} M) (staining with L-7007 LIVE/DEAD kit)

We have demonstrated that $\text{Ce}_{0.8}\text{Gd}_{0.2}\text{O}_{2-x}$ nanoparticles in all studied concentrations (10^{-4} M – 10^{-9} M) do not cause the death of cells in culture and the appearance of positive propidium iodide-stained cells. Quantitative assessment of the proportion of viable cells confirmed the absence of a significant difference with the control group, with no introduced nanoparticles.

The morphological analysis of the nuclear apparatus of human MSC (Fig. 5) after cultivation with $\text{Ce}_{0.8}\text{Gd}_{0.2}\text{O}_{2-x}$ nanoparticles (10^{-4} M – 10^{-9} M) showed no increase in the proportion of cells with a damaged or altered nucleus. Both in the control and in the experimental groups with nanoparticles, a significant amount of mitotic division was observed, which confirms the active proliferation of the cell culture. Quantitative assessment of the proportion of cells with a compromised nuclear apparatus did not reveal a significant difference with the control untreated group, which indirectly confirms the lack of genotoxic effect of the $\text{Ce}_{0.8}\text{Gd}_{0.2}\text{O}_{2-x}$ nanoparticles.

The loss of the mitochondrial membrane potential is a typical feature of the apoptosis development. This is the earliest event in the process of programmed cell death, preceding the externalization of phosphatidylserine to the

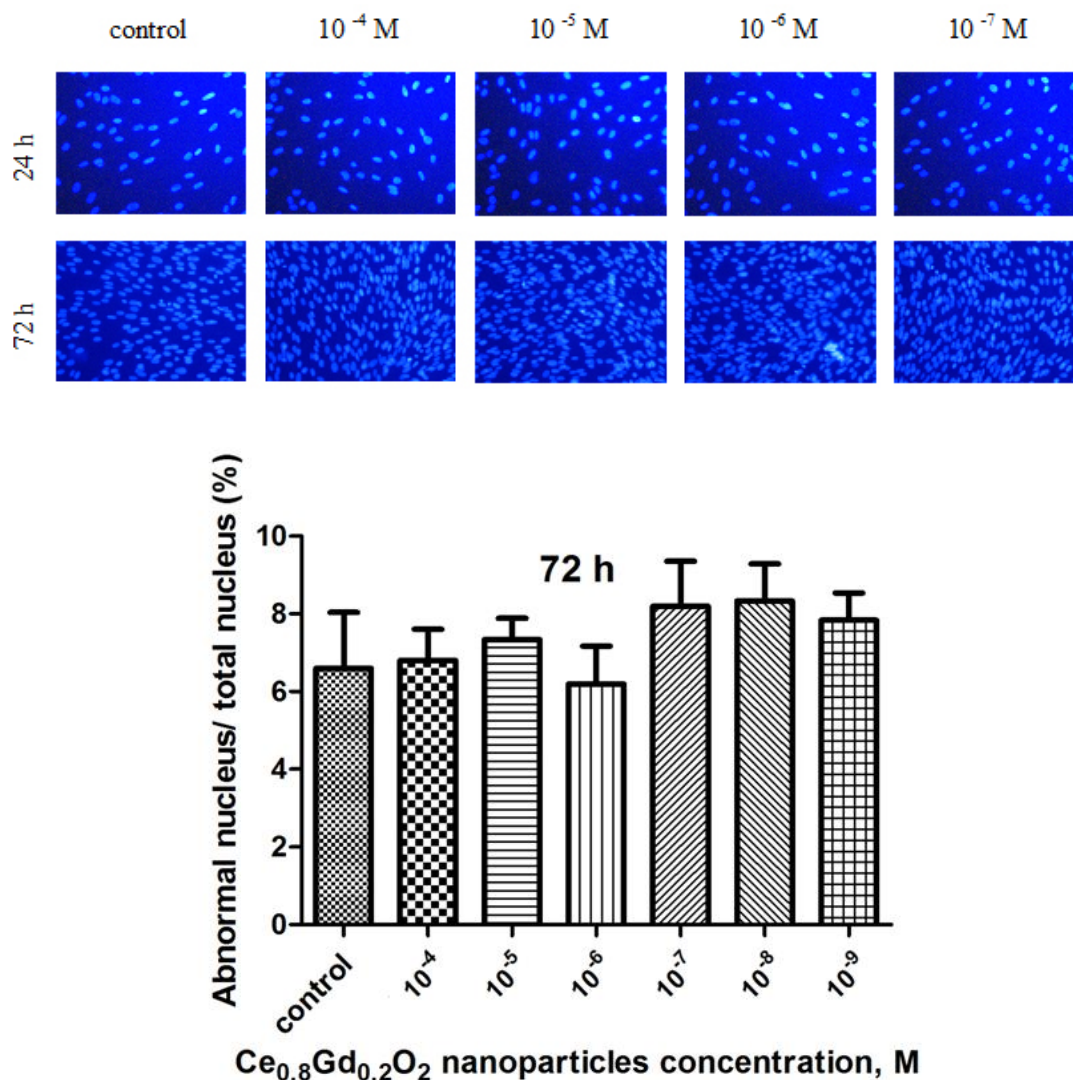


FIG. 5. Micrographs of human MSC after 72 hours of cultivation with $\text{Ce}_{0.8}\text{Gd}_{0.2}\text{O}_{2-x}$ nanoparticles (10^{-4} M – 10^{-9} M) and a quantitative estimation of the proportion of cells with nuclear apparatus abnormalities (fragmentation or change in the morphology of the nucleus) after 72 hours of cultivation (staining with Hoechst 33342)

plasma membrane and coinciding with the activation of the caspase cycle [32,33]. The analysis of mitochondrial potential level (Fig. 6) for human MSC after incubation with $\text{Ce}_{0.8}\text{Gd}_{0.2}\text{O}_{2-x}$ nanoparticles did not reveal its decrease in all studied concentrations (10^{-4} M – 10^{-9} M), which confirms the absence of a negative effect on the oxidative phosphorylation processes and the metabolic activity of mitochondria as a whole.

4. Conclusions

Thus, in the present work we performed a comprehensive analysis of the cytotoxicity of citrate-stabilized cerium dioxide nanoparticles doped with gadolinium towards human MSC culture. It was demonstrated that $\text{Ce}_{0.8}\text{Gd}_{0.2}\text{O}_{2-x}$ nanoparticles retain their size within 10 nm after the dilution in a culture medium containing serum. The $\text{Ce}_{0.8}\text{Gd}_{0.2}\text{O}_{2-x}$ nanoparticles do not exhibit a cytotoxic effect on human MSC in a wide range of concentrations (10^{-4} – 10^{-11} M), do not reduce the level of their mitochondrial potential and do not lead to an increase in the proportion of apoptotic cells in the culture.

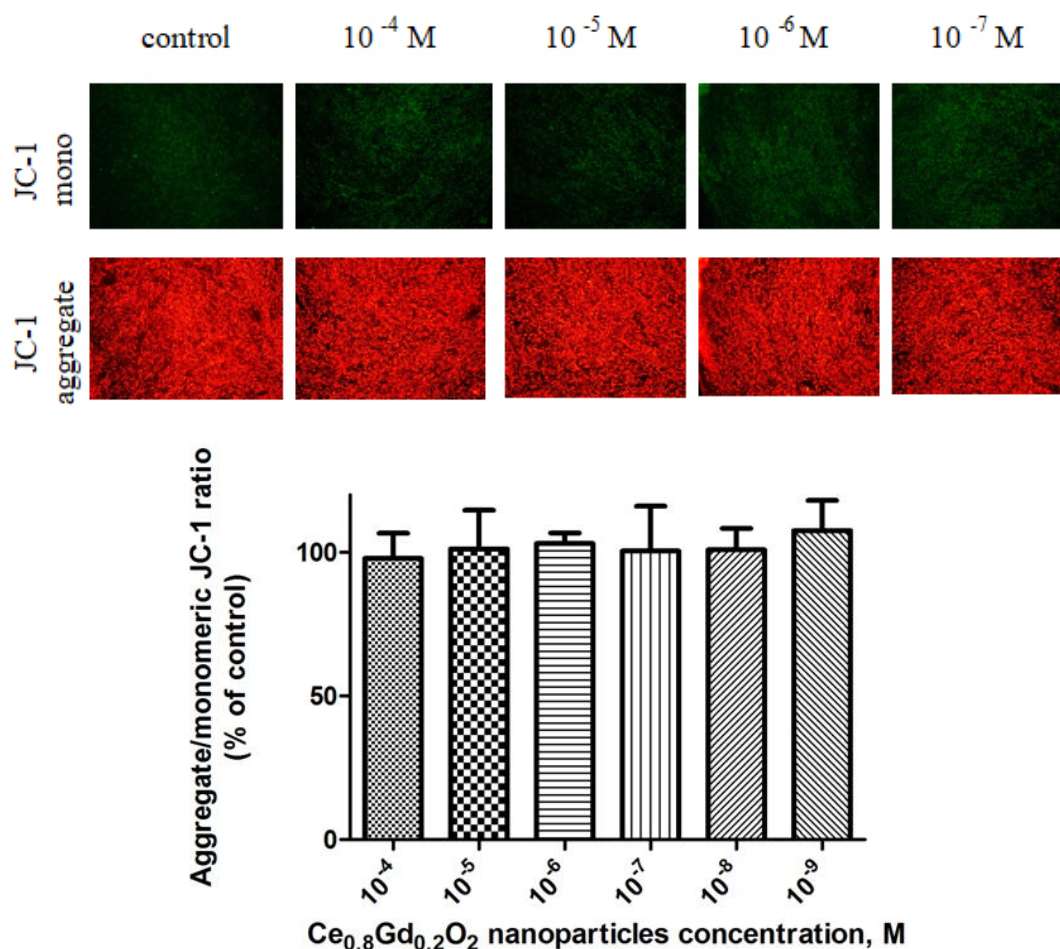


FIG. 6. Microphotographs and a histogram of quantitative assessment of the mitochondrial potential level for the human MSC after 72 hours of cultivation with $\text{Ce}_{0.8}\text{Gd}_{0.2}\text{O}_{2-x}$ nanoparticles (10^{-4} M – 10^{-9} M) (staining with JC-1)

Acknowledgements

This research has been supported by the Russian Science Foundation (project 17-73-10417).

References

- [1] Khodke M.R., Joshi S.V. An investigative study on application of carbon nanotubes for strain sensing. *Nanosystems: Phys., Chem., Math.*, 2016, 7 (4), P. 755–758.
- [2] Suganthi G., Arockiadoss T., Uma T.S. ZnS nanoparticles decorated graphene nanoplatelets as immobilisation matrix for glucose biosensor. *Nanosystems: Phys., Chem., Math.*, 2016, 7 (4), P. 637–642.
- [3] Karthikeyan N., Narayanan V., Stephen A. Visible light degradation of textile effluent using nanostructured $\text{TiO}_2/\text{Ag}/\text{CuO}$ photocatalysts. *Nanosystems: Phys., Chem., Math.*, 2016, 7 (4), P. 695–698.
- [4] Rokesh K., Jeganathan K., Jothivenkatachalam K. Zinc oxide-palladium material an efficient solar-light driven photocatalyst for degradation of congo red. *Nanosystems: Phys., Chem., Math.*, 2016, 7 (4), P. 740–746.
- [5] Mubofu E.B., Mlowe S., Revaprasadu N. Cashew nut shells as source of chemicals for preparation of chalcogenide nanoparticles. *Nanosystems: Phys., Chem., Math.*, 2016, 7 (4), P. 724–727.
- [6] Nanjunda Reddy B.H., Venkata Lakshmi V., Vishnu Mahesh K.R., Mylarappa M., Raghavendra N., Venkatesh T. Preparation of chitosan/different organomodified clay polymer nanocomposites: studies on morphological, swelling, thermal stability and anti-bacterial properties. *Nanosystems: Phys., Chem., Math.*, 2016, 7 (4), P. 667–674.
- [7] Bobo D., Robinson K.J., Islam J., Thurecht K.J., Corrie S.R. Nanoparticle-Based Medicines: A Review of FDA-Approved Materials and Clinical Trials to Date. *Pharm Res.* 2016, 33 (10), P. 2373–87.
- [8] Popov A.L., Shcherbakov A.B., Zholobak N.M., Baranchikov A.Ye., Ivanov V.K. Cerium dioxide nanoparticles as third-generation enzymes (nanozymes). *Nanosystems: Phys., Chem., Math.*, 2017, 8 (6), P. 760–781.

- [9] Shcherbakov A.B., Ivanov V.K., Zholobak N.M., Ivanova O.S., Krysanov E.Y., Baranchikov A.E., Spivak N.Ya., Tretyakov Y.D. Nanocrystalline ceria based materials-Perspectives for biomedical application. *Biophysics*, 2011, **56**, P. 987–1004.
- [10] Ivanov V.K., Shcherbakov A.B., Baranchikov A.E., Kozik V.V. Synthesis, structure, physicochemical properties and biological activity of nanodispersed cerium dioxide. Tomsk, Tomsk State University, 2013.
- [11] Ivanov V.K., Shcherbakov A.B., Usatenko A.V. Structure-sensitive properties and biomedical applications of nanodispersed cerium dioxide. *Russ. Chem. Rev.*, 2009, **78**, P. 855–871.
- [12] Tarnuzzer R.W., Colon J., Patil S., Seal S. Vacancy engineered ceria nanostructures for protection from radiation-induced cellular damage. *Nano Lett.*, 2005, **5**, P. 2573–2577.
- [13] Karakoti A.S., Singh S., Kumar A., Malinska M., Kuchibhatla S.V.N.T., Wozniak K., Self W.T., Seal S. PEGylated nanoceria as radical scavenger with tunable redox chemistry. *J. Am. Chem. Soc.*, 2009, **131**, P. 14144–14145.
- [14] Korsvik C., Patil S., Seal S., Self W.T. Superoxide dismutase mimetic properties exhibited by vacancy engineered ceria nanoparticles. *Chem. Commun.*, 2007, P. 1056–1058.
- [15] Shcherbakov A.B., Ivanov V.K., Sirota T.V., Tretyakov Y.D. Inhibition of adrenaline autooxidation by nanocrystalline ceria. *Doklady Chem.*, 2011, **437**, P. 60–62.
- [16] Das S., Dowding J.M., Klump K.E., McGinnis J.F., Self W., Seal S. Cerium oxide nanoparticles: applications and prospects in nanomedicine. *Nanomedicine*, 2013, **8**, P. 1483–1508.
- [17] Ivanova O.S., Shekunova T.O., Ivanov V.K., Shcherbakov A.B., Popov A.L., Davydova G.A., Tretyakov Y.D. One-stage synthesis of ceria colloid solutions for biomedical use. *Doklady Chem.*, 2011, **437**, P. 103–106.
- [18] Shcherbakov A.B., Zholobak N.M., Ivanov V.K., Ivanova O.S., Marchevsky A.V., Baranchikov A.E., Tretyakov Y.D. Synthesis and antioxidant activity of biocompatible maltodextrin-stabilized aqueous sols of nanocrystalline ceria. *Russ. J. Inorg. Chem.*, 2012, **57**, P. 1411–1418.
- [19] Karakoti A.S., Munusamy P., Hostetler K., Kodali V., Kuchibhatla S., Orr G., Pounds J.G., Teeguarden J.G., Thrall B.D., Baer D.R. Preparation and characterization challenges to understanding environmental and biological impacts of nanoparticles. *Surf. Interface Anal.*, 2011, **44**, P. 882–889.
- [20] Zholobak N.M., Shcherbakov A.B., Bogorad-Kobelska A.S., Ivanova O.S., Baranchikov A.Ye., Spivak N.Ya., Ivanov V.K. Panthenolstabilized cerium dioxide nanoparticles for cosmeceutic formulations against ROS-induced and UV-induced damage. *J. Photochem. Photobiol. B*, 2014, **130**, P. 102–108.
- [21] Gasyмова G.A., Ivanova O.S., Baranchikov A.Ye., Shcherbakov A.B., Ivanov V.K., Tretyakov Yu.D. Synthesis of aqueous sols of nanocrystalline ceria doped with gadolinia. *Nanosystems: Phys., Chem., Math.*, 2011, **2** (3), P. 113–120 (in Russian).
- [22] Xiao Y.D., Paudel R., Liu J., Ma C., Zhang Z.S., Zhou S.K. MRI contrast agents: Classification and application (Review). *Int. J. Mol. Med.*, 2016, **38** (5), P. 1319–1326.
- [23] Zhou Z., Lu Z.-R. Gadolinium-Based Contrast Agents for MR Cancer Imaging Wiley Interdiscip Rev Nanomed Nanobiotechnol., 2013, **5** (1), P. 1–18.
- [24] Ramalho J., Ramalho M., Jay M., Burke L.M., Semelka R.C. Gadolinium toxicity and treatment Magnetic Resonance Imaging, 2016, **34**, P. 1394–1398.
- [25] Aime S., Barge A., Botta M., Casnati A., Fragai M., Luchinat C., Ungaro R. A Calix[4]arene Gd III Complex Endowed with High Stability, Relaxivity, and Binding Affinity to Serum Albumin *Angewandte Chemie International Edition*, 2001, **40** (24), P. 4737–4739.
- [26] Zholobak N.M., Popov A.L., Shcherbakov A.B., Popova N.R., Guzyk M.M., Antonovich V.P., Yegorova A.V., Scrypnets Y.V., Leonenko I.I., Baranchikov A.Ye., Ivanov V.K. Facile fabrication of luminescent organic dots by thermolysis of citric acid in urea melt, and their use for cell staining and polyelectrolyte microcapsule labeling. *Beilstein Journal of Nanotechnology*, 2016, **7**, P. 1905–1917.
- [27] Patil S., Sandberg A., Heckert E., Self W., Seal S. Protein adsorption and cellular uptake of cerium oxide nanoparticles as a function of zeta potential. *Biomaterials*, 2007, **28** (31), P. 4600–7.
- [28] Popov A.L., Popova N.R., Selezneva I.I., Akkizov A.Y., Ivanov V.K. Cerium oxide nanoparticles stimulate proliferation of primary mouse embryonic fibroblasts in vitro. *Materials Science and Engineering: C*, 2016, **68**, P. 406–413.
- [29] Popov A.L., Ermakov A.M., Savintseva I.V., Selezneva I.I., Poltavtseva R.A., Zaraisky E.I., Poltavtsev A.M., Stepanov A.A., Ivanov V.K., Sukhikh G.T. Citrate-stabilized nanoparticles of CeO₂ stimulate proliferation of human mesenchymal stem cells in vitro. *Int. J. Nanomech. Sci. Tech.*, 2016, **7** (3), P. 1–12.
- [30] Popov A.L., Ermakov A.M., Savintseva I.V., Selezneva I.I., Poltavtseva R.A., Zaraiskii E.I., Poltavtsev A.M., Stepanova I.E., Ivanov V.K., Sukhikh G.T. Biosafety and effect of nanoparticles of CeO₂ on metabolic and proliferative activity of human mesenchymal stem cells in vitro. *Int. J. Nanomech. Sci. Tech.*, 2016, **7** (2), P. 165–75.
- [31] Muller F., Lustgarten M., Jang Y., Richardson A., van Remmen H. Trends in oxidative aging theories *Free Radic. Biol. Med.*, 2007, **43**, P. 477–503.
- [32] Zacharias L.C., Estrago-Franco M.F., Ramirez C., Kenney M.C., Takahashi W.Y., Seigel G.M., Kuppermann B.D. The effects of commercially available preservative-free FDA-approved triamcinolone (Triesence®) on retinal cells in culture. *J. Ocul. Pharmacol. Ther.*, 2011, **27** (2), P. 143–50.
- [33] Gründker C., Föst C., Fister S., Nolte N., Günthert A.R., Emons G. Gonadotropin-releasing hormone type II antagonist induces apoptosis in MCF-7 and triple-negative MDA-MB-231 human breast cancer cells in vitro and in vivo. *Breast Cancer Research*, 2010, **12**, P. R49.



NANOSYSTEMS:

PHYSICS, CHEMISTRY, MATHEMATICS

INFORMATION FOR AUTHORS

The journal publishes research articles and reviews, and also short scientific papers (letters) which are unpublished and have not been accepted for publication in other magazines. Articles should be submitted in English. All articles are reviewed, then if necessary come back to the author to completion.

The journal is indexed in Web of Science Core Collection (Emerging Sources Citation Index), Chemical Abstract Service of the American Chemical Society, Zentralblatt MATH and in Russian Scientific Citation Index.

Author should submit the following materials:

1. Article file in English, containing article title, the initials and the surname of the authors, Institute (University), postal address, the electronic address, the summary, keywords, MSC or PACS index, article text, the list of references.
2. Files with illustrations, files with tables.
3. The covering letter in English containing the article information (article name, MSC or PACS index, keywords, the summary, the literature) and about all authors (the surname, names, the full name of places of work, the mailing address with the postal code, contact phone number with a city code, the electronic address).
4. The expert judgement on possibility of publication of the article in open press (for authors from Russia).

Authors can submit a paper and the corresponding files to the following addresses: nanojournal.ifmo@gmail.com, popov1955@gmail.com.

Text requirements

Articles should be prepared with using of text editors MS Word or LaTeX (preferable). It is necessary to submit source file (LaTeX) and a pdf copy. In the name of files the English alphabet is used. The recommended size of short communications (letters) is 4-6 pages, research articles– 6-15 pages, reviews – 30 pages.

Recommendations for text in MS Word:

Formulas should be written using Math Type. Figures and tables with captions should be inserted in the text. Additionally, authors present separate files for all figures and Word files of tables.

Recommendations for text in LaTeX:

Please, use standard LaTeX without macros and additional style files. The list of references should be included in the main LaTeX file. Source LaTeX file of the paper with the corresponding pdf file and files of figures should be submitted.

References in the article text are given in square brackets. The list of references should be prepared in accordance with the following samples:

- [1] Surname N. *Book Title*. Nauka Publishing House, Saint Petersburg, 2000, 281 pp.
- [2] Surname N., Surname N. Paper title. *Journal Name*, 2010, **1** (5), P. 17-23.
- [3] Surname N., Surname N. Lecture title. In: Abstracts/Proceedings of the Conference, Place and Date, 2000, P. 17-23.
- [4] Surname N., Surname N. Paper title, 2000, URL: <http://books.ifmo.ru/ntv>.
- [5] Surname N., Surname N. Patent Name. Patent No. 11111, 2010, Bul. No. 33, 5 pp.
- [6] Surname N., Surname N. Thesis Title. Thesis for full doctor degree in math. and physics, Saint Petersburg, 2000, 105 pp.

Requirements to illustrations

Illustrations should be submitted as separate black-and-white files. Formats of files – jpeg, eps, tiff.



NANOSYSTEMS:

PHYSICS, CHEMISTRY, MATHEMATICS

Журнал зарегистрирован

Федеральной службой по надзору в сфере связи, информационных технологий и массовых коммуникаций

(свидетельство ПИ № ФС 77 - 49048 от 22.03.2012 г.)

ISSN 2220-8054

Учредитель: федеральное государственное автономное образовательное учреждение высшего образования

«Санкт-Петербургский национальный исследовательский университет информационных технологий, механики и оптики»

Издатель: федеральное государственное автономное образовательное учреждение высшего образования

«Санкт-Петербургский национальный исследовательский университет информационных технологий, механики и оптики»

Отпечатано в Учреждении «Университетские телекоммуникации»

Адрес: 197101, Санкт-Петербург, Кронверкский пр., 49

Подписка на журнал НФХМ

На первое полугодие 2019 года подписка осуществляется через

ОАО Агентство «Роспечать»

Подписной индекс 57385 в каталоге «Издания органов научно-технической информации»